Helsinki University of Technology Radio Laboratory Publications
Teknillisen korkeakoulun Radiolaboratorion julkaisuja
Espoo, September 2006 REPORT S 281

SHAPED REFLECTOR ANTENNA DESIGN AND ANTENNA MEASUREMENTS AT SUB-MM WAVELENGTHS

Janne Häkli

Dissertation for the degree of Doctor of Science in Technology to be presented with due permission for public examination and debate in Auditorium S1 at Helsinki University of Technology (Espoo, Finland) on the 29 September 2006 at 12 o'clock noon.

Helsinki University of Technology
Department of Electrical and Communications Engineering
Radio Laboratory

Teknillinen korkeakoulu
Sähkö- ja tietoliikennetekniikan osasto
Radiolaboratorio

Distribution:
Helsinki University of Technology
Radio Laboratory
P.O. Box 3000
FI-02015 TKK
Tel. +358-9-451 2252
Fax. +358-9-451 2152

ISBN 951-22-8339-5 (printed)
ISBN 951-22-8340-9 (electronic)
http://lib.tkk.fi/Diss/2006/isbn9512283409

ISSN 1456-3835

Otamedia Oy
Espoo 2006

Preface

This dissertation describes research work that I carried out in MilliLab at the Radio Laboratory of the Helsinki University of Technology (TKK) during 1999-2005. This work has been part of research projects funded by the European Space Agency (ESA) under contracts No. 13096/98/NL/SB, CCN-01 and 19131/05/NL/LvH. The research has been in part funded by the Academy of Finland and TEKES under their centre-of-excellence – program and by Graduate School in Electronics, Telecommunications and Automation (GETA). The financial support of the following foundations is gratefully acknowledged: Emil Aaltonen Foundation, the Finnish Cultural Foundation, the Foundation for Commercial and Technical Sciences, the Foundation of the Finnish Society of Electronics Engineers, the Foundation of Technology, Nokia Foundation, and Ulla Tuominen Foundation.

I am grateful for my supervisor Professor Antti Räisänen for the opportunity to work in the fascinating field of the submillimetre wave antenna measurements. It has been especially interesting to learn about reflector antenna synthesis and apply it to sub-millimetre wave CATR feed design. The world of high-precision mechanics has also been a lot of fun to explore; not to mention the antenna testing. I am also grateful to Professor Räisänen for his comments on this thesis and keeping my doctoral studies progressing even during hectic times in research projects. I thank Professor Jussi Tuovinen from VTT for his participation in the projects and his suggestions and comments over the years. Dr. Juha Ala-Laurinaho deserves my thanks as the instructor of my Master's and Licentiate thesis. His background in mathematics and the help he provided to an electrical engineer with the mathematics is also much appreciated. I am also grateful to Mr. Jerzy Lemanczyk from ESA / ESTEC for his constructive criticism on our research in the ESA funded projects.

I wish to thank Associate Professor Manuel Sierra Castañer of Technical University of Madrid (UPM) and Dr. Axel Murk from University of Bern for pre-examining this thesis and making valuable observations on the work. The people in our sub-millimetre wave hologram research group deserve my warmest thanks for being dedicated and professional colleagues and most of all, being very nice people to work with and to have fun outside the lab. I especially appreciate the fruitful co-operation with Mr. Tomi Koskinen and working with Ms. Anne Lönnqvist on many occasions – for example as 'coal miners' placing absorbers to measurement set-ups. Dr. Juha Mallat is thanked for his brilliant ideas and his legendary humour. They and the other members (current and former) of our group and the current hologram CATR project team are also thanked for numerous others things that I cannot list there – instead I only list here their names: Dr. Jussi Säily, Dr. Ville Möttönen, Mr. Ville Viikari, Mr. Aki Karttunen, Mr. Matti Vaaja, Mr. Jukka Heinonen, and Mr. Aleksi Tamminen. Thank you for the co-operation and everything else over the years. Mr. Eino Kahra from the Radio Laboratory workshop and Mr. Henry Rönnberg from the Metsähovi Observatory workshop are acknowledged for their valuable help with the various mechanical structures needed in the construction of the measurement set-ups.

The whole personnel of the Radio Laboratory deserve warm thanks for providing a pleasant and inspiring environment to work in. I regret that I cannot mention everyone who has worked in the Lab over the years here, but I would like to mention just a few. First, the other Master's thesis workers who started the same year in the Radio Laboratory as I and who have already completed their doctoral degrees or just completing it: Dr. Kati Sulonen, Dr. Outi Kivekäs, Dr. Ilkka Salonen, and Mr. Pasi Suvikunnas. The shared experience of starting the

post-graduate studies and research work helped all of us in the early stages of our post-graduate studies despite our different individual research topics and, it made it more fun. Second, I thank Dr. Tommi Laitinen, Dr. Jari Salo and Dr. Dmitri Lioubtchenko for the interesting discussions on science and research.

Finally, I would like thank all my friends, who have provided much needed diversions to the immersion in the research – in many faraway places on six continents of the world. I'm also grateful to my parents, my late grandfather and other relatives for all their support and encouragement.

"For in much wisdom is much grief; and he who increases knowledge increases sorrow."

Ecclesiastes 1:18

Espoo, August 10, 2006

Janne Häkli

HELSINKI UNIVERSITY OF TECHNOLOGY
P. O. BOX 1000, FI-02015 TKK
http://www.tkk.fi

ABSTRACT OF DOCTORAL DISSERTATION

Author Janne Häkli

Name of the dissertation

Shaped reflector antenna design and antenna measurements at sub-mm wavelengths

Date of manuscript 29.8.2006 | Date of the dissertation 29.9.2006

☒ Monograph ☐ Article dissertation (summary + original articles)

Department Electrical and Communications Engineering
Laboratory Radio Laboratory
Field of research Radio Engineering
Opponent(s) Professor Per-Simon Kildal
Supervisor Professor Antti Räisänen
(Instructor)

Abstract

In this thesis, a ray-tracing based synthesis procedure for shaped dual reflector antennas at the sub-mm wavelengths is developed. A dual reflector feed system (DRFS) consisting of two shaped hyperboloid reflectors for hologram based compact antenna test range (CATR) is designed. The DRFS provides a shaped hologram illumination improving the hologram performance and manufacturability. The DRFS operation is verified with simulations and planar near-field measurements at 310 GHz. The measured and simulated beams are within ±0.3 dB from each other.

The applicability of the DRFS for providing a shaped illumination for the holograms in CATRs is verified experimentally with quiet-zone field amplitude and phase measurements of test holograms at 310 GHz. The shaped hologram illumination eliminates narrow slots in the hologram pattern, which simplifies the etching of the pattern. In addition, the shaped illumination allows the holograms to operate also at the linear horizontal polarisation as previously the hologram operation was limited to the vertical polarisation.

Cross-polarisation properties of the holograms are investigated using a polarization grid to suppress the cross-polarisation in the hologram illumination by 21 dB. It is concluded that the hologram contributes mostly to the cross-polarisation level of a hologram-based CATR. By the placing the cross-polarisation grid behind the hologram, the cross-polarisation level in the quiet-zone can be reduced to below -33 dB.

For improving the measurement accuracy of planar near-field measurements at sub-mm wavelengths, the measurement errors and their contribution to the measurement uncertainty are determined. The measurement system is improved for more accurate near-field measurements. Error correction techniques based on error measurements are used to reduce the phase measurement uncertainty from ±14° to ±8° at 310 GHz in one-dimensional scans of a plane wave corresponding to the quiet-zone of a hologram.

A hologram-based CATR is constructed for testing a 1.5 m reflector antenna (ADMIRALS RTO) at 322 GHz. The measured radiation pattern of the RTO corresponds reasonably well to the simulated pattern, but the quiet-zone field non-ideality affects the measurement results. As estimated effect of the quiet-zone does not explain all the discrepancies between the measurements and simulations, it is concluded that the reflector surface differs from the simulated surface.

Keywords reflector antennas, compact antenna test range, near-field measurements, sub-millimetre wave

ISBN (printed) 951-22-8339-5 | ISSN (printed) 1456-3835

ISBN (pdf) 951-22-8340-9 | ISSN (pdf)

ISBN (others) | Number of pages 217

Publisher Helsinki University of Technology Radio Laboratory

Print distribution Helsinki University of Technology Radio Laboratory

☒ The dissertation can be read at http://lib.tkk.fi/Diss/2006/isbn9512283395

TEKNILLINEN KORKEAKOULU PL 1000, 02015 TKK http://www.tkk.fi	VÄITÖSKIRJAN TIIVISTELMÄ

Tekijä Janne Häkli

Väitöskirjan nimi

Muotoiltujen heijastinantennien suunnittelu ja antennimittaukset alimillimetriaaltoalueella

Käsikirjoituksen jättämispäivämäärä 29.8.2006	Väitöstilaisuuden ajankohta 29.9.2006

☒ Monografia ☐ Yhdistelmäväitöskirja (yhteenveto + erillisartikkelit)

Osasto	Sähkö- ja tietoliikennetekniikka
Laboratorio	Radiolaboratorio
Tutkimusala	Radiotekniikka
Vastaväittäjä(t)	Professori Per-Simon Kildal
Työn valvoja	Professori Antti Räisänen
(Työn ohjaaja)	

Tiivistelmä

Tässä väitöskirjassa kehittiin säteenseurantaan perustuva kahden muotoillun heijastinantennin synteesimenetelmä alimillimetriaaltoalueelle. Menetelmän avulla suunnitellaan kahteen muotoiltuun hyperboloidiheijastimeen perustuva kvasioptinen syöttö hologrammiin perustuvaan kompaktiin antennimittauspaikkaan. Kvasioptinen syöttö mahdollistaa hologram muotoillun valaisun avulla merkittäviä parannuksia hologrammin toimintaan: valmistettavuus helpottuu ja hologrammi voi toimia myös vaakapolarisaatiolla. Tähän asti hologrammin toiminta on rajoittunut pystypolarisaatiolle. Kvasioptisen syötön toiminta testataan simuloinnein ja planaarisen lähikenttämittauksin 310 GHz:n taajuudella. Mitattu ja simuloitu keila vastaavat toisiaan ±0.3 dB:n tarkkuudella. Syötön soveltuvuus hologrammien valaisuun varmistetaan koehologrammien mittausten avulla ja parannukset hologrammien toimintaan osoitetaan mittausten avulla.

Hologrammien ristipolarisaatio-ominaisuuksia tutkitaan polarisaattorihilan avulla, joka vähentää ristipolarisaatiota 21 dB hologrammin valaisussa. Tämän kokeen perusteella hiljaisen alueen ristipolarisaatio aiheutuu pääasiassa hologrammin itsensä tuottamasta ristipolarisaatiosta. Käyttämällä polarisaattorihilaa hologrammin ja hiljaisen alueen välissä voidaan mittauspaikan ristipolarisaatiotaso laskea alle -33 dB:n.

Planaaristen lähikenttämittausten tarkkuuden parantamiseksi alimillimetriaaltoalueella tarkastellaan mittausvirhelähteitä ja niiden vaikutusta mittausepävarmuuteen. Mittausjärjestelmää parannetaan mittausten tarkkuuden ja toistettavuuden parantamiseksi. Erillisiin virheen mittauksiin perustuvia virheenkorjausmenetelmiä käytetään vaiheen mittausepävarmuuden pienentämiseksi. Näiden menetelmien avulla mittausepävarmuus pienenee ±14°:sta ±8°:een 310 GHz:llä tasoaallon vaiheen mittauksessa kentän pysty- ja vaakaleikkauksissa.

Hologrammiin perustuva kompakti antennimittauspaikka rakennetaan 1.5-metrin heijastinantennin testaamiseksi taajuudella 322 GHz. Antennin mitattu suuntakuvio vastaa simuloitua suuntakuviota melko hyvin, mutta mittauspaikan epäideaalinen hiljainen alue vaikuttaa mittaustulokseen. Kaikki erot mitatun suuntakuvion ja simulointien välillä, kun otetaan huomioon arvioitu hiljaisen alueen kentän vaikutus, eivät johdu hiljaisen alueen kentästä. Näin ollen voidaan todeta että testattavan antennin peilin pinnan muoto poikkeaa simuloinneissa käytetystä pinnasta.

Asiasanat	heijastinantennit, kompakti antennimittauspaikka, lähikenttämittaukset, alimillimetriaallot		
ISBN (painettu)	951-22-8339-5	ISSN (painettu)	1456-3835
ISBN (pdf)	951-22-8340-9	ISSN (pdf)	
ISBN (muut)		Sivumäärä	217
Julkaisija	Teknillisen korkeakoulun Radiolaboratorio		
Painetun väitöskirjan jakelu	Teknillisen korkeakoulun Radiolaboratorio		

☒ Luettavissa verkossa osoitteessa http://lib.tkk.fi/Diss/2006/isbn9512283395

Contents

Symbols

a	axial ratio, function, radius, half vertex distance of a hyperboloid
b	constant, parameter
c	velocity of light, parameter, half distance between the foci of a hyperboloid
d	distance
e	eccentricity
f	function, floating term, focal length
f_{main}	focal length of the main reflector
f_{sub}	focal length of the sub-reflector
f_{system}	system focal length
i	index
j	imaginary unit
k	wave number, coefficient
$\bar{k}$	propagation vector
k_0	wave number in free-space
l	length
n	index of refraction, index
$\bar{n}$	surface normal
n_{ray}	number of the ray ring
n_{tube}	number of the flux tube ring
m	index
m_{ray}	number of the ray
m_{tube}	number of the flux tube
$po1$	number of current elements in the radial direction
$po2$	number of current elements in the angular direction
r	distance
$\bar{r}, \bar{r}'$	vector
r_0	radius of the minimum sphere
r_{sub}	sub-reflector distance from the main reflector
r_{main}	main reflector distance from the main reflector
$s,\ s_0$	distance
$\bar{s}$	directional vector
$\bar{s}_i$	directional vector of the incident ray
$\bar{s}_r$	directional vector of the reflected ray
t	time, parameter
u	mean
$\bar{u}, \hat{u}$	unit vector
w	lock-window
x	Cartesian coordinate, variable
y	Cartesian coordinate
z	Cartesian coordinate

A area, attenuation factor
$\overline{A}$ plane wave spectrum
$\overline{A}_e$ electric vector potential
$\overline{A}_m$ magnetic vector potential
$\overline{B}$ magnetic flux
C path, coefficient
D diffraction coefficient, coefficient, diameter
$\overline{D}$ electric displacement field
$\overline{E}$ electric field
$\overline{E}_a$ electric field intensity in an aperture
E_{ave} average amplitude of the electric field
$\overline{E}_d$ diffracted electric field
$\overline{E}_{fr}$ fringe electric field
$\overline{E}_{GO}$ electric field computed with the geometrical optics approximation
$\overline{E}_{GTD}$ electric field computed with the geometrical theory of diffraction
E_{hor} amplitude in the horizontal pattern cut
$\overline{E}_i$ incident electric field
E_{in} amplitude of the input electric field
E_{out} amplitude of the output electric field
$\overline{E}_{PO}$ electric field related to physical optics approximation
$\overline{E}_r$ reflected electric field
$\overline{E}_t$ tangential electric field
$\overline{E}_{TE}$ transverse electric field
$\overline{E}_{tot}$ total electric field
$\overline{E}_{TM}$ transverse magnetic field
E_{tr} transmitted electric field
E_{ver} amplitude in the vertical pattern cut, vertical field component amplitude
F polynomial, focus, function
F_0 system focus
F_1, F_2 foci of the reflectors
$\overline{\overline{G}}$ dyadic Green's function
$\overline{H}$ magnetic field vector
$\overline{H}_a$ magnetic field vector in an aperture
$\overline{J}_e$ electric current
$\overline{J}_{es}$ electric current density
$\overline{J}_m$ magnetic current
$\overline{J}_{ms}$ magnetic current density
L length
$\overline{L}$ eikonal
M number of rays

$\overline{M}$ vector wave function
N number, number of ray rings, the order of a function
$\overline{N}$ vector wave function
P power, power density, point, polynomial
P_i incident power
P_{in} input power
P_{out} output power
P_{probe} power in the probe pattern
P_r receiver power
Q modal coefficient
R radial distance, radius
$\overline{R}$ direction vector
$\overline{\overline{R}}$ probe pattern
S surface
T transmittance
T_B binarised transmittance
W weighting function

α angle, parameter, scaling factor
α_{main} offset angle of the main reflector
α_{sub} offset angle of the sub-reflector
β angle, parameter, scaling factor
γ angle
ε permittivity, number, error
ε_0 permittivity of vacuum
η wave impedance
θ angle, beam width
$\hat{\theta}$ unit vector
θ_{feed} half beam width of the feed horn
θ_{main} half beam width of the main reflector
λ wavelength
μ permeability
μ_0 permeability of vacuum
ν spatial carrier frequency, velocity
ρ, ρ' radial distance
$\rho_{in,\max}$ radius of the input aperture rim
$\rho_{out,\max}$ radius of the output aperture rim
ρ_c threshold radial distance
ρ_e electric charge
ρ_m magnetic charge
σ standard deviation
τ tilt angle
ϕ, ϕ' angle, polar coordinate

$\hat{\phi}$	unit vector
χ	parameter, length of the ray, polarisation ratio
χ_1, χ_1^*	excess spatial bandwidth factor
φ	phase
ψ	parameter, angle, phase
ψ_e	phase correction term
ω	angular frequency
Δr	difference in the distance
$\Delta\theta$	difference in the angle, angular spacing
X	cross-polarisation ratio
Ψ	phase term

Abbreviations

AUT	Antenna under test
CATR	Compact antenna test range
DRFS	Dual reflector feed system
FDTD	Finite-difference time-domain
GO	Geometrical optics
GRASP	General reflector and antenna farm analysis software by Ticra
GTD	Geometrical theory of diffraction
MVNA	Millimetre wave network analyser
NIST	National Institute of Standards and Technology, USA
PCB	Printed circuit board
PO	Physical optics
PTD	Physical theory of diffraction
QZ	Quiet-zone
RCS	Radar cross section
RMS	Root mean squared
RSS	Root sum of squares
SWE	Spherical wave expansion
TE	Transverse electric
TM	Transverse magnetic
UTD	Uniform geometrical theory of diffraction

1 Introduction

1.1 Background

Sub-millimetre waves (300 GHz – 3 THz), or the THz-frequencies as they are also often called, have important applications in astronomy, space science, remote sensing, limb sounding, and in imaging for security applications. These applications require an antenna for receiving the sub-millimetre waves and many of the applications are best suited for spaceborne instruments as many of the interesting molecules (H_2O, O_2, O_3, etc.) are most abundant in the Earth's atmosphere making. The observation of spectral lines originating from extraterrestrial sources inside the atmosphere are impossible inside the atmosphere because of the high atmospheric attenuation. Examples of scientific satellite projects of the European Space Agency (ESA) scheduled to be launched in the near future include Herschel (formerly FIRST) and Planck, which both have large sub-mm wavelength antennas. Planned remote sensing instruments for the future with sub-mm wavelength antennas include for example Submillimeter Observation of Processes in the Atmosphere Noteworthy for Ozone (SOPRANO).

The sub-millimetre wavelength antennas, as all antennas, should be tested with measurements of the antenna properties to ensure that no significant design or manufacturing errors have occured. This is especially important in highly expensive space missions as normally the antenna cannot be repaired or replaced after the launch. Accurate antenna pattern measurements of electrically large sub-mm wavelength antennas and reliable antenna testing are very demanding. Currently, no large-scale antenna measurement facilities exist for short sub-millimetre wavelengths and there is a great need to develop and improve the measurement techniques and facilities.

In the Radio Laboratory of Helsinki University of Technology (TKK), a compact antenna test range (CATR) based on a hologram was invented in the early 1990's and it has been since applied at sub-millimetre wavelengths also. The main advantage of using a hologram as the collimating element in a CATR is the inexpensive and relatively simple manufacturing of the hologram; the hologram pattern can be etched on a metal-plated dielectric film using photolithography. The hologram manufacturing is relatively simple as high accuracy is only needed in the two-dimensional pattern instead of in three-dimensions as in the case of the reflectors conventionally used in CATRs. The CATR based on a hologram is a highly promising technique for sub-mm wavelength antenna measurements and testing.

1.2 Objectives and scope of the research

The main objectives of the research resulting into this doctoral thesis has been to improve further the hologram based compact antenna test range for sub-millimetre wave antenna testing, to investigate and develop sub-millimetre wavelength antenna measurement techniques and to develop the necessary methods and other means to carry out this research. In addition, the aim is to demonstrate the applicability of the hologram CATR for practical sub-mm wavelength antenna tests.

Although the hologram has many advantages in CATR applications, it has also disadvantages. The main challenge in the development of the hologram CATR has been the accurate manufacturing of large holograms up to several metres in diameter. In addition, the holograms have operated at only one polarisation (linear vertical) and the cross-polarisation level has also been relatively high for testing antennas with low cross-polarisation levels. The aim of the research is to improve these features in the hologram CATR.

To achieve these improvements a shaped hologram illumination is needed and the objective of the research is to develop a dual reflector feed system for providing the shaped hologram illumination. In addition, the aim is to study the causes of the undesired properties of the hologram and to find means to improve them by increasing the knowledge on the hologram at sub-millimetre wavelengths. The measurement accuracy of a planar near-field scanner is improved for extending the usability of an existing microwave scanner for sub-mm wavelengths and to allow accurate testing of the holograms and the developed dual reflector feed system.

1.3 Scientific contribution

The main scientific contributions of this doctoral thesis are the following:

i) The development of a ray-tracing based synthesis procedure for shaped dual reflectors. The procedure is a significantly modified version of the previously published methods making it especially suitable for designing a dual reflector feed system for sub-mm wavelength holograms.

ii) Designing of a dual reflector feed system (DRFS) consisting of two shaped hyperboloid reflectors that radiates a shaped diverging beam. This is a novel type of a reflector feed at sub-millimetre waves.

iii) The improvement of the hologram performance for CATR applications. The shaped hologram illumination allows the holograms to operate better also at the horizontal linear polarisation and facilitates the hologram manufacturing by simplifying the etching of the hologram patterns. The improvements have been verified experimentally with near-field measurements.

iv) Improved measurement accuracy in sub-millimetre wavelength planar near-field measurements. The investigation of the measurement errors allows reduction of the measurement uncertainty and the extension of the frequency range of an existing microwave near-field scanner for antenna testing at higher frequencies.

v) Increased knowledge and understanding of the sub-millimetre wavelength hologram operation. The measurements of the holograms carried out and the analysis of the results provide new information helping the design of the holograms and the development of the hologram CATR.

vi) The demonstration of the applicability of the hologram CATR for sub-millimetre wavelength antenna testing. The antenna test campaign and the associated research carried out prior to it demonstrate the capability to perform antenna testing at sub-millimetre wavelengths in a hologram based CATR specially constructed for the tests in question.

vii) Analysis of the operation of the 1.5 m reflector antenna under test at the frequency of 322 GHz based on the radiation pattern measurements and simulations. Based on this analysis, it can be concluded that two-dimensional contour maps of the antenna pattern should be measured to fully understand the antenna operation at sub-millimetre wavelengths.

The main results of this thesis have been published in scientific journals [O1–O4], and in total the author of this thesis has authored and co-authored over 65 conference and journal publications on the topics of this thesis and related topics. The international publications include [O1–O52].

1.4 Contents of the thesis

The first part of this thesis covers the theoretical back-ground of the physical phenomena related to the issues investigated in this thesis and the methods used. In Chapter 2, basic reflector antennas are described with emphasis on the analysis methods for the reflector antenna radiation. The reflector antenna synthesis methods described in the literature are also reviewed. Chapter 3 discusses the sub-millimetre wavelength antenna measurement techniques and describes the radiation properties of the antennas.

The second part of thesis describes the developed ray-tracing based synthesis procedure for shaped dual reflector antennas and its use on designing a dual reflector feed system (DRFS) for a hologram CATR. Chapter 4 contains the description of the synthesis procedure and an analysis on the accuracy of the procedure. In Chapter 5, the design of the DRFS is discussed and the designed antenna structure is described. In addition, the simulation and measurement results for the DRFS beam at the frequency of 310 GHz are presented.

In the third part of this thesis, in Chapter 6, the possibilities to improve the hologram performance in CATRs using the shaped hologram illumination with the DRFS are investigated. These improvements include the hologram operation at the linear horizontal polarisation, reduced cross-polarisation level and simplification of the hologram manufacturing. This investigation is based on quiet-zone field measurements of the test holograms.

The final part of this thesis deals with sub-millimetre wavelength antenna testing. In Chapter 7, the measurement accuracy with the planar near-field scanner is discussed together with the improvements and upgrades done to the measurement system. The measurement uncertainties for phase, amplitude and cross-polarisation level are determined. In addition, error correction techniques used to reduce the phase measurement uncertainty are described. Chapter 8

describes the constructed hologram-based CATR for testing a 1.5 m reflector antenna at 322 GHz. The quiet-zone field and antenna measurement results are presented together with the analysis of the results and with conclusions on the antenna operation. Chapter 9 contains the conclusions.

1.5 Contribution of the author

This thesis describes the research done mostly by the author: the author developed the synthesis procedure for the dual reflector feed system (DRFS), wrote the computer programs, designed the DRFS, performed the GRASP-simulations and the near-field measurements of the DRFS and test holograms, performed the study on the measurement accuracy of the near-field scanner and was responsible for most of the improvements to the measurement system described in Chapter 7. The design and the construction of the hologram CATR, and the measurements of the 1.5 m antenna described in Chapter 8 were done as a collective team effort by the hologram research group at TKK. The author participated to this work as a member of the team. The simulations of the antenna under test and the analysis of the antenna measurement results were done by the author.

The work was supervised by Professor Antti Räisänen and in part co-supervised by Professor Jussi Tuovinen. Dr. Juha Ala-Laurinaho had an advisory role and he was also a co-supervisor in the work as the instructor in the author's Master's and Licentiate thesis, which covered some parts of this thesis.

The sub-millimetre wave research group has supported the author's research. Especially, Tomi Koskinen has designed all the holograms, and done the hologram simulations and measured the hologram manufacturing errors and analysed their effect on the hologram performance. He also assisted in some of the hologram measurements. Anne Lönnqvist assisted in many of the hologram measurements and helped in the construction of the measurement set-ups. Her help in the using the sub-millimetre wave vector network analyser was also significant. Dr. Jussi Säily developed and assembled the automated measurement system allowing computer controlled sub-mm wavelength near-field measurements and he also developed the cable flexing phase correction system. Dr. Juha Mallat adviced with the use of the measurement equipment. He had also a general advisory role as the MilliLab Senior Scientist and his innovation of using an extension arm with the digital feeler pin allowed the precise alignment of the DRFS in the near-field measurements. Ville Viikari wrote the computer program for computing the effect of quiet-zone field on the simulated antenna radiation pattern discussed in Chapter 8 and computed the plane wave spectrum for the quiet-zone field.

In addition to the above mentioned members of the sub-millimetre research group, the following undergraduate students (at the time) assisted in the research work: Eero Rinne tested some algorithms for the DRFS synthesis software and Aleksi Tamminen did additional DRFS measurements and assisted in the preparations for the polarisation grid measurements. Most of the mechanical parts were designed and manufactured by Eino Kahra and Henry Rönnberg.

2 Reflector antenna analysis and synthesis

An antenna can be defined as a device for radiating and receiving radio waves [1]. Reflector antenna consists of a primary feed and of a reflector or several reflectors. The reflector transforms the feed radiation into the radiation of the reflector antenna through reflections. The opening of the reflector into the free-space, the aperture, can be also considered as the source of the antenna radiation. Reflector antennas are therefore aperture radiators. Primary feed in a reflector antenna can be, for example, a horn, a dipole or a microstrip antenna. Horn antennas are commonly used as feeds at sub-millimetre wavelengths.

2.1 Common reflector antenna types

Reflector antennas are used in terrestrial and satellite communication applications, in radar applications, and in radio astronomy. Typical uses for reflector antennas include radio links, satellite broadcasting and reception antennas, and radio telescopes. Reflector antennas are especially suitable for high-gain narrow beam antennas with low side-lobes. They can also be used for multiple beams and shaped beams. The reflector surfaces used in reflector antennas are usually based on conic sections. Paraboloid, ellipsoid and hyperboloid surfaces are presented in Figure 2.1. Spherical surfaces can also be used in reflector antennas.

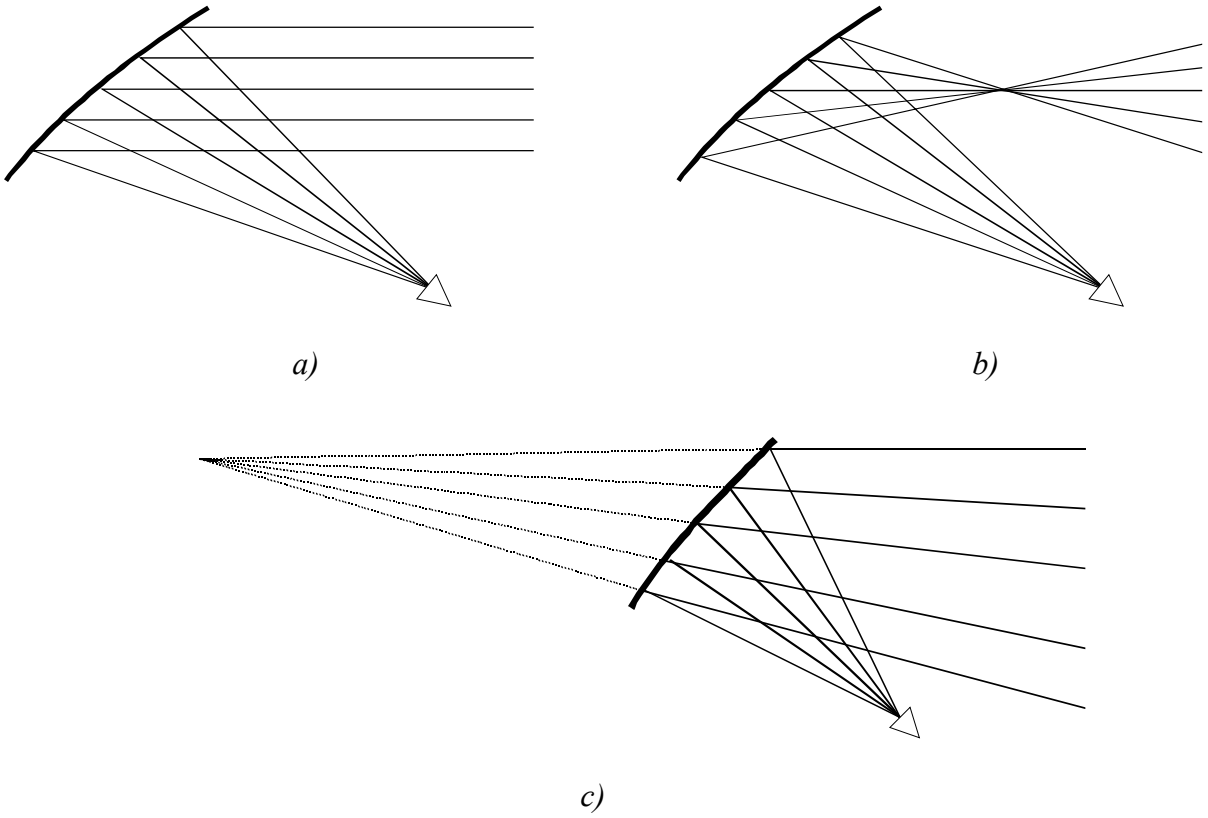

Figure 2.1 *Conic sections – a) paraboloid, b) ellipsoid, c) hyperboloid.*

A paraboloid reflector collimates the radiation originating from the focus. An ellipsoidal surface focuses the beam originating from one focus to the other and a hyperboloid reflector

has a virtual focus behind the reflector from where the radiation from the focus appears to originate. Paraboloidal antennas are used for narrow beam antennas. Ellipsoidal and hyperboloidal reflectors are usually used to relocate focal points in quasi-optical systems and as sub-reflectors for paraboloids. Cylindrical or torus-shaped reflector surfaces can also be used.

2.1.1 Single reflector antennas

Paraboloid antennas are usually used in applications where high gain is desired. The simplest antenna structure uses a front-fed paraboloid with the feed in the paraboloid focus. It has the disadvantage that the feed and its support structure block the antenna aperture. This blockage reduces the aperture efficiency and antenna gain. In addition, scattering from the feed structure increases side-lobes in the radiation pattern. Aperture blockage can be avoided by using an offset feed. However, the offset structure is mechanically more complicated and the asymmetrical structure causes cross-polarisation. Matched feeds can be used to compensate the cross-polarisation [2]. Front- and offset fed paraboloid antennas are illustrated in Figure 2.2.

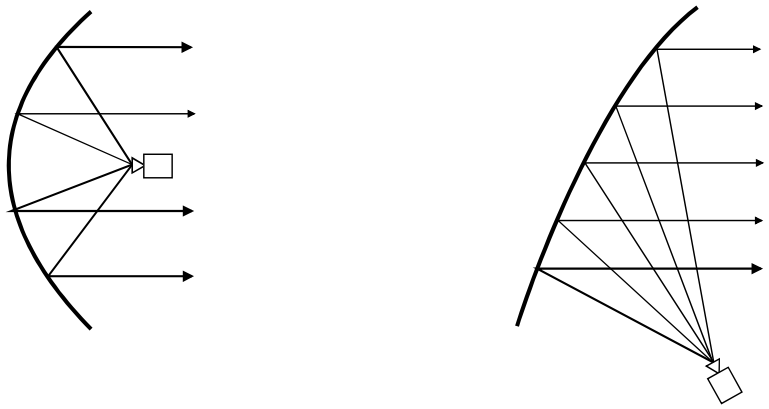

Figure 2.2 *Front-fed and offset fed paraboloid antennas.*

Concave spherical mirrors have been used widely in optics as it is relatively easy to achieve the accuracy needed in optics with them. Spherical surface focuses the incident radiation from wide angular region around the direction of the antenna axis onto a caustic surface [3]. This deviation from a single focal point is called spherical aberration. It can be compensated using a suitable feed. Spherical reflectors can be used in beam scanning and multiple beam applications as they allow relatively large angular coverage [4,5].

2.1.2 Dual and multi-reflector antennas

A second reflector in a reflector antenna allows improved control of the antenna radiation. The smaller auxiliary reflector is usually called the sub-reflector and the larger reflector is called the main reflector. The basic dual paraboloid antennas are based on the optical telescopes invented in the 17th century by Cassegrain and Gregory. The Cassegrain antenna has a hyberboloidal sub-reflector, which increases the effective focal length of the system. Gregorian antennas have an ellipsoidal sub-reflector for decreasing the effective focal length. The offset versions of these antennas are shown in Figure 2.3.

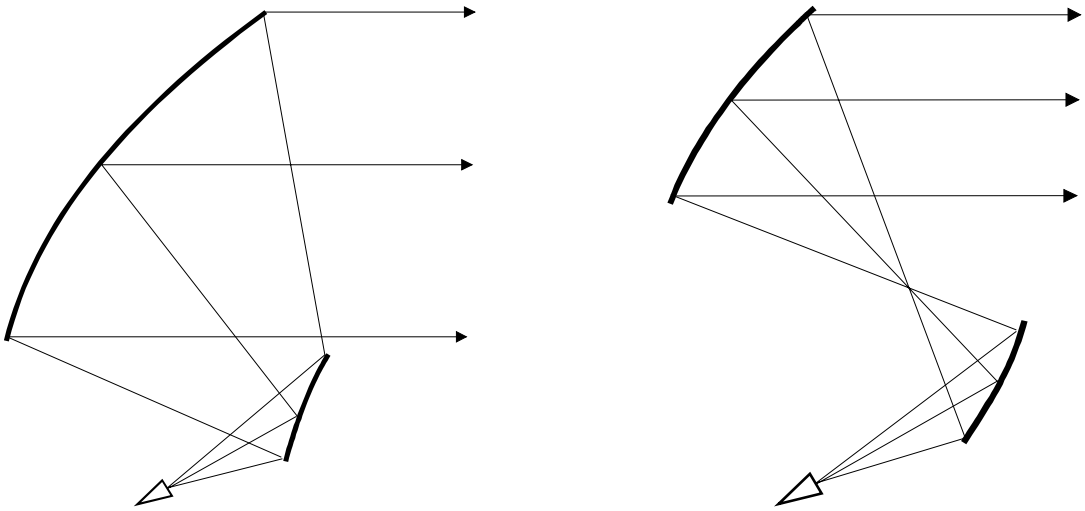

Figure 2.3 *Offset Cassegrain and Gregorian antennas.*

The increased effective focal length of the Cassegrain antenna reduces spill-over and side-lobe level. The primary feed can be also located more conveniently when offset structure is used, but asymmetrical offset configuration causes cross-polarisation. This cross-polarisation can be mostly compensated using a compensated design that fulfils so called Mizugutch-condition, when the cross-polarisation of an asymmetrical sub-reflector cancels the cross-polarisation caused by the main reflector [6].

Several reflectors can be used to even more accurate control of the antenna radiation and to relocate the primary feed to a more convenient location. A Cassegrain-antenna with a quasi-optical feed with several mirrors can be considered as a multi-reflector antenna system. Shaped sub-reflectors are also used to improve the performance of a non-shaped main reflector.

2.1.3 Shaped reflector antennas

Antenna performance can be improved by shaping the reflector surfaces to achieve more control on the antenna radiation. Shaping can be used to increase the aperture efficiency and gain of the antenna, to reduce side-lobe level, to improve the beam scanning capabilities of an antenna and to optimise other antenna characteristics. Shaping can be applied both to the main reflector surface and to the sub-reflector or only to either one of them. For example, the spherical aberration in the case of a spherical reflector can be corrected with a shaped sub-reflector [7,8].

Commonly used approach to reflector antenna shaping is to shape the sub-reflector to control the aperture field amplitude and correct the phase with shaping of the larger main reflector [9]. Another approach is to use two shaped sub-reflectors as a reflector feed for a much larger non-shaped main reflector or reflectors, see e.g. [10–13].

Shaped reflector antennas can also be used for shaped beams when a selected coverage or different radiation to different directions is desired. Most common applications are in satellite broadcasting or communications where geographical coverage is preferred. The beam can be shaped to follow the outlines the continent or country that is the service area. Such beams are usually called contoured beams. Contoured beams are achieved with suitable reflector shaping with a single feed or with array type feeds. Both approaches can also be used simultaneously [14]. The beam forming network may be complicated and may have high losses [2] and therefore shaped reflectors are usually preferred due to their smaller mass and lower losses. The advantage of the multiple feeds is the ability to reconfigure the antenna, for example when the coverage region should be changed. Re-configurable reflector antennas have also been investigated during the past years. Examples of re-configurable reflector antenna designs are presented for example in [14, 15].

2.2 Analysis of reflector antenna radiation

Reflector antenna radiation can be computed from the surface currents on the reflectors or from the main reflector aperture field if the reflector antenna is considered as an aperture radiator. Corresponding reflector antenna analysis methods can be called current distribution method and aperture distribution method [9]. In optics, rays are used to describe propagation of light through media. Ray optics can also be used for radiowaves.

2.2.1. Radiation of current sources

The electromagnetic radiation is described with generalized time-harmonic Maxwell's equations:

$$\nabla \times \overline{E} = -j\omega\overline{B} - \overline{J}_m \tag{2.1}$$

$$\nabla \times \overline{H} = j\omega\overline{D} + \overline{J}_e \tag{2.2}$$

$$\nabla \cdot \overline{B} = \rho_m \tag{2.3}$$

$$\nabla \cdot \overline{D} = \rho_e, \tag{2.4}$$

where $\overline{E}$ is the electric field, $\overline{H}$ is the magnetic intensity, $\overline{D}$ is the electric displacement field, and $\overline{B}$ is the magnetic flux. The electric and magnetic currents are $\overline{J}_e$ and $\overline{J}_m$, ρ_e and ρ_m are the electric and magnetic charge and the angular frequency is $\omega=2\pi f$. Magnetic current and charge are non-physical, but helpful mathematical aids.

The analysis of the radiation of surface currents can be often simplified by introducing auxiliary functions called vector potentials [16, 17]

$$\overline{A}_e = \frac{\mu}{4\pi}\int_s \overline{J}_{es}\frac{e^{-jkR}}{R}ds', \tag{2.5}$$

$$\overline{A}_m = \frac{\varepsilon}{4\pi}\int_s \overline{J}_{ms}\frac{e^{-jkR}}{R}ds', \tag{2.6}$$

where $\overline{A}_e$ is the electric vector potential, $\overline{A}_m$ is the magnetic vector potential, ε is the permittivity, μ is the permeability and $\overline{J}_{es}$ and $\overline{J}_{ms}$ are the electric and magnetic current densities on the reflector surface *S*. The distance from the surface point to the observation point is $R = \left|\overline{r} - \overline{r}'\right|$, where $\overline{r}$ is the vector to the observation point and $\overline{r}'$ is the vector to the point in the surface containing the surface currents. The wave number k is related to the angular frequency ω with

$$k = \omega\sqrt{\mu\varepsilon} = \frac{2\pi}{\lambda}. \tag{2.7}$$

The electric and magnetic fields can be determined with the help of Equations (2.5) and (2.6) [3,17]:

$$\overline{E} = -j\omega\overline{A}_e - j\frac{1}{\omega\mu\varepsilon}\nabla\left(\nabla\cdot\overline{A}_e\right) - \frac{1}{\varepsilon}\nabla\times\overline{A}_m, \tag{2.8}$$

$$\overline{H} = \frac{1}{\mu}\nabla\times\overline{A}_e - j\omega\overline{A}_m - j\frac{1}{\omega\mu\varepsilon}\nabla\left(\nabla\cdot\overline{A}_m\right). \tag{2.9}$$

The geometry related to the surface current radiation analysis is illustrated in Figure 2.4.

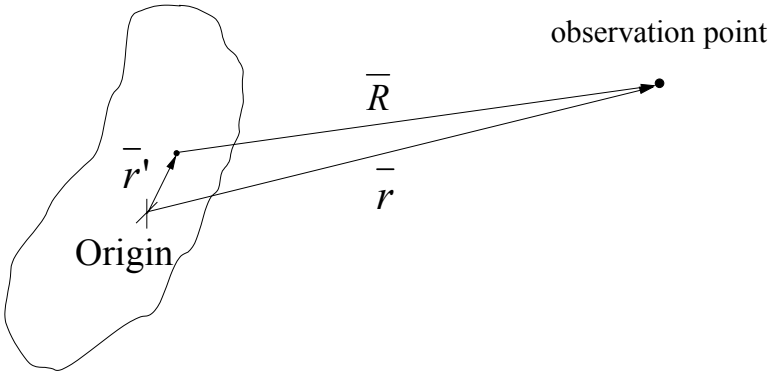

Figure 2.4 *Radiation of currents on a surface.*

Applying the differential operators in Equations (2.8) and (2.9), the electric and magnetic fields become [17]

$$\overline{E}(\overline{r}) = \frac{\eta}{4\pi}\int_S \left(\overline{J}_{es}\left(-\frac{j}{kR} - \frac{1}{k^2R^2} + \frac{j}{k^3R^3} \right) + (\overline{J}_{es}\cdot\hat{R})\hat{R}\left(\frac{j}{kR} + \frac{3}{k^2R^2} - \frac{3j}{k^3R^3} \right) \right) e^{-jkR} k^2 ds' - \frac{1}{4\pi}\int_S \overline{J}_{ms}\times\hat{R}\frac{1}{k^2R^2}(1+jkR)e^{-jkR}k^2 ds' \quad (2.10)$$

$$\overline{H}(\overline{r}) = \frac{1}{4\pi}\int_S \overline{J}_{es}\times\hat{R}\frac{1}{k^2R^2}(1+jkR)e^{-jkR}k^2 ds' + \frac{1}{4\pi\eta}\int_S \left(\overline{J}_{ms}\left(-\frac{j}{kR} - \frac{1}{k^2R^2} + \frac{j}{k^3R^3} \right) + (\overline{J}_{ms}\cdot\hat{R})\hat{R}\left(\frac{j}{kR} + \frac{3}{k^2R^2} - \frac{3j}{k^3R^3} \right) \right) e^{-jkR} k^2 ds' \quad (2.11)$$

where

$$\hat{R} = \frac{\overline{R}}{R} = \frac{\overline{r} - \overline{r}'}{|\overline{r} - \overline{r}'|}. \quad (2.12)$$

2.2.2. Radiation of an aperture

Reflector antennas can be considered as aperture antennas and the radiation can be computed from the electric and magnetic fields in the aperture. Radiation of the aperture antennas is discussed in numerous books on antenna theory, for example in [2,3]. The aperture plane divides antenna structure into two parts: into a half-space with sources and into a source-free half-space, where the radiation is computed. The field-equivalence principle (the generalized Huygen's principle) allows an arbitrary electromagnetic radiation source to be replaced by its equivalent current sources on a closed surface containing all the sources. The aperture plane of the reflector antenna or the surface of the reflector can be considered as such surface. The aperture plane is assumed infinite so that it forms a surface enclosing all the sources. The aperture of a reflector antenna is illustrated in Figure 2.5. The reflector antenna radiation analysis can be reduced to the problem of determining the equivalent surface currents on the aperture plane.

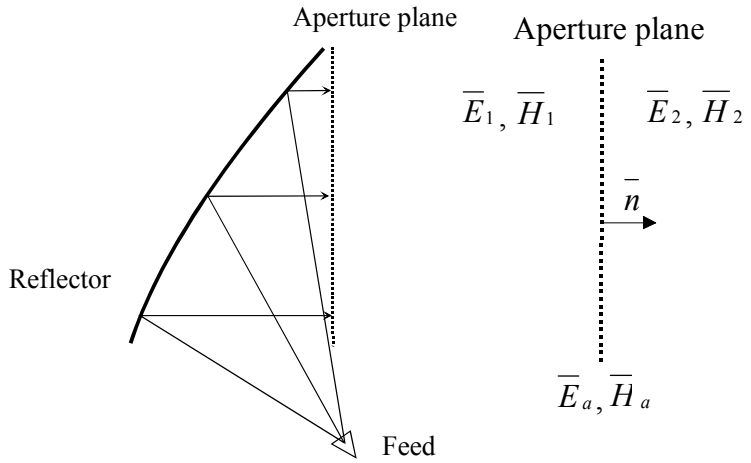

Figure 2.5 *Aperture of a reflector antenna.*

The equivalent surface current densities radiate the same field outside the aperture as the original sources inside it. The sources inside aperture can be removed and source-free fields $\overline{E}_1$ and $\overline{H}_1$ corresponding to the fields radiated by the sources are assumed to exist inside the aperture. Requirement for the continuity of tangential field components at the aperture boundary result into [9]

$$\overline{J}_{es} = \overline{n} \times \left(\overline{H}_2 - \overline{H}_1 \right), \tag{2.13}$$

$$\overline{J}_{ms} = -\overline{n} \times \left(\overline{E}_2 - \overline{E}_1 \right), \tag{2.14}$$

where $\overline{n}$ is the normal of the aperture pointing outside and $\overline{E}_2$ and $\overline{H}_2$ are the tangential electrical and magnetic fields outside the aperture. According to the field-equivalence principle fields inside the boundary (aperture) do not need to be known as the radiation outside the aperture is determined by the equivalent sources on the boundary. If $\overline{E}_1$ and $\overline{H}_1$ are chosen to be zero, Equations (2.13) and (2.14) can be written into the following form at the boundary [9]

$$\overline{J}_{es} = \overline{n} \times \overline{H}_a, \tag{2.15}$$

$$\overline{J}_{ms} = -\overline{n} \times \overline{E}_a. \tag{2.16}$$

The radiation of the aperture can be computed with Equations (2.8)-(2.11). Determination of equivalent surface currents is in general difficult and several approximate techniques have been developed for this purpose.

2.2.3 Physical optics

Determination of the surface currents is needed for computation of the reflector antenna radiation. By assuming zero fields inside the closed surface, the inside can be filled with a perfect electric conductor or with a perfect magnetic conductor. Assuming further the surface flat and infinite the method of images gives the resulting surface current densities on a perfect magnetic conductor [2]

$$\overline{J}_{es} = 2\overline{n} \times \overline{H}_a , \tag{2.17}$$

$$\overline{J}_{ms} = 0 . \tag{2.18}$$

This approximation resulting into Equation (2.17) is called the physical optics (PO) approximation. Physical optics is commonly used in reflector antenna analysis.

2.2.4 Geometrical optics

Geometrical or ray optics can be considered as a zero-wavelength approximation of exact electromagnetic theory. The relation of geometrical optics (GO) to Maxwell's equations is discussed in detail in [18]. GO is useful approximation for analysis of electrically large antennas as it easily allows the approximate computation of electromagnetic fields from known values at a certain point by tracing the corresponding rays.

Time-harmonic fields can be expressed as asymptotic series, which represent the exact field. The electric field (and the magnetic field) solved from the exact electromagnetic theory can be expanded into power series in inverse powers of the angular frequency ω [3,18]

$$\overline{E}\left(\overline{r}\right) = \sum_{m=0}^{\infty} \frac{\overline{E}_m\left(\overline{r}\right)}{\left(j\omega\right)^m} e^{-jk_0 L\left(\overline{r}\right)} , \tag{2.19}$$

where $k_0 = \sqrt{\mu_0 \varepsilon_0}$ and $L\left(\overline{r}\right)$ is an operator called eikonal function. The equiphase wave fronts are given by the level surfaces of the eikonal function. At high frequencies the fields are described approximately by the 0^{th} order equation:

$$\overline{E}\left(\overline{r}\right) \approx \overline{E}_0\left(\overline{r}\right) e^{-jk_0 L\left(\overline{r}\right)} . \tag{2.20}$$

This approximation is called the geometrical optics approximation.

2.2.4.1 Propagation of the field along the ray

The series approximation of the fields is substituted into the Maxwell's equations in source-free space, i.e., into Equations (2.1)-(2.4) without the charges and currents. The coefficients of powers of ω are equated and fields are solved [9]. Direction of the ray can be defined as [9]

$$\bar{s} = \frac{\nabla \bar{L}}{n}, \tag{2.21}$$

where n is the index of refraction

$$n = \frac{\sqrt{\varepsilon\mu}}{\sqrt{\varepsilon_0 \mu_0}}. \tag{2.22}$$

The solution of the fields along a ray are [3]

$$\bar{E}_0(s) = \bar{E}_0(s_0) e^{-\frac{1}{2}\int_{s_0}^{s} \frac{\nabla^2 \bar{L}}{n} ds}, \tag{2.23}$$

$$\bar{H}_0(s) = \sqrt{\frac{\varepsilon}{\mu}} \bar{s} \times \bar{E}_0(s), \tag{2.24}$$

where s_0 and s are the distances along the ray from the reference or origin point. $\bar{E}_0$, $\bar{H}_0$ and $\nabla \bar{L}$ are perpendicular to each other and the surfaces of constant L determine the phase fronts. The Poynting vector and the power flow in lossless media are in the direction of $\nabla \bar{L}$, i.e, in the ray direction [3]. The electric field $\bar{E}_0(s)$ at any point on a ray is completely determined from a known field at one point on the ray. The phase on a wave front is given by [3]

$$\phi = \omega t - \frac{\omega}{c} L(\bar{r}) \tag{2.25}$$

and the optical path length l along a ray path C is defined as [3]

$$l = \int_C n ds. \tag{2.26}$$

The phase difference between point P and a point P_0 where the field is known can be computed from the optical path length

$$\Delta\phi = -\frac{2\pi}{\lambda_0} \int_{P_0}^{P} n ds, \tag{2.27}$$

where λ_0 is the free-space wavelength.

2.2.4.2 Reflection of the ray at a boundary

Electromagnetic energy propagating between two points will follow any ray path that makes optical path length stationary (minimum). In homogeneous medium, ray paths are straight lines. Snell's reflection law and refraction law can be derived from Fermat's principle. Reflected ray $\bar{s}_r$ and incident ray $\bar{s}_i$ are coplanar with each other and with the normal $\bar{n}$ of the surface. Both rays make equal angles with the surface normal.

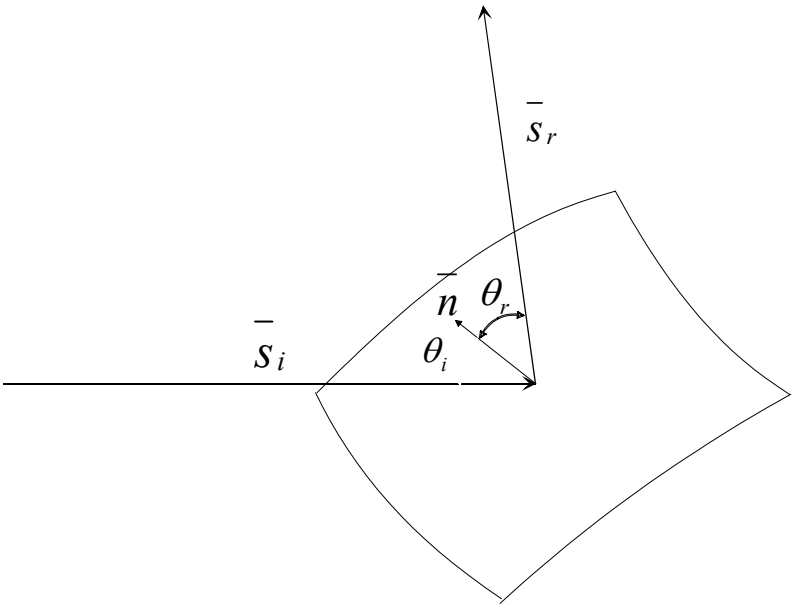

Figure 2.6 *Reflection at a planar boundary.*

The Snell's reflection law can be expressed in the following forms [3]

$$\bar{n} \times \left(\bar{s}_r - \bar{s}_i \right) = 0 , \tag{2.28}$$

$$\bar{n} \cdot \left(\bar{s}_r + \bar{s}_i \right) = 0 , \tag{2.29}$$

$$\bar{s}_r = \bar{s}_i - 2\left(\bar{s}_i \cdot \bar{n} \right)\bar{n} , \tag{2.30}$$

$$\bar{s}_i = \bar{s}_r - 2\left(\bar{s}_r \cdot \bar{n} \right)\bar{n} . \tag{2.31}$$

At the boundary of the free-space and a perfect conductor, the reflected field amplitude is equal to the incident amplitude, but the phase of the reflected field is opposite to the incident field making the total field at boundary zero.

2.2.4.3 Propagation of power

The power propagates to the direction of the rays. Rays passing through a closed curve define a ray tube or a flux tube. The total power within the cross section of the flux tube must be constant since power propagates in the direction of the rays only. When the flux tube cross section A_0 and power density P_0 are know at one location and the flux tube cross section area dA is known, power density within the flux tube can be solved from

$$P \cdot dA = P_0 \cdot dA_0 . \tag{2.32}$$

When the cross section of the flux tube decreases, the power density increases and vice versa. The power is related to the electric and the magnetic fields through the Poynting vector $\overline{E} \times \overline{H}$, which is the power density vector. The time averaged Poynting vector gives the transmitted average power density as

$$P_{ave} = \frac{1}{2} \mathrm{Re}\left(\overline{E} \times \overline{H}^{*} \right). \tag{2.33}$$

The geometrical optics approach to the propagation of the electromagnetic waves is not valid at caustics where there are two or more rays intersecting at a point. The flux tube area becomes zero and the power density would become infinite.

2.2.5 Edge diffraction

Physical optics (PO) and geometrical optics (GO) both assume the scatterers to be infinite in size. In reality, reflector antennas have a finite size. A discontinuity in the medium, such as an edge, acts as a Huygen's source. The phenomenon that allows the electromagnetic field to propagate around the edge is called diffraction. The total electric can be expressed as [19]

$$\overline{E}_{tot} = \overline{E}_i + \overline{E}_r + \overline{E}_d , \tag{2.34}$$

where $\overline{E}_i$ is the incident direct radiation from the source, $\overline{E}_r$ is the reflected field and $\overline{E}_d$ is the diffracted field. The incident and reflected fields can be computed using PO or GO where they exist. In general, diffracted field consists of edge and surface diffracted fields. Surface diffracted field can be usually neglected in reflector antenna analysis. The diffracted field can be solved from diffraction integrals. Diffraction is discussed in literature in detail, for example in [18, 20].

In the analysis of reflector antennas, edge diffraction is included into physical optics and geometrical optics with approximate techniques called physical theory of diffraction (PTD) and geometrical theory of diffraction (GTD). PTD and GTD are described in the following sections.

Diffracted field in complicated geometries can be determined with the help of so-called canonical problems. A canonical problem is the simplest boundary value problem, which locally approximately corresponds to the actual edge geometry. The diffraction field can then

be computed for this simpler geometry. Examples of canonical problems include a half-plane, a wedge and a curved surface.

2.2.5.1 Geometrical theory of diffraction

Geometrical theory of diffraction (GTD) includes diffraction in the geometrical optics. The GTD was invented by Keller [21]. The diffracted field, as the incident field, is described with rays. The diffracted rays from the edge form a so-called Keller's cone, illustrated in Figure 2.7.

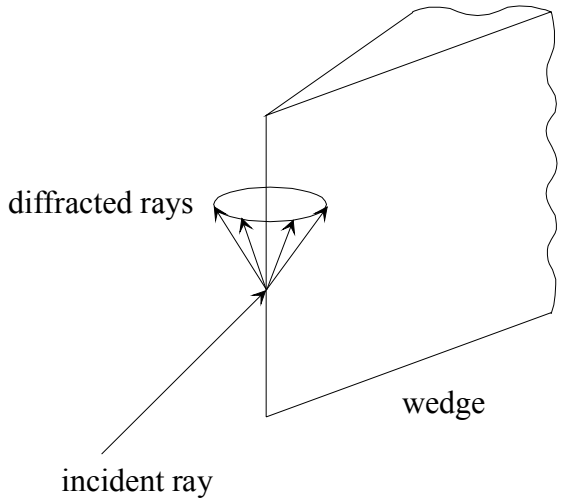

Figure 2.7 *Diffraction from a wedge.*

The total field at the observation point is the sum of the GO and diffracted rays:

$$\overline{E}_{tot} = \overline{E}_{GO} + \overline{E}_{GTD}, \tag{2.35}$$

where $\overline{E}_{GO}$ includes the field components by the incident and the reflected rays and $\overline{E}_{GTD}$ is the diffracted field. The initial value of the diffracted field is determined with the help of diffraction coefficients and the diffracted rays propagate as normal GO rays. Diffracted field is calculated in general from [22]

$$\overline{E}_{GTD} = \overline{E}_i \cdot DA(s_0, s)e^{-jks}, \tag{2.36}$$

where $\overline{E}_i$ is the incident field at the point of diffraction, D is the diffraction coefficient and $A(s_0, s)$ is the spatial attenuation or spreading factor. The source is located at the distance s_0 from the diffraction point and observation point is at the distance of s. If the incident wave is planar, cylindrical or conical wave, the attenuation factor is [22]

$$A(s_0, s) = \frac{1}{\sqrt{s}}, \tag{2.37}$$

and in the case of an incident spherical wave

$$A(s_0, s) = \sqrt{\frac{s_0}{s(s+s_0)}} \rightarrow \frac{\sqrt{s_0}}{s}, s >> s_0. \tag{2.38}$$

The diffraction coefficients are, in general, dyadic. The diffracted fields can be computed if the diffraction coefficients can be determined. A complicated geometry can be approximated by dividing it into canonical problems that are solved independently, and the results are superpositioned to the final GTD component of the radiation.

Geometrical theory of diffraction cannot predict the field at the shadow and reflection boundaries. These boundaries limit the regions of space where there is neither incident field nor reflected field (shadow region) and where there are both incident and reflected field components (reflection boundary). These limitations are corrected for example in the uniform geometrical theory of diffraction (UTD) [19]. Sometimes all GO based diffraction theories are called GTD for simplicity.

2.2.5.2 Physical theory of diffraction

In physical theory of diffraction (PTD), the total scattered field is expressed as in Equations (2.34) and (2.35) as [23]

$$\overline{E}_{tot} = \overline{E}_{PO} + \overline{E}_{fr}, \tag{2.39}$$

where a fringe field $\overline{E}_{fr}$ is added to the physical optics field $\overline{E}_{PO}$. This extension to physical optics was first developed by Ufimtsev. The fringe field can be computed from equivalent edge currents. Equivalent edge currents were first used by Michaeli [24,25]. Other approaches can be formulated to the same form.

The diffracted field, the so-called fringe or PTD field, is computed by integrating the equivalent edge currents along the illuminated edges of the scatterer. In GRASP8-reflector antenna analysis software, the edge currents are determined from integration of the fringe wave current along incremental infinite strips on the canonical half-plane [17]. The PTD field can be divided into transverse electric (TE) and transverse magnetic field (TM) components [17]

$$d\overline{E}_{TM} = dz' E_{iz} \frac{e^{-jkr}}{4\pi r} \frac{\sin\theta}{\sin^2\theta_0} \frac{2\sin\frac{\phi_0}{2}}{\left|\cos\frac{\phi_0}{2}\right| + \sin\frac{\alpha}{2}} \hat{\theta}, \tag{2.40}$$

$$d\overline{E}_{TE} = dz'\eta H_{iz}\frac{e^{-jkr}}{4\pi r}\frac{1}{\sin\theta_0}\frac{sign(\pi-\phi_0)}{\sin\frac{\alpha}{2}\left(\left|\cos\frac{\phi_0}{2}\right|+\sin\frac{\alpha}{2}\right)} \left[\left(\cos\phi\cos\theta+\cot\theta_0\sin\theta\left(1+2\left|\cos\frac{\phi_0}{2}\right|\sin\frac{\alpha}{2}\right)\right)\hat{\theta}-\sin\phi\hat{\phi}\right], \quad (2.41)$$

where *dz'* is the incremental arc length along the edge, η is the impedance of free space and $\overline{E}_{iz}$, $\overline{H}_{iz}$ are the *z*-components of the incident field. Direction of the incident field is defined by θ_0 and ϕ_0 and the coordinates of the observation point in relation to the diffraction point are *r*, θ, and ϕ. The angle α is defined from [17]

$$\sin\frac{\alpha}{2}=\sqrt{\frac{1-\sin\theta\cos\phi\sin\theta_0+\cos\theta_0\cos\theta}{2\sin^2\theta_0}}. \quad (2.42)$$

The PTD field depends on the direction of the incident field and the PTD approximation in Equations (2.40)-(2.41) are valid only if the incident field is locally a plane wave. GRASP8W-software is used in the reflector analyses in this thesis and the reflector edge diffraction is computed using physical theory of diffraction as described in this Section.

2.3 Synthesis of shaped reflector antennas

The procedure, where the antenna structure is determined from the desired radiation is called antenna synthesis. In dual reflector synthesis, the reflectors are determined from the known primary feed radiation and from the required radiation of the reflector antenna. The dual reflector antenna synthesis problem is illustrated in Figure 2.8.

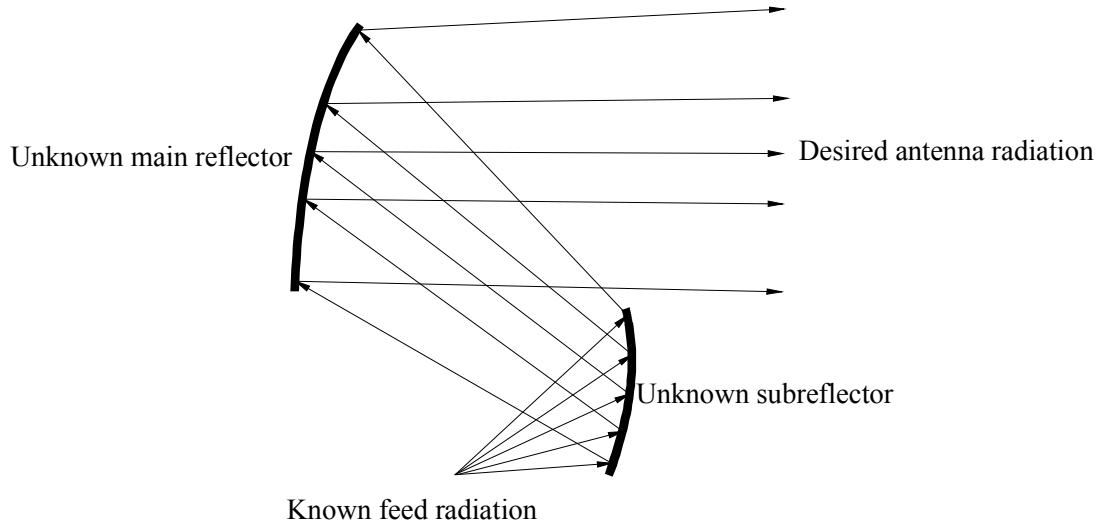

Figure 2.8 *Dual reflector synthesis problem.*

Numerous reflector antenna synthesis methods have been developed since the 1940's. The methods can be divided into so-called direct and indirect methods. In the direct methods, the reflector surfaces are determined directly from the desired antenna radiation. In the indirect methods, the aperture field radiating the desired antenna radiation is determined first and the aperture field is realised by shaping the reflector surfaces appropriately. The shaped reflector antenna synthesis methods are also divided into geometrical optics (GO) and physical optics based methods (PO) based on the method used to compute the radiation. PO based methods are often called diffraction synthesis methods, as they usually include the diffraction with PTD [2]. GO based methods are mostly used in the indirect synthesis of shaped beam reflector antennas. Examples of the synthesis methods found in the literature for dual offset reflectors are described in the following.

2.3.1 Indirect synthesis methods

In indirect synthesis methods the aperture field distribution is determined first from the desired reflector antenna radiation. This procedure is called aperture field synthesis. The far field of an aperture antenna is essentially the Fourier transformation of the aperture field. In principle, the aperture field can be determined with inverse Fourier transformation from the far-field pattern. However, the computation of the discrete inverse Fourier transformation requires a sufficient number of complex field samples and usually it is not practical or even possible. Several techniques have been developed for aperture field synthesis for shaped or contoured beam antennas. Examples of aperture field synthesis techniques are described in [26, 27]. These methods are based on search procedures: the aperture field is varied within an

optimisation loop until desired radiation is achieved. The aperture field is parameterised and the phase is represented with sinusoidal series in [26]. In [27], the aperture field is represented with Zernike polynomials and the coefficients of these polynomials are optimised. The actual reflector surfaces are then usually determined using geometrical optics based reflector synthesis methods so that the desired aperture field is realised.

Spherical wave expansions (SWE) can be also used to specify the near field on a spherical surface enclosing the antenna from the desired far field radiation pattern [28]. The truncated sphere where the fields are specified is composed of annular segments, where the fields are decomposed into separate functions of θ and ϕ. The field is assumed invariant of θ and the ϕ dependence is expanded into Fourier series. The coefficients of these series in annular segments and the corresponding modes of the SWE are determined. Reflector surfaces are determined using GO synthesis method described in [29].

2.3.1.1 Geometrical optics based synthesis methods

Geometrical optics based synthesis methods are based on the principles of geometrical optics: the conservation of energy within flux tubes, Snell's reflection law and the phase dependence on the ray path length. The input field in the synthesis problem of dual offset reflectors is the known radiation pattern of the primary feed. The output field is usually the aperture field of the antenna. Both fields are described with rays. The ray distribution in the output is determined from the input rays so that each input ray has a corresponding output ray and the output rays correspond to the desired aperture amplitude and phase. Determination of the rays in the output aperture from the rays in the input aperture is called aperture mapping. Several geometrical optics based mathematical synthesis problem formulations exist in the literature, for example [29–33].

2.3.1.1.1 Formulation of the synthesis problem with partial differential equations

The solution of the reflector surfaces from the input and output fields of the reflector system can be formulated into elliptic form of Monge-Ampère type second-order nonlinear partial differential equation [29]. The ray directions are described with complex coordinates to simplify the formulation of the problem. The Monge-Ampère equation is linearised applying a finite difference model and solved with numerical iteration. The solution gives the reflector surfaces at discrete points corresponding to each ray.

The nonlinear second order Monge-Ampère partial differential equation is derived from first-order partial differential equations which formulate the problem exactly [32]. These partial differential equations are the Snell's reflection law, conservation of energy condition and the total derivative condition [32]

$$\frac{\partial^2 r}{\partial\theta\partial\phi} = \frac{\partial^2 r}{\partial\phi\partial\theta}, \tag{2.43}$$

where the subreflector surface is determined by r in spherical coordinates and r is a function of the ray coordinates in input and output aperture. The total derivative condition ensures that the reflector surface is smooth. Levi-Civita's theorem, that states that the Snell's law is

automatically satisfied on the second reflector if the Snell's law is satisfied on the first reflector and the path length is known, is used simplify the Snell's law formulations on the reflections. Conservation of energy results into the mapping equations that are needed to obtain the solutions for the points on the reflector surfaces. The first order partial differential equations associated with the synthesis problem can be solved by numerical progressive integration [32]. The solution starts from the reflector rims, which allows the rims to remain fixed.

2.3.1.1.2 Ray tracing based synthesis formulation

The dual offset reflector synthesis problem can be formulated also with linear non-differential equations [33]. The wave fronts and reflector surfaces are presented with local biparabolic expansions corresponding to the surface curvature. This method is based on tracing differential ray strip through the reflections. Ray strips are flat bundles of rays tracing out ribbons with varying widths which twist in space. The strip is one-dimensional and it is orthogonal to the ray direction. The width of the strip is much smaller than wave front curvatures. This formulation of the synthesis problem with linear equations allows simpler and more easily controlled solution than the partial differential equation based approach [33].

The synthesis procedure is shown in Figure 2.9. The synthesis is done ray by ray and it starts with the geometry of the system.

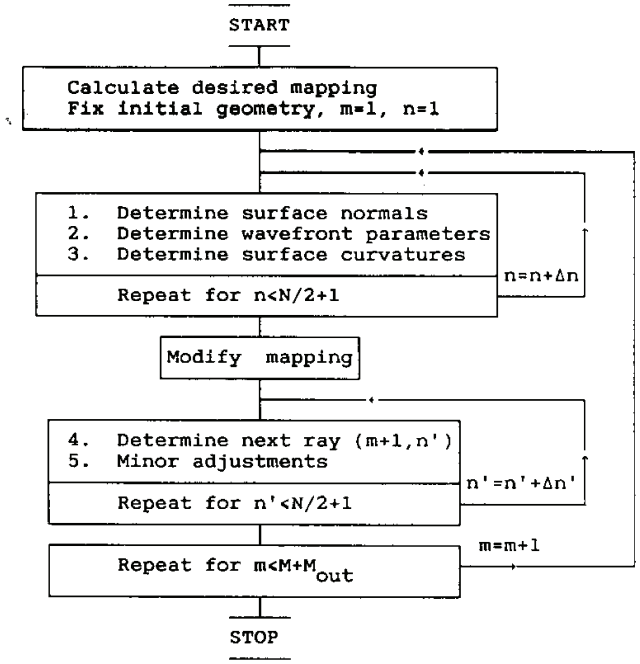

Figure 2.9 *Ray tracing based synthesis procedure [33].*

The initial geometry is fixed at the beginning of the synthesis. The geometry is defined by the primary feed phase centre, the reflector centre and the aperture centre points. Diameters of the elliptical aperture in *x*- and *y*-direction are also specified together with the desired amplitude distribution in the aperture. Feed radiation pattern is specified and the angle of the subreflector rim is fixed. The output aperture phase is assumed constant [33]. The reflectors

are specified in polar grids consisting of nodes corresponding to rays. The polar grids are thinned to give approximately even ray distribution on the reflector surfaces.

The output aperture is elliptic and the aperture field is assumed constant on ellipses around the aperture centre. The conservation of energy means that the power within an ellipse in the output aperture must be the same as the power within the corresponding circle in the feed radiation pattern. Mapping functions can be determined from this condition. The exact solution of the synthesis requires the desired mapping to be modified by allowing the mapping to float. The circles of constant θ in the feed pattern in polar coordinates map onto ellipses in the aperture *xy*-plane, but the radial lines are allowed to be curved. The mapping is written as [33]

$$x = \rho(\theta)\cos\phi', \tag{2.44}$$

$$y = a\rho(\theta)\sin\phi', \tag{2.45}$$

where a is the axial ratio of the output aperture ellipse and

$$\phi' = \phi + f(\theta,\phi). \tag{2.46}$$

The floating term $f(\theta,\phi)$ can be expanded into a Fourier series. The coefficients of Fourier expansion are found after initial synthesis of the reflectors.

The ray wave fronts are specified by principal directions and radii of curvature. The wave front is described with a local biparabolic expansion. The principal directions of curvature do not change along a ray in free space, but the principle radii of curvature have to be calculated as the ray is traced between the reflections. The reflector surfaces are also defined with local biparabolic expansions.

At first the mapping is determined with Equations (2.44) and (2.45) without the floating term in Equation (2.46). The partial derivatives and the Jacobian determinant of the mapping functions are determined for the ray-by-ray synthesis. Constant phase in the aperture results in equal ray path lengths and rays are parallel to the *z*-axis in the aperture. Feed radiation pattern is used to determine the wave front parameters of the input ray and the desired aperture field is used to determine the ray parameters at the output. The output ray wave front curvature is zero as the aperture phase is constant.

The centre ray path is known from the reflector geometry: centre ray passes through the reflector centres into the centre of aperture. The reflector surface normals for both reflectors are computed with Snell's law. The wave front parameters for the ray between the reflectors have to be determined for the computation of the reflector surface curvature parameters. Two input differential ray strips are introduced and they are defined by [33]

$$\overline{\Delta\theta_i} = s_i\Delta\theta\bar{u}_\theta, \tag{2.47}$$

$$\overline{\Delta\phi_i} = s_i\Delta\phi\sin\theta\bar{u}_\phi. \tag{2.48}$$

s_i is the length of the input ray from the feed phase centre to the subreflector. These ray strips are traced to the subreflector and the wave front parameters for the incident ray are determined. The ray strips after the reflection are $\overline{\Delta\theta}_r$ and $\overline{\Delta\phi}_r$. The ray strips $\overline{\Delta\theta}$ and $\overline{\Delta\phi}$ in the output aperture must coincide after the reflections on the reflectors with [33]

$$\overline{d\theta} = \left(\frac{\partial x}{\partial \theta} \bar{u}_x + \frac{\partial y}{\partial \theta} \bar{u}_y \right) \Delta\theta , \tag{2.49}$$

$$\overline{d\phi} = \left(\frac{\partial x}{\partial \phi} \bar{u}_x + \frac{\partial y}{\partial \phi} \bar{u}_y \right) \Delta\phi . \tag{2.50}$$

Mapping of $x(\theta,\phi)$ and $y(\theta,\phi)$ is defined by Equations (2.44) and (2.45) and the partial derivatives can be computed from these. The ray strips are traced backwards from aperture to the main reflector and reflected from it resulting into ray strips $\overline{d\theta}_m$ and $\overline{d\phi}_m$ after the reflection. Ray path between the reflectors is known together with the ray strips at both reflectors. These ray strips must correspond to each other when traced across the reflector separation along the ray. Four linear equations for determining curvature parameters for the ray strips between the reflectors are derived and presented in [33]. The equations generally do not have an exact solution, as there are only three variables in them. The floating mapping is used to introduce a fourth variable into them permitting the exact solution. The determination of the unknown wave front parameters is called dynamic ray tracing [33].

The wave front parameters are known for the ray and the reflector surface curvature parameters are determined from the wave front parameters of the incident and reflected wave. Three linear equations for determining the reflector surface curvature parameters from the incident and reflected ray wavefront parameters are derived and presented in [33,34]. The main reflector surface curvature parameters are determined from the output rays that are traced back to the main reflector. The biparabolic expansion around the ray reflection points is defined by these surface curvature parameters.

The next ray is launched from the feed phase centre and it intercepts the subreflector at a point on the local biparabolically expanded surface around the previous point (centre point for the second ray in the synthesis). The desired endpoint of the ray is determined by the mapping. The output ray is traced backwards to the interception of the biparabolic surface expansion of the main reflector. The ray path is defined by these interception points and by the starting point at feed location together with the endpoint in the aperture. This procedure for determining the ray path is called kinematic ray tracing [33].

The ray path length may deviate from the desired path length resulting into phase errors in the aperture because the step size between the rays is too large or the synthesis is not exact. The build-up of path length errors is avoided by adjusting the ray path by moving the reflection points or by allowing the mapping to float [33]. The synthesis procedure is repeated for all rays resulting into numerically specified reflector surfaces at the discrete reflection points.

The floating mapping is described by the term $f(\theta,\phi)$ in the mapping Equations (2.44)–(2.45) and it corresponds to the curving of the radial lines in the coordinate grid. The floating mapping can be derived after an initial synthesis is done without the floating mapping as described previously. The modified mapping changes the partial derivates and the Jacobian of

the original mapping. The floating term $f(\theta,\phi)$ can be expanded into Fourier series and the following can be obtained [33]

$$f(\theta,\phi)=\sum_{i=1}^{I} f_i(\theta)\sin(i\phi), \tag{2.51}$$

$$\frac{\partial f}{\partial \theta}=\sum_{i=1}^{I} f_i'(\theta)\sin(i\phi), \tag{2.52}$$

$$\frac{\partial f}{\partial \phi}=\sum_{i=1}^{I} f_i(\theta) i\cos(i\phi), \tag{2.53}$$

where $f_i'(\theta)=df_i'(\theta)/d\theta$. The Fourier expansion coefficients are found by considering ray paths with the same θ , $\frac{\partial f}{\partial \theta}$ can be solved for each of these rays as described in [33]. The inverse Fourier transform is utilized to find the expansion coefficients $f_i'(\theta(m))$ for all the rays with the same θ. The Fourier coefficients $f_i(\theta)$ of $f(\theta,\phi)$ at $\theta(m+1)$ are determined with numerical integration [33]

$$f_i(\theta(m+1))=f_i(\theta(m))+f_i'(\theta(m))[\theta(m+1)-\theta(m)]. \tag{2.54}$$

The modified mapping can be calculated and it is used instead of the original mapping in the synthesis procedure. The synthesis proceeds with modifying the mapping on the ray ring.

2.3.1.1.3 Approximate solutions of the synthesis problem

The reflector surfaces can be approximated with locally planar surfaces. This approach has been used for example in [13, 35–37]. In [35], circularly symmetric aperture distribution with constant phase is realised with rotationally symmetric reflectors that are shaped only in the radial direction around the reflector centres. The reflectors are assumed planar between co-centric rings and the surfaces are numerically solved by extrapolation from known points. Similar approach is used in [36]. Approach in [13] is similar to [35], except the local planar surface is determined in an anterior point that is defined with interpolation from two previously computed adjacent points (located on the previous ring in the ray grid). Snell's law on both reflectors and other principles of geometrical optics are used to formulate the ordinary linear equations to solve the reflection points for a ray.

The synthesis method described in [37] is similar to the method described in [33], except, that the reflector surfaces are assumed locally planar instead of doubly curved surfaces. An iterative algorithm is used to find the subreflector surface normal at the reflection point, i.e., the local tangent plane of the surface, so that the desired ray path is achieved. The main reflector surface is determined from the ray path length condition with the theorem of Levi-Civita.

2.3.2. Direct synthesis methods

Reflector surfaces can be directly determined from the desired antenna radiation. In these so-called direct synthesis methods, the reflector surfaces are optimised until the desired radiation pattern is achieved. Typically, reflector surfaces are parameterised and presented with series, whose coefficients are determined with an optimisation procedure, where the reflector radiation is computed and compared to the desired radiation. Diffraction effects are usually included in the reflector optimisation and therefore, these methods are called diffraction synthesis methods.

The reflector surfaces can be characterised with polynomial and Fourier series [26]. Antenna radiation is computed using physical optics. The coefficients of these series are varied until the gain of the antenna is within a prescribed tolerance at the specified points. Analytical gradient based optimisation is used for direct dual reflector synthesis in [38]. An analytical expression of the penalty function related to the gain deviation is used to reduce the number of iterations needed for good convergence. Direction of the step is determined with the method of steepest descent, i.e., from the gradient of the penalty function. The step length is determined by finding the distance to the minimum of the function in the direction of the step. The synthesis procedure begins with an initial GO solution to the synthesis problem. At first, the sub-reflector is assumed fixed and the induced current distribution on the main reflector is computed. The main reflector shape is then optimised to produce the desired far field using analytical formulation of the gain deviation at each of the observation points. Secondly, the main reflector illumination is optimised and, finally, the sub-reflector shape is optimised to produce the desired main reflector illumination using the analytical gradient approach. The optimisation procedure is repeated until satisfactory antenna pattern is achieved.

In [23], a generalised diffraction synthesis technique is described. This method is capable to synthesise both single and dual shaped reflector antennas with a single or array feed. The whole antenna system is characterised, parameterised and optimised. The reflector surfaces are described with a global surface expansion based on the following expansion [23]

$$z'(t,\psi) = \sum_{n=0}^{N}\sum_{m=0}^{M}\left(C_{nm}\cos n\psi + D_{nm}\sin n\psi\right)F_m^n(t), \tag{2.55}$$

where t is a parameter describing the radial distance from the reflector surface ($0 \le t \le 1$), ψ is the angle around the centre, C_{nm} and D_{nm} are the expansion coefficients and $F_m^n(t)$ is the modified Jacobi polynomials defined by [23]

$$F_m^n(t) = \sqrt{2(n+2m+1)}\cdot P_m^{(n,0)}\left(1-2t^2\right)\cdot t^n. \tag{2.56}$$

Jacobi polynomials $P_n^{(\alpha,\beta)}(x)$ are defined in general as

$$(1-x)^{\alpha}(1+x)^{\beta}P_n^{(\alpha,\beta)}(x) = \frac{(-1)^n}{2^n\cdot n!}\left(\frac{d}{dx}\right)^n\left[(1-x)^{n+\alpha}(1+x)^{n+\beta}\right]. \tag{2.57}$$

The reflector radiation is computed with physical optics and physical theory of diffraction. The coefficients of the surface expansion are then optimised so that the desired radiation pattern is achieved.

A different approach to reflector surface presentation is used in [39]. The reflector surfaces are divided into elements that produce a stepped surface. The partial field contribution of each surface element to the directivity pattern is computed for each element. The reflector elements are moved along an axis (for example along the surface normal), which corresponds to a phase change in the partial field. Method of successive projections is used to optimise the reflector surfaces so that given constrains for the antenna directivity pattern are met [39]. The stepped reflectors are smoothed to produce the continuous reflector surfaces.

3 Antenna measurements

Antenna measurements are needed for the final verification of the antenna operation. Modern simulation and analysis methods predict often quite accurately the antenna characteristics, but for some complicated structures only measurements can give accurate information on the antenna properties. In all cases, it is beneficial to verify the computed results with measurements to ensure that antenna was correctly modelled in the simulations and correctly assembled. In this chapter, antenna radiation characteristics and techniques to measure them at sub-millimetre wavelengths are discussed.

3.1 Antenna radiation characteristics

Reciprocity theorem applies to most antennas and, therefore, properties of an antenna used to receive electromagnetic waves are the same as the properties for the same antenna when it is used to transmit electromagnetic waves. The space surrounding an antenna is commonly divided into three parts based on the behaviour of the antenna radiation: a reactive near field region, a radiating near field region, and a far field region. The regions are illustrated in Figure 3.1.

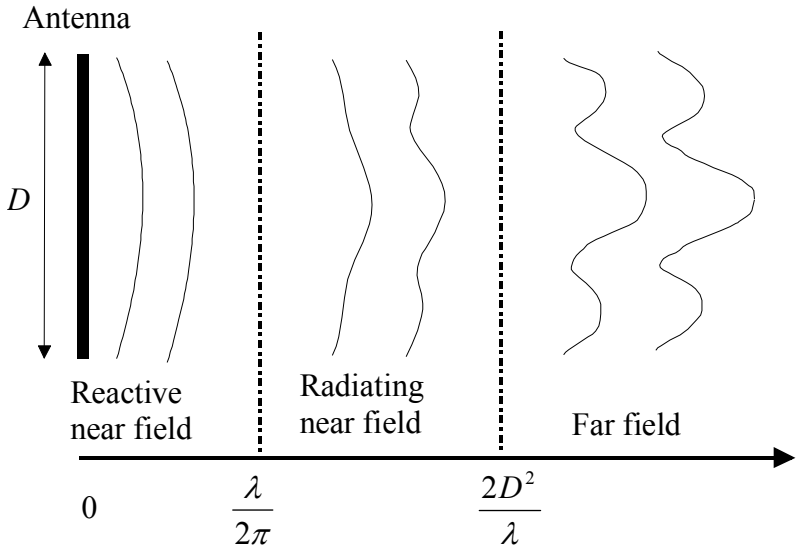

Figure 3.1 *Near field and far field regions of an antenna.*

In the reactive near field, the reactive field dominates and power is not propagating. The borders between the regions are not exact or unique as there are various criteria to separate the regions. Outer boundary of the reactive near field is usually defined as

$$R = \frac{\lambda}{2\pi}. \tag{3.1}$$

The antenna is assumed large compared to the wavelength λ. The radiating near field, or Fresnel region as it is also called for antennas focused at infinity, is a transition region between the reactive near field and the far field region. In this region, the radiation fields

predominate, but the angular field distribution depends on the distance from the antenna. The radial field component may also be significant in this region. The far-field region is defined to begin at

$$R = \frac{2D^2}{\lambda}, \tag{3.2}$$

where D is the maximum dimension of the antenna. At this distance the phase error due to the maximum path length difference between different points on the antenna is $\pi/8$. In the far field, the field components are essentially transverse and the angular distribution of the field is independent of the distance. This is exactly true only at infinite distance from the antenna. The far field region is also called Fraunhofer region analogical to optical terminology.

3.1.1 Radiation pattern

Radiation pattern (antenna pattern) is the spatial distribution of a quantity that characterises the electromagnetic field generated by an antenna [40]. These quantities that characterise the field are amplitude, phase, and polarisation. The radiation pattern of an antenna is completely described by the amplitude and phase of the field components in two particular orthogonal polarisations [41]. Spatial distribution of related properties, such as power flux density, radiation intensity and directivity, are sometimes also determined. The distribution can be expressed as a mathematical function or as a graphical presentation.

A pattern cut is any path on a surface over which a radiation pattern is obtained [40]. A far-field pattern is obtained in the far field of the antenna. The far field pattern is the angular distribution (θ, ϕ) of the field quantity on constant radius sphere. The standard antenna spherical coordinate system is illustrated in Figure 3.2 [41].

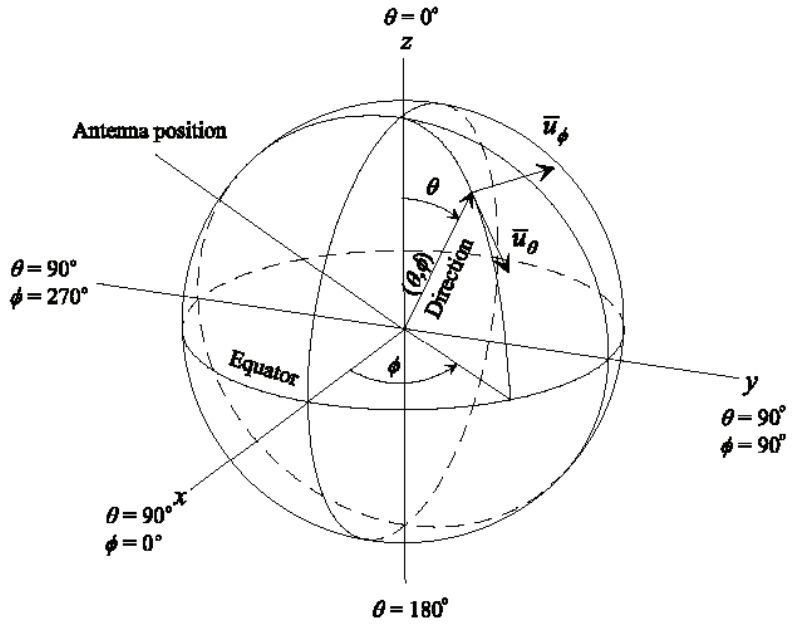

Figure 3.2 *Standard spherical coordinate system [41].*

Horizon coordinates are often used in antenna measurements as this coordinate system is a natural choice for an antenna positioner. The direction is defined with two angles: azimuth and elevation. Azimuth is the horizontal angle measured from the reference direction along the horizon clockwise and elevation is the angle above the horizon.

3.1.1.1 Amplitude pattern

Presentation of the antennas field's amplitude distribution is called an amplitude pattern. A power pattern is the distribution of the power density, which is related to the electric field amplitude through the Poynting vector. Power pattern is usually presented in decibels (dB)

$$P(\theta,\phi) \propto 10\log E^2(\theta,\phi). \tag{3.3}$$

Power (and amplitude) patterns are often normalised, i.e. power relative to a selected reference is presented. Antenna parameters that can be obtained from the antenna power pattern include the beamwidth and sidelobe levels. Usually the half-power (-3 dB) beamwidth is determined as the angular width of the beam between the points were the beam power drops to half of the peak power. Other power levels can also be used as the reference to the beamwidth definition. Sidelobe levels are specified in several ways [42]: by peak level outside the main beam, by average power or by median power. Sidelobe level is usually reported in relation to the main beam peak level. Extra peaks in the main beam region are often called shoulders.

3.1.1.2 Phase pattern

Distribution of the phase in the radiated field of an antenna is called the phase pattern of an antenna. The phase is relative quantity and it is defined in relation to a phase reference, such as a separate reference signal. A single-frequency field component of the angular frequency ω can be presented as a scalar function of time as [41]

$$E(t) = E_0\cos(\omega t + \psi_0) = \mathrm{Re}\{E_0 e^{j\psi_0} e^{j\omega t}\}, \tag{3.4}$$

where E_0 is the amplitude of the field and ψ_0 is the phase at t=0. The phase ψ is the angle of the complex number $E_0 e^{j(\omega t+\psi_0)}$. If the field E propagates along the x-axis with a velocity $v = \omega/k$ (k is the wave number) then the field at point x at time t is [41]

$$E(t,x) = E_0\cos(\omega t + \psi_0 - kx). \tag{3.5}$$

At point x, $E(t,x)$ is represented by $E(t,0)$ shifted in the positive direction by x/v. This is considered as a phase delay as the phase is decreased by kx in the propagation from 0 to x. The complex time factor $e^{j\omega t}$ can also be written as $e^{-i\omega t}$ [41]. For positively travelling wave the phase factor e^{-jkr} becomes then e^{ikr} and the phase is increased by the amount kx in the direction of propagation.

The definition of the phase described here is valid only for linearly polarised fields. A specified component in the far field can be expressed as [41]

$$E_u(\theta,\phi,r) = E(\theta,\phi)e^{j\psi(\theta,\phi)}\frac{e^{-jkr}}{r}\bar{u}, \tag{3.6}$$

where (θ,ϕ,r) specifies the observation point in spherical coordinates. For linear polarisation, unit vector $\bar{u}$ is real and the phase is defined unambiguously as in the scalar case. In the case of the circularly and elliptically polarised fields, $\bar{u}$ is complex and must be specified for every direction (θ,ϕ) to define the phase.

The phase centre is a reference point, which can be used as centre point of a sphere in the far field of the antenna so that the phase of a field component is essentially constant over the significant portion of the surface of that sphere [40]. In general, antennas may not have a clear phase centre. The apparent phase centre over the direction of observation (θ,ϕ) varies and apparent phase centres over the observation sphere form a surface in space [41].

3.1.1.3 Polarisation pattern

Polarisation pattern is the spatial distribution of the polarisation of the field vector in the radiated field of the antenna [41]. Alternatively, polarisation pattern is defined as the response of the linearly polarised probe antenna as it is rotated in a plane normal to the direction of the incident field so that the direction of the probe antenna polarisation is rotated. In the far field, the radiated field is essentially a plane wave and the magnetic field is orthogonal to the electric field. Polarisation of a wave is the time varying direction and relative amplitude of the electric-field vector, i.e., it is described by the figure traced by the extremity of the field vector at a fixed location in space as function of time as observed along the direction of propagation [22]. Polarisation is classified as linear, circular and elliptical based on the shape of the figure that the electric field vector end point draws as the function of time.

Instantaneous field in the far field propagating in the direction of the *z*-axis can be written as [22]

$$\overline{E}(t,z) = \overline{E}_x(t,z)\bar{u}_x + \overline{E}_y(t,z)\bar{u}_y, \tag{3.7}$$

where field components are given by

$$\overline{E}_x(t,z) = \mathrm{Re}\left\{E_x e^{j(\omega t - kz + \psi_x)}\right\}, \tag{3.8}$$

$$\overline{E}_y(t,z) = \mathrm{Re}\left\{E_y e^{j(\omega t - kz + \psi_y)}\right\}. \tag{3.9}$$

The polarisation is in general elliptical; circular and linear polarisations are special cases of the elliptical polarisation. Polarisation ellipse is illustrated in Figure 3.3. Polarisation is elliptic when the time-phase difference between the field components is not equal to $\pi/2$ (nor equal to its multiples), or the phase difference is equal to odd multiples of $\pi/2$ and the components do not have equal magnitudes. The polarisation ellipse is defined by the axial

ratio and by the tilt angle τ of the ellipse. When observed in the direction of propagation if the end point of the field vector rotates clockwise, the sense of the polarisation is right-handed. Opposite direction of rotation corresponds to left-handed polarisation.

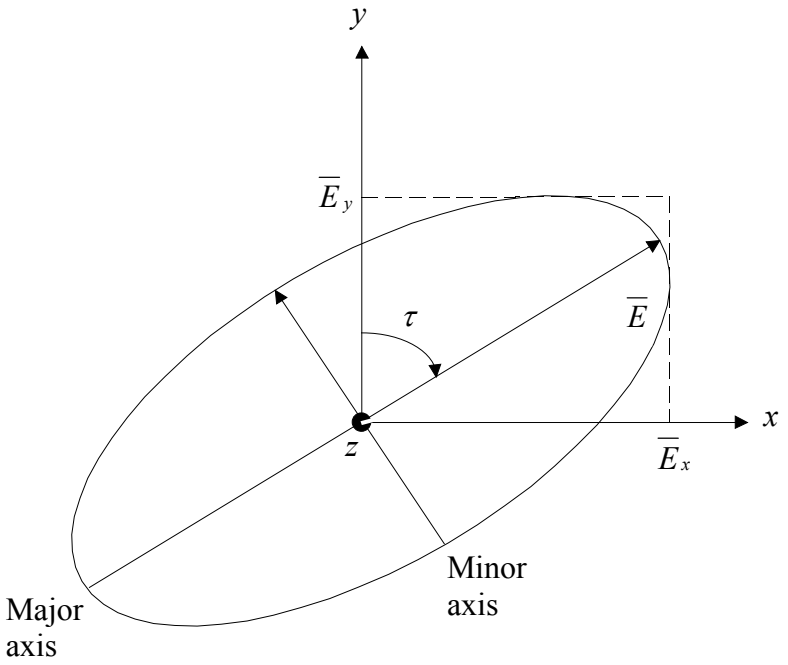

Figure 3.3 *Polarisation ellipse.*

If the amplitudes of the field components are equal and the time-phase difference between them is an odd multiple of $\pi/2$, elliptical polarisation reduces to circular polarisation. Similarly, if the phase-difference is a π (or its multiple) polarisation reduces to a linear polarisation.

Co-polarisation is the polarisation that the antenna is intended to radiate or to receive [40]. The orthogonal polarisation to the co-polarisation is called cross polarisation. For linear (and elliptical) polarisation, there are several definitions of the direction of the polarisation in the far field of an antenna. Three definitions for a linearly polarised wave propagating in the direction of z-axis are presented in [43]:

1) In Cartesian coordinates one coordinate axis is the direction co-polarisation and the other is the direction of cross-polarisation

2) In spherical coordinates the directions of the polarisations are in the directions of the tangent vectors of the coordinate sphere (θ, ϕ)

3) The directions of the polarisations are defined in the directions of the antenna movements in an elevation-over-azimuth-type antenna positioner.

3.1.2 Directivity and gain

Directivity is ratio of the power radiated in a given direction to the power averaged over all directions

$$D(\theta,\phi) = \frac{dP/d\Omega}{P_{tot}/4\pi} = 4\pi\frac{dP/d\Omega}{P_{tot}}, \tag{3.10}$$

where P_{tot} is the total power

$$P_{tot} = \int P(\theta,\phi)d\Omega = \int_0^{2\pi}\int_0^{\pi} P(\theta,\phi)\sin\theta d\theta d\phi . \tag{3.11}$$

The maximum value of directivity $D(\theta,\phi)$ is often called the directivity of the antenna and it is a measure of the ability of an antenna to concentrate the radiated power to a certain direction. An isotropic radiator radiates uniformly to all directions. Directivity is often expressed in reference to an isotropic radiator in decibels denoted with dBi.

The gain of an antenna is the ratio of the radiation intensity, in a given direction, to the radiation intensity that would be obtained if the power accepted by the antenna were radiated isotropically [40]. Therefore, the gain is defined as

$$G(\theta,\phi) = \eta D(\theta,\phi), \tag{3.12}$$

where η is efficiency of the antenna, which includes the losses within the antenna. Impedance and polarisation mismatch losses are not included.

3.2 Antenna measurement techniques

Antenna measurements are usually used to determine the radiation pattern of an antenna; the directional distribution of amplitude, phase and polarisation. Other antenna characteristics can also be measured, such as the antenna input impedance for matching to the transmitter or receiver, bandwidth, and antenna efficiency. Antenna measurement methods can be divided into near field and far field methods. In compact antenna test ranges, a plane wave corresponding to the far field is generated using a collimating or focusing element.

3.2.1 Far field measurements

In far field antenna tests, the antenna under test (AUT) is used as receiving or transmitting antenna. When the distance between the AUT and the receiving antenna is large, the incident wave over the whole AUT is essentially a plane wave. By rotating the AUT using an antenna positioner, the angular distribution of the desired antenna radiation property is obtained.

Far-field distance for electrically large antennas at sub-millimetre wave region is very large – for example for a 2-metre diameter antenna at 300 GHz the minimum far-field distance given by $2D^2/\lambda$ is about 8 km. In practice, a longer distance is needed as phase and amplitude taper in the plane wave due to finite distance causes filling of first nulls and increases the first side-lobe level near the main beam in the directional pattern. For very low-sidelobe antennas with first sidelobes below -40 dB distance of $6D^2/\lambda$ or even longer is needed for measurement uncertainty of 1 dB [44, 45]. At sub-mm wavelengths region the atmospheric attenuation may be up to several decibels per metre due to absorbtion caused by molecular resonances of the gases in the atmosphere. Computed atmospheric opacity, i.e., attenuation, as function of the frequency is shown in Figure 3.4 [46]. The high attenuation and the potentially high variation of it due to fluctuations in the air pressure and humidity make far-field measurements impractical for large sub-mm wave antennas.

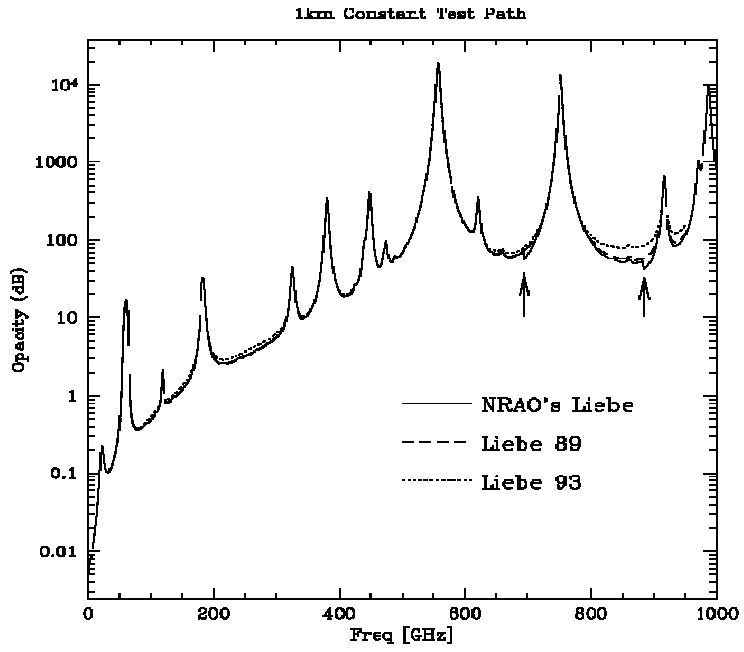

Figure 3.4 *Computed atmospheric opacity at sub-millimetre wavelengths [46].*

3.2.2 Compact antenna test ranges

In a compact antenna test range (CATR), the plane wave needed for antenna radiation pattern measurements is generated with a collimating element from the spherical wave radiated by the feed. The collimating element is often called a focusing element as the element can be also considered as a receiving device. The region in space where the plane wave exists is called the quiet-zone (QZ) of the CATR. Typically it is required that the quiet-zone field amplitude is within 1 dB peak-to-peak and the phase is within 10º peak-to-peak for accurate measurements. These requirements are mainly for systematic deviations from the plane, such as for the amount of amplitude taper and for phase front curvature. Scattering from objects in the measurement hall, for example edge diffraction from the collimating element edges and reflections from the walls, cause ripples to the quiet-zone field. These scatterers may cause extra sidelobes to the measured antenna pattern as the main beam amplifies the scattered field when it is pointing to the direction of the scatterer. The allowed ripple in the quiet-zone caused by the scattering may therefore be much lower than 1 dB peak-to-peak depending on the directivity of the AUT and the level of the sidelobes that is being investigated.

The collimating element in a CATR is usually a reflector or a set of reflectors. Lenses and holograms can also be used in compact antenna test ranges at millimetre and sub-millimetre wavelengths. In the following sections, different types of CATRs are described.

3.2.2.1 Reflector based compact antenna test ranges

The reflector compact antenna test ranges are based on the collimating ability of a parabolic reflector. Compact antenna test ranges based on a single reflector, a dual reflector or a triple reflector configuration have been developed since the 1960's [47]. For a fixed reflector size, the edge diffraction induced ripples in the quiet-zone size limit the lowest usable frequency of the range. Edge diffraction can be reduced by reducing the edge illumination, by shaping the reflector edges or by serrating the edges. The high-frequency limit of the reflector operation is set by the surface accuracy of the reflector. Typically surface accuracy of the order of $\lambda/100$–$\lambda/50$ is required, which ensures that potential path length difference does not affect the quiet-zone field phase significantly. Compact antenna test ranges based on reflectors are used at frequencies up to 200 GHz [48, 49] and their use is being investigated at the frequencies up to 500 GHz [50].

3.2.2.1.1 Single reflector CATR

The CATR based on a 3-metre single offset paraboloid reflector was patented by Johnson in 1967 and it is described in [51]. Typical quiet-zone diameter for a single reflector CATR is about one third of the reflector diameter. The quiet-zone field amplitude may be tapered due to finite focal length of the paraboloid causing spreading of the beam or to the radiation pattern of the primary feed [47]. The offset fed paraboloid suffers from relatively high cross-polarisation level. The typical cross-polarisation level is -30 dB [47]. The principle of the CATR based on a single reflector is shown in Figure 3.5.

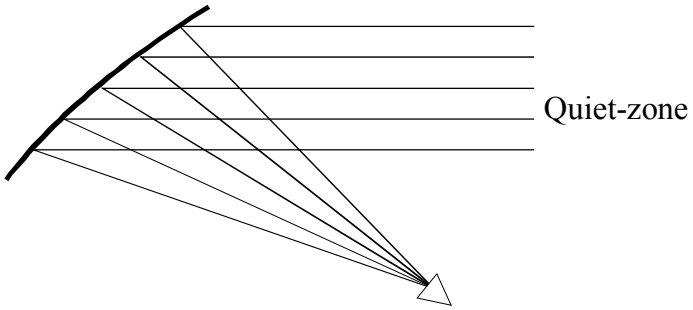

Figure 3.5 *CATR based on a single parabolic reflector.*

3.2.2.1.2 Dual reflector CATR

Two reflectors allow more control of the reflector antenna radiation. In a CATR, dual reflector structure allows a larger quiet-zone size in relation to the main reflector diameter. A dual cylindrical parabolic antenna was proposed by Vokurka in 1976, described for example in [52]. The spherical wave from the primary feed is transformed into a cylindrical wave by the sub-reflector, which is transformed into a planar wave by the main reflector. Cylindrical paraboloid surfaces are easier and more economical to manufacture than doubly curved surfaces. The disadvantage of this configuration is the relative high cross-polarisation level in the vertical plane of the quiet-zone. A schematic of the dual cylindrical reflector CATR is shown in Figure 3.6.

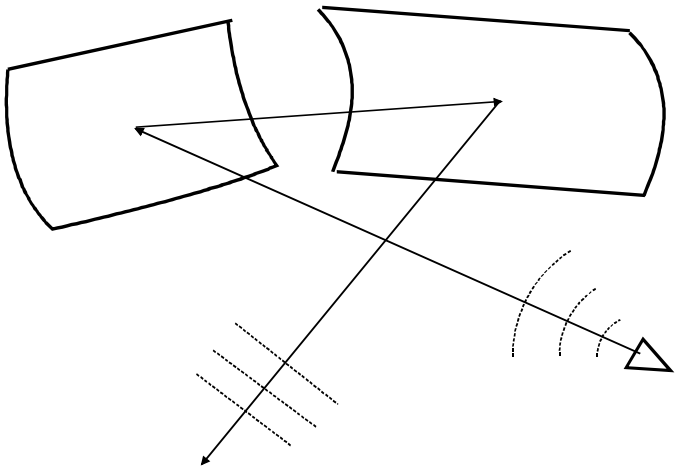

Figure 3.6 *CATR based on dual parabolic cylindrical reflectors.*

The cross-polarisation caused by an offset reflector can be eliminated by using another reflector and by selecting the offset angles so that the cross-polarised fields caused by the reflectors cancel each other [6]. The cross-polarisation level is due to the feed cross-polarisation. Possible configurations for a CATR include a Cassegrain antenna and Gregorian antenna. An example of a CATR based on a cross-polarisation compensated offset Cassegrain configuration is described in [49]. The size of the hyperbolic subreflector is 5.6 m × 5.3 m and that of the parabolic main reflector is 7.5 m × 6.0 m. The quiet-zone size is 5.0 m × 5.5 m × 6.0 m and the maximum cross-polarisation level is -35 dB. A Gregorian configuration is proposed in [53]. The configuration has a caustic between the reflectors, which allows the sub-reflector to be placed into a separate chamber. Absorber fence is placed between the reflectors to reduce the edge diffraction disturbances from the sub-reflector to the quiet-zone and direct feed illumination. The aperture in the fence, however, acts as an additional

diffraction source limiting the benefits of this approach. Cassegrain and Gregorian CATR configurations are presented in Figure 3.7.

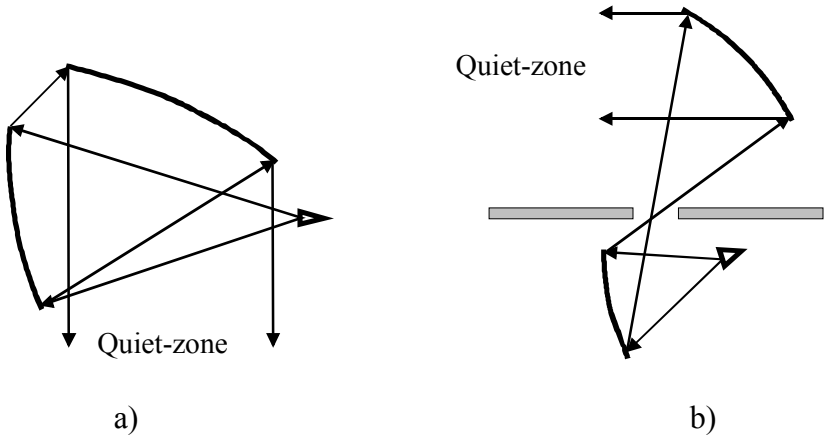

Figure 3.7 *a) Cassegrain type CATR, b) Gregorian type CATR.*

Shaped reflectors can be used in CATRs for improved quiet-zone field quality and size. Shaped Gregorian design is described in [54]. Edge diffraction from the main reflector is reduced by introducing a Gaussian amplitude taper to the main reflector illumination. The shaping also increases the aperture efficiency of the CATR and quiet-zone diameters of the order of 75 % of the main reflector diameter have been reported [47].

Spherical surfaces are relatively easy and economical to manufacture and they have been used for CATRs. A shaped sub-reflector is used compensate the spherical aberration [8]. The achieved quiet-zone size is about 70 % of the projected aperture of the spherical reflector.

3.2.2.1.3 Tri-reflector CATR

A dual reflector feed system (DRFS) can be used to increase the quiet-zone size of an existing single reflector CATR [13]. The increase in the quiet-zone size is due to the improved control of the main reflector illumination, which allows suitable amplitude taper to reduce edge diffraction without deforming the phase distribution. The approach can be also used with a spherical main reflector [55].

3.2.2.2 Compact antenna test range based on a lens

A lens can be used as a collimating device in a CATR. Lens-type CATR has the advantage of high area utilisation, low edge diffraction and good cross-polarisation performance [47]. The main advantage compared to the reflectors is lower surface accuracy requirement. A lens is a refractive component and the velocity in the dielectric is reduced by its refractive index, which results into $\left(\sqrt{\varepsilon_r}-1\right)/2$ times lower surface accuracy requirement and consequently to lower manufacturing costs. The disadvantage of the lens-type CATR is the relativily long length and also highly homogenous dielectric material is needed. The principle of the CATR based on a lens is presented in Figure 3.8. Examples of this type of a CATR are described in [56–58].

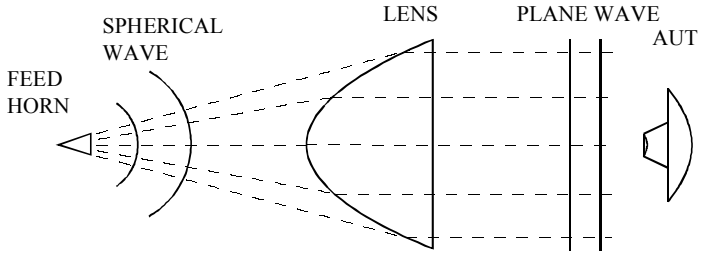

Figure 3.8 *Lens-type compact antenna test range.*

3.2.2.3 Compact antenna test range based on a hologram

Holography was invented by Gabor in 1947 and he received the Nobel Prize in Physics for it in 1971 [59]. Optical holography is traditionally based on recording the interference pattern of a reference light and the reflected light from an object on a film. When the film is illuminated with the reference light a three-dimensional image is seen. Optical holograms are called reflection holograms when the reference light and the viewing point are on the same side of the hologram. In the case of a transmission hologram, the viewing point is on the opposite side of the hologram than the reference light. Modern holograms are usually computer generated, i.e., the interference pattern is computed and fabricated directly instead exposing the pattern on a film [60].

Millimetre wave hologram was proposed for a collimating element in a CATR in 1992 [61]. The hologram is the interference pattern of the feed radiation pattern illuminating the hologram aperture and the desired quiet-zone plane wave. Transmission-type holograms are used in CATR applications. Hologram based CATRs have been used to test antennas at the frequencies of 39, 119, and 322 GHz [O3, 62, 63]. The schematic of the hologram CATR is presented in Figure 3.9.

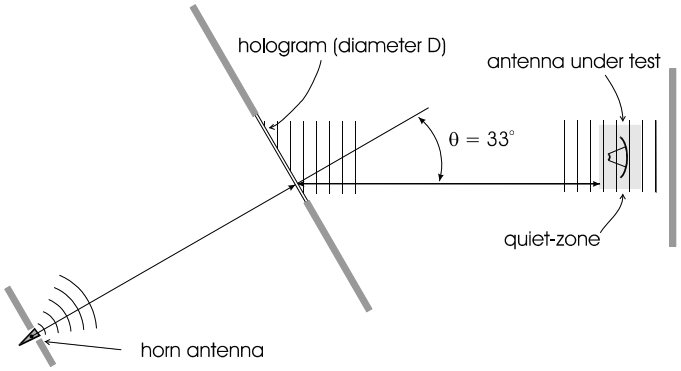

Figure 3.9 *Hologram based compact antenna test range.*

In general, the hologram changes the amplitude and the phase of the electromagnetic field that illuminates it. Holograms are usually realised so that only the amplitude or the phase modification in the field is considered. Corresponding holograms are called amplitude and phase holograms. Amplitude holograms have been mostly used for CATRs, but phase holograms are also being investigated [O10].

3.2.2.3.1 Hologram design

The transmission-type amplitude holograms for CATRs are generated with a computer. The transmitted electromagnetic field E_{tr} is related to the incident field E_i on the hologram by [O10]

$$E_{tr}(x,y) = T(x,y)E_i(x,y), \tag{3.13}$$

where the coordinates (*x,y*) are in the plane of the hologram. The transmittance of a general amplitude hologram is expressed as [64]

$$T(x,y) = \frac{1}{2}\{1 + a(x,y)\cos[\Psi(x,y)]\}, \tag{3.14}$$

where $a(x,y)$ is a real function proportional to the relation of transmitted and incident amplitudes. The phase term is [64]

$$\Psi(x,y) = \psi(x,y) + 2\pi\nu x, \tag{3.15}$$

where $\psi(x,y)$ is the normalized phase of the field incident on the hologram and ν is the spatial carrier frequency that separates the different diffraction orders produced by the hologram. The desired plane wave propagates to the angle

$$\theta = \arcsin(\nu\lambda). \tag{3.16}$$

For the holograms in CATR applications θ=33º as shown in Figure 3.9 has been selected to ensure good separation of the diffraction orders so that the other orders propagating in the direction of the normal of the hologram do not disturb the quiet-zone field. The θ=33º has been selected as an suitable compromise to keep the CATR compact in size while allowing sufficient separation between the quiet-zone and the direction of the hologram normal. The hologram structure is quantized to facilitate the hologram manufacturing. The transmittance of the hologram is binarised for a simple pattern and the binarised transmittance is given by [64]

$$T_B(x,y) = \begin{cases} 0, & 0 \le \frac{1}{2}[1 + \cos\Psi(x,y)] \le b \\ 1, & b < \frac{1}{2}[1 + \cos\Psi(x,y)] \le 1 \end{cases}, \tag{3.17}$$

where

$$b = 1 \quad (1/\pi)\arcsin a(x,y). \tag{3.18}$$

The binary amplitude hologram pattern is in principle formed from regions that block the incident field completely and from regions that pass the field unattenuated. These regions can be realised using intact metal to block the field and slots in the metal to allow the field to be

transmitted. The amplitude of the hologram transmittance is modulated by the widths of the slots and the phase is modulated by the locations of the slots. In practice, binarised transmittance is not achieved as the actual operation of the hologram structure is non-ideal. Accurate analysis of the hologram operation is needed to optimise the hologram structure.

The actual transmission of the hologram structure is computed using finite-difference time-domain (FDTD) method [65]. Currently it is not possible to compute the transmission of the whole three-dimensional hologram structure with FDTD even using super computers as the holograms are up to several thousands of wavelengths in diameter. Therefore, only one horizontal cut of the hologram is analysed at the time with two-dimensional FDTD analysis. The pattern is assumed infinite in the vertical direction. As the pattern changes slowly in the vertical direction, the radiated field on the plane of the hologram cut can be computed with reasonable accuracy assuming the transmitted field as a horizontal line source. The whole hologram aperture field can be approximated using several horizontal cuts. The quiet-zone field is computed with aperture integration, i.e., physical optics (PO), from the aperture field determined with FDTD simulations. An example of the hologram pattern is shown in Figure 3.10 together with the simplified structure that is used in the FDTD analysis.

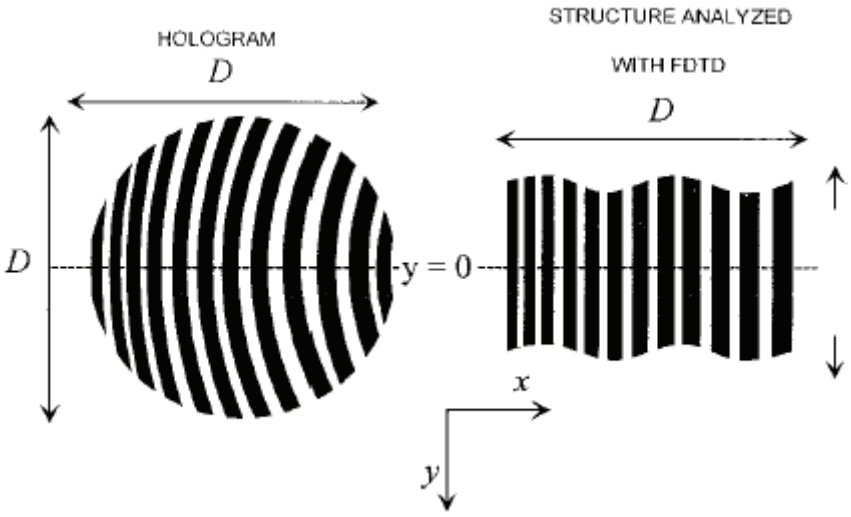

Figure 3.10 *An example of a hologram pattern and the simplified structure used in the simulations [64, 65].*

The design of the holograms is an iterative process where the hologram structure is optimised so that the transmitted field produces the desired plane in the quiet-zone. The quiet-zone field amplitude is adjusted using a weighing function $W(\rho)$ in Equation (3.18) to modify the aperture field of the hologram. The weighing function is included into the term $a(x,y)$ as [64]

$$a(x,y) = \frac{W(\rho)}{|E_i(x,y)|}, \tag{3.19}$$

where $\rho = \sqrt{x^2 + y^2}$. The weighing function is formed so that the amplitude is tapered towards the aperture edge to reduce edge diffraction. Function $a(x,y)$ determines the widths of the slots in the hologram pattern, i.e., amplitude taper results to narrower slots in the

pattern near the hologram edges. The quiet-zone field phase is modified by adding an extra correction term $\psi_e(x)$ to the phase of the transmittance [64]

$$\Psi(x,y) = \psi(x,y) + 2\pi\nu x + \psi_e(x). \tag{3.20}$$

The phase term $\Psi(x,y)$ determines the locations of the slots in the pattern and small changes in this term affect the quiet-zone phase significantly without affecting the amplitude. First, the hologram pattern is generated with selected functions and the resulting quiet-zone field is computed. Then, the weighting function and the phase correction term are adjusted iteratively until satisfactory quiet-zone field amplitude and phase are achieved. Typically, the quiet-zone field is optimised at the distance of the focal length of the hologram behind the hologram aperture. The feed location and alignment is also adjusted to optimise the quiet-zone field [66].

3.2.2.3.2 Hologram manufacturing

The optimised binarised transmittance is realised with a metallization pattern on a dielectric film, which consists of metal-free slots and metal stripes between them. The dielectric film, which is usually mylar, provides mechanical support for the hologram pattern and it is included in the model of the hologram structure in FDTD analysis [65]. Metallization patterns can be formed using either selective deposition or etching [O32]. Á cross-cut of the hologram structure is shown in Figure 3.11.

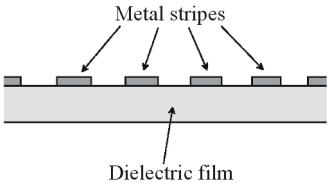

Figure 3.11 *Cross-cut of the hologram structure.*

Conventional printed circuit board (PCB) manufacturing techniques can be used to manufacture the holograms. The process is based on photolithography, where the metal-plated dielectric film is coated with photosensitive resist. The resist is selectively exposed to light using photomasks and the slots are etched to the metallization using suitable chemicals. The accuracy of the etched slot width is about the same as the thickness of the metallization as completely vertical edges are difficult to achieve in the etching process. Additional inaccuracy in the pattern is caused by the potential inaccuracy in the photomask and by the pattern distortions caused by the exposure of the mask. The achieved overall pattern accuracy of the order of 20–40 μm is not sufficient for frequencies much above 300 GHz. Maximum hologram size is limited by the size of the photomasks available and by the size of the actual manufacturing equipment. Circuit board manufacturing up to the size of 600 mm × 600 mm is commonly available. PCB-techniques have been used to manufacture holograms up to 600 mm in diameter at frequencies around 300 GHz as this method is very inexpensive.

Improved accuracy in the hologram pattern slot widths can be achieved using direct laser writing of the pattern on the photoresist [O32]. The metallized mylar film is placed on a

cylinder and the laser beam is scanned over the surface. By rotating the cylinder, selective exposure of the photoresist is achieved over the whole surface. Chemical wet etching is used to etch the slots into the metallization. Currently, the maximum size of the pattern is limited due to the available manufacturing equipment to 1.5 m × 6.0 m. The accuracy of the laser writing is about 5 μm and the estimated achievable accuracy in the slot widths is around 10 μm [67]. This method is currently used to fabricate large hologram patterns [O4].

Holograms up to several metres in diameter are needed for testing large antennas. The current size of the available manufacturing equipment is not sufficient for making large holograms for full-sized CATRs in one piece. Several methods for making the holograms in separate pieces have been investigated [O32]. The pieces are joined to form the complete hologram. Seams in the hologram should be electrically invisible and the pieces should be aligned accurately as discontinuities in the pattern act as diffraction sources. Misaligned pieces may also radiate to different directions, which distorts the quiet-zone field. Horizontal seams, i.e., seams perpendicular to the polarisation, have been found to cause less disturbances to the quiet-zone field than vertical seams [68].

Tape was used to connect seven pieces up to 1.2 m × 1.0 m to form a 2.4 m × 2.0 m hologram at the frequency of 119 GHz [63]. At sub-millimetre wavelengths, the tape changes the thickness of the dielectric film significantly causing a discontinuity, which disturbs the quiet-zone field. Similarly the overlap acts as a diffraction source when the holograms pieces are glued together. It was discovered that soldering provides the desired electrically invisible seam with sufficient mechanical durability as the thickness of the metallization is not a critical parameter to the hologram operation [O32]. The metal stripes in the hologram pattern are soldered together manually. Soldering paste does not adhere to the metal-free slots and the solder itself does not affect the hologram operation [O32]. Naturally, potential misalignment of the pieces has a significant effect on the quiet-zone field. A hologram CATR based on a 3-m diameter hologram at the frequency of 322 GHz that was manufactured in three pieces on a 50 μm thick mylar-film with a 17 μm thick copper layer is shown in Figure 3.12. The hologram pieces were joined together by soldering.

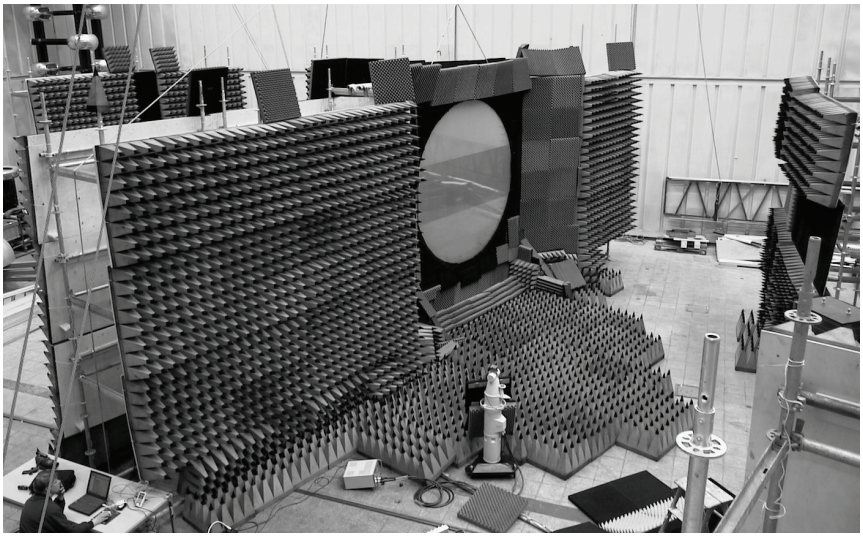

Figure 3.12 *Large hologram based CATR at 322 GHz [O3].*

Manufacturing of large metallization patterns with the required accuracy for sub-millimetre wavelength holograms is difficult. The relative error in slot widths is the greatest near the

hologram pattern edges, where the slots are very narrow. Narrow slots are difficult to etch. Amplitude taper can be introduced into the hologram illumination eliminating the narrow slots in the pattern. Shaped illumination can also be used to increase the quiet-zone size through better control of the aperture field [13]. Increased quiet-zone size in relation to the hologram size reduces the required hologram size for testing an antenna. Currently, the quiet-zone diameter is about 50–60 % of the hologram diameter then the hologram is illuminated with a corrugated horn. In this thesis, the possibilities to facilitate the hologram manufacturing with a modified hologram illumination are investigated.

3.2.2.3.3 Advantages and disadvantages of the hologram CATR in antenna testing

The main advantage of using a hologram as a collimating element in a sub-millimetre wavelength CATR over conventional reflectors is much lower manufacturing costs. High accuracy is only needed in two-dimensions instead of three-dimensions as the hologram is a planar transmission type device. The required surface flatness for a hologram is about 1/12 of the surface accuracy of a reflector at the same frequency [69]. This flatness can be relatively easily achieved by tensioning the hologram into a frame.

Another advantage is the light weight and transportability of the hologram. Combined with the low cost this allows building antenna test specific compact antenna test ranges at the selected test site. The CATR in Figure 3.11 was assembled in a hall and it was disassembled two months later right after the antenna tests [O3, O4].

The operation of the hologram is frequency dependent as the locations of the slots in the pattern depend on the phase of the incident field. Also the direction of the desired plane wave changes with the frequency. If the changes are compensated by tuning the feed position, a bandwidth of about ±5–10 % of the operating frequency is achieved [68]. The narrow bandwidth is not a very serious disadvantage as the low cost of the holograms permits making separate holograms for the different frequencies. In addition, at sub-millimetre wavelengths the receivers are also usually narrow band devices and the measurements can be often done at a single frequency at the time.

The hologram structure consists of narrow slots and of metal stripes between them. Intact metal covers over 50 % of the hologram surface resulting to high reflection loss. The efficiency of the amplitude holograms is below 10 %, i.e., less than 10 % of the power radiated by the feed is radiated as a plane wave into the quiet-zone [70]. The relatively high losses of over -10 dB reduce the available power, i.e., dynamic range, in the quiet-zone for antenna testing. Phase holograms consist of milled grooves instead of slots in the metallization and, therefore, in principle there is no blocking and higher efficiency can be achieved [71]. Phase holograms are investigated for potential use in radar cross section (RCS) measurements at sub-millimetre wavelengths.

The transmission of narrow slots depends on the polarisation. At the polarisation parallel to the slot, the slot width has a strong effect on the transmission coefficient, but at the polarisation perpendicular to the slot the transmission is only weakly affected by the slot width. Therefore, the narrowing of the slots towards the hologram edges does not produce amplitude taper at the horizontal polarisation as the hologram slots are in vertical direction. The quiet-zone field has large ripples due to edge diffraction at the horizontal polarisation [65] and the holograms can be used only at the vertical polarisation. The amplitude taper in

the hologram illumination realised with a dual reflector feed system allows the holograms to operate at the horizontal polarisation also.

The slots in the hologram pattern are curved forming arcs of ellipses. The direction of parallel and perpendicular polarisation changes as the slot direction changes. This causes depolarisation of the field. The cross-polarised field in the hologram illumination is also transmitted into the quiet-zone. This cross-polarisation and cross-polarised field generated by the hologram cause the total cross-polarisation level to be about -20 dB at maximum in the quiet-zone [72]. The potential improvement to the cross-polarisation level is investigated in this thesis by using a polarising grid in front of the feed to eliminate the cross-polarisation in the hologram illumination.

3.2.2 Near-field measurements

The near-field measurements are based on sampling the radiating field of the antenna in the radiating near-field on a surface using a probe antenna and computing the corresponding far-field radiation. The surface can be a planar, a cylindrical or a spherical surface. In principle, the radiation can be computed from the equivalent sources on this surface as described in Section 2.2. The equivalent surface currents are determined from the near-field scanning data. An example of this approach is described in [73].

Modal expansions are usually used to simplify the near-field to far-field transformation. The measured near-field is used to determine the coefficients of the planar, cylindrical or spherical wave functions. The radiated electric field of the antenna under test can be computed from the measured tangential electric field on a surface with [74]

$$\bar{E}(r) = \oint_S \left[\bar{n}' \times \bar{E}(\bar{r}')\right] \cdot \bar{\bar{G}}(\bar{r}', \bar{r})\, dS', \tag{3.21}$$

where the dyadic Green function is

$$\bar{\bar{G}}(\bar{r}', \bar{r}) = \sum \left[\bar{N}_m^*(\bar{r}')\bar{M}_m(\bar{r}) - \bar{M}_m^*(\bar{r}')\bar{N}_m(\bar{r})\right]. \tag{3.22}$$

The Green function is given in terms of two orthogonal vector wave functions $\bar{M}$ and $\bar{N}$. The point on the surface *S* is $\bar{r}'$ and the observation point is $\bar{r}$. The surface normal is $\bar{n}'$. The geometry is illustrated in Figure 3.13. The determination of vector wave solutions $\bar{M}$ and $\bar{N}$ allow relatively simple near-field to far-field transformations for planar, cylindrical and spherical scanning surfaces.

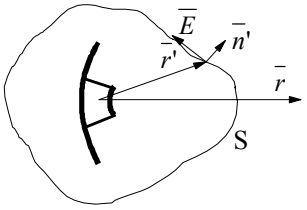

Figure 3.13 *Determination of the radiated electric field from the measured tangential electric field.*

In general, the probe pattern has to be compensated in the transformation for accurate results as the probe receives (or transmits) radiation differently from different directions.

The first near-field antenna measurements were done in the early 1950's [74] and the data was used to directly examine the amplitude and phase in the radiated field of the antenna without computing the corresponding far-field. In the mid-1950's, the far-field pattern was computed from the near-field without compensating the effect of probe pattern on the results. A probe correction method based on a plane wave scattering matrix was introduced into the planar near-field measurements in 1963 by Kerns from National Institute of Standards and Technology (NIST), USA [74]. The measurement system utilising this method was later constructed at the NIST [75].

The probe-corrected formulas for near-field scanning in spherical coordinates were derived by Jensen of the Technical University of Denmark in 1970. More practical probe-correction methods that allowed the determination of the spherical mode coefficients for the antenna under test were published in mid-1970's by Jensen and others. In 1973, probe compensated cylindrical near-field scanning was implemented for the first time by Leach and Paris at the Georgia Institute of Technology. [74]

3.2.2.1 Planar near-field measurements

In planar near-field measurements, the radiating near-field of the antenna under test is probed by scanning the field over a planar surface. The scanning can be done in *xy*-, polar, or in bi-polar configuration. The different planar scanning configurations are illustrated in Figure 3.14. In the *xy*-scanning, the sampling is done in a rectangular grid. An example of a *xy*-scanner at sub-mm wavelengths is described in [76]. In the polar scanning, the sampling is done in a polar grid and only single linear scan is needed if the antenna under test is rotated [77]. In the bi-polar scanning, the antenna under test is rotated axially and the probe sweeps an arc as the scanner arm is rotated around a second axis parallel the AUT rotation axis [78]. The samples form co-centric rings with samples along radial arcs.

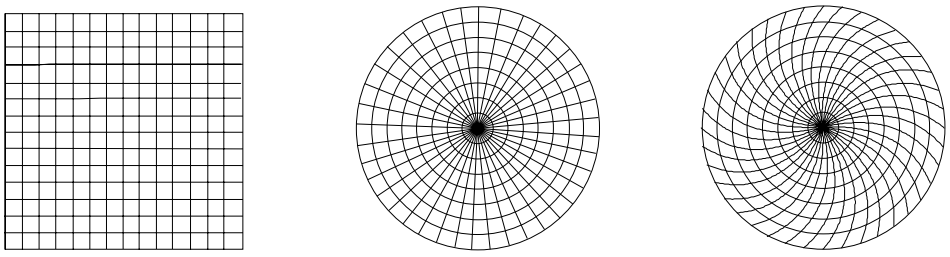

a) *b)* *c)*

Figure 3.14 *Sampling grids in a) rectangular, b) polar, and c) bipolar near-field scanning.*

3.2.2.1.1 Scanning in a rectangular grid

The measured fields in a rectangular grid on a planar surface can be expressed as a plane wave expansion, i.e., as a plane wave spectrum $\overline{A}(k_x, k_y)$ [42]. The propagation vector $\overline{k}$ is defined as

$$\overline{k} = k_x \overline{u}_x + k_y \overline{u}_y + k_z \overline{u}_z , \tag{3.23}$$

where

$$k_x = \frac{2\pi}{\lambda} \sin\theta \cos\phi , \tag{3.24}$$

$$k_y = \frac{2\pi}{\lambda} \sin\theta \sin\phi , \tag{3.25}$$

$$k_z = \frac{2\pi}{\lambda} \cos\theta . \tag{3.26}$$

(θ, ϕ) are the directional angles of the spherical coordinates. The tangential electric field $\overline{E}_t$ on a plane at z_0 can be expressed with the plane wave expansion as [42, 74]

$$\overline{E}_t(x, y, z_0) = \frac{1}{2\pi} \int_{-\infty}^{\infty} \int_{-\infty}^{\infty} \overline{\overline{R}}(k_x, k_y) \cdot \overline{A}(k_x, k_y) e^{-j(k_x x + k_y y + k_z z)} dk_x dk_y , \tag{3.27}$$

where $\overline{\overline{R}}(k_x, k_y)$ describes the receiving properties of the probe, i.e., the probe pattern. The plane wave spectrum $\overline{A}(k_x, k_y)$ of the measured field can be determined from tangential electric field as [42, 74]

$$\overline{A}(k_x, k_y) = \frac{e^{jk_z z_0}}{2\pi} \overline{\overline{R}}^{-1}(k_x, k_y) \cdot \int_{-\infty}^{\infty} \int_{-\infty}^{\infty} \overline{E}_t(x, y, z_0) e^{j(k_x x + k_y y)} dx dy , \tag{3.28}$$

which is the Fourier transformation of the tangential electric field $\overline{E}_t(x, y, z_0)$ with the compensation for the probe pattern $\overline{\overline{R}}(k_x, k_y)$. The far-field pattern at the distance *r* can be computed as [42]

$$\overline{E}(r) = j \frac{2\pi k_z}{r} \overline{A}(k_x, k_y) e^{-jkr} . \tag{3.29}$$

When the near-field of the AUT is sampled in a uniformly spaced rectangular grid, the efficient fast Fourier transform (FFT) algorithm can be used to compute the far-field pattern of the antenna.

The scanning plane has to cover the angular region, in which the radiation pattern of the AUT is to be determined. The maximum angle that is covered is $\theta_{\max}$. The related geometry is illustrated in Figure 3.15.

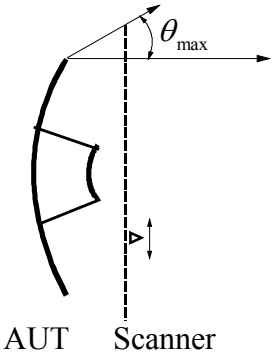

Figure 3.15 *Planar scanning geometry.*

The maximum sampling spacing in the case of the spatially limited near-field sampling that covers the angular region, where $\theta \le \theta_{\max}$, is [79]

$$\Delta x = \Delta y = \frac{\lambda}{2\sin\theta_{\max}}. \tag{3.30}$$

The maximum sampling spacing corresponds to the Nyqvist sampling theorem $\Delta x = \Delta y = \lambda/2$, when $\theta_{\max}$ approaches 90°. If the near-field is probed in the reactive near-field of the AUT, where the evanescent waves are present, the sampling interval has to be decreased to determine the far-field radiation pattern accurately [74,79].

3.2.2.1.2 Scanning in a polar grid

The far-field pattern can be determined from the measured near-field data using a Jacobi-Bessel expansion [77] or other plane polar expansions such as in [80], or by using fast Fourier transformation after the data has been interpolated to a uniformly spaced rectangular grid [81, 82]. The minimum number of the near-field measurement points that are needed for the FFT based near-field to far-field transformation is investigated in [82]. The maximum radial spacing $\Delta\rho$ is [82]

$$\Delta\rho = \frac{\lambda d}{2r_0\chi_1} \tag{3.31}$$

and the maximum angular spacing $\Delta\phi$ is

$$\Delta\phi(\theta) = \frac{\lambda}{2r_0\chi_1^*(\theta)\sin\theta}, \tag{3.32}$$

where d is the distance of the measurement plane from the AUT, r_0 is radius of the minimum sphere enclosing the AUT, θ is the direction angle of the sampling point, and χ_1 is the excess spatial bandwidth factor, i.e., the oversampling factor, that has to be slightly larger than unity to ensure accurate determination of the far-field pattern. The excess bandwidth factor χ_1^* is defined as [82]

$$\chi_1^*(\theta) = 1 + (\chi_1 - 1)(\sin(\theta))^{-2/3}. \tag{3.33}$$

The sampling interval corresponds to the Nyqvist sampling theorem inside the minimum sphere, where the sampling interval becomes $\lambda/(2\chi_1)$. The scanning geometry is illustrated in the Figure 3.16.

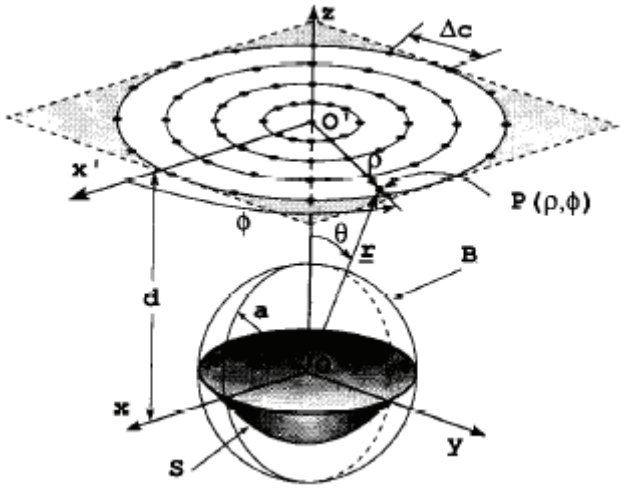

Figure 3.16 *Plane polar scanning geometry [82].*

The radial spacing increases with the measurement distance d and the angular spacing is independent of the measurement distance and decreases with θ. The total number of the samples is the same regardless of the measurement distance when the angular extent of the measurements zone remains the same. The scanning plane has to cover the angular extent, where the far-field pattern of the AUT is to be determined as in the case of the sampling in a rectangular grid.

3.2.2.1.3 Scanning in a bi-polar grid

The far-field pattern of the AUT is determined from the bi-polar near-field data using interpolation to the rectangular sampling grid, which allows the use of the FFT, or Jacobi-Bessel or Fourier-Bessel transforms, which allow the direct use of the bi-polar near-field samples [83]. The bi-polar sampling positions are converted to polar coordinates for these transformations. Alternative approach is to determine the equivalent currents and compute their far-field radiation [84].

The sampling spacing in the bi-polar scanning is studied in [78]. The spacing in the angular direction of the AUT rotation $\Delta\alpha$ is the same as the corresponding angular spacing $\Delta\phi$ in the

polar coordinates (ρ, ϕ) in the case of the plane polar scanning given by (3.32). The sampling increment of the bi-polar scanner arm rotation $\Delta\beta$ is [78]

$$\Delta\beta(\rho) = 2\sin^{-1}\left(\frac{\rho + \Delta\rho}{2L}\right) - 2\sin^{-1}\left(\frac{\rho}{2L}\right), \tag{3.34}$$

where L is the scanner arm length, ρ is the radial distance of the sampling point in the polar coordinates of the scanning plane, and $\Delta\rho$ is the corresponding radial increment in a plane polar scan given by (3.31). If even sampling spacing is needed, the smallest spacing on the scanning plane should be used. Alternative, the bi-polar scanning can be done by rotating the AUT and the scanner arm simultaneously, when the probe traces a spiral over the scanning plane [85]. This allows faster scanning. The sampling geometries are illustrated in the Figure 3.17.

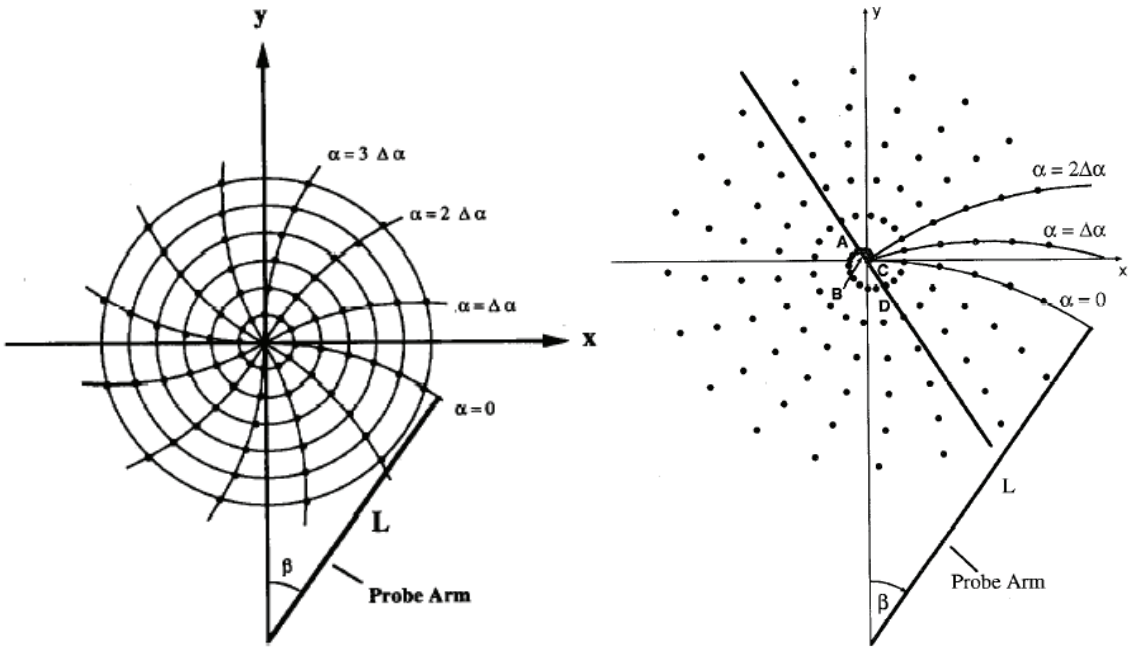

a) *b)*

Figure 3.17 *Bi-polar scanning geometries: a) basic [78], b) spiral sampling [85].*

3.2.2.2 Cylindrical near-field measurements

The near-field of the antenna under test can be sampled over a cylindrical surface. The probe is scanned in the vertical direction and the AUT is rotated in the azimuth direction to form a cylindrical scanning surface. This geometry allows large angular coverage in horizontal direction in the determination of the far-field pattern of the AUT. The cylindrical near-field measurement geometry is presented in Figure 3.18.

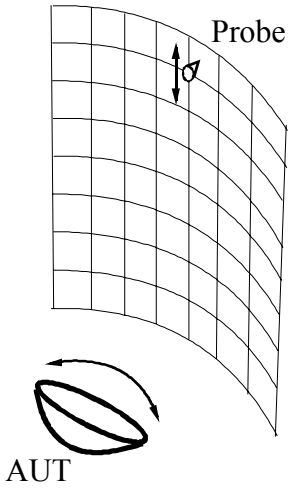

Figure 3.18 *Cylindrical near-field sampling.*

The measured near-field is expanded into vector wave modes with cylindrical Bessel and Hankel functions utilising fast Fourier transform and FFT is also used to determine the corresponding far-field radiation [86]. The equivalent current method for cylindrical near-field to far-field transformation can be used also and it has been used for example in [87].

The maximum sampling interval in the angular direction ϕ in the cylindrical coordinates (r, ϕ, z) is [86, 88]

$$\Delta\phi = \frac{\pi}{kr_0} = \frac{\lambda}{2r_0}, \tag{3.35}$$

where $k=2\pi/\lambda$, and r_0 is the radius of the minimum sphere enclosing the AUT. Using a sampling expansion technique the sampling spacing can be decreased in the z-direction from $\lambda/2$ to

$$\Delta z = \frac{\lambda/2}{a/r_0}, \tag{3.36}$$

where a is the cylinder radius.

3.2.2.3 Spherical near-field measurements

Omni-directional coverage of the far-field pattern measurement can be achieved relatively easily using spherical near-field scanning. A spherical scanning surface is realised by rotating the antenna in both θ- and ϕ-directions in the spherical coordinates (r, θ, ϕ) while keeping the probe stationary. An alternative approach is to move the probe over a sphere or move the probe over a circular path and rotate the AUT in the azimuth direction. An example of a spherical near-field scanner is shown in Figure 3.19.

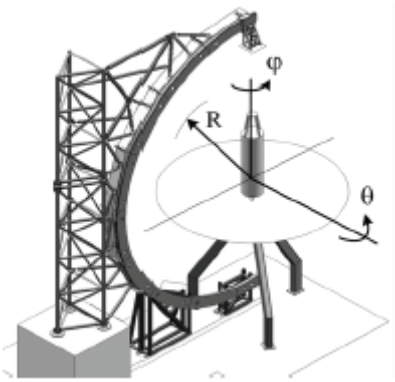

Figure 3.19 *A spherical near-field scanner [89].*

The near-field of the antenna $\overline{E}(r,\theta,\phi)$ is expanded into spherical wave modes so that [90]

$$\overline{E}(r,\theta,\phi)=\frac{k}{\sqrt{\eta}}\sum_{s=1}^{2}\sum_{n=1}^{N}\sum_{m=-n}^{n}Q_{smn}\,\overline{F}_{smn}(r,\theta,\phi), \tag{3.37}$$

where Q_{smn} are the modal coefficients to the spherical wave functions $\overline{F}_{smn}(r,\theta,\phi)$. The number of modes N depends on the variation of the field in the directions of the spherical angles θ and ϕ. The number of the modes can be determined from [91]

$$N=kr_0+n_1, \tag{3.38}$$

where $k=2\pi/\lambda$ is the wavenumber, r_0 is the radius of the minimum sphere, and n_1 is a number depending on the desired accuracy of the spherical wave expansion. Typically, n_1=10 is selected. The optimal number of modes is studied in [91] and the required sampling spacing is less than 180°/N. To completely characterise the radiated field, the field must be sampled according the Nyqvist sampling theorem on the minimum sphere, i.e., the maximum angular sampling intervals are

$$\Delta\theta=\Delta\phi=\frac{\lambda}{2r_0}, \tag{3.39}$$

where r_0 is radius of the minimum sphere enclosing the AUT. An alternative approach for determining the far-field from the measured near-field is to determine the equivalent sources and compute their radiation. An example of this approach in the spherical near-field scanning is described in [92].

3.2.2.4 Applicability of the near-field measurements for sub-millimetre waves

The near-field measurements have certain advantages over compact antenna test ranges (CATRs) such as the possibility to direct observation or holographic reconstruction of the aperture field of a reflector or an array antenna to characterise possible faults in the antenna structure [93, 94]. Also, planar near-field scanning can be done in a smaller volume than what a CATR occupies.

At sub-millimetre wavelengths, the near-field scanning has some additional challenges compared to lower frequencies. The needed positioning (of the order of $\lambda/100$–$\lambda/50$) and pointing accuracy of the probe (and the AUT) result into very high accuracy requirements for the scanner mechanics. The large number of samples that are needed for measuring electrically large antennas makes the measurements time-consuming and high-stability is needed in the measurement equipment – in both mechanical and electrical equipment. Temperature changes may induce drift in the electrical instrumentation and dimensional changes in the mechanical structure due to thermal expansion. These effects have to be minimised for accurate antenna measurements and accurate temperature control is needed. The applicability of the near-field measurements and other antenna measurement techniques to sub-millimetre waves is studied in [95].

An example of a sub-millimetre wave planar near-field scanner operating at the frequency of 550 GHz is described in [76]. The 0.8 m x 0.8 m scanner is constructed of granite to ensure high mechanical stability of the structure and a vertical granite plate was used as a *z*-coordinate reference to achieve high planarity of the scanner surface. An alternative to a highly accurate scanner structure is to measure the probe position with high precision using laser interferometers and to correct the non-ideal probe position either computationally [96, 97] or mechanically [89]. Near-field scanning has been also used to evaluate the quiet-zone field of a CATR at millimetre waves [98] and at sub-millimetre waves [O4, O11].

In this thesis, planar near-field scanning is used to verify the radiated beam of the designed dual reflector feed system at the frequency of 310 GHz and to evaluate the quiet-zone field quality of the test holograms at 310 GHz and of the hologram based CATR at 322 GHz.

4 Dual reflector feed system synthesis

The hologram illumination can be modified with a shaped dual reflector feed system (DRFS). A numerical dual reflector synthesis procedure has been developed for designing the DRFS [O1]. The developed procedure is based on geometrical optics (GO). Geometrical optics employs a high frequency approximation of the Maxwell's equations, which allows fast computation of the electromagnetic field. Therefore, the synthesis methods based on GO are well suited for electrically large reflectors at high frequencies. At sub-millimetre wavelengths, even reflectors with relatively small physical dimensions are electrically large. The geometrical optics based synthesis methods have also the advantage of being in principle frequency independent, which eliminates the need to optimise the synthesised antennas separately for different frequencies.

The developed synthesis procedure is based on the ray-tracing principle presented in [33], but the implementation of the procedure is somewhat different and certain modifications have been adapted to simplify the software implementation. The electromagnetic fields are represented by plane waves that propagate along the rays and the reflector surfaces are approximated with planar sections at the computation points. The reflector surfaces are extrapolated from a previous point to the next to ensure continuity of the surfaces. Similar approximations have been used in for front-fed dual reflector antennas in [36] and for dual offset reflectors in [13, 37]. However, in the developed synthesis procedure the dual reflector feed structure is treated as an independent antenna instead of the considering it as a part of a reflector antenna system with a parabolic main reflector and the DRFS is considered as a shaped beam antenna. This results in a somewhat different approach in the synthesis than in [13, 36, 37].

4.1 Synthesis procedure

The developed synthesis procedure starts with the definition of the system geometry. The electromagnetic fields are represented by locally planar waves, which propagate along the rays. The ray distribution in the output beam, which illuminates the hologram is determined with so-called input-output aperture mapping. Finally, the reflector surfaces are determined so that the input ray distribution is transformed to the output ray distribution via reflections on the reflector surfaces. The steps in the synthesis procedure are illustrated in Figure 4.1. The synthesis procedure is described in more detail in the following sections.

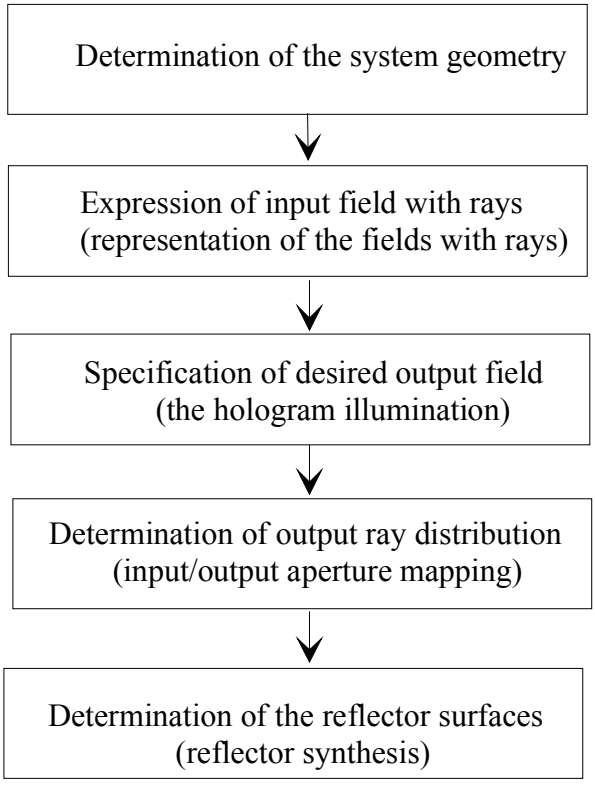

Figure 4.1 *The structure of the synthesis procedure.*

4.1.1 Definition of the system geometry

Reflector antennas are commonly based on conic sections, i.e., paraboloid, ellipsoid and hyperboloid surfaces are used as reflectors. The reflectors based on the conic sections are shown in Figure 2.1. These reflector surfaces are defined by their focal points: the paraboloid as only one focal point as the ellipsoid and the hyperboloid have two. The foci of the ellipsoid are on the same side of the surface and the hyperboloid has one focus in front of the surface and a virtual focus behind it. In general, the reflector surfaces can be shaped surfaces without clear focal points. In this thesis, a shaped surface is called a hyperboloid-, ellipsoid- or paraboloid-type shaped surface or a shaped hyperboloid (ellipsoid or paraboloid), when the shaped reflector has focal regions that resemble the focal points of the corresponding conic section.

The dual reflector feed system (DRFS) for illuminating holograms has a diverging beam as the hologram is used as the collimating element in a compact antenna test range. The hologram design is simplified greatly if the electromagnetic wave illuminating the hologram can be considered to originate from a hologram focus, i.e., it is a spherical wave. The basic DRFS geometry is shown in Figure 4.2 for a dual hyberboloid structure, which is used as the baseline geometry in this chapter to facilitate the discussion. The first reflector is called the sub-reflector and the second reflector the main reflector. The classical conic sections are a useful approximation of the actual shaped reflector surfaces in the definition of the confocal system geometry.

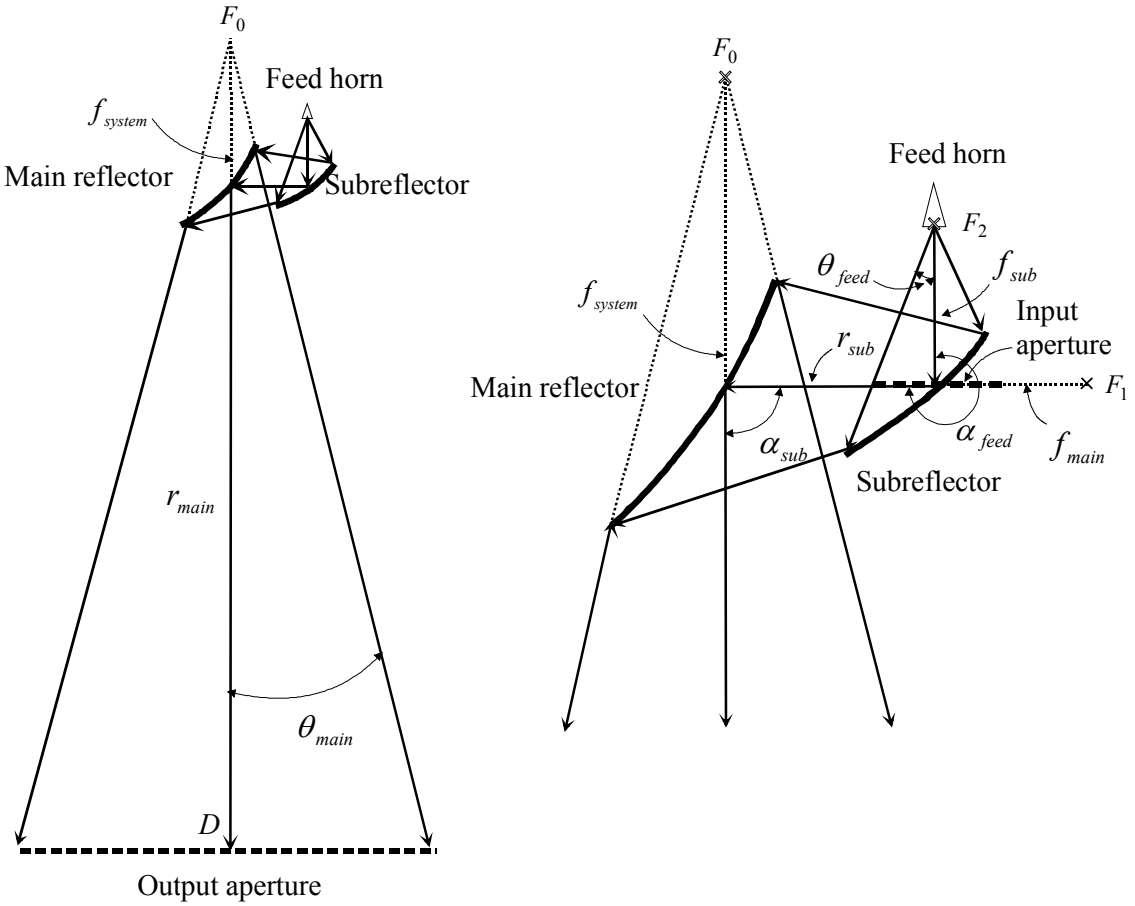

Figure 4.2 *Basic geometry of the dual reflector feed system [O1].*

The system geometry is defined by the foci F_0, F_1, and F_2. The system (hologram focus) is at F_0, F_1 is the common focus of the reflectors and the primary feed is placed at F_2. The system focus is relocated to F_2 as the beam shaping is done with the reflectors. The focal length of the system is denoted with f_{system}, and f_{main} and f_{sub} are the main reflector and sub-reflector focal lengths. The main reflector distance from the output aperture (the hologram aperture) centre is r_{main} and the sub-reflector distance from the main reflector is r_{sub}. The offset angles, α_{sub} for the sub-reflector and α_{feed} for the primary feed, are defined as shown in Figure 4.2. These parameters define the basic shapes of the reflectors and the system focal length is defined as

$$r_{main} + r_{sub} + f_{sub} = f_{system}. \tag{4.1}$$

The input and output aperture rims are defined by the focal lengths f_{system} and f_{sub}, and by the input and output beam half-beam widths θ_{feed} and θ_{main}. The choice between an ellipsoid and a hyperboloid is controlled by selection of r_{main} and r_{sub} in relation to the focal lengths f_{system} and f_{main}. The following two cases can be identified:

i) $r_{main} < f_{system}$, the main reflector is a hyperboloid-type surface.
ii) $r_{main} > f_{system}$, the main reflector is an ellipsoid-type surface.

Similarly, r_{sub} in relation to f_{main} defines which conic section the sub-reflector is. In the case of an ellipsoid, the reflected rays pass through a focus in front of the reflector, and in the case of a hyperboloid, they originate from a virtual focus behind the reflector. The incident rays on the reflector originate from a focus in both cases.

4.1.2 Ray representation of the electromagnetic fields

The input field, the primary feed radiation, and the output field illuminating the hologram are represented by rays. In geometrical optics, i.e., in ray optics, the equiphase wave fronts surfaces around the ray are often described using a second-order model based on the principal radii of curvature in the principal directions of curvature [3,9]. Alternatively, the principal curvatures, which are the reciprocals of the principal radii of curvature, can be used [34,99]. In the developed synthesis procedure, the wave fronts around the rays are described with a first-order approximation, i.e., with local plane waves, to simplify the calculations. The second- and first-order wave front approximations are illustrated in Figure 4.3.

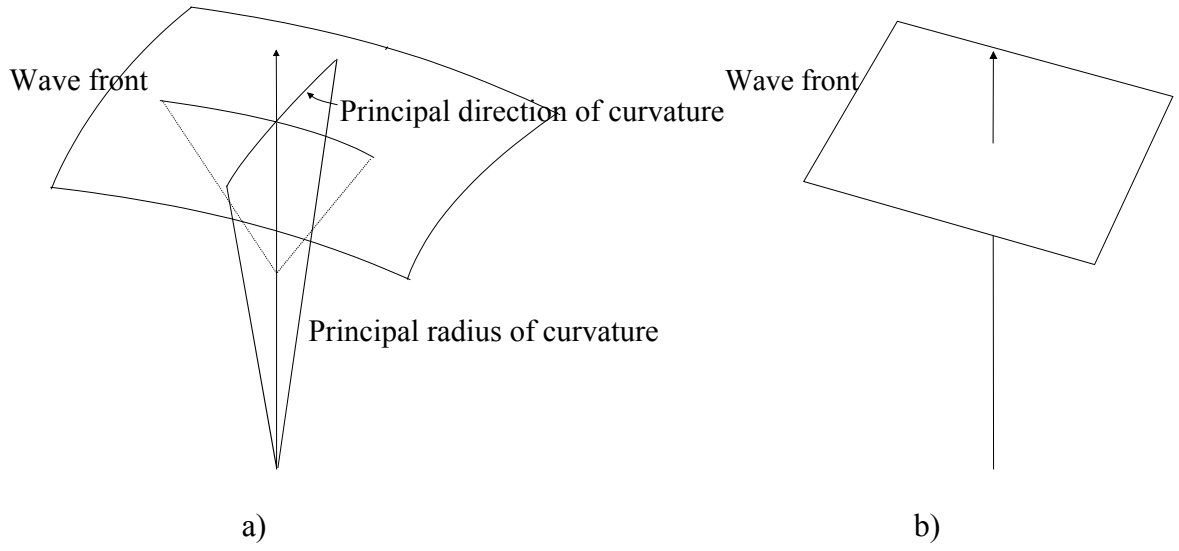

Figure 4.3 *Equiphase wave fronts: a) second-order approximation, and b) first-order approximation.*

The wave fronts are represented with local plane waves, which propagate in the direction of the rays. Each ray is considered as a phase and amplitude sample of the electric field and the fields are specified at these points. The ray direction is described with the spherical

coordinates (θ,ϕ) with origin at the ray origin and the phase at the ray grid points is determined from the ray path lengths. The power propagates in flux tubes bounded by four adjacent rays. The rays form a grid consisting of N co-centric rings with M rays on each ring and each node in the grid represents a ray. The first ring is the centre point and the rays with ϕ=0° are duplicated to rays with ϕ=360°. This facilitates the representation of the ray grids as N x M arrays in the software implementation of the synthesis procedure. The flux tubes form a (N-1) x (M-1) array. The ray grid and a flux tube are illustrated in Figure 4.4.

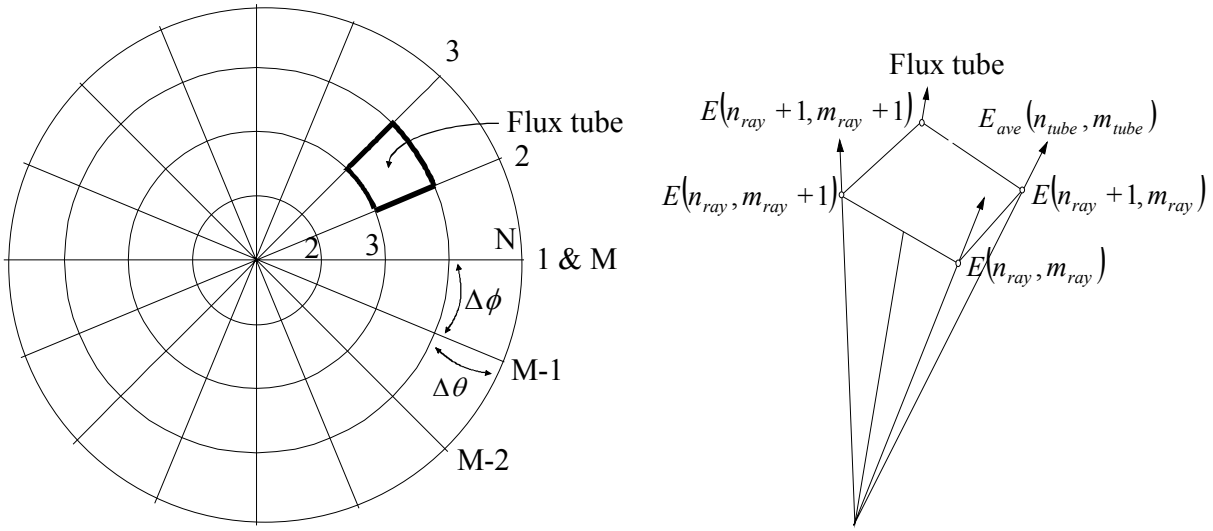

Figure 4.4 *The ray grid and the flux tube.*

The propagating power within a flux tube (n_{tube},m_{tube}) with surface area $dA(n_{tube}, m_{tube})$ is computed from the real part of the Poynting vector

$$P(n_{tube}, m_{tube}) = \frac{1}{2}\mathrm{Re}\left(\int_{S(n_{tube}, m_{tube})} \overline{E} \times \overline{H} \bullet d\overline{S}\right) \approx \frac{1}{2\eta} E_{ave}^2(n_{tube}, m_{tube}) dA(n_{tube}, m_{tube}), \tag{4.2}$$

where η is the free-space wave impedance for plane waves and

$$H = \frac{1}{\eta} E. \tag{4.3}$$

The average of the electric field amplitudes in the flux tube corners is used to approximate the field distribution inside the tube. The average electric field is computed with

$$E_{ave}(n_{tube}, m_{tube}) = \frac{1}{4}\left(E(n_{ray}, m_{ray}) + E(n_{ray}, m_{ray}+1) + E(n_{ray}+1, m_{ray}) + E(n_{ray}+1, m_{ray}+1)\right). \tag{4.4}$$

4.1.3 Aperture mapping

The output ray distribution has to be defined from the input ray distribution so that desired output field is achieved. The ray distribution in the input aperture is mapped onto the output aperture with a suitable mapping function or numerically. The properties of the geometrical optics mappings are studied in [100].

The circular input aperture rim of the dual reflector feed system is defined by the beam width of the primary feed θ_{feed} and by the distance of the feed phase centre f_{sub} from the sub-reflector centre (see Figure 4.2). The aperture was selected to be circular and the input aperture radius $\rho_{in,\max}$ is then given by

$$\rho_{in,\max} = f_{sub} \tan\theta_{feed} . \tag{4.5}$$

The input rays originate from the feed phase centre and the inception points with the input aperture form the input ray grid. The input ray distribution was selected so that the ray grid is evenly spaced in the polar coordinates (ρ,ϕ), i.e., $\Delta\rho$ and $\Delta\phi$ are constant in the grid. The aperture ray grid forms co-centric rings as shown in Figure 4.4. The input field is specified at the nodes (the ray locations) of the aperture grid. The total power in the input of the DRFS is computed as the sum of the power propagating in the flux tubes inside the aperture

$$P_{in} = \sum_{m_{tube}=1}^{M-1}\sum_{n_{tube}=1}^{N-1} P(n_{tube},m_{tube}) = \frac{1}{2\eta}\sum_{m_{tube}=1}^{M-1}\sum_{n_{tube}=1}^{N-1} E_{in,ave}^2(n_{tube},m_{tube})\,dA(n_{tube},m_{tube}), \tag{4.6}$$

where $E_{in,ave}(n_{tube},m_{tube})$ is the average amplitude within a flux tube computed with (4.4). The total power is conserved in the reflections (omitting the effect of non-ideal reflectivity) and the total power propagating through the output aperture must be equal to the total power propagating through the input aperture, i.e., $P_{out} = P_{in}$. The output aperture field, i.e., the hologram illumination, is also specified numerically in an even polar grid (ρ',ϕ'). The defined output field amplitude E_{out} has to be scaled so that the total power inside the output aperture is equal to the total propagating power inside the input aperture. The power scaling factor β is solved from

$$\beta = \frac{\frac{1}{2\eta}\sum_{m_{tube}=1}^{M-1}\sum_{n_{tube}=1}^{N-1} E_{in,ave}^2(n_{tube},m_{tube})\,dA(n_{tube},m_{tube})}{\frac{1}{2\eta}\sum_{m_{tube}=1}^{M-1}\sum_{n_{tube}=1}^{N-1} E_{out,ave}^2(n_{tube},m_{tube})\,dA'(n_{tube},m_{tube})}, \tag{4.7}$$

where $dA(n_{tube},m_{tube})$ is the area of the flux tube in the input and $dA'(n_{tube},m_{tube})$ is the flux tube area in the output. The output amplitude is scaled with the amplitude scaling factor $\alpha = \sqrt{\beta}$, i.e., the normalised output amplitude is

$$E_{out,norm} = \alpha E_{out} . \tag{4.8}$$

The power propagating inside a flux tube is also conserved, so that

$$\frac{1}{2\eta}\int_{\phi_m'}^{\phi_{m+1}'}\int_{\rho_n'}^{\rho_{n+1}'}E_{out,norm}^2(\rho',\phi')\rho'\,d\rho'\,d\phi' = \frac{1}{2\eta}\int_{\phi_m}^{\phi_{m+1}}\int_{\rho_n}^{\rho_{n+1}}E_{in}^2(\rho,\phi)\rho'\,d\rho'\,d\phi\,, \tag{4.9}$$

where ρ' and ϕ' are the polar coordinates of the rays in the output aperture, and ρ and ϕ are the polar coordinates in the input aperture. In general, the corner rays (ρ_n',ϕ_n'), (ρ_n',ϕ_{n+1}'), (ρ_{n+1}',ϕ_n'), and (ρ_{n+1}',ϕ_{n+1}') for each flux tube in the output aperture should be solved from (4.9). This is complicated for an arbitrary field distribution and some assumptions have to be made for the flux tube shape to reduce the number of unknowns in (4.9). In [33], the circles in the input aperture are mapped onto ellipses in the output aperture.

A rotationally symmetric output field distribution is often sufficient and this is also the case in the hologram illumination. However, in general a circularly symmetric mapping is not possible for dual offset reflectors [29]. Concentric rings in the input aperture do not map to concentric rings in the output. Approximate solutions are possible, for example by a controlled modification of the mapping with so-called floating mapping, where the radial lines in the output grid are allowed to curve [33]. In the developed synthesis procedure, a rotationally symmetric mapping is assumed for simplicity and the resulting errors are assumed negligible. The propagating power is conserved within concentric rings and (4.9) can be rewritten as

$$\frac{1}{2\eta}\int_{\rho_n'}^{\rho_{n+1}'}E_{out,\rho}^2(\rho')2\pi\rho'\,d\rho' = \frac{1}{2\eta}\int_{\rho_n}^{\rho_{n+1}}E_{in,\rho}^2(\rho)2\pi\rho d\rho\,, \tag{4.10}$$

where $E_{out,\rho}(\rho')$ is the normalised circularly symmetric amplitude in the output aperture and $E_{in,\rho}(\rho)$ is the rotationally symmetric amplitude in the input aperture. The propagating power within the ring *n* in the input is determined as the sum of the propagating power in the flux tubes in that ring

$$P_{in,\rho}(n_{tube}) = \frac{1}{2\eta}\sum_{m_{tube}=1}^{M\text{-}1}E_{in,ave}^2(n_{tube},m_{tube})dA(n_{tube},m_{tube})\,. \tag{4.11}$$

The output and input fields are specified at the ray locations (the nodes in the ray grid) and the field between the rays has to be estimated in order to solve the output ray rings from (4.10) with progressive integration. The circularly symmetric amplitudes are obtained by averaging the amplitudes in each ring in the ray grids

$$E_{out,\rho}(n_{ray}) = \frac{1}{M\text{-}1}\sum_{m_{ray}=1}^{M\text{-}1}E_{out,norm}(n_{ray},m_{ray}), \tag{4.12}$$

$$E_{in,\rho}(n_{ray}) = \frac{1}{M\text{-}1}\sum_{m=1}^{M\text{-}1}E_{in}(n_{ray},m_{ray}). \tag{4.13}$$

The determination of the ray rings, i.e., solving progressively ρ_{n+1}' from (4.10), is greatly simplified if the power density $E_{out,\rho}^2(\rho')$ is assumed to be linear between the ray rings, i.e., it is assumed inside the flux rings formed by the ray rings that

$$E_{out,\rho}^2(\rho') = k(n_{tube})\rho' + b(n_{tube}), \tag{4.14}$$

where

$$k(n_{tube}) = \frac{E_{out,\rho}^2(n_{ray}+1) - E_{out,\rho}^2(n_{ray}+1)}{\rho'(n_{ray}+1) - \rho'(n_{ray})}, \tag{4.15}$$

$$b(n_{tube}) = E_{out,\rho}^2(n_{ray}). \tag{4.16}$$

The locations of the ray rings in the output aperture are solved by progressively integrating the piecewise continuous power density in the radial direction starting from the aperture center $\rho'(1) = 0$. The procedure to determine the output ray rings is the following: first, the power propagating within each ring is determined with (4.11), second, the output power density (the square of the output amplitude) is linearised between the specified points to form a piecewise continuous rotationally symmetric power density function, and third, the ρ-coordinate $\rho'(n_{ray}+1) = \rho_{n+1}$' for the next ray ring in the ray grid can be solved progressively from

$$\frac{1}{2\eta}\int_{\rho_n'}^{\rho_{n+1}'} E_{out,\rho}^2(\rho') 2\pi\rho' \, d\rho' = P_{in,\rho}(n_{tube}), \tag{4.17}$$

where $E_{out,\rho}^2(\rho')$ is the piecewise continuous power density given by (4.14). The progressive determination of the output ray ring distribution results into a floating output aperture rim, i.e., the radius of the output aperture is determined by the rim of the last ring of flux tubes in the aperture. The input rays originate from the feed phase centre at the sub-reflector focus and the output rays originate from the system focus. The phase in the output aperture is given by the path lengths $l(n_{ray}, m_{ray})$ of the rays

$$l(n_{ray}, m_{ray}) = \sqrt{\rho'(n_{ray}, m_{ray}) + f_{system}^2}, \tag{4.18}$$

where $\rho'(n_{ray}, m_{ray})$ is the radial distance from the output aperture centre.

The aperture mapping described here is very simply and approximate. In [33], floating of the mapping is used to control the mapping errors. In the mapping used, the error in the mapping is not controlled and it assumed reasonably small so that it can be omitted. The non-ideal mapping results also to depolarisation of the DRFS beam as non-ideal mapping causes cross-polarisation [100].

4.1.4 Synthesis of the reflector surfaces

The determination of the reflector surfaces from the known incident and reflected fields is called reflector synthesis. In the dual reflector feed system synthesis, the incident rays on the sub-reflector (the input rays) and the reflected rays from the main reflector (the output rays) are known and the reflector surfaces are determined so that the incident field represented by the input rays is transformed into the output ray distribution corresponding to the desired output field, i.e., the hologram illumination. The dual reflector synthesis problem is illustrated in Figure 4.5.

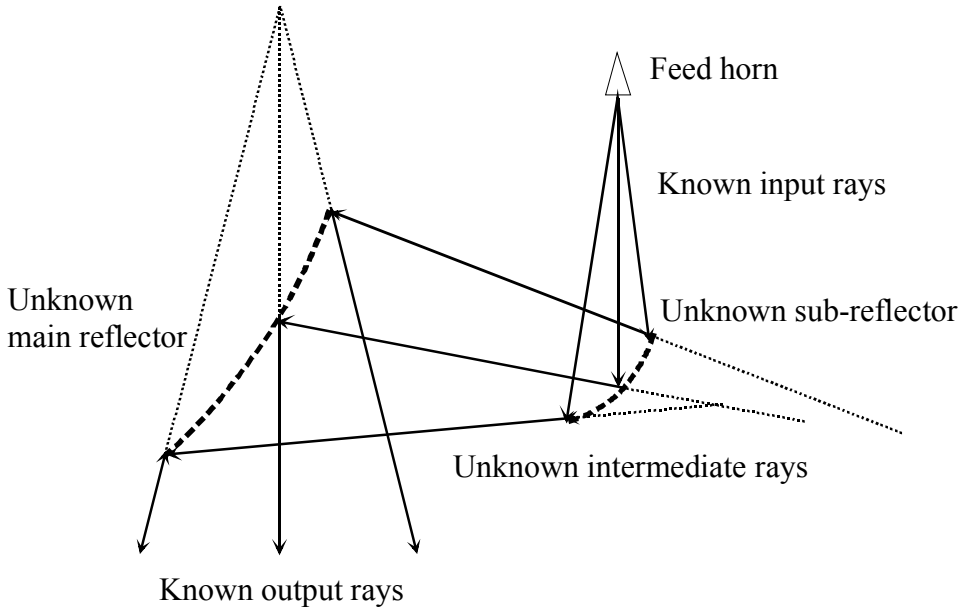

Figure 4.5 *Dual reflector synthesis problem.*

To simplify the calculations in the developed synthesis procedure, the reflector surfaces are approximated locally with tangential planes. This first-order surface approximation has also been used in [13, 36, 37]. In [33], the surfaces are represented with a second order model based on bi-parabolic expansion. The first reflector, the sub-reflector, is used to modify the amplitude and the second reflector, the main reflector, is used to correct the phase. The amplitude and phase are assumed decoupled in these field modifications by the reflectors, which is not exactly true. This assumption facilitates greatly the beam shaping and it is approximately valid. The main steps in the reflector surface synthesis are shown in Figure 4.6 and they are discussed next.

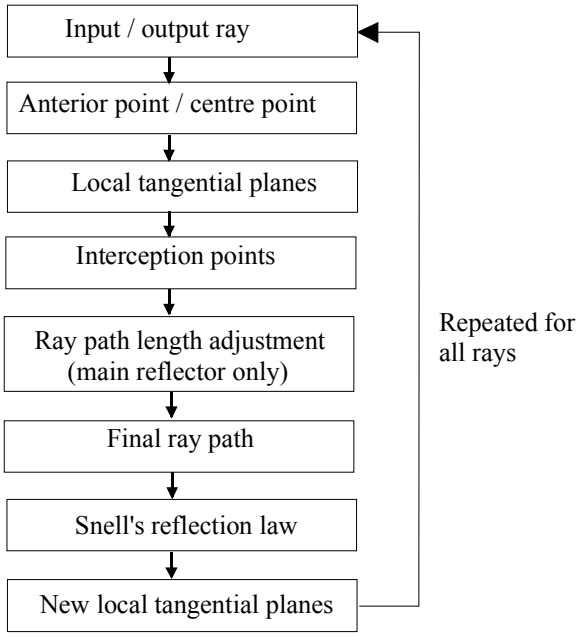

Figure 4.6 *Main steps in the reflector synthesis procedure.*

The input rays are known as they originate from the feed phase centre at the sub-reflector focus and they form an evenly spaced polar grid on the input aperture. The input aperture is located at the distance f_{sub} from the feed phase centre (see Figure 4.2). The output rays originate from the system focus and the end-points on the output aperture are determined with the input-output aperture mapping.

The synthesis procedure begins with the centre ray, for which the complete ray path is know from the system geometry. The centre ray originates from the sub-reflector focus and it is reflected from the sub-reflector and the main reflector centre points (where n=1), which are defined by the locations of the reflectors in the DRFS, and it passes through the output aperture at the centre of the aperture. The Snell's reflection law is used to find the surface normal $\bar{n}_{sub}$ from the incident ray direction vector $\bar{s}_{i,sub}$ and from the reflected ray direction vector $\bar{s}_{r,sub}$

$$\bar{n}_{sub} = \frac{\bar{s}_{r,sub} - \bar{s}_{i,sub}}{\left|\bar{s}_{r,sub} - \bar{s}_{i,sub}\right|} = n_{x,sub}\hat{u}_x + n_{y,sub}\hat{u}_y + n_{z,sub}\hat{u}_z , \tag{4.19}$$

where ($\hat{u}_x, \hat{u}_y, \hat{u}_z$) are the unit vectors in Cartesian sub-reflector coordinates with the origin at the sub-reflector focus, the z-axis is in the direction of the centre input ray and y-axis is vertical. The surface normal determines the local tangential plane at the centre point. Similarly, the centre ray in the output originates from the system focus and it is reflected via the main reflector centre point to the centre of the output aperture. The Snell's reflection law is applied to the main reflector and the surface normal $\bar{n}_{main}$ is solved as in the case of the sub-reflector as

$$\bar{n}_{main} = \frac{\bar{s}_{r,main} - \bar{s}_{i,main}}{\left|\bar{s}_{r,main} - \bar{s}_{i,main}\right|} = n_{x,main}\hat{u}_x + n_{y,main}\hat{u}_y + n_{z,main}\hat{u}_z , \tag{4.20}$$

where $(\hat{u}_x, \hat{u}_y, \hat{u}_z)$ are the unit vectors in the Cartesian main reflector coordinates with the origin at the system focus. The next ray is launched from the feed phase centre towards the sub-reflector and it intercepts the local tangential plane on the sub-reflector. The input ray is defined in the sub-reflector coordinates with the vector $\bar{s}_{sub}$, which is defined as

$$\bar{s}_{sub} = \chi_{sub}\bar{s}_{i,sub} = \chi_{sub}\left(s_{ix,sub}\hat{u}_x + s_{iy,sub}\hat{u}_y + s_{iz,sub}\hat{u}_z\right). \tag{4.21}$$

The length of the ray χ_{sub} from the feed phase centre to the interception points with the local tangential plane is determined as

$$\chi_{sub} = \frac{n_{x,sub}x_{a,sub} + n_{y,sub}y_{a,sub} + n_{z,sub}z_{a,sub}}{n_{x,sub}s_{ix,sub} + n_{y,sub}s_{iy,sub} + n_{z,sub}s_{iz,sub}}, \tag{4.22}$$

where $s_{ix,sub}$, $s_{iy,sub}$ and $s_{iz,sub}$ are the Cartesian components of the ray direction vector $\bar{s}_{sub}$ and $(x_{a,sub}, y_{a,sub}, z_{a,sub})$ are the coordinates of the anterior, i.e., the centre point. In general, the anterior point is the closest previously determined point on the reflector surface in the radial direction in the input aperture grid. The next point on the sub-reflector is solved from (4.21) after the ray length χ_{sub} has been determined with (4.22). The approximation of the reflector surface with a local tangential plane ensures that the surface is physical and the total differential condition [37] is satisfied locally on the tangential plane.

Similarly to the sub-reflector, the next output ray is launched from the system focus towards the main reflector and the interception point with the local tangential plane is determined. Equations (4.21) and (4.22) become for the main reflector in the main reflector coordinates

$$\bar{s}_{main} = \chi_{main}\bar{s}_{i,main} = \chi_{main}\left(s_{ix,main}\hat{u}_x + s_{iy,main}\hat{u}_y + s_{iz,main}\hat{u}_z\right), \tag{4.23}$$

where

$$\chi_{main} = \frac{n_{x,main}x_{a,main} + n_{y,main}y_{a,main} + n_{z,main}z_{a,main}}{n_{x,main}s_{ix,main} + n_{y,main}s_{iy,main} + n_{z,main}s_{iz,main}}. \tag{4.24}$$

The next point on the main reflector is initially obtained with (4.23) and (4.24). The phase is corrected to correspond to the spherical wave originating from the system focus by adjusting the ray path to correspond the ray path length obtained with (4.18). This is achieved by iteratively adjusting χ_{main} with bisection until the path length error is smaller than the selected error ε. Typically, ε is selected to be a fraction of the wavelength. The ray path length is computed from the known coordinates of the feed phase centre, the reflection points on the reflectors, and from the ray end-point in the output aperture. The adjustment of χ_{main} corresponds to moving the reflection point along the output ray towards or away from the system focus. The reflector surface shape is simultaneously slightly changed, i.e., the phase is corrected at the expense of the amplitude.

After the ray path length adjustment also the point on the main reflector is known and the complete ray path is determined. The Snell's reflection law can then be used to find the surface normal vectors and the corresponding local tangential planes. This synthesis procedure is repeated for all the rays starting from the ray grid centre and proceedings towards

the aperture rim ring-by-ring in the grid and in counter-clockwise direction in the ray rings. The local tangential plane for each ray is determined at the reflection point of the previous ray in the radial direction in the ray grid.

4.1.5 Applicability of the synthesis procedure for different reflector geometries

The developed synthesis procedure was implemented as modular MATLAB®-software to facilitate potential modifications to the software. The synthesis procedure is in principle independent of the reflector shape that is to be synthesised. This and the modular structure of the programs allow the synthesis of various confocal dual reflector systems with relatively minor modifications to the software.

Different shaped reflector configurations based on conic sections can be realised by defining the corresponding output ray distribution, i.e., the input-output aperture mapping, and by specifying the reflector foci and reflector locations appropriately so that the correct surface based on the conic sections is realised. The selection of the foci and the reflector locations in relation to the foci select whether the surface is an ellipsoid-type surface or a hyperboloid-type shaped surface. A shaped parabolic main reflector can be synthesised by specifying the output rays to have separate origins so that the output rays are parallel.

4.2 Accuracy of the synthesis method

The developed numerical synthesis procedure is based on ray tracing, i.e., on geometrical optics (GO). As a numerical method, it is inherently approximate and it is based on high frequency approximation of the Maxwell's equations (GO). The factors affecting the accuracy of the synthesis procedure are discussed in this section. Inaccurate synthesis procedure may result to incorrect reflector surfaces and to deviations in the hologram illumination.

The ray tracing based geometrical optics approach to the synthesis of the dual reflectors does not include diffraction effects and only the co-polarized field is included in the synthesis. The diffraction effects and potential depolarisation, and their minimisation are discussed in Chapter 5 together with the design of the dual reflector feed system. The approximations made in the synthesis problem formulation decrease the accuracy of the synthesis. The inaccuracies related to the numerical implementation of the synthesis procedure are discussed next.

4.2.1 First-order model of the surfaces

In the synthesis procedure, the phase wave fronts (the equiphase surfaces) and the reflector surfaces are approximated with local tangential planes. This first-order model is very simple and approximate description of arbitrary curved surfaces. The resulting error in the description of the surfaces can be reduced by increasing the number of rays in the ray grid, i.e., by using a denser grid.

To estimate the error in the tangential plane approximation of a curved surface let us consider the case of a spherical surface with radius R. The error in the surface is denoted with Δr and it

is equal to the deviation of the tangential plane from the sphere. The angular spacing of the rays in the spherical coordinates is $\Delta\theta$. The geometry is shown in Figure 4.7.

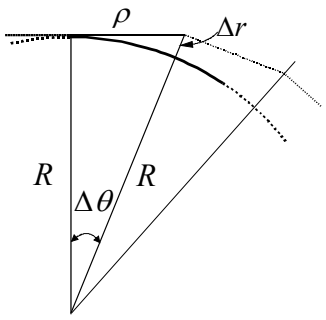

Figure 4.7 *Representation of a spherical surface with tangential planes determined at an anterior point*.

The following expression can be derived from the geometry for Δr

$$\Delta r = R\left(\sqrt{1+\tan^2\Delta\theta}\,-1\right). \tag{4.25}$$

The error in the surface is cumulative as an anterior point is used in the determination of the tangential planes and the total deviation after n approximations (rays) is

$$\Delta r_{tot} = n\Delta r = nR\left(\sqrt{1+\tan^2\Delta\theta}\,-1\right). \tag{4.26}$$

For example, when a spherical surface with the radius of the curvature R=200 mm and $n\Delta\theta$=15°, is described with local tangential plane with the maximum allowed error Δr_{tot} of $\lambda/100$ at 300 GHz (10 μm) in the surface description, the required number of tangential planes n, i.e., rays, is about 700. This number of rays is rather large and the error in the synthesis due to this first order surface approximation of the reflector surfaces can be significant. In the presentation of the electromagnetic field with local plane waves the error is less significant as the actual field amplitude and phase are sampled at each point and the error does not cumulate. The related geometry is shown in Figure 4.8.

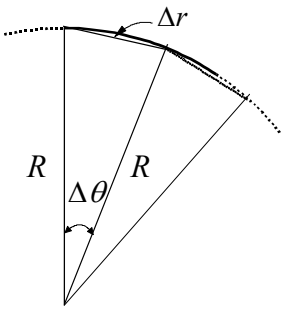

Figure 4.8 *Representation of a spherical wave with plane waves*.

The maximum error in the representation of a spherical wave with local plane waves occurs in the centre of the flux tube. From the geometry it can be derived that the surface error Δr is given by

$$\Delta r = R(1 - \cos(\Delta\theta / 2)), \tag{4.27}$$

where R is the radius of the curvature and $\Delta\theta$ is the angular spacing between the rays, i.e. the flux tube width. For example, when the maximum allowed phase error is 10° at 300 GHz, i.e., Δr=27.8 μm, in the angular range of 10° for a spherical wave with R=1.8 m, the number of flux tubes needed is 16. This error is much less significant than the error due to the representation of the reflector surfaces with local tangential planes.

4.2.2 Numerical accuracy of the synthesis procedure

The accuracy of the developed ray tracing method depends on the number of rays used in the synthesis. The surface description accuracy was discussed in Section 4.2.1 and (4.26) gives an estimate for the resulting surface error. However, (4.26) may give somewhat high estimate on the surface error as it is derived for a spherical surface and the actual radius of curvature varies over a shaped reflector surface. Therefore, to study the effect of the numerical inaccuracy in the reflector synthesis ideal non-shaped hyperbolic reflectors with focal points corresponding to the focal points of the centre ray in the shaped reflector design were synthesised using different sized ray grids.

The hyperboloid surfaces can be computed analytically from

$$z = c - \frac{a}{b}\sqrt{b^2 + x^2 + y^2}\ , \tag{4.28}$$

where $b = \sqrt{c^2 - a^2}$ and a is half of the vertex distance and c is half of the distance between the focal points. The Cartesian coordinates (x,y,z) define the coordinate system in relation to the hyperboloid foci. Numerically determined reflector points are compared to the points computed with (4.28). The focal points for the sub-reflector and main reflector hyperboloids are known for the DRFS geometry defined by the parameters described in Figure 4.2. The centre ray intercepts the hyperboloid at the reflector centre points and the parameters in (4.28) can be easily solved. The geometry of this test DRFS is defined by the parameters presented in Table 4.1.

Table 4.1 *Selected DRFS geometry.*

D=736 mm	α_{sub}=90°
f_{system}=1800 mm	α_{feed}=270°
f_{sub}=100 mm	θ_{main}=11.55°
f_{sub}=100 mm	θ_{feed}=21°
r_{main}=1550 mm	
r_{sub}=150 mm	

The non-shaped hyperboloid surfaces do not shape the output beam and only the focal point of the system is relocated. This non-shaped beam was used as the objective in the reflector synthesis in this test. The computed maximum deviation of the synthesised reflector surfaces from the hyperboloid surfaces as the function of the number of rays in the ray grid is shown in Table 4.2.

Table 4.2 *Error in the synthesised hyperboloid surfaces* [O1].

Ray grid size N x M	Maximum deviation in the main reflector surface	Maximum deviation in the sub-reflector surface
54 x 51	36.9 µm	32.0 µm
107 x 101	18.3 µm	16.0 µm
212 x 201	9.2 µm	7.9 µm
318 x 301	6.1 µm	5.3 µm
423 x 401	4.6 µm	4.0 µm
529 x 501	3.7 µm	3.2 µm

The deviation of the synthesised reflector surfaces from the hyperboloid surfaces is approximately inversely proportional to the square root of the total number of rays used in the synthesis procedure. It can be estimated based on this test that about 200 × 200 rays are needed in the synthesis for maximum reflector surface error of λ/100 at 300 GHz and about 400 × 400 rays are needed at 600 GHz. As an example, the surface deviation of the reflector surfaces synthesised with 423 × 401 rays from the non-shaped hyperboloids are shown in Fig. 7. The shape of the deviations is similar with different number of rays.

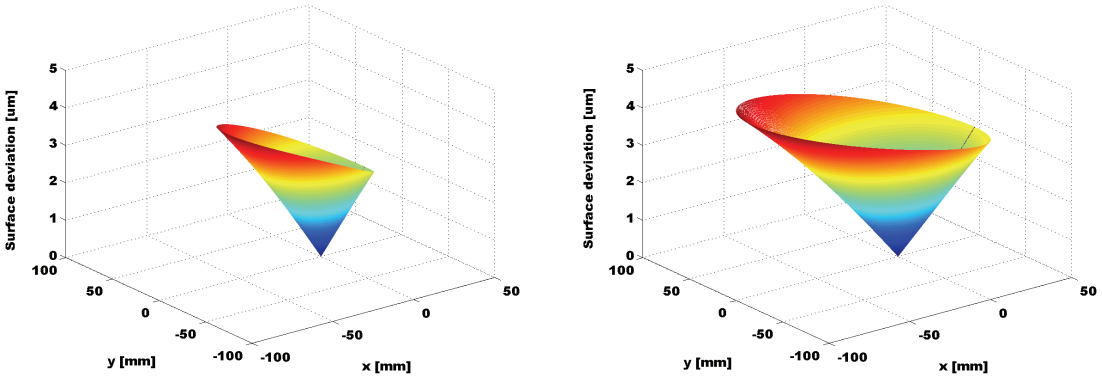

Sub-reflector *Main reflector*

Figure 4.9 *Deviation of the synthesised sub-reflector and main reflector surfaces from calculated hyperboloid surfaces when 423 x 401 rays were used [O1].*

As it can be seen in Figure 4.9 the synthesised surface shape deviates systematically from the correct shaped due to the fact that the previous point in the radial direction on the reflector surfaces is used to compute the next tangential plane on the surface. This extrapolation of the next point from the previous point causes the surface shaping to lag slightly behind the correct shape. The cumulative error seen in Figure 4.9 is similar to the error predicted by (4.26) and the error is mainly caused by the first-order reflector surface model. Similar error can be also observed when a DRFS with shaped dual-hyperboloids is synthesised with different number of rays. The surface deviation of the DRFS reflectors when the DRFS described in the Chapter 5 is synthesised with 423 × 401 rays compared to the same reflectors synthesised with 634 × 601 rays is presented in Figure 4.10.

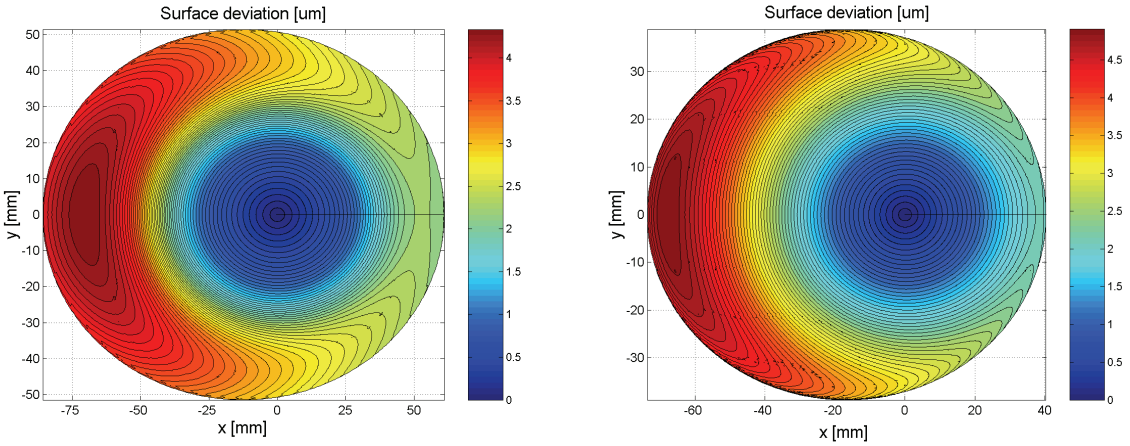

a) *b)*

Figure 4.10 *Surface deviation on the reflector surfaces:*
a) main reflector,
b) sub-reflector.

The deviation in the surface shape is at its maximum on the reflector edges and the maximum surface deviations with different numbers of the rays in the synthesis are collected into the Table 4.3. With 423 × 401 rays, the maximum surface deviations are less than 5 µm for both reflectors, which corresponds well to the surface deviations in the case of the non-shaped hyperboloids as can be seen by comparing Tables 4.3 and 4.2.

Table 4.3 *Maximum reflector surface deviations as the function of the number of rays.*

Rays	107 × 101	212 × 201	318 × 301	423 × 401	529 × 501
Main reflector	39.9 µm	17.7 µm	7.5 µm	4.4 µm	1.6 µm
Subreflector	45.1 µm	20.0 µm	8.4 µm	5.0 µm	1.7 µm

4.2.3 Aperture mapping

The accuracy of the dual reflector feed system synthesis depends not only on the accuracy of the reflector surface synthesis, which was discussed in the previous section, but also on the accuracy of the aperture mapping. The determined output ray distribution sets the objective for the DRFS synthesis and any error in the synthesis objective naturally affects the accuracy of the final output beam. The main source of the error due the aperture mapping is the assumption of the rotationally symmetric fields in the input and output aperture as in general a rotationally symmetric mapping is not possible [29] and the input aperture field is not in reality rotationally symmetric as the primary feed has a non-symmetric radiation pattern. The contribution of these effects is a part of the potential overall discrepancies in the DRFS performance, which is studied with simulations and measurements discussed in Chapter 5.

In the aperture mapping, certain approximations are used to facilitate the numerical calculations. Their effect on the numerical accuracy of the aperture mapping is discussed here. The DRFS geometry was defined with the parameters presented in Table 4.1 and the output aperture field is defined to have the phase of a spherical wave originating from the system focus with a simple rotationally symmetric Butterworth-type amplitude distribution

$$E_{out}(\rho') = \frac{\alpha}{\sqrt{1+(\rho'/\rho_c)^{2N}}}, \tag{4.29}$$

where ρ' is the radial distance in the polar coordinates in the output aperture. The following values were selected: ρ_c=210 mm and N=5. The output amplitude is scaled by factor α so that the total power in the output aperture is equal to the power in the input aperture. To facilitate the computation of the flux tube areas, the flux tubes in the circular aperture are assumed to be quadrangles in Cartesian coordinates instead of the sections of circles in polar coordinates as illustrated in Figure 4.11.

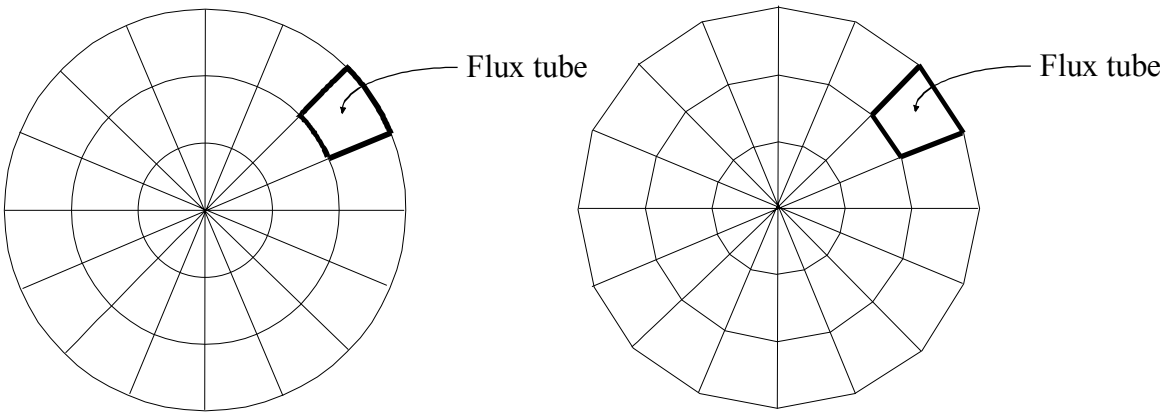

Figure 4.11 *Simplification of the input flux tube shape.*

The resulting error in the total surface area of the flux tubes, when 421 x 401 rays are used, is 0.0041 % compared to the area of the aperture circle, which is can be considered negligible. The total error due to the numerical determination of the aperture mapping can be estimated by computing the average amplitude within each flux tube in the output aperture from the propagating power $P_{in}(n_{tube}, m_{tube})$ and from the flux tube area $dA(n_{tube}, m_{tube})$

$$E_{ave,out}\left(n_{tube},m_{tube}\right)=\sqrt{\frac{2\eta P_{in}\left(n_{tube},m_{tube}\right)}{dA\left(n_{tube},m_{tube}\right)}}\,, \tag{4.30}$$

where the flux tube area is computed from the known corner ray coordinates in the output aperture. This average amplitude $E_{ave,out}\left(n_{tube},m_{tube}\right)$ is compared to the amplitude computed with (4.29) at the flux tube center. The radiation pattern of a 310 GHz corrugated feed horn is used to compute the input aperture field and the propagating power $P_{in}\left(n_{tube},m_{tube}\right)$in each flux tube. The beam of the horn is slightly narrower in the vertical direction than in the horizontal direction: at the rim of the input aperture, the edge illumination is -19.6 dB in the horizontal plane and -19.77 dB in the vertical plane. The result of the comparison of the amplitude in the output aperture computed from the flux tubes to the desired aperture field within a 600 mm diameter centre region of the output aperture is shown in Figure 4.12.

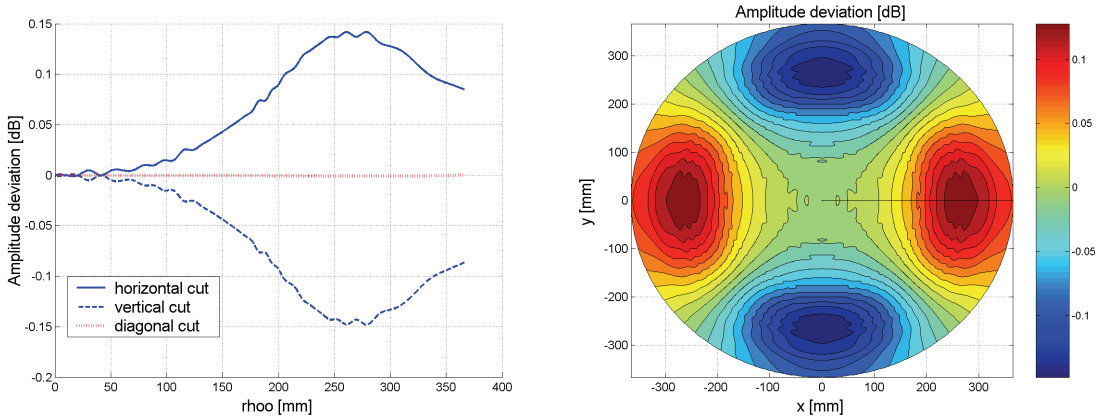

Figure 4.12 *Amplitude deviation in the synthesis objective field compared to the desired output aperture amplitude.*

The maximum deviation is about 0.15 dB, which is close to the non-symmetry in the input beam. The -3 dB beam width in the output is about 0.5 % wider in the objective beam in the synthesis than in the desired output beam. This deviation seems to indicate that the numerical accuracy of the aperture mapping is sufficient, but the assumption of a rotationally symmetric fields (and mapping) is a more significant error source, especially as such a mapping is not exactly realisable with offset reflectors.

5 Design of the dual reflector feed system for a CATR based on hologram

The developed dual reflector feed system (DRFS) synthesis procedure was used to design a demonstration DRFS for a compact antenna test range based on a hologram. The design of the DRFS is discussed in this chapter and the main steps in the design of the system are shown in Figure 5.1.

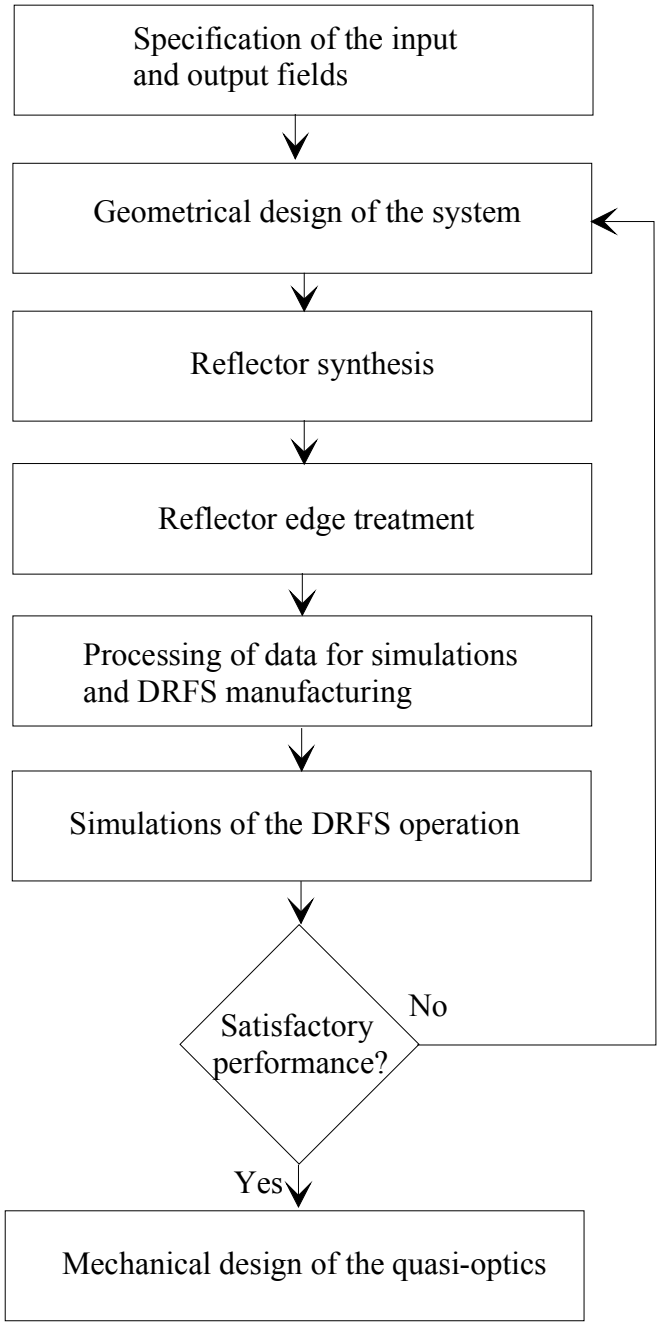

Figure 5.1 *The design of the dual reflector feed system.*

The design of the DRFS begins with the specification of the input field (the radiation of the primary feed) and the desired hologram illumination, which is the output field of the system. Then the geometry of the DRFS is specified with the locations of the reflectors and the conic sections corresponding to the shaped reflectors are selected before the synthesis of the shaped surfaces. After the synthesis the reflector edges are shaped to reduce edge diffraction and the reflector surface data is formatted for the simulations of the reflector operation and for manufacturing the designed DRFS. The design of the DRFS is verified with simulations of the DRFS radiation using physical optics (PO) and physical theory of diffraction (PTD) analysis with commercial reflector antenna simulation software GRASP by Ticra. Finally, the physical structure of the DRFS is determined in the mechanical design of the system.

5.1 Definition of the input and output fields

In the reflector synthesis, the reflector surface is determined from the given incident electromagnetic field, i.e., input field, and from the specified reflected electromagnetic field, i.e., the output field. As the input field is transformed by the reflectors in the dual reflector feed system to the output field, the natural starting point of the DRFS design is the specification of these fields. At this point, the number of the rays in the synthesis is also selected.

5.1.1 Definition of the input aperture field

The input field entering the dual reflector feed system is specified in the input aperture, which is defined as the circle centred around the point where the centre ray intercepts the sub-reflector (see Figure 4.2) with the rim radius $\rho_{in,\max}$ given by

$$\rho_{in,\max} = \tan\theta_{feed} f_{sub}, \tag{5.1}$$

where θ_{feed} is the half-beam width of the feed horn corresponding to the selected edge illumination taper of the sub-reflector and f_{sub} is the distance of the feed horn from the sub-reflector centre, i.e., the focal length of the sub-reflector hyperboloid.

The input rays form co-centric rings in the input aperture (see Figure 4.4) and the amplitude of the electric field at the ray locations at the nodes of the ray grid can be computed from the radiation pattern of the primary feed as the sub-reflector is in the far-field of the primary feed. The input aperture field amplitude for each ray is determined from the radiation pattern of the primary feed by interpolation from the horizontal and vertical pattern cuts, i.e., by assuming the equi-amplitude contours in the pattern to be elliptical. The amplitude $E_{in}(\theta,\phi)$ for the ray with spherical coordinates (θ,ϕ) with the origin at the primary feed phase centre (sub-reflector hyperboloid focus) is computed from the horizontal and vertical electrical fields with

$$E_{in}(\theta,\phi) = \sqrt{E_{hor}{}^2(\theta)\cos^2(\phi) + E_{ver}{}^2(\theta)\sin^2(\phi)}, \tag{5.2}$$

where E_{hor} and E_{ver} are the amplitudes in the horizontal and vertical pattern cuts of the primary feed pattern. The interpolation of the electric field amplitude from the pattern cuts is illustrated in Figure 5.2.

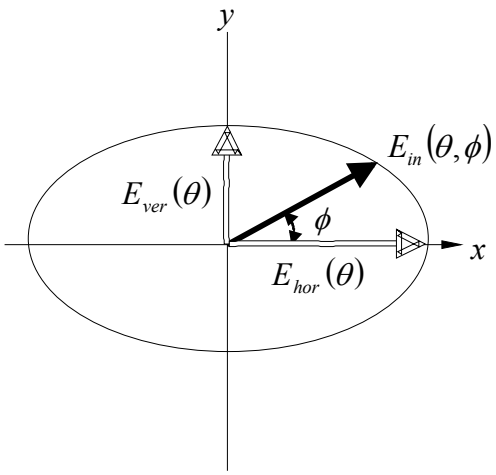

Figure 5.2 *Determination of the amplitude for the input rays from the horizontal and vertical cuts of the primary feed pattern.*

The primary feed used is a corrugated horn with a 4-mm diameter aperture radiating a Gaussian beam at 310 GHz. The same horn is used to illuminate holograms directly when the DRFS is not used. The theoretical radiation pattern of the feed horn is shown in Figure 5.3.

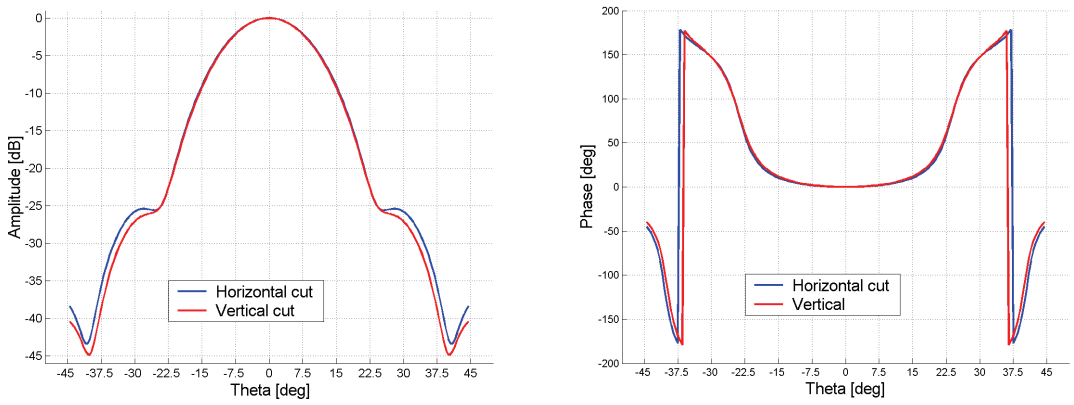

a) *b)*

Figure 5.3 *Feed horn pattern cuts: a) amplitude and b) phase.*

Typically, the measured radiation of the corrugated horns corresponds very well to the theoretical predictions at sub-millimetre wavelengths [101]. The measured radiation pattern of a 600 GHz corrugated horn manufactured by the manufacturer of the horn used, Thomas Keating Ltd, shows also a good agreement to the theory [102]. The radiation of the feed used in the DRFS was measured at 310 GHz by the author of this thesis and by others with reasonable agreement to the theoretical radiation pattern considering the estimated measurement uncertainty, and, therefore, it was concluded that the theoretical radiation pattern can be used to compute the input aperture field in the DRFS design. After the designed

DRFS had been tested, the radiation pattern of the feed horn was verified with planar near-field measurements as more precise measurements were then possible. The measured feed horn patterns are shown in Figures 6.21 and 6.22 and they correspond well to the theoretical pattern.

The number of rays in the input aperture grid, and in the synthesis, was selected to be 423 x 401, i.e., 400 x 400 flux tubes, and 22 extra tubes were selected to extent the output aperture grid outside the actual hologram aperture to ensure that no interpolation oscillations or other computation effects near the rim of the computation space occur inside the hologram aperture. The amplitude for each ray is computed using (5.2) and the phase is specified in the output aperture with the ray path length. The phase pattern of the feed horn was not taken into the account in the reflector synthesis, but it could have been included into the synthesis by including the phase as a path length difference in the desired ray path length, which is specified for each ray.

5.1.2 Definition of the output aperture field

The output field leaving the dual reflector feed system is specified in the output aperture. The output aperture rim is formed by the circle centred at the point where the centre ray intercepts the hologram aperture (see Figure 4.2) with the rim radius $\rho_{out,\max}$ given by

$$\rho_{out,\max} = D/2 = \tan\theta_{main} f_{system}, \tag{5.3}$$

where D is the diameter of the output aperture, θ_{main} is the half-beam width of the main reflector, i.e., the DRFS, and f_{system} is the focal length of the system.

The output aperture amplitude E_{out} is specified in a similar evenly spaced polar grid as in the input aperture. A simple Butterworth-type amplitude function was selected for the hologram illumination , i.e.,

$$E_{out}(\rho') = \frac{\alpha}{\sqrt{1+(\rho'/\rho_c)^{2N}}}, \tag{5.4}$$

where ρ' is the radial distance in the polar coordinates in the output aperture and the following conservative values were selected for a DRFS demonstration: ρ_c=210 mm and N=5. The edge taper was selected to be below -15 dB to reduce edge diffraction and the order of the Butterworth-function was kept low to avoid highly shaped reflector surfaces. The demonstration DRFS is designed to illuminate a 600-mm diameter hologram, but ρ_c scales accordingly for larger holograms if the F/D-ratio of the hologram is the same as the output beam has then the same angular width in the spherical coordinates. The selected hologram illumination in the hologram aperture is illustrated in Figure 5.4.

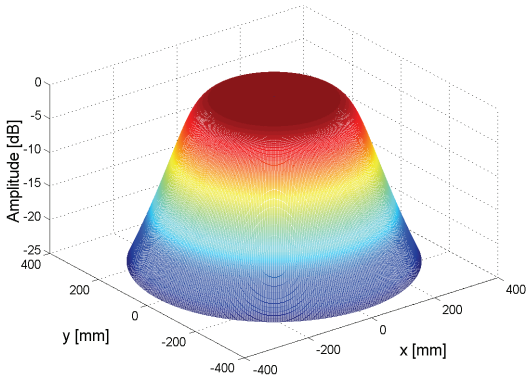

Figure 5.4 *Illumination in the hologram aperture.*

5.2 Geometrical design

The geometry of the dual reflector feed system structure is defined by the locations of the reflectors and the primary feed in relation to each other, by the focal lengths of conic sections corresponding of the DRFS structure, and by the offset angles of the reflectors and the primary feed. The DRFS geometry has an effect on the performance of the DRFS, i.e., the achievable performance is affected by the basic DRFS structure.

5.2.1 Factors to be considered in the selection of the DRFS structure

In this section, the factors affecting the selection of the DRFS geometry are discussed. For example, the following issues have to be considered in the selection of the DRFS structure:

- Direct radiation from the primary feed
- Far-field requirements
- Multiple reflections
- Edge diffraction
- Cross-polarisation
- Mechanical design and manufacturability.

5.2.1.1 Direct radiation from the primary feed

The direct radiation from the primary feed to the hologram aperture would cause disturbances to the hologram illumination and it has to be eliminated by blocking the hologram aperture with the sub-reflector surface from the feed horn. Similarly, the direct illumination of the main reflector by the primary feed has to be avoided by pointing the feed horn away from the main reflector. Also, the spill-over from the reflectors should not intercept the hologram aperture. In order to realise this, the offset angles and focal lengths of the reflectors (and the distance between them and the primary feed) have to be chosen carefully.

5.2.1.2 The far-field requirement

The DRFS synthesis is done using a geometrical optics (GO) based synthesis procedure, in which the electromagnetic fields are approximated with local plane waves. This approximation is valid only in the far-field. Hence, in this sense the distances between the reflectors and the primary feed should be maximised. The minimum far-field distance is given by (3.1). The primary feed of the DRFS is a corrugated horn with a 4-mm aperture at 310 GHz and the far-field distance is then approximately 33 mm.

5.2.1.3 Edge diffraction disturbances

A discontinuity in the reflector surface, such as an edge, causes diffraction. Edge diffraction is discussed in more detail in Section 2.5.5 of this thesis. The disturbances in the DRFS beam caused by the edge diffraction, i.e., ripple, should be minimised and the best way to achieve is to minimise the edge illumination by using a large input and output beam-width in relation to the radiation pattern of the corrugated horn used. Additionally, suitable edge treatment can be used to reduce the edge diffraction. The possible edge treatments used for CATR reflectors are briefly discussed here.

An alternative and complementary approach to lowering the edge illumination on the reflectors is to shape the edge to reduce the diffraction coefficient and to direct the diffracted field away from the direction of the desired radiation. This can be achieved using serrations [103], rolled edges [103–105] or resistive sheets (R-cards) [106] or coatings.

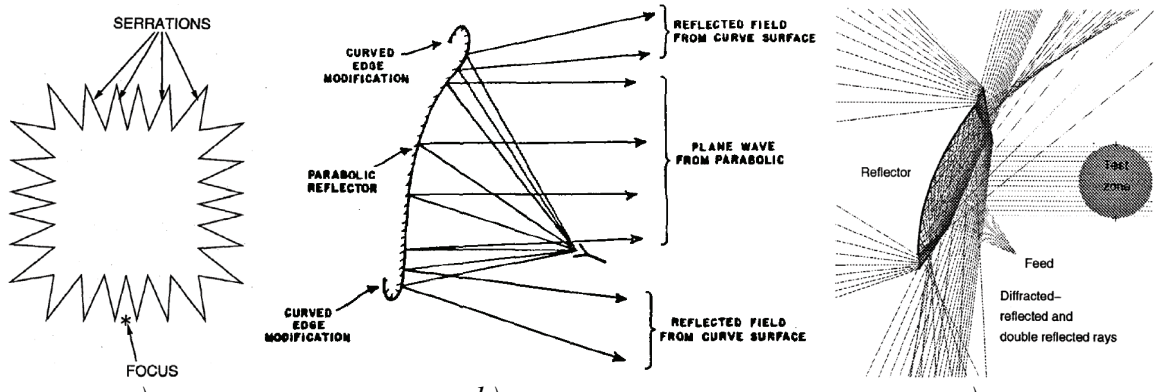

a) *b)* *c)*

Figure 5.5 *Different reflector edge treatments to reduce edge diffraction*
a) serrated edge [103]
b) rolled edge [104]
c) R-card fence [106].

The serrations reduce the overall edge diffraction as the diffraction from a corner (or a tip) is lower than the diffraction from a straight edge and the diffracted fields are directed outside the desired radiation direction [103]. A rolled edge can be used to reduce edge diffraction as the diffraction from a rolled edge is lower than from a straight edge as the discontinuity in the reflector surface is smaller and the rolled edge also directs the reflected field away from the direction of the desired radiation. The diffraction can be minimised further by using a blended

rolled edge [105]. The discontinuity in the junction of the reflector surface and the rolled edge due to the change in the radius of the curvature is minimised by blending the reflector surface gradually with the ellipse forming the rolled edge. This approach gives the lowest edge diffraction in a reflector-based CATR [103].

A different approach is to use resistive sheets or coatings to reduce the edge diffraction disturbances. The discontinuity related to the reflector edges can be reduced by using a resistive coating to gradually decrease the reflectivity of the surface towards the edge. Resistive sheets, or R-cards as they are also called, can be placed in front of the reflector edges [106]. The R-cards with gradually decreasing transmittance introduce an amplitude taper to the reflector aperture, i.e., gradually decrease the edge illumination to reduce edge diffraction. Additionally, the geometry of the R-cards can be selected so that they also reflect the unwanted fields away from the direction of the desired field. At sub-millimetre wavelengths suitable resistive materials with controllable resistivity may not be easy to manufacture and this approach is probably not very feasible.

5.2.1.4 Cross-polarisation level

The total cross-polarisation level in the beam of an reflector antenna is caused by the depolarisation in the antenna and by the cross-polarised field of the primary feed, which is reflected from the reflectors. The asymmetrical structure of an offset reflector causes depolarisation and the offset angle affects the cross-polarisation level in the output beam. In a dual reflector system, such as a Cassegrain-antenna, the cross-polarisation level can be optimised by compensating the depolarisation caused by the main reflector with the depolarisation caused by the sub-reflector by selecting the offset angles properly [6]. The structure is then equivalent to a front-fed reflector antenna.

A compensated structure can be designed for hyperboloidal and ellipsoidal dual reflector antenna also. The condition for the equivalent front-fed reflector is in this generalised case [107]

$$\tan\beta = \frac{-e_{main}\left(1-e_{sub}{}^2\right)\sin\alpha}{e_{main}\left(1+e_{sub}{}^2\right)\cos\alpha - e_{sub}\left(1+e_{main}{}^2\right)}, \tag{5.5}$$

where α is the tilt angle of the sub-reflector axis in relation to the main reflector axis, β is the angle between the sub-reflector axis and the primary feed axis, e_{main} is the eccentricity of the main reflector, and e_{sub} is the eccentricity of the sub-reflector. The DRFS geometry should be selected so that (5.5) is satisfied in order to minimise the cross-polarisation level in the hologram illumination.

The effect of the type of the conic section used as the baseline for the DRFS configuration on the achievable cross-polarisation level has been studied in [108]. In [108], the lowest cross-polarisation levels when a spherical reflector is illuminated with a DRFS are achieved when a dual shaped ellipsoid or a dual shaped hyperboloid configuration is selected. This conclusion indicates that a properly designed dual ellipsoid or a dual hyperboloid structure should be a favourable solution for a low cross-polarisation level in the hologram illumination.

5.2.1.5 Multiple reflections and manufacturability of the DRFS

The reflections inside the dual reflector feed system may cause disturbances to the beam illuminating the holograms. Multiple reflections between the reflectors may cause a standing wave, which causes disturbances to the DRFS beam. The internal reflections can be minimised by covering the structures outside the reflector surfaces with absorbing material and the multiple reflections can be minimised by proper selection of the DRFS geometry. Keeping the offset angles and distances between the reflectors large in relation to the reflector size reduces the potential reflections between the reflectors.

The manufacturing costs for the DRFS increase dramatically if the system size becomes large as the manufacturing tolerances should be better than or of the order of λ/100, i.e., about 10 μm at 310 GHz. The size of the reflectors should be kept to the minimum to reduce the costs and the overall dimensions should be minimised to keep the DRFS structure compact and reasonably light. Unfortunately, these requirements are mostly in contradiction with the other factors that have to be considered in the DRFS design.

5.2.2 Selected dual reflector feed system structure

The factors described in the Section 5.2.1 have to be taken into the account when selecting the dual reflector feed system structure. As the factors often cause contradictive requirements for the DRFS structure, design trade-offs have to be carefully considered.

A dual shaped hyperboloid configuration was selected as it allows a reasonably compact structure for a diverging beam and in principle a low cross-polarisation level in the beam [108]. The distance of the primary feed from the sub-reflector (f_{sub}) was selected to be 100 mm to ensure that all the parts of the sub-reflector are well in the far-field of the corrugated horn and the local plane wave assumption is valid. To reduce edge diffraction disturbances the edge illumination on the sub-reflector, i.e., the taper at the input beam edge was selected to be about -17.5 dB, which resulted in to the input half-beam width (θ_{feed}) of 20°. The focal length of the system (f_{system}), i.e., the hologram focal length, was selected to be 1800 mm with the hologram diameter of 600 mm. The output aperture diameter D is slightly larger than the hologram, D=700 mm, as the beam has to be well controlled also outside the hologram aperture rim. The corresponding output half-beam width (θ_{main}) is 11°.

The DRFS geometry is defined by selecting the appropriate focal length f_{main} for the main reflector, the distance between the reflectors r_{sub}, the distance between the output aperture and the main reflector r_{main} (see Figure 4.2), and by selecting the offset angles for the reflectors (α_{sub} and α_{feed}). The sub-reflector was placed between the primary feed and the output aperture. The selection of the geometry was done by plotting the beam, the reflector edges, and possible spill-over directions for various configurations and by selecting the one of the potential designs, which allowed the smallest reflector size and a compact, simple structure with sufficient space for the transmitter behind the primary feed. This graphical approach was used as the systematic optimisation of the DRFS geometry would have been a very complicated multi-parameter optimisation problem. The manufacturability and the compactness of the structure were favoured instead of minimising the cross-polarisation with

(5.5). The selected parameters are listed in Table 5.1 and the structure is illustrated in Figure 5.6.

Table 5.1. *Selected values for the parameters defining the DRFS geometry.*

Output aperture diameter D	700 mm
System (hologram) focal length f_{system}	1800 mm
Main reflector focal length f_{main}	375 mm
Sub-reflector focal length f_{sub}	100 mm
Main reflector distance from the output aperture r_{main}	1550 mm
Sub-reflector distance from the output aperture r_{sub}	150 mm
Sub-reflector offset angle α_{sub}	90°
Feed offset angle α_{feed}	270°
Half-beam width for the input beam θ_{feed}	20°
Half-beam width for the output beam θ_{main}	11°

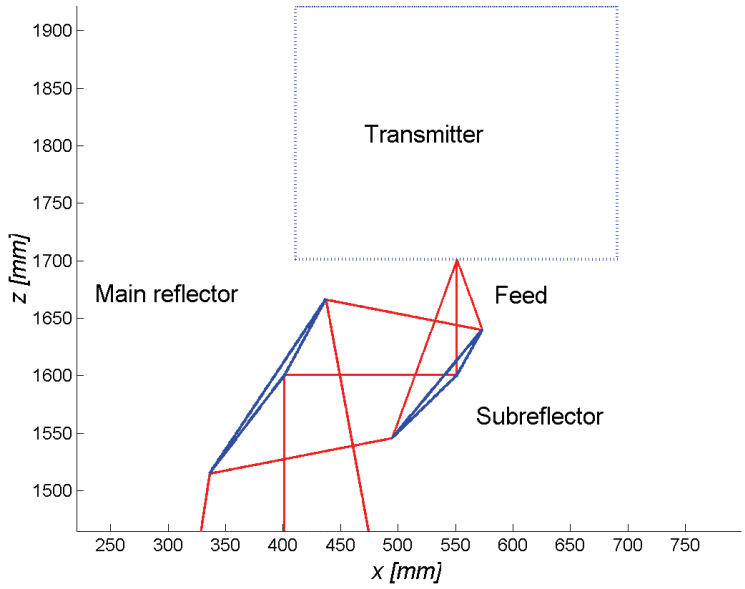

Figure 5.6 *The selected DRFS geometry.*

The selected parameters in the Table 5.1 define a concave hyperboloid-type sub-reflector and a convex hyperboloid-type main reflector.

5.3 Determination of the reflector surfaces

The reflector surfaces are determined from the known primary feed radiation and from the desired hologram illumination using the synthesis procedure described in Chapter 4. The number of flux in the synthesis is selected to be 400 × 400. The number of flux tubes is increased to 422 in the radial direction to allow extra tubes outside the output aperture in order to avoid potential interpolation oscillations and other numerical disturbances to the synthesised reflector surfaces. These extra tubes increase the output aperture diameter to D=736 mm and the corresponding half-beam widths for the input and output beams are θ_{feed}=21° and θ_{main}=11.55°, respectively. The total number of rays used in the synthesis is 423 × 401.

5.3.1 Synthesised reflector surfaces

The reflector surfaces were synthesised with 423 × 401 rays. The resulting reflector surfaces are shown in Figure 5.7.

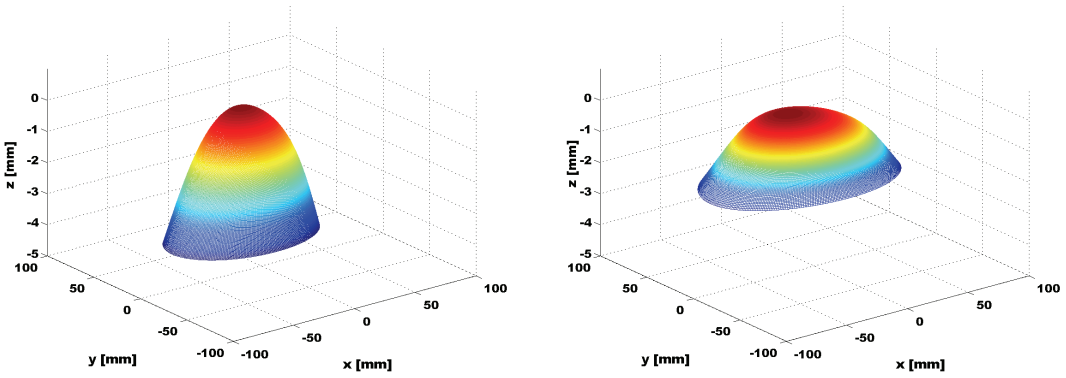

Sub-reflector *Main reflector*

Figure 5.7 *Synthesised sub-reflector surface (inverted for clarity) and main reflector surface [O1].*

The concave sub-reflector size is about 114 mm × 78 mm × 4.3 mm and the convex main reflector size is 147 mm × 103 mm × 2.5 mm.

5.3.2 Reflector edge treatment

The reflector surfaces are milled onto metal plates. The transition from the shaped synthesised reflector surface to the flat metal plate is a discontinuity in the surface, which acts as a diffraction source. The disturbances to the DRFS beam have to be minimised with a suitable treatment of this transition.

The methods to reduce reflector edge diffraction were discussed in Section 5.2.1.3. The serrations are not applicable to the treatment of the transition from the shaped surface to a flat

surface and resistive coatings or sheets are not very practical at sub-mm waves. Therefore, the only possibility is to use a rolled or rounded transition to reduce diffraction. The blended rolled edge has been found to be very efficient in reducing diffraction ripples in the quiet-zone of a reflector-based CATR [103]. A simple rounding is added to the synthesized surface to reduce the discontinuity in the transition to the flat plate surface from the shaped surface.

The reflector rim is numerically specified and the points on the rim are not on a plane so a plane is fitted to the synthesized reflector aperture. This plane is then relocated outside the reflector rim above the reflector plate surface and the reflector surface is then linearly extrapolated to this plane as the distance to this plane is slightly different for each computed point on the rim. The extrapolated part was selected to be at minimum 50 μm high. The transition from the shaped reflector surface to the surface of the metal plate is rounded by fitting an arc of a circle to the transition at each point of the rim. The height of the rounding was selected to be λ/4 at 310 GHz (about 240 μm) and the radius of the rounding is selected so that the surface tangent, i.e., the first derive of the surface, is correct at the end of extrapolated part and on the metal plate surface. For more efficient diffraction reduction, the higher order derivatives of the surface should be also considered. The reflector edge treatment is illustrated in Figure 5.8.

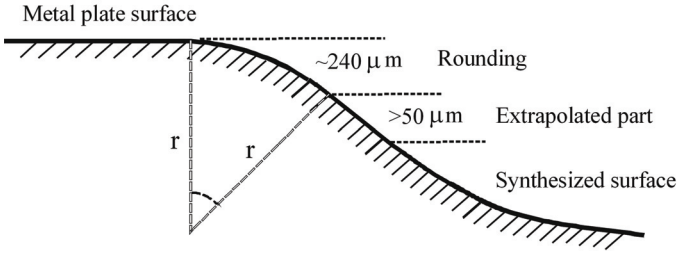

Figure 5.8 *Reflector edge treatment.*

The reflector sizes are increased to 122 mm × 83 mm × 4.6 mm and 165 mm × 119 mm × 2.8 mm for the sub-reflector and the main reflector, respectively.

5.3.3 Final reflectors

The synthesised reflector surfaces with the rounded transition are manufactured by milling the surfaces on metal plates. This structure is modelled in the simulations by adding a flat plate around the rounded edge. The structure is shown in Figures 5.9-5.11.

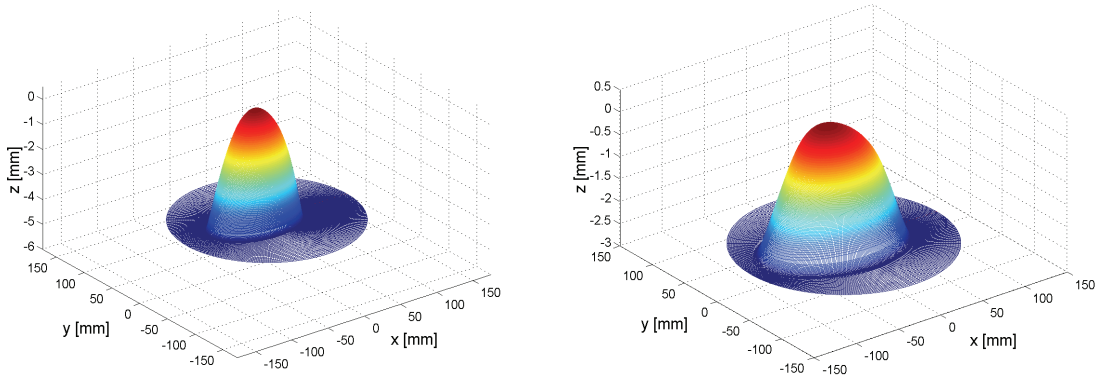

Subreflector surface (inverted) *Main reflector surface*

Figure 5.9 *The reflector surfaces.*

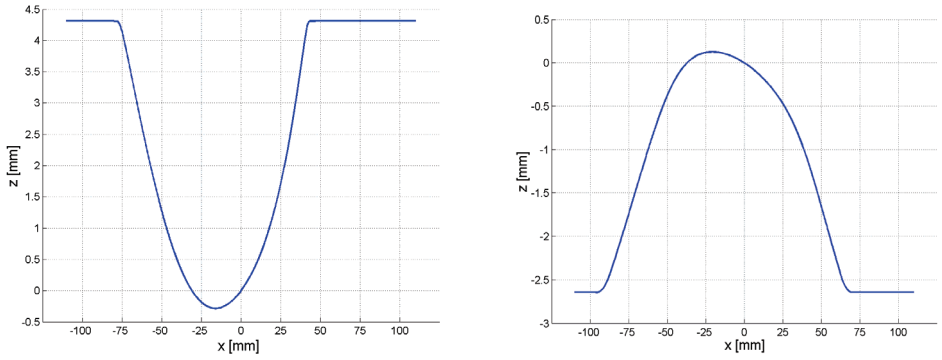

Subreflector *Main reflector*

Figure 5.10 *Horizontal cross-cuts of the reflector plates.*

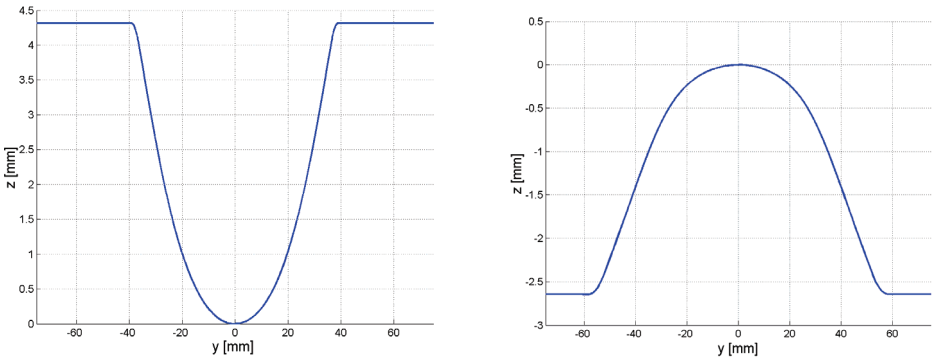

Subreflector *Main reflector*

Figure 5.11 *Vertical cross-cuts of the reflector plates.*

5.4 Verification of the DRFS operation with simulations

The dual reflector feed system design is verified and optimised using GRASP-simulations of the radiated beam. The design described in Section 5.3 is the final DRFS design and the simulation results are presented here for this design. The design could have been optimised further if higher beam quality had been required.

5.4.1 Modelling of the dual reflector feed system in simulations

In the simulations, the reflector surfaces were described with 5028 irregularly spaced points picked from the synthesised reflector points so that a sufficient density of the points was ensured in the shaped region of the reflector surfaces, in the rounded edge and in the flat plate outside the rounded reflector rim. The flat plate represents the metal plate on which the reflector surfaces are milled. These surfaces were cut along elliptical rims specified by the horizontal and vertical half-axes, which were selected to be 62 mm and 42 mm for the sub-reflector, and 85 mm and 60 mm for the main reflector as shown in Figure 5.9.

The primary feed, a 310 GHz corrugated horn, was modelled in GRASP as a tabulated feed, i.e., it was specified numerically with the simulated half-beam amplitude and phase pattern cuts at the vertical polarisation (see Figure 5.3 for the horizontal and vertical cuts). The cross-polarised pattern in the diagonal cut with the assumption of a rotationally symmetric pattern was used in some early simulations of the co-polarised field. This is a somewhat inaccurate estimate of the cross-polarisation level of the actual horn used in the vertical pattern cut and in the horizontal pattern cut. In later cross-polarisation simulations, the cross-polarisation level of the corrugated horn was assumed zero in the horizontal and vertical cuts.

5.4.2 Analysis of the dual reflector feed system

The GRASP simulations were done using physical optics (PO) and physical theory of diffraction (PTD) analysis of the reflector radiation. These reflector antenna analysis methods

are described in Section 2.2 of this thesis. In the PO, the equivalent surface current is computed from the incident field at each computation point and the radiation of the current elements on the reflector surface is then computed. In the PTD, the currents on the reflector rim are computed from the incident field using the diffraction coefficients and the radiation of these PTD current elements can then be determined.

A sufficiently large number of the current elements is needed for the convergence of the analysis, i.e., to ensure that the computed radiation in the angular range under investigation does not depend on the selection of the current elements on the reflector surfaces. In GRASP, the current elements are defined in a polar grid with *po1* and *po2*. A rule-of-thumb to estimate the number of current elements needed for a single shaped reflector is given in [17] as

$$po1 = 3.5\frac{D_x}{\lambda}, \tag{5.6}$$

$$po2 = 3.5\frac{D_y}{\lambda}, \tag{5.7}$$

where D_x and D_y are the reflector dimension in the *x*- and *y*-direction, respectively, and λ is the wavelength. Using (5.6) and (5.7), the number of current elements needed is estimated to be 440 × 300 (*po1* × *po2*) for the sub-reflector, and 600 × 420 for the main reflector. The number of the edge current elements in the PTD is equal to *po2*. These estimates for the required number of the surface current elements were tested by reducing the number of the current elements slightly and comparing the result to the DRFS radiation incident on the hologram aperture computed with these values. No difference was noticed and the number of the current elements for all the simulations was selected to be 440 × 300 on the sub-reflector and 650 × 420 on the main reflector, respectively. The number of the current elements is limited by the computation time, which increases roughly in proportion to the square of the current element number on each reflector. In GRASP8W, there is an automated tool for computing the number of current elements required for a given level of convergence and it was used later after these simulations to verify that there were a sufficient number of current elements in the PO analysis. The required number of the current elements obtained with the convergence test in GRASP8W for convergence at the -120 dB level in the DRFS radiation was 233 × 536 for the sub-reflector and 154 × 268 for the main reflector. This result confirms that the selected number of the current elements is sufficient for the simulation of the DRFS radiation incident on the hologram aperture.

The DRFS analyses is performed as follows in GRASP: first, the incident field on the sub-reflector is computed from the primary feed radiation and then the induced 440 × 300 surface currents are determined using PO and 300 edge current elements are calculated for the PTD analysis. Second, the fields radiated by these surface current elements are computed and the induced currents by these fields are determined at the 650 × 420 points on the main reflector (and at 420 points on the main reflector rim). Finally, the fields radiated by these surface current elements on the main reflector are integrated at the specified output field computation points to get the simulated radiation of the DRFS. Typical computation time for obtaining simulated beam cuts for the DRFS with these surface current elements was up to 50 hours on a PC depending on the number of points, where the field was computed.

5.4.3 Co-polarised DRFS beam

The dual reflector feed system was designed to operate at the linear vertical polarisation as this is the polarisation of the holograms fed directly with a corrugated feed horn. The incident field on a 600 mm diameter hologram aperture located at the distance of 1800 mm from the system focus was simulated with GRASP at the frequency of 310 GHz. The horizontal and vertical cuts of the complex aperture field and the two-dimensional contour maps were computed. The simulated amplitude and phase in the aperture cuts are shown in Figure 5.12 together with the desired rotationally symmetric hologram illumination. The phase is presented as the phase deviation from a spherical wave originating from the hologram focus located 1800 mm from the hologram and the amplitude is normalised to 0 dB at the beam centre. The two-dimensional contour maps of the simulated hologram illumination radiated by the DRFS are presented in Figure 5.13.

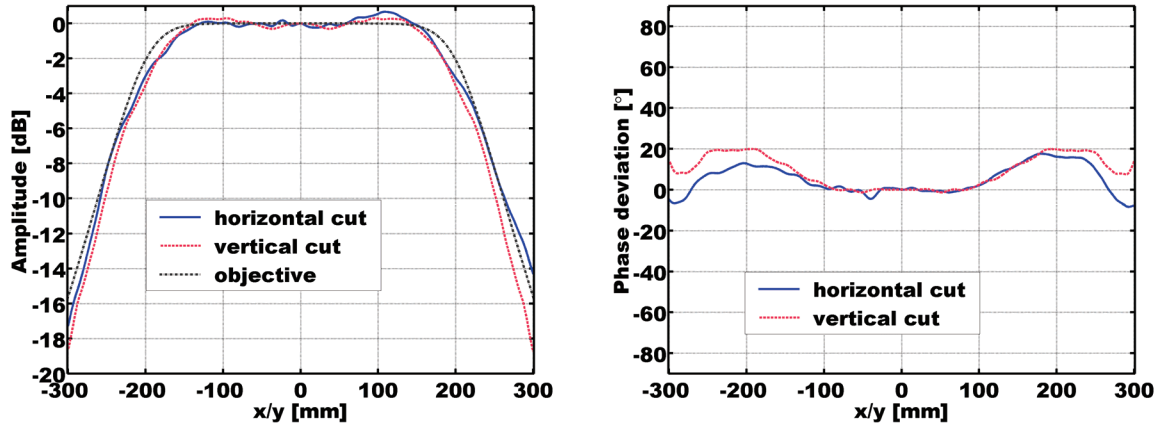

a) *b)*

Figure 5.12 *Simulated cross-cuts of the hologram aperture illumination at 310 GHz [O1]:*
a) amplitude,
b) phase deviation from the spherical wave.

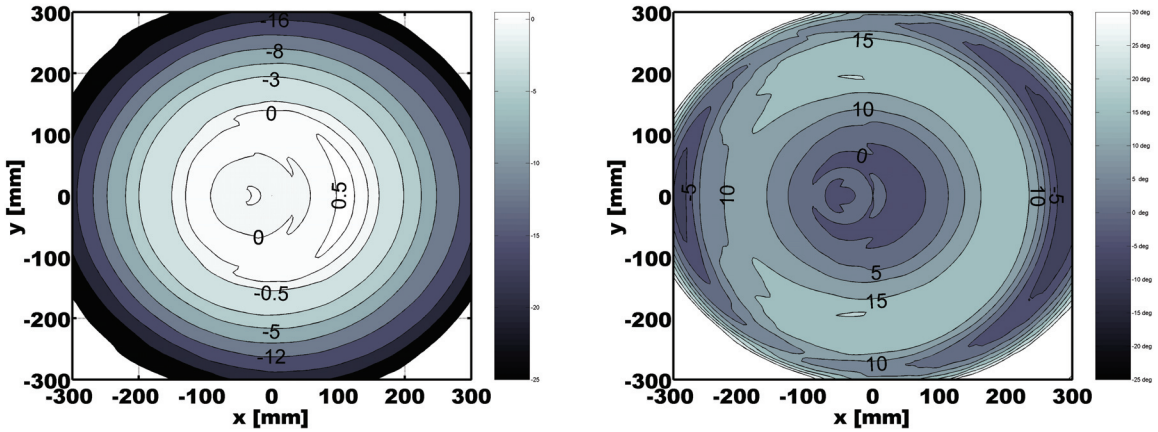

a) *b)*

Figure 5.13 *Simulated contour maps of the hologram aperture illumination by the DRFS at the frequency of 310 GHz [O1]:*
a) amplitude
b) phase deviation from the spherical wave

The simulated DRFS beam corresponds well to the desired hologram illumination at 310 GHz, but the simulated beam is slightly narrower than the objective beam. The deviations are the largest in the shoulder of the beam, where the beam and the reflectors are most shaped. The central region of the beam illuminating the hologram is most significant for the quiet-zone field quality and the deviations from the desired hologram illumination there are typically 0.6 dB peak-to-peak in the amplitude and less than 20° in phase. The phase curvature can be mostly compensated in the central region by moving the DRFS closer to the hologram aperture. The hologram edge illumination varies between -17 dB and -18.7 dB, which together with the non-symmetrical reflector shapes causes non-symmetrical diffraction ripples. The maximum and typical simulated ripples and deviations are summarised in Table 5.2.

Table 5.2 *DRFS beam width and beam deviation in different simulated beam crosscuts.*

	–3 dB beam width	Maximum amplitude ripple peak-to-peak	Typical amplitude ripple peak-to-peak	Maximum phase deviation
Desired illumination	6.7°	-	-	-
Horizontal cut	6.0°	0.9 dB	0.4 dB	18°
Diagonal cut	6.0°	0.9 dB	0.6 dB	19°
Vertical cut	6.1°	0.6 dB	0.6 dB	20°

As the DRFS design is based on the geometrical optics, the beam shape in the angular domain is in principle independent of the radial distance, i.e., the beam shape does not change as the function of the distance. This was investigated by simulating the radiation of DRFS at different distances ranging from 0.9 to 10.8 metres (0.5 to 6 times the designed nominal focal length of the system). The results are shown in Figures 5.14 and 5.15.

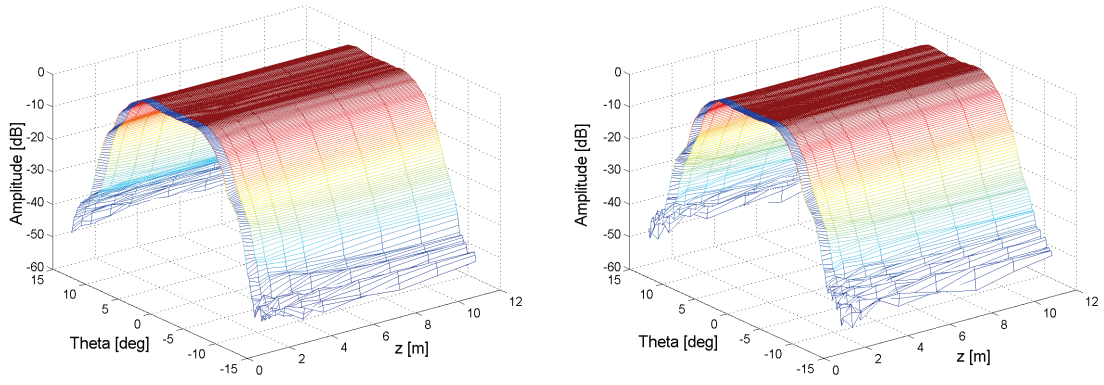

a) *b)*

Figure 5.14 *Simulated normalised DRFS beam amplitude at 310 GHz:*
a) horizontal cut,
b) vertical cut.

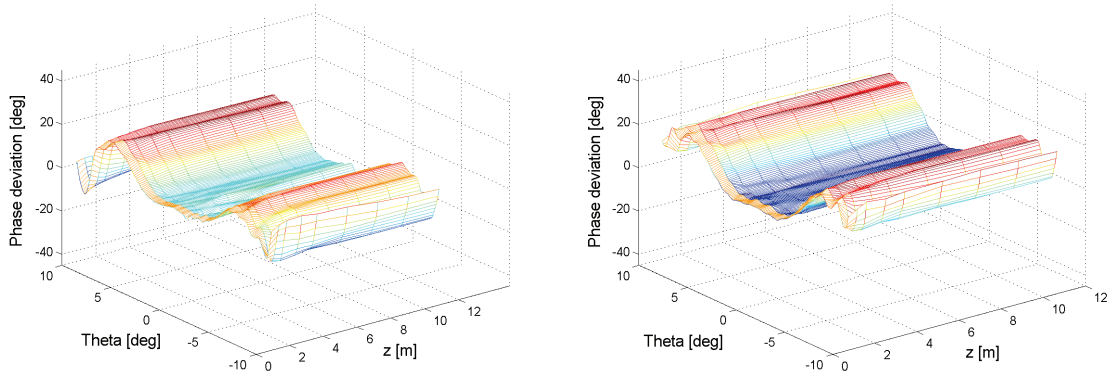

a) *b)*

Figure 5.15 *Simulated normalised DRFS beam phase deviation at 310 GHz:*
a) horizontal cut,
b) vertical cut.

The same DRFS can be used to illuminate a hologram of any size provided that the ratio of the hologram aperture D and the focal length f_{system} remains the same, i.e., $f_{system} / D = 3$ and the distance between the DRFS and the hologram is sufficiently large so that the hologram can be considered to be in the far-field of the DRFS. The far-field assumption and the variation of the DRFS beam as the function of the distance is discussed further in Section 5.4.5.4.

5.4.4 Cross-polarised dual reflector feed system beam

The cross-polarised field is at the linear horizontal polarisation and this field component in the hologram illumination propagates also to the quiet-zone of the hologram in a CATR. Therefore, it should be minimised in order to minimise the final cross-polarisation level in the quiet-zone. The driving factor in the DRFS design was the manufacturability of the system and the cross-polarisation performance was not completely optimised. The cross-polarisation level in the hologram illumination radiated by the DRFS was simulated at 310 GHz using GRASP; the simulation results are shown in Figure 5.16. The simulated cross-polarisation level in the DRFS in the diagonal cut of the primary feed pattern (the input beam of the DRFS) and the cross-polarisation level in the diagonal DRFS beam cut on the hologram aperture are shown in Figure 5.17.

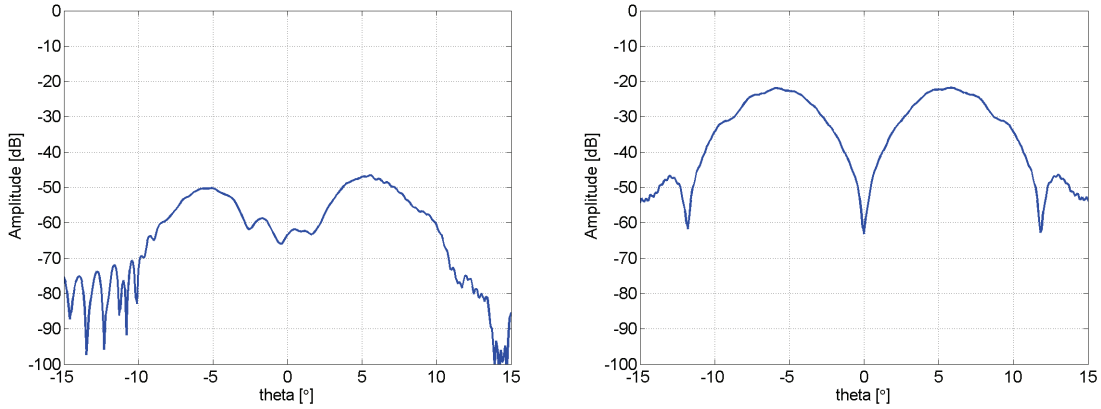

Figure 5.16 *Simulated cross-polarisation level in the DRFS beam cut at 310 GHz:*
a) horizontal cut,
b) vertical.

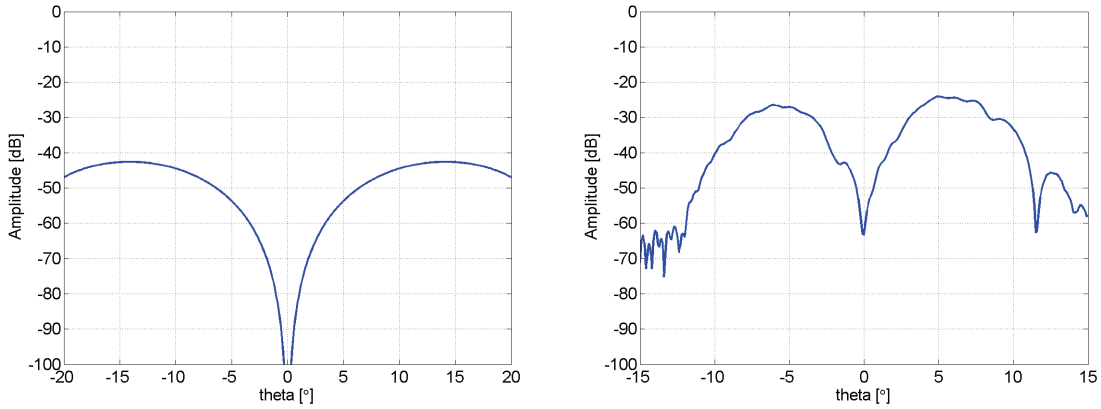

a) *b)*

Figure 5.17 *Simulated cross-polarisation level in the diagonal beam cut at 310 GHz:*
a) feed horn,
b) dual reflector feed system.

As can be seen in Figure 5.17, the cross-polarisation level is higher in the output of the DRFS (about -24 dB at maximum) than in the input of the DRFS (about -43 dB). The DRFS causes depolarisation of the field and the cross-polarisation performance should be optimised with a proper selection of the DRFS reflector offset angles if a lower cross-polarisation level is desired.

5.4.5 Effect of the non-idealities on the simulated DRFS beam

The numerical approximations and their effect on the accuracy of the reflector surface synthesis are discussed in Section 4.2. In this section, the effect of the physical phenomena which are not included in the DRFS design, are discussed. The most important phenomena are the diffraction and the depolarisation of the field. In the synthesis procedure, the sub-reflector is assumed to modify only the amplitude of the field and the main-reflector is assumed to correct the phase without modifying further the amplitude, i.e., the amplitude and phase are assumed decoupled. This assumption is not exactly correct and it causes an error in the DRFS

synthesis. The output aperture, i.e., the hologram aperture, is also assumed to be in the far-field of the DRFS in the synthesis, but it is actually in the radiating near-field. This may result into inaccuracy in the DRFS design.

5.4.5.1 Edge diffraction

The discontinuities in a reflector surface, such as a change in the radius of the curvature and an edge, cause diffraction. These effects are discussed in Sections 2.2.5 and 5.3.2. As the DRFS reflectors are shaped and they are finite in size, diffraction plays a major role in the DRFS operation. The diffraction effects are not included in the ray-tracing based synthesis of the reflectors and GRASP simulations were used to verify the performance by simulating the edge diffraction using PTD as described in Sections 2.2.5.2 and 5.4.2.

The transition of the synthesised shaped reflector surface to the flat metal plate was rounded as described in Section 5.3.2. The rounding was added to the reflector surfaces after relatively large diffraction ripples were noticed in the first simulations of the designed DRFS structure. The effectiveness of this simple rounding in reducing the ripples is illustrated in Figures 5.18 and 5.19, where the rounded transition is compared to the untreated edges of the synthesised reflector surfaces. The curves have been shifted for clarity.

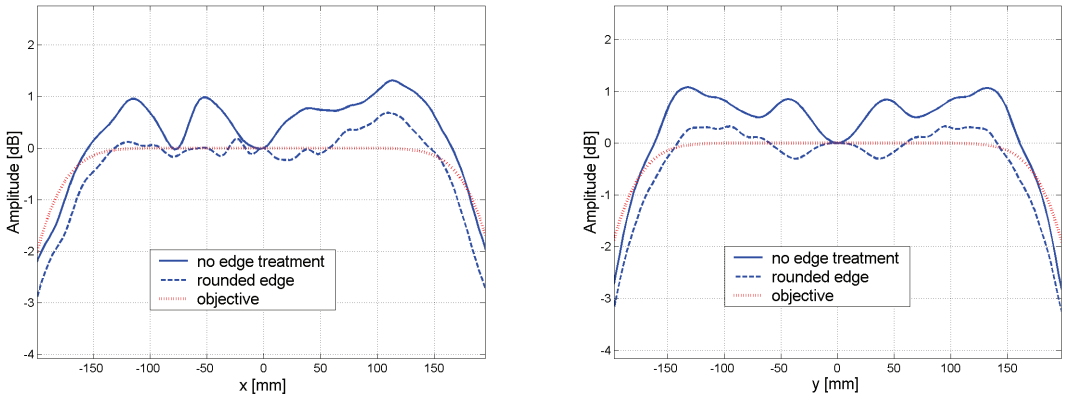

a) *b)*

Figure 5.18 *Effect of shaped reflector edge rounding on the simulated amplitude ripple:*
a) horizontal cut of the hologram aperture,
b) vertical cut of the hologram aperture.

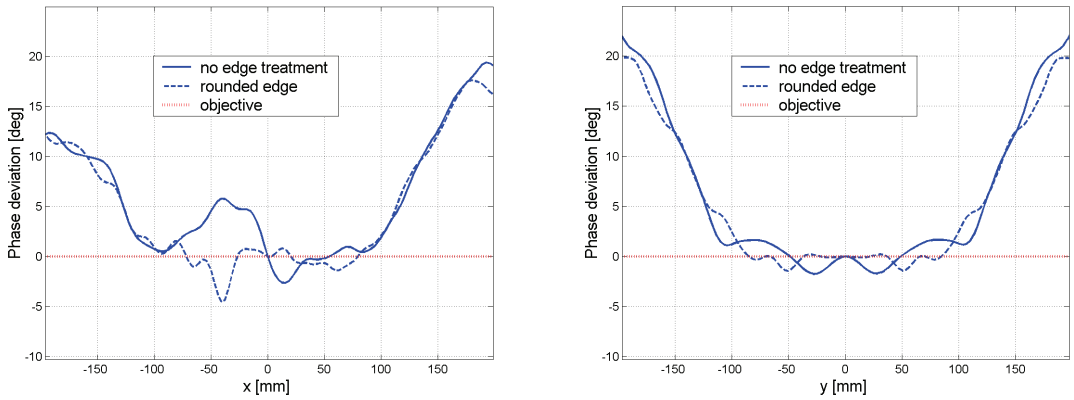

a) *b)*

Figure 5.19 *Effect of shaped reflector edge rounding on the simulated phase ripple:*
a) horizontal cut of the hologram aperture,
b) vertical cut of the hologram aperture.

With the rounded transition, the amplitude ripple in the centre of hologram illumination is reduced from approximately 1.0 dB peak-to-peak to about 0.4 dB peak-to-peak. The phase ripple is reduced from about 9° to about 5° peak-to-peak. If a further reduction in the diffraction ripples is needed, a more advanced transition with more gradual change in the shape of reflectors could be designed by minimising the second and higher order derivatives of the surfaces in the transition from the shaped surfaces to the planar surfaces.

The diffraction effects could be investigated further by using only geometrical optics to analyse the DRFS radiation so that only the reflected field is computed and by comparing this field to the field including the diffraction using PTD. Unfortunately, the multi-object GTD analysis needed for this is an add-on to the GRASP and it was not available for this work. The development of in-house GO analysis software was considered to be outside the scope of this work.

5.4.5.2 Depolarisation of the field

The DRFS synthesis is carried using only the co-polarised field (vertical polarisation) and as the field is depolarised by the DRFS as discussed in Section 5.4.4, a design error may result from ignoring the potential depolarisation power loss. The effect of the field depolarisation on the DRFS beam was investigated by comparing the simulated co-polarised field component incident on the hologram aperture to the total field amplitude of all the field components. The total field is formed by the *x*-, *y*- and *z*-direction field vectors, i.e., by the cross-polarised and co-polarised field components and by the field component in the direction of the propagation as the hologram aperture is in the radiating near-field of the DRFS. The deviation of the co-polarised field amplitude from the total field amplitude is shown in Figure 5.20.

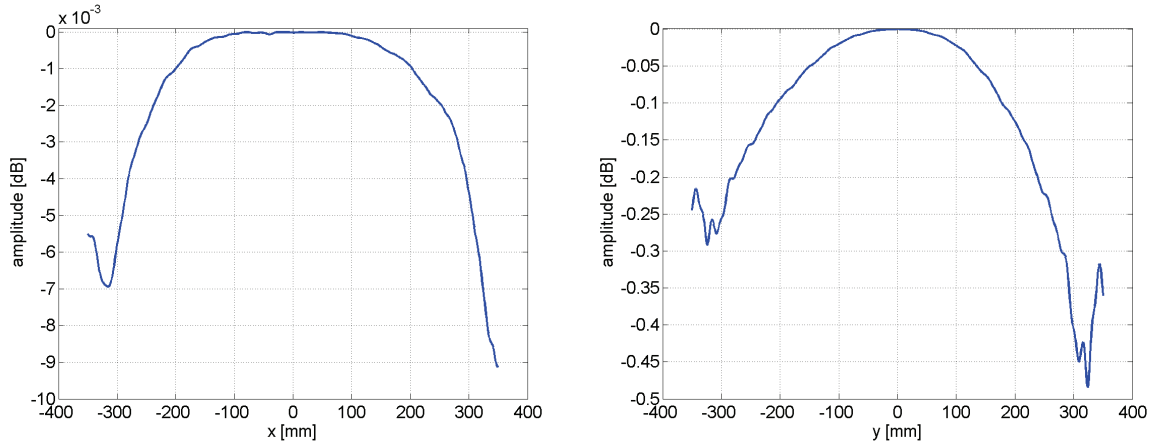

a) *b)*

Figure 5.20 *Deviation of the co-polarised field amplitude from the total field amplitude:*
a) in the horizontal cut of the hologram aperture,
b) in the vertical cut of the hologram aperture.

The co-polarised field component is at maximum about 0.4 dB lower than the total field amplitude at the rim of the hologram aperture at y=300 mm. In the horizontal cut, no significant difference is observed as the maximum deviation is less than 0.01 dB. The reliability of the simulated cross-polarised field is somewhat affected by the limited data on the cross-polarisation performance of the primary feed horn, but as the depolarisation by the DRFS is in any case much larger than the feed horn cross-polarisation, it can be concluded that the depolarisation of the field in the DRFS narrows slightly the DRFS beam. The simulated beam is narrower than the objective hologram illumination as can be seen in Figure 5.12. However, the depolarisation of the field is not significant enough a factor to explain alone the narrower simulated DRFS beam than the objective at the hologram edge, but it is a partial cause for the beam narrowing. For more accurate DRFS design, the depolarisation could be also considered in the DRFS synthesis.

5.4.5.3 Assumption of decoupled field amplitude and phase

In the DRFS synthesis, the sub-reflector is assumed to modify only the amplitude of the beam and the main reflector is assumed to correct the phase without altering the amplitude. In reality, the field amplitude and phase cannot be decoupled as they cannot be determined independently of each other. A change in the field amplitude will also cause a change to the phase of the field. This can be understood by considering a ray bundle in ray-optics. The spacing of the rays determines the flux tubes and the amplitude of the field (or the power density) and the ray path length defines the phase. In general, it is not possible to change the ray spacing (defined by the ray directions and the propagated distance) without affecting the relative length of the rays.

In the DRFS synthesis procedure, the phase is corrected by adjusting the ray path length by moving the reflection point on the main reflector along the output ray. This correction does not allow the amplitude to change as the output ray spacing remains the same. Unfortunately, the fixed output amplitude prevents further correction of the phase beyond what is shown in Figure 5.12. In order to reduce the phase deviation from the ideal spherical wave more, the amplitude should be also modified. For example in [33], a floating aperture mapping is used

to change the ray distribution in a controlled fashion. A more precise synthesis procedure would require simultaneous modification of the amplitude and phase for the best performance.

5.4.5.4 Far-field assumption

In the far-field of an antenna, the radiation pattern is not dependent on the distance, and in the near-field, the radiated beam depends on the distance. The dependence on the radial distance is stronger near the antenna and it weakens when the observation point is moved further away from the antenna. In the geometrical optics based synthesis procedure, it is assumed that the output aperture (the hologram aperture) is in the far-field of the DRFS and the radiated field is solely the GO reflected field from the reflectors. The far-field distance for the main reflector of the DRFS computed with (3.2) is about 50 metres. The validity of the far-field assumption at the shorter distances can be tested by comparing the simulated DRFS beam at different distances as shown in Figures 5.14 and 5.15. The cross-cuts of the beam at a few different distances are shown in Figures 5.21–5.23.

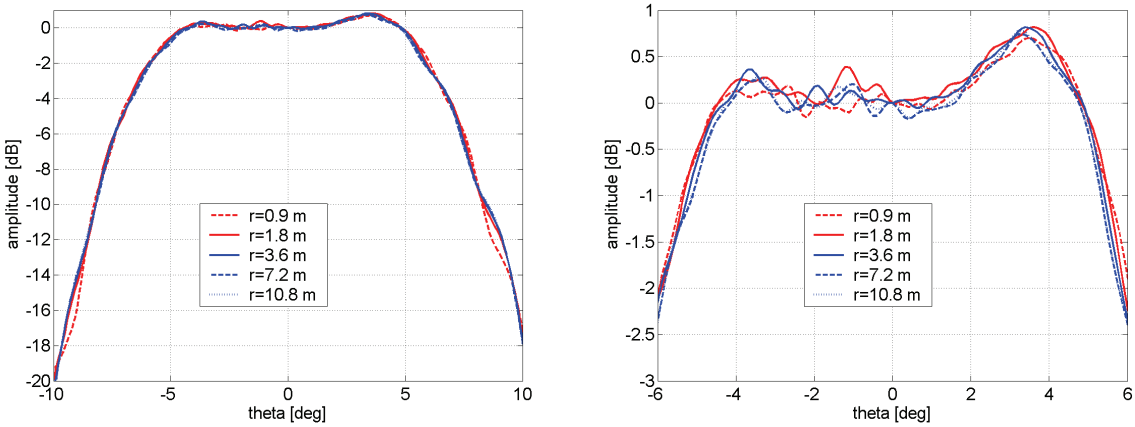

Figure 5.21 *Simulated variation of the co-polarised field amplitude in the horizontal beam cut as the function of the distance at 310 GHz.*

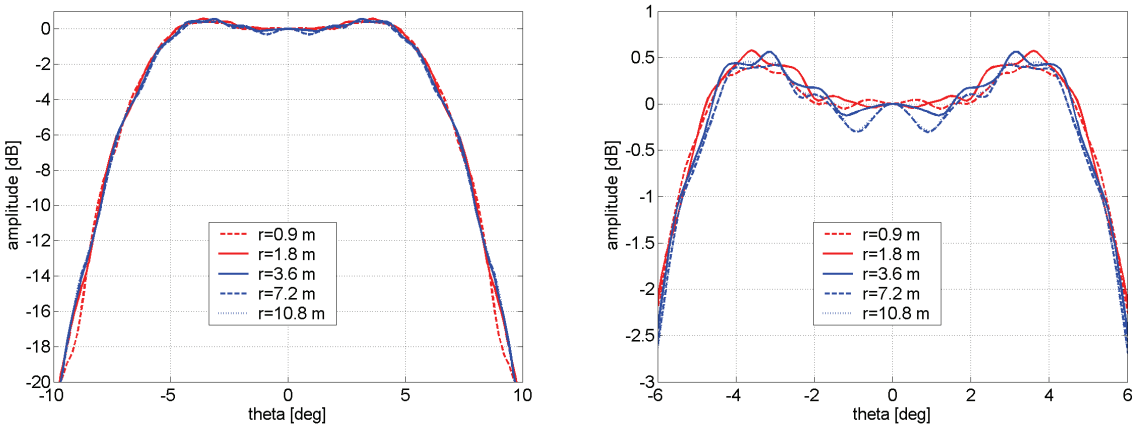

Figure 5.22 *Simulated variation of the co-polarised field amplitude in the vertical beam cut as the function of the distance at 310 GHz.*

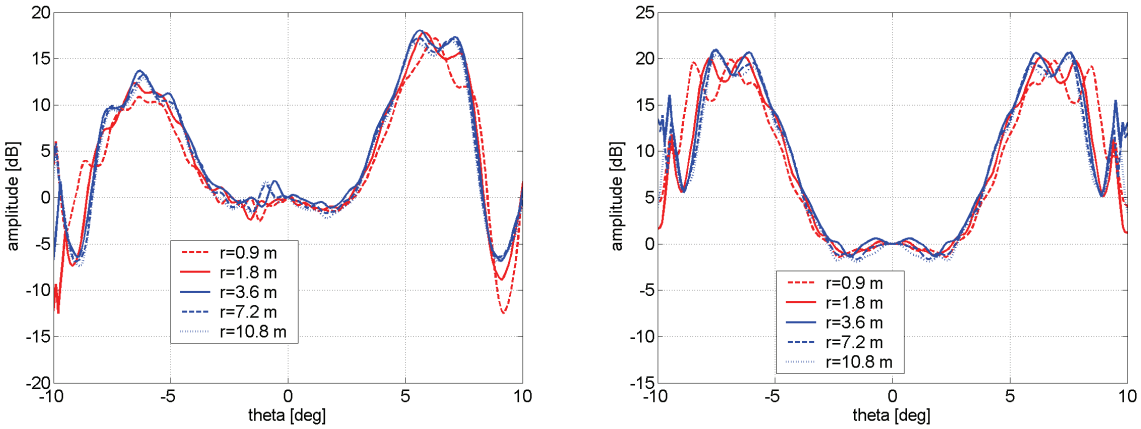

Figure 5.23 *Simulated variation of the phase deviation from the ideal spherical wave as the function of the distance at 310 GHz:*
a) horizontal beam cut,
b) vertical beam cut.

As can be seen in Figures 5.21–5.23, the general shape of the DRFS beam determined by the reflected field and the level of ripples do not vary significantly with the distance, but the location of the diffraction ripple maxima and minima are sensitive to the distance r as the phase difference between the diffracted field component and the reflected field varies as the function of the distance at each observation angle. The hologram illumination amplitude near the hologram edge at $\theta \approx 9.5°$ varies at maximum about 2 dB peak-to-peak with the distance from 0.9 m to 10.8 m and the phase deviation from the ideal spherical wave varies at maximum about 15° peak-to-peak. The largest deviations can be observed for the shortest distance (r=0.9 m) from the DRFS focus as one would expect as the near-field effects are then the strongest. Typical variation in the amplitude is about 0.3 dB peak-to-peak in the central region of the hologram at a selected observation point and less than 3° in the phase, peak-to-peak. The overall level of the ripples is approximately independent of the distance.

The variation in the DRFS beam amplitude and phase ripples indicates that the near-field effects cannot be ignored completely in the design of the dual reflector feed system The variation of the field as the function of the distance decreases as the distance increases towards the far-field region. In the DRFS design, the DRFS operation has to be verified at the planned distance of the hologram to be illuminated by the DRFS and a sufficiently large distance has to be selected. For the designed DRFS, the selected distance of 1.8 m is sufficient for assuming the hologram to be approximately in the far-field of the DRFS in the synthesis of the reflectors. The level of the diffraction ripples should also be minimised in order to minimise the potential variation in the DRFS beam as the function of the distance.

5.5 Conclusions on the DRFS design

The simulated dual reflector feed system performance and factors affecting it are summarised here and the possibilities to improve the DRFS design procedure for improved performance are discussed.

5.5.1 Simulated dual reflector feed system performance

The simulated DRFS performance was found to be satisfactory and the DRFS beam can be used to illuminate a 600-mm demonstration hologram at 310 GHz. However, the simulated DRFS beam is slightly narrower than the objective beam. The deviations in the beam shape are the largest around the shoulders of the beam, where the beam and the reflectors are most shaped. The central region of the beam illuminating the hologram has the greatest effect on the quiet-zone field quality. In this region, the deviations from the desired hologram illumination are typically only 0.6 dB peak-to-peak in the amplitude and less than 20° in phase. The maximum amplitude deviation is 0.9 dB, as can be seen in Figure 5.12. The phase deviation shows a phase curvature that can be mostly compensated in the central region by moving the DRFS closer to the hologram aperture. In the quiet-zone of a CATR, it is typically required that the field does not deviate from the plane wave more than 1 dB peak-to-peak in amplitude and 10° in phase. The simulated amplitude and phase deviations in the hologram illumination by the DRFS are lower than these values, but for accurate measurements of the very low side-lobes of a high-gain antennas even better quiet-zone field quality is needed.

5.5.2 Summary on the accuracy of the DRFS design procedure

The synthesis of the reflectors in the dual reflector feed system is based on a ray-tracing and it is therefore based on the approximations of the geometrical optics with further approximation of the wavefronts and surfaces with local tangential planes. The synthesis procedure does not include the account diffraction effects and the depolarisation of the field by the DRFS and the output aperture is assumed to be located in the far-field of the DRFS. The physical phenomenon affecting the DRFS beam quality the most is diffraction. Depolarisation of the field is also an issue, but it affects the DRFS beam less than the diffraction ripples in the most important central region of the hologram aperture. The diffraction ripple maxima and minima locations vary with the distance from the DRFS as the output aperture is in the radiating near-field, but the level of ripples is approximately constant. Therefore, the assumption of the DRFS operation in the far-field can be used in the design but the performance of the designed system has to be verified by simulating the radiation at the distance from the DRFS to be used in the actual application of the system.

The achievable accuracy of the DRFS design is also dependent on the accuracy of the reflector synthesis procedure. The numerical approach and the first-order approximation of the reflector surfaces with local tangent planes result into error in the reflector shapes in the DRFS. This numerical inaccuracy causes surface errors up to 5 μm at the reflector edges as the error is cumulative. The error may cause phase errors up to a few degrees at 310 GHz and it may be significant at the highly shaped portions of the reflectors as the tangential planes are determined at an anterior point, which makes the surface shape to lag behind the correct one. The main factor affecting the accuracy of the synthesis is to the author's understanding the

decoupling of the amplitude and phase in the synthesis, i.e., the assumption that the amplitude and phase can be modified independently without considering them both at the same time. It was discovered during the optimisation of the DRFS that the phase deviation from an ideal spherical wave, which was up to 20°, could not be reduced without modifying the amplitude objective. Fortunately, the phase deviation can be mostly compensated by moving the DRFS closer to the hologram and this approach was then adopted instead of modifying the synthesis software.

5.5.3 Potential improvements to the design procedure

The performance of the DRFS, or any other system, can be improved most efficiently by identifying the most significant factors affecting the performance and focusing on improving them. These factors were identified in the previous sections. The basis of the DRFS performance is the synthesis of the reflector surfaces and the overall design of the system. The potential improvements to the synthesis accuracy can be achieved either using a more advanced synthesis method or by improving the accuracy of the current method. The different shaped reflector antenna synthesis methods were discussed in Section 2.3. Using a diffraction synthesis method based on physical optics and physical theory of diffraction analysis of the reflector radiation, the diffraction effects and other effects can be included into the synthesis. The reflector surfaces are optimised iteratively until the simulated DRFS performs meets the selected criteria. This approach would give a superior performance compared to geometrical based synthesis methods, but the computation time would be very high for more accurate synthesis as the GRASP simulations of the current DRFS took up to 50 hours to complete. Naturally, an optimised synthesis and analysis program would provide faster analysis but the PO and PTD analysis has to be performed for each iteration of the reflector surfaces. Alternatively, the current GO synthesis procedure could be improved as it has the advantage of fast computation time - only minutes for the entire DRFS synthesis.

The accuracy of current ray-tracing based procedure for the reflector surface synthesis can be mostly improved by modifying both amplitude and phase in the output for the best performance. This can be achieved by modifying the input-output aperture mapping, i.e., by changing the output ray distribution in a controlled fashion to allow more precise spherical wave phase. Similar approach has been used in [33] with the so-called floating mapping. The second-order surface models, such as in [33], could be used to reduce the number of rays needed in the synthesis and to increase the numerical accuracy of the procedure, but the numerical accuracy is currently reasonably good.

Currently the input-output aperture mapping is limited to the rotationally symmetric cases. As a rotationally symmetric mapping is not in general possible with offset reflectors [29], and in order to compensate local distortions and non-symmetries in the output aperture field, a general input-output aperture mapping algorithm could be developed so that any specified output aperture field distribution could be realised approximately. In addition, the phase error in the radiation pattern of the primary feed could be compensated by specifying the ray path length objective accordingly for each ray in the synthesis.

In addition to the synthesis procedure, the design of the DRFS affects the performance. The depolarisation in the DRFS and the resulting power loss at the co-polarisation affecting the beam shape can be minimised by selecting the offset angles for the reflectors so that the cross-polarisation is minimised. The diffraction ripples in the beam can be minimised by using a

lower edge illumination on the reflectors (currently about -17 dB on the sub-reflector and on the main reflector) and by improving the rounding of the shaped reflector edge for more gradual transition from the shaped reflector surface to the flat metal plate surface.

Most of the potential improvements to the ray-tracing based synthesis procedure and to the DRFS design are being carried under the author's instructions in a Master's thesis, where an improved DRFS for operation at 650 GHz is being developed. The results show a significant improvement in the beam quality, i.e., lower ripple and less deviations from the objective hologram illumination.

5.6 Construction of the DRFS structure

The assembly and manufacturing tolerances for the dual reflector feed system were studied in order to select a suitable construction of the DRFS and a manufacturer, who can meet the required manufacturing tolerances. The reflector surface accuracy has to be sufficiently high for proper DRFS performance and the reflector locations and orientations have to be precisely correct. The required reflector surface accuracy and precision in the reflector placement is estimated next and the constructed dual reflector feed system is presented.

5.6.1 Required reflector surface accuracy

The required reflector surface accuracy could be estimated with a Monte Carlo analysis of the effects of random surface errors on the DRFS beam. Unfortunately, this kind of an analysis would be very time consuming as a large number of different surfaces have to be simulated in order to get a statistical sample of the possible surface errors. Therefore, a simpler approach was selected to get an estimate on the order of the surface accuracy needed.

The effect of a surface error on the DRFS beam phase can be estimated by considering reflection of a plane wave from a locally planar surface as shown in Figure 5.24. Let's consider a simple case, where a surface error is assumed only to cause the *z*-coordinate of the local surface plane to change by Δz.

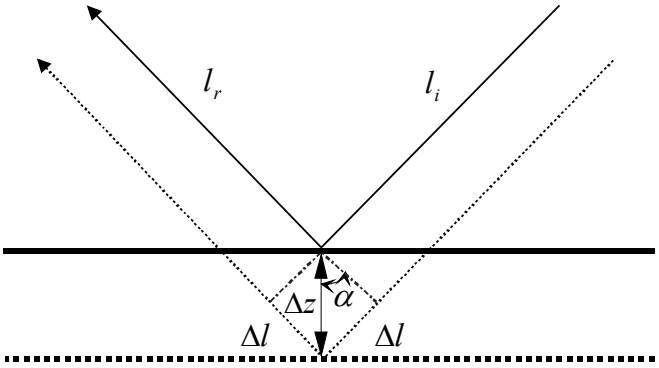

Figure 5.24 *Effect of a surface error to the ray path length.*

The ray path length l_i from the source to the surface and the ray path length l_r from the reflection point to the observation point are increased by Δl:

$$\Delta l_{i,r} = \Delta z \sin \alpha , \tag{5.8}$$

where α is the angle between the ray direction and the surface plane. The distances are assumed very large compared to Δz so that the ray direction remains constant. The total ray path length deviation caused by a z-coordinate shift due to a milling inaccuracy is $2\Delta l_{i,r}$. The corresponding approximate phase deviation caused by the surface error is

$$\Delta \Psi_{surface} = \frac{2\Delta l_{i,r}}{\lambda} \bullet 360° . \tag{5.9}$$

Assuming the milling errors to be random and uncorrelated on both reflector surfaces the total phase deviation caused by the milling inaccuracy in the DRFS can be estimated as a root of sum of squares of the individual reflector surface accuracies. The angle α in the DRFS is approximately 45° and there are two reflectors. If the allowed maximum phase deviation in the quiet-zone of a CATR is ±5° and assuming the contribution of the DRFS and the hologram to be uncorrelated, the maximum allowed contribution of the DRFS is then about ±3.5°. The contribution of the DRFS can be further divided into the contribution of the reflector surface errors and into the contribution of the reflector misalignment and dislocation. For uncorrelated contributions, each of these may cause at maximum phase errors up to ±2.5°. The corresponding maximum allowed surface error Δz is ±4.8 μm at 310 GHz and the reflector surface milling tolerances should then smaller than 5 μm. Some of the potential systematic reflector surface errors may be compensated at least partially by adjusting the position of the DRFS in relation to the hologram, which may relax this requirement slightly.

5.6.2 Assembly tolerances for the DRFS

The reflector locations and alignment in the DRFS have to correct in order not to cause significant deviations to the hologram illumination. The effect of reflector and feed misalignment and dislocation was studied with GRASP8 simulations in order to determine the required assembly tolerances for the DRFS. In the simulations, one object at the time, a reflector or the feed horn, was rotated or moved at the time from its designed orientation. The other objects were kept at stationary in the designed configuration.

The tolerances for misalignment and dislocation were first estimated coarsely. After the order of magnitude for the tolerances was found the effect of dislocation and misalignment of each object was estimated more accurately. The tolerances for the xyz-translation and $\theta\psi$-rotation, i.e., rotation around the vertical y-axis and around the wave propagation direction (z-axis), for the feed horn, for the sub-reflector and for the main reflector were studied with about 120 simulation runs. Both horizontal and vertical field cuts of the DRFS beam incident on the hologram aperture were computed in 101 points on a cut with 300 × 300 surface current elements on the reflectors. The number of the current elements was reduced in order to decrease the computation time. Some of the results for the simulated phase and amplitude at the vertical linear polarisation at 310 GHz for sub-reflector dislocation and misalignment are shown in Figures 5.25–5.29 as examples. The effect of rotation around the horizontal axis,

i.e., the *x*-axis, was not investigated in order to reduce the number of time consuming simulations. The effect of this rotation is probably similar to the rotation around the vertical axis.

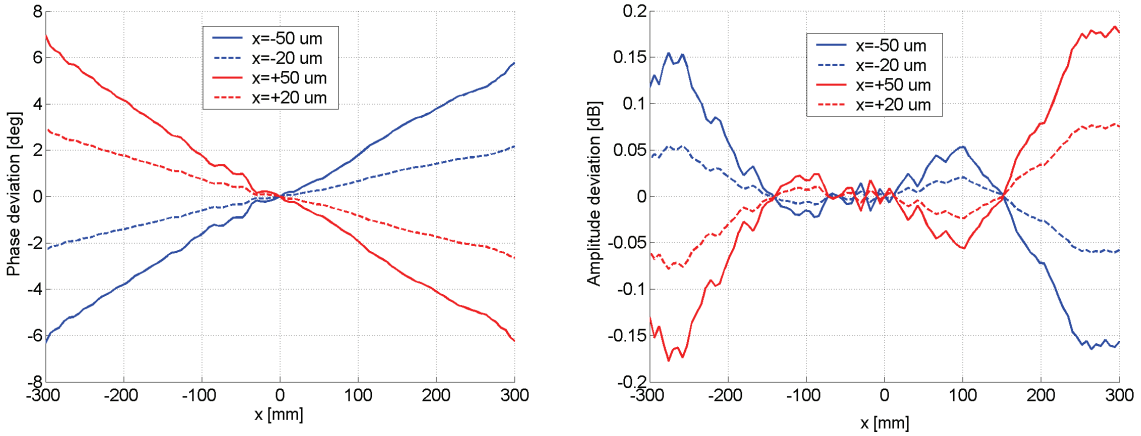

a) *b)*

Figure 5.25 *Effect of sub-reflector dislocation in the x-direction on the hologram illumination in the horizontal crosscut of the hologram aperture at 310 GHz:*
a) phase deviation,
b) amplitude deviation.

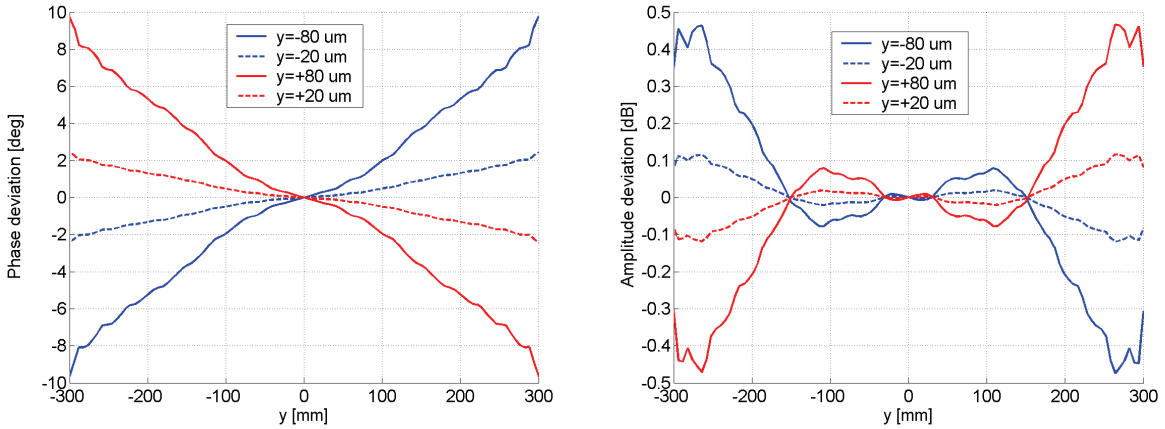

a) *b)*

Figure 5.26 *Effect of sub-reflector dislocation in y-direction on the hologram illumination in the vertical crosscut:*
a) phase deviation,
b) amplitude deviation.

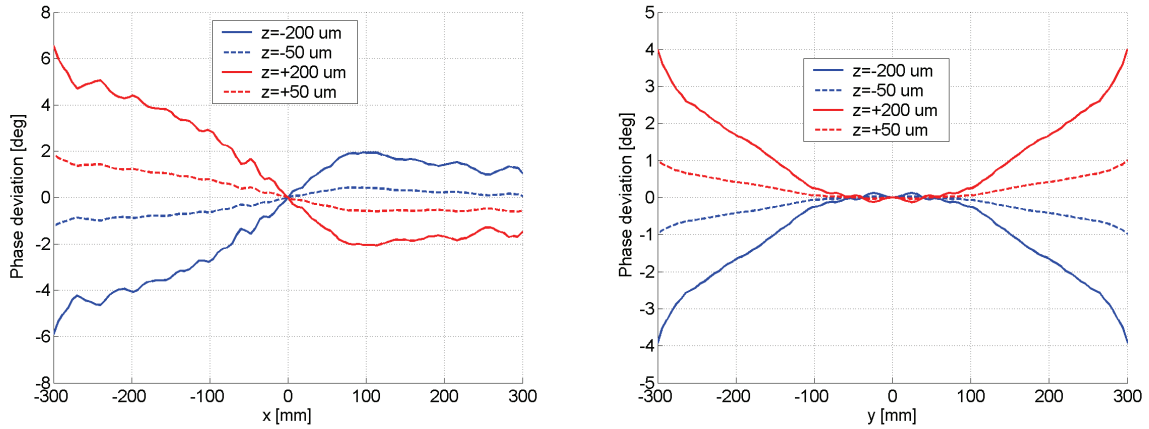

a) *b)*

Figure 5.27 *Effect of sub-reflector dislocation in the z-direction on the phase in the hologram illumination:*
a) horizontal cross-cut,
b) vertical cross-cut.

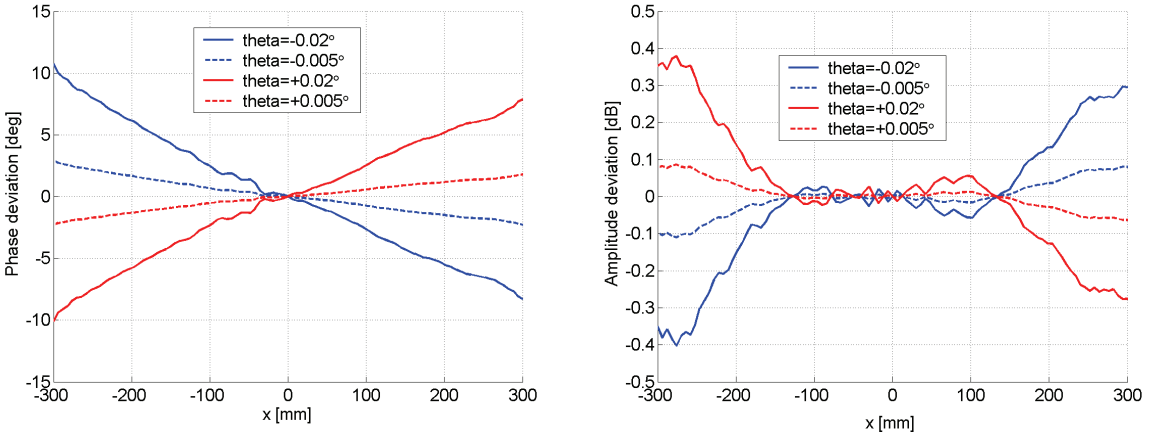

a) *b)*

Figure 5.28 *Effect of sub-reflector rotation around the vertical axis on the hologram illumination in the horizontal crosscut:*
a) phase deviation
b) amplitude deviation.

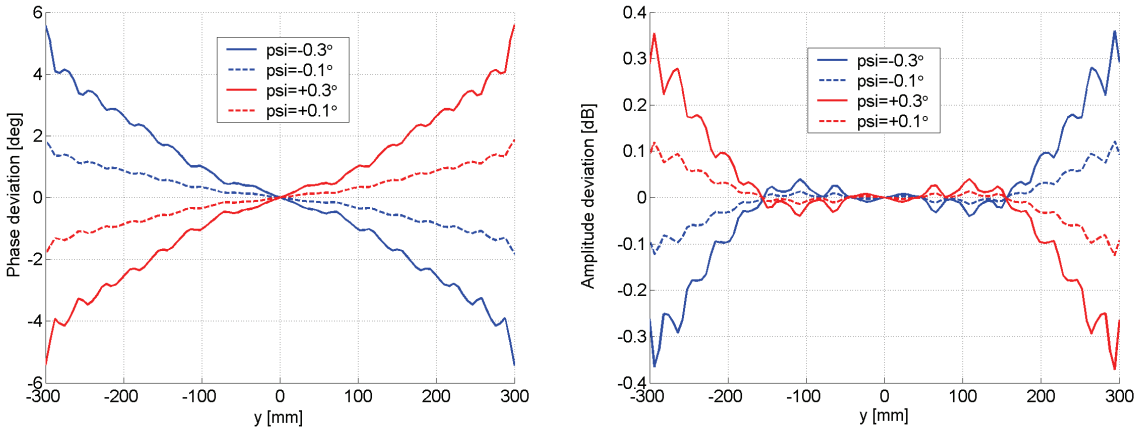

a) *b)*

Figure 5.29 *Effect of sub-reflector rotation around the beam axis on the hologram illumination in the vertical crosscut:*
a) phase deviation,
b) amplitude deviation.

As can be seen in Figures 5.25–5.29, the deviation from the desired hologram illumination shows a nearly linear dependence on the amount of the dislocation or the misalignment of the reflectors in the DRFS. The potential dislocations and misalignments have in general a greater effect on the phase of the radiation and the maximum allowed single reflector dislocation in the DRFS can be estimated from the simulated phase deviations, if at maximum, a phase error of 3.5° due to this error is allowed. The results are summarised in Table 5.3.

Table 5.3 *Estimated maximum allowed single dislocation and misalignment error in the DRFS.*

Object	*x* [μm]	*y* [μm]	*z* [μm]	Rotation around *x*-axis [°]	Rotation around *y*-axis [°]	Rotation around *z*-axis [°]
Feed horn	25	25	160	0.2*	0.2**	***
Sub-reflector	25	30	100	0.006*	0.006	0.2
Main reflector	60	80	200	0.006*	0.006	0.9

**Assumed to be the same as the tolerance for rotation around the y-axis*
***Estimated value from amplitude deviation*
****Not applicable as the feed horn pattern is nearly rotationally symmetric*

The DRFS is most sensitive to the feed horn and sub-reflector dislocations in the horizontal and vertical directions as an error of the order of 30 μm causes a phase error of about 3.5°. The feed horn rotation around the direction of the beam propagation could not be estimated as the nearly rotationally symmetric horn pattern does not vary much as the function of the rotation angle and this tolerance should be estimated from the polarisation error. The sensitivity of the polarisation to the rotation of the horn around the *z*-axis is discussed in Chapter 7, where the polarisation measurement accuracy is considered. The reflector dislocation is more significant than the misalignments as an error in the dimensions of the DRFS structure will not only cause a dislocation of a reflector, but also a misalignment and no misalignments are possible without a corresponding error in the dimensions of the DRFS structure. The dimensions of the DRFS structure have to be larger than the reflector sizes and the spacing of the reflectors (150 mm). Therefore, the tolerances for the rotation around horizontal *x*-axis and vertical *y*-axis result into approximately same tolerance for the *xy*-dimensions of the DRFS structures supporting the reflectors as the tolerance for the reflector dislocation.

These tolerances shown in Table 5.3 correspond to the case where the DRFS is placed at the designated hologram focus and the beam deviations due to the dislocation or the misalignment of a reflector can be at least partially compensated by adjusting the DRFS location and alignment in relation to the hologram. This relaxes the required manufacturing tolerances for the DRFS structure. A single manufacturing error in only one direction for a single reflector is not possible and incorrect dimensions in the DRFS structure affect all the reflector locations and alignments in more than one direction. The total tolerance for several simultaneous manufacturing errors can be estimated as the root sum of squares (RSS) of the individual errors assuming the errors to be independent and uncorrelated. As discussed here, this is not entirely valid assumption but it is a very useful simplification for a rough estimate on the manufacturing tolerances.

The total effect of the reflector misalignment and dislocation $\Delta\Psi_{structure}$ can be estimated as the RSS of the individual phase deviations $\Delta\Psi_i$ caused by the N possible dislocations and misalignments in the DRFS structure:

$$\Delta\Psi_{structure} = \sqrt{\sum_{i=1}^{N} \Delta\Psi_i^2}\,, \tag{5.10}$$

which can be approximated as

$$\Delta\Psi_{structure} = \sqrt{N}\Delta\Psi_i \tag{5.11}$$

by assuming the individual phase errors $\Delta\Psi_i$ to be equal. The number of the possible dislocations and misalignments is therefore 15, i.e., N = 15 as there are three objects with three possible dislocations, which contribute to two possible misalignments. The possible rotation around the z-axis is ignored. The tolerances for the reflector dislocation and misalignment can be estimated by allowing the total maximum phase deviation in the hologram illumination caused by the potential DRFS manufacturing errors to be ±2.5° and by allowing equal and uncorrelated contributions to the reflector surface manufacturing tolerances and to the tolerances in the DRFS structural dimensions. The allowed contribution of each individual error solved from (5.11) is $\Delta\Psi_i$=0.65°. The results are summarised in Table 5.4.

Table 5.4 *Estimated dislocation and misalignment tolerances in the DRFS structure.*

Object	x [μm]	y [μm]	z [μm]	Rotation around x-axis [°]	Rotation around y-axis [°]
Feed horn	6	6	40	0.05*	0.05**
Sub-reflector	6	8	25	0.002*	0.002
Main reflector	15	20	50	0.002*	0.002

** assumed the same as the rotation around the y-axis*
*** estimated from the amplitude deviation*

The tolerances shown in Table 5.4 are extremely tight and it may be possible that they cannot be met completely. They are also quite pessimistically estimated as the possible compensation of the beam deviations by adjusting the DRFS position and alignment is not considered and also the estimation involves approximations and assumptions, which may result into tighter tolerances than actually required. In addition, as the central region of the hologram contributes most significantly to the quiet-zone field, the tolerances could be relaxed approximately by a factor of 1.5 because of this. In any case, the objective in the DRFS manufacturing should be the dimensional tolerances of the order of ±10 μm for the DRFS structure.

5.6.3 Construction of the dual reflector feed system

The tight tolerances, ±5 μm for the reflector surfaces and ±10 μm for the dual reflector feed system dimensions, make the manufacturing of the DRFS challenging. The only feasible way to achieve this high precision is to realise the system as an integrated quasi-optical system. Thomas Keating Ltd in England was chosen to manufacture the DRFS reflector surfaces, because of the high accuracy of their milling equipment and their previous experience with quasi-optical systems. The milling machine used at Thomas Keating Ltd has been calibrated with laser interferometers. The positioning accuracy of the milling machine is better than 3 μm in the xy-direction and better than 2 μm in the z-direction [109]. This accuracy should be sufficient for milling the DRFS reflector surfaces.

The same manufacturer as for the milling of the reflector surfaces is used to assemble the DRFS as an integrated quasi-optical system to ensure the high precision. The final mechanical design and the technical drawings were done at Thomas Keating Ltd under the author's instruction. The DRFS was manufactured by milling the reflector surfaces on aluminium plates, which were attached to the inner walls of the structure. For the precise alignment and positioning of the primary feed, an aperture with a clamp is constructed in the rear of the system. The horn is inserted into the aperture and this aperture together with the outer surface of the horn and its flange are used as a mechanical reference to place the phase centre at the correct position. The inside of the DRFS structure is lined with absorbing material, TK THz RAM, to prevent internal reflections. A three-dimensional model of the structure is shown in Figure 5.30 together with a photograph of the constructed system.

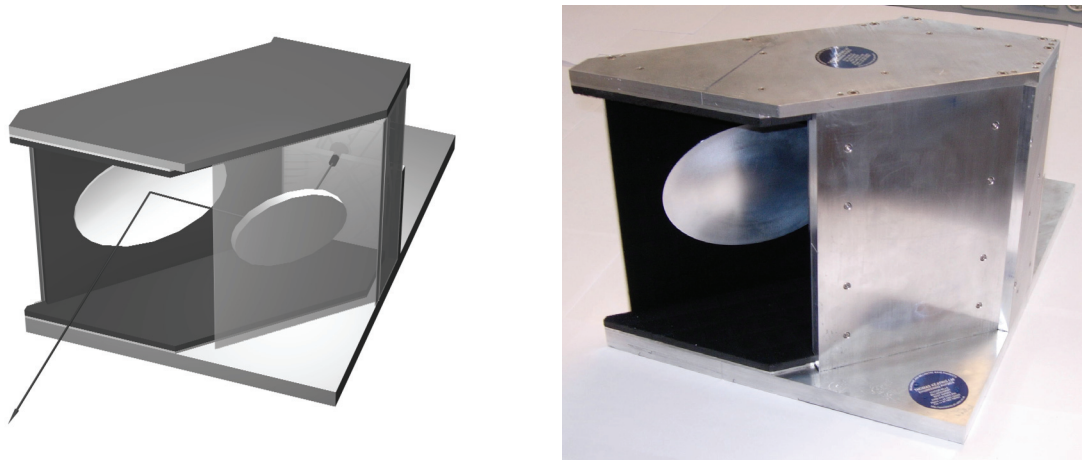

a) *b)*

Figure 5.30 *DRFS structure:*
a) three-dimensional model,
b) photograph of the system.

5.7 Verification of the DRFS operation with near-field probing

The final verification of the operation of any system can only be achieved by testing the system with measurements in a specific test configuration and/or in the final application. Although the modern computer-aided design tools predict the performance of an antenna quite accurately, the reliability of the simulation depends on how accurately the antenna structure is modelled in the simulations. The measurements provide an independent verification of the antenna operation to the computations and simulations. The field radiated by the DRFS at 310 GHz was measured with planar near-field probing for the final verification of the DRFS operation to ensure that no design or manufacturing errors were done.

5.7.1 Measurement set-up for the DRFS beam measurements

The dual reflector feed system beam measurements were done by probing the field radiated by the DRFS with a corrugated horn at 310 GHz [O2, O18, O19]. The probe was a similar horn as the primary feed of the DRFS. The DRFS was located 1800 mm from a planar *xy*-scanner (Orbit/FR AL-4951) so that the field is measured at the planned location of the 600-mm diameter hologram aperture. The electrical instrumentation was based on AB Millimetre MVNA-8-350 vector network analyser with ESA-1 and ESA-2 submillimetre wave extensions: the ESA-1 is a Gunn diode pumped frequency multiplier used as the transmitter, and the ESA-2 is a Gunn diode pumped harmonic mixer, which is used as the receiver. The transmitter and the receiver are phase-locked into a common reference, which enables both amplitude and phase measurements. The dynamic range in the DRFS beam probing was about 67 dB. The measurement set-up is shown in Figure 5.31 together with the probe and receiver mounting on the scanner.

Figure 5.31 *DRFS beam measurement set-up and the probe mounting.*

The scanner and the most of the walls of the measurement room were covered with mm-wave absorber material (Eccosorb VFX-NRL2). The antenna-under-test, the DRFS, was placed on an optical table and it was aligned perpendicular to the scanner plane by using a digital feeler pin attached to an extension arm fixed to the probe mounting. The planarity of the *xy*-scanner movement was measured using a Leica 3D laser tracker and the measured *z*-coordinate variations were computationally corrected from the measured phase data.

The bending of the local oscillator (LO) signal cable going from the MVNA to the harmonic mixer of the receiver causes phase measurement errors as the electrical length of the cable changes at the LO frequency of 17.2 GHz. The LO cable bending induced phase measurement errors can be compensated using a correction system designed in the Radio Laboratory [110]. Probe correction was done using the theoretical radiation pattern of the probe and by assuming the DRFS to radiate a spherical wave originating from the hologram focus. The estimated phase measurement uncertainty in the near-field probing of the DRFS beam was about ±8–14°. The measurement uncertainty and the error compensation techniques used to decrease it are described in Chapter 7.

5.7.2 Measured DRFS radiation

The field radiated by the dual reflector feed system was measured on the plane of the 600 mm hologram aperture so that the measured field corresponds to the field incident on the hologram, i.e., to the hologram illumination. The amplitude and the phase of the field were probed at 310 GHz at the linear vertical polarisation, which was the co-polarisation and at the linear horizontal polarisation, which is the cross-polarisation as defined in the Ludwig's first definition of the polarisation [43]. The measured field in the horizontal and vertical cross-cuts of the measurement area are shown in Figures 5.32 and 5.33 together with the simulated field cuts. The amplitude is normalised to 0 dB at the centre of the measurement area and the phase is presented as the deviation from the spherical wave originating from the system focus located 1800 mm from the scanner plane. The phase deviation was computed by comparing the processed measured phase to the phase of the spherical wave at the corresponding probe position. In Figure 5.34, the measured contour maps of the DRFS field are presented.

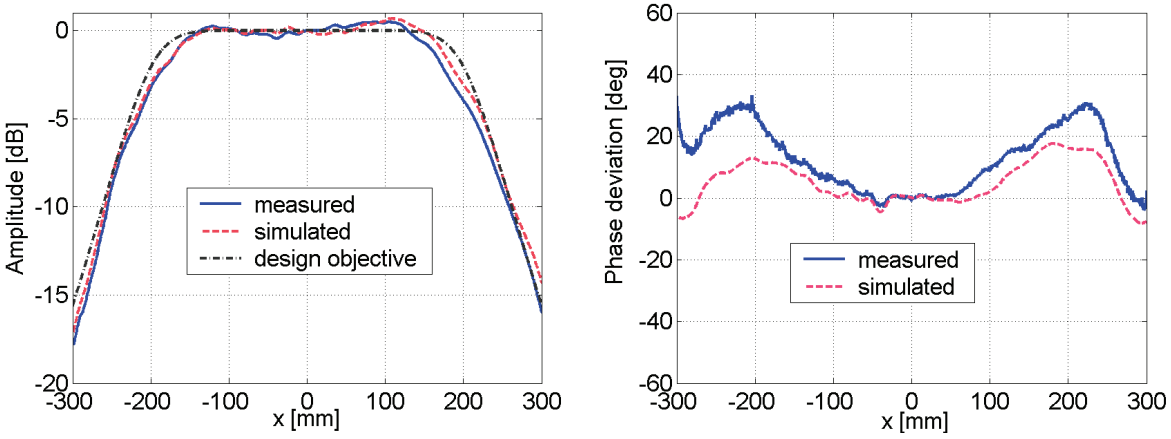

a) *b)*

Figure 5.32 *The measured and simulated hologram illumination a) amplitude and b) phase deviation from the spherical wave at 310 GHz at the co-polarisation in the horizontal cut of the hologram aperture [O2].*

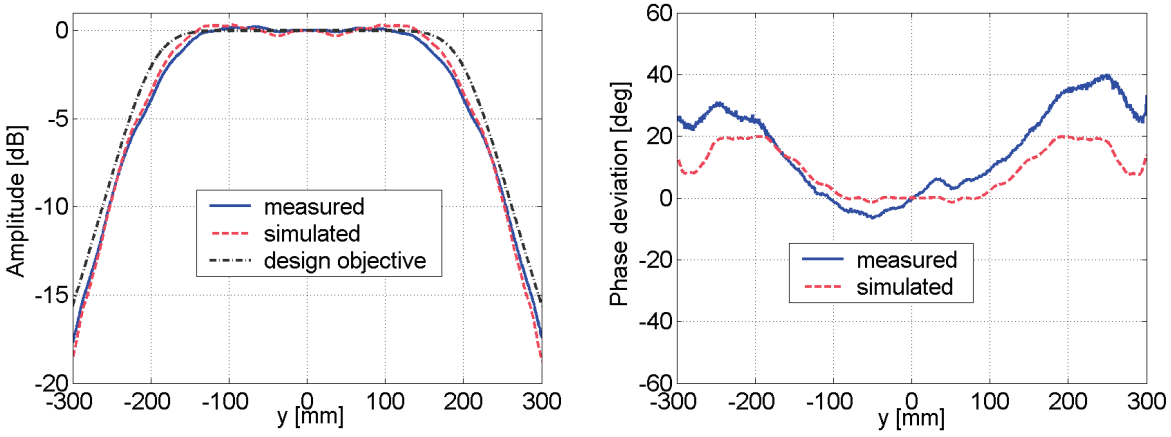

a) *b)*

Figure 5.33 *The measured and simulated hologram illumination a) amplitude and b) phase deviation from the spherical wave at 310 GHz at the co-polarisation in the vertical cut of the hologram aperture [O2].*

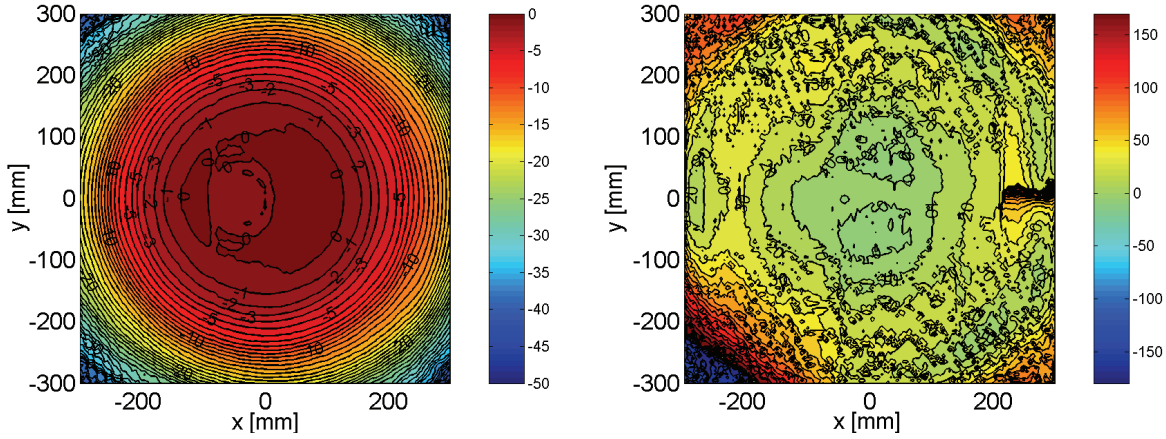

a) *b)*

Figure 5.34 *The measured contour maps of the hologram illumination a) amplitude [dB], and b) phase deviation [°] from the spherical wave at 310 GHz at the co-polarisation.*

The spikes in the measured phase observed in Figure 5.34 at the bottom and top regions of the 300 mm × 300 mm measurement area were most likely caused by interference from the scanner drives to the IF signal. Unfortunately, these spikes were noticed only after processing the data and the measurements could not be repeated when the problem was corrected by re-positioning the cables. The measured amplitude and phase show very good agreement with the simulations; the measured amplitude is within ±0.3 dB from the simulated amplitude in the beam cross-cuts in the central region of the beam. Both the measured and the simulated phase are within 30º from the desired spherical wave – the maximum difference between the measured phase deviation from the spherical wave and the simulated one is less than 20º. Considering the estimated phase uncertainty, ±8º, the difference between the measured and simulated phase seen in Figures 5.32 and 5.33, indicates that the effective focal length of the

DRFS is slightly longer than the designed 1800 mm. This may be caused by slightly incorrect shape of the reflectors (local curvature) or by a small error in the DRFS dimensions, i.e. in the distances between the objects in the DRFS structure. The somewhat non-monotonic and non-symmetric phase behaviour seen in the vertical cut of the measured field suggests that there may be more than one small misalignment or dislocation of the reflectors in the structure. Nevertheless, the slight systematic phase deviation can be mostly eliminated by adjusting the DRFS distance from the hologram to compensate the increased effective focal length. The measured phase deviation from the spherical wave in the vertical field cut when the DRFS is moved 12 mm closer to the near-field scanner is shown in Figure 5.35.

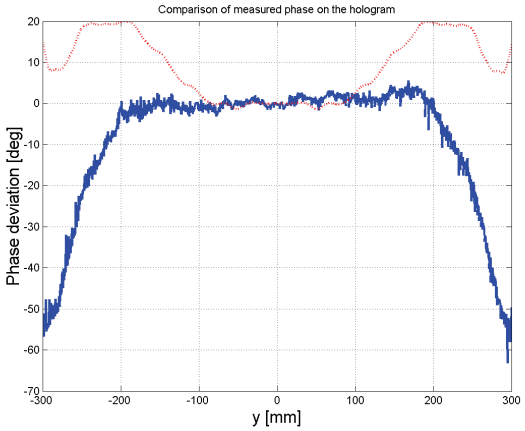

Figure 5.35 *The measured phase deviation from the spherical wave in the vertical cut of the hologram aperture when the DRFS is moved closer to the near-field scanner.*

The cross-polarisation level in the hologram illumination by the DRFS was measured by rotating the probe by 90° to measure the horizontally polarised field component. The measured cross-polarisation level is presented in Figure 5.36.

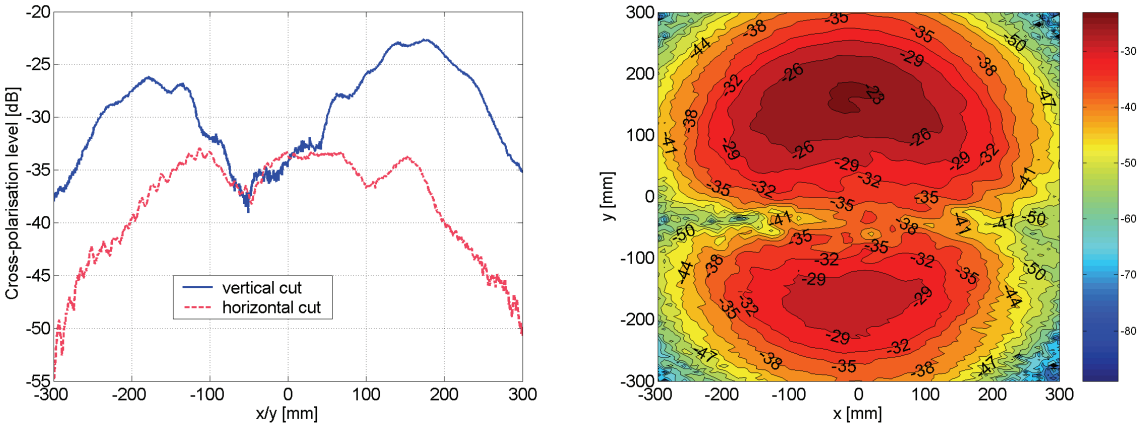

a) *b)*

Figure 5.36 *Measured cross-polarisation level in the hologram illumination at 310 GHz:*
a) horizontal and vertical cuts,
b) contour map.

The maximum cross-polarisation level in the hologram illumination is approximately -23 dB, which corresponds well to the simulated cross-polarisation level shown in Figure 5.16. The

measured cross-polarisation level is affected by the polarisation properties of the probe, which depends on the orientation of the probe and on the cross-polarisation isolation of the probe. The polarisation measurement uncertainty and the factors affecting it are discussed in Chapter 7.

A quick test was done later by an under-graduate student under the author's supervision to verify the DRFS operation also at the horizontal linear polarisation at the frequency of 310 GHz by rotating both the feed horn in the DRFS and the probe horn by 90°. The measured amplitude at the vertical (VV) and the horizontal (HH) polarisation are shown in Figure 5.37. No measurement error compensation techniques were used in these measurements.

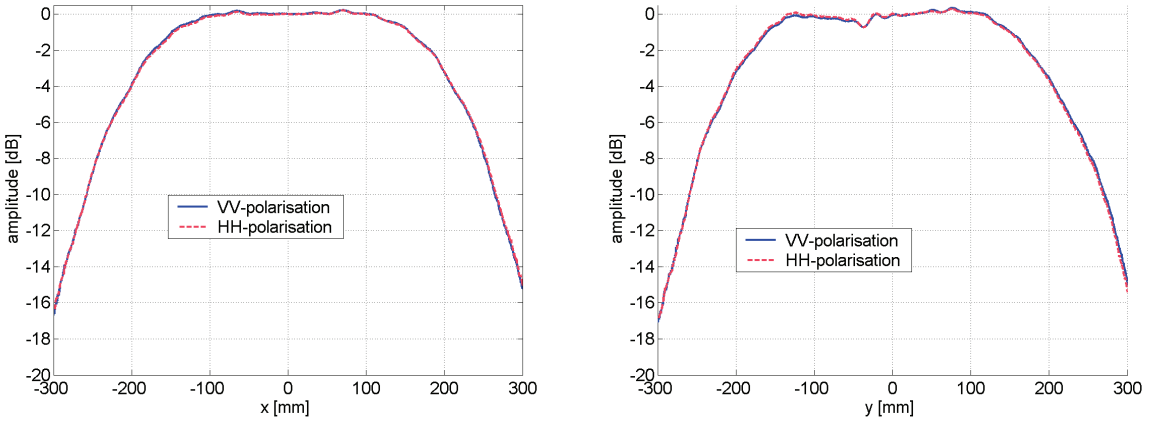

a) *b)*

Figure 5.37 *Measured cuts of the hologram illumination at 310 GHz at both linear polarizations:*
a) horizontal cut,
b) vertical cut.

The measured DRFS radiation is within 0.2 dB the same at both polarisations. As can be seen comparing the Figures 5.32 and 5.33 to Figure 5.37, the shape of the measured beam is slightly different in these later measurements shown in Figure 5.37, but the reasons for this were not investigated further as the purpose of this quick test was to verify only that the DRFS beam shape does not depend significantly on the polarisation.

The measurements of the radiated field by the DRFS incident on the hologram aperture with the planar near-field scanner showed good correlation with the simulated field, which provided the final verification that the DRFS design was correctly done and that there were no significant manufacturing errors in the DRFS construction. The DRFS operates as designed.

6 Dual reflector feed system in a hologram-based CATR

The dual reflector feed system is designed to illuminate the hologram in a compact antenna test range based on a hologram and the final verification of the DRFS operation is obtained by using the DRFS to illuminate a demonstration hologram. The shaped hologram illumination with the dual reflector feed system allows improvements to the hologram CATR: the simplification of the hologram manufacturing, improved polarisation performance and potentially lower cross-polarisation in the quiet-zone. These improvements to the hologram CATR are discussed next together with the measurement results for the test holograms at 310 GHz.

6.1 Demonstration CATR based on a hologram

The final test for the applicability of the designed dual reflector feed system for illuminating holograms in CATRs, is the actual use of the DRFS with a hologram. For this purpose, 600-mm diameter holograms were designed in the Radio Laboratory by Tomi Koskinen for the frequency of 310 GHz and they were optimised for operation at the vertical linear polarisation. First, a hologram illuminated directly with the corrugated horn was designed and procured for comparison and, second, a hologram illuminated by the DRFS was designed and procured. The performance of these holograms was compared by measuring the quiet-zone fields produced by the holograms with the planar near-field scanner and with the same measurement instrumentation, which was used for probing the DRFS beam as described in Chapter 5.

6.1.1 Structure of the CATR

The CATRs constructed were based on 600-mm diameter holograms: one illuminated with the corrugated horn directly and the other with the DRFS. The size of the hologram was determined by the maximum diameter of the pattern available with an inexpensive printed circuit board manufacturing processes in Finland. The focal length of the holograms was 1800 mm and the quiet-zone field was optimised in the design of the holograms for the vertical polarisation at the same distance from the hologram. Also, the feed position and alignment were optimised to produce the best quiet-zone field quality. The offset angle of the holograms was 33°, i.e., the plane wave propagates into this angle from the hologram surface normal. The CATR structure is illustrated in Figure 6.1.

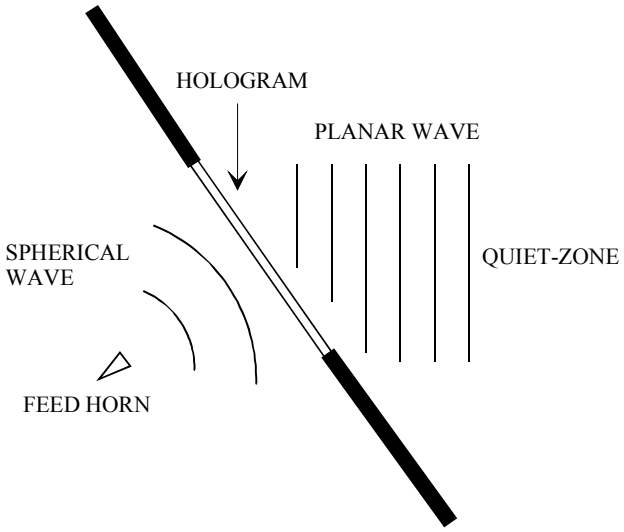

Figure 6.1 *Compact antenna test range based on a hologram.*

6.1.2 Quiet-zone field measurements

The quiet-zone field of the test holograms was probed with the planar near-field scanner using the same corrugated horn as the probe, which was used to probe the DRFS beam. It is similar to the one used to illuminate the hologram and which is used as the primary feed in the DRFS. The feed was placed on an optical table and the feed position and alignment were adjusted for optimal quiet-zone field quality. Photographs of the measurement set-up for the hologram illuminated with the DRFS are shown in Figure 6.2.

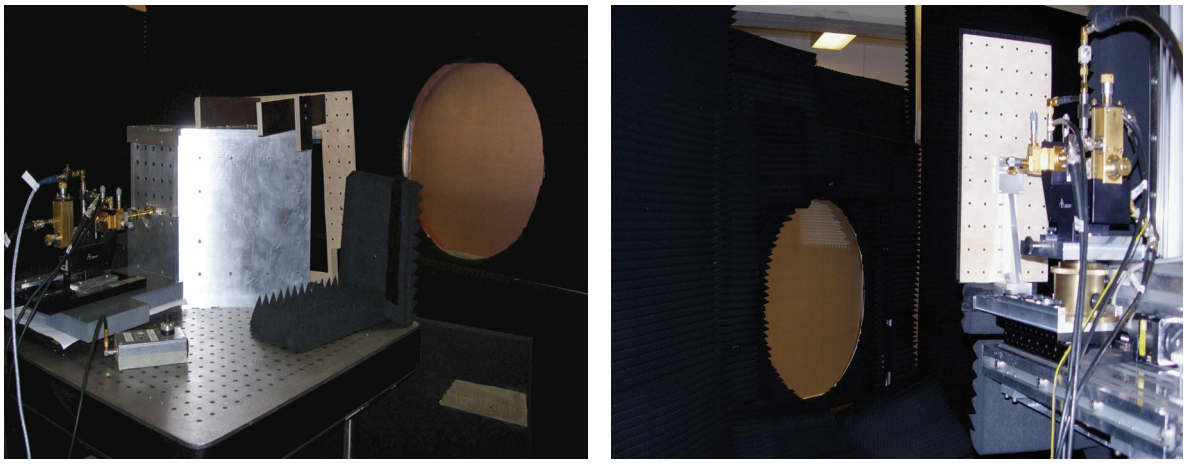

a) *b)*

Figure 6.2 *The measurement set-up for measuring the quiet-zone field of the hologram illuminated with the DRFS:*
a) rear-view of the DRFS showing the transmitter,
b) view behind the near-field scanner showing the probe mounting and the receiver.

6.1.2.1 Co-polarised quiet-zone field

Both the amplitude and the phase were measured at the frequency of 310 GHz. The measured co-polarised quiet-zone field of the hologram illuminated directly with the corrugated horn is shown in Figures 6.3 and 6.4, and the measured quiet-zone field for the hologram illuminated with the DRFS at the co-polarisation is shown in Figures 6.5 and 6.6. As in the case of the DRFS beam probing, error compensation techniques were used to reduce the measurement uncertainty and these techniques are described in Chapter 7. The estimated uncertainty in the phase measurements was ±8°.

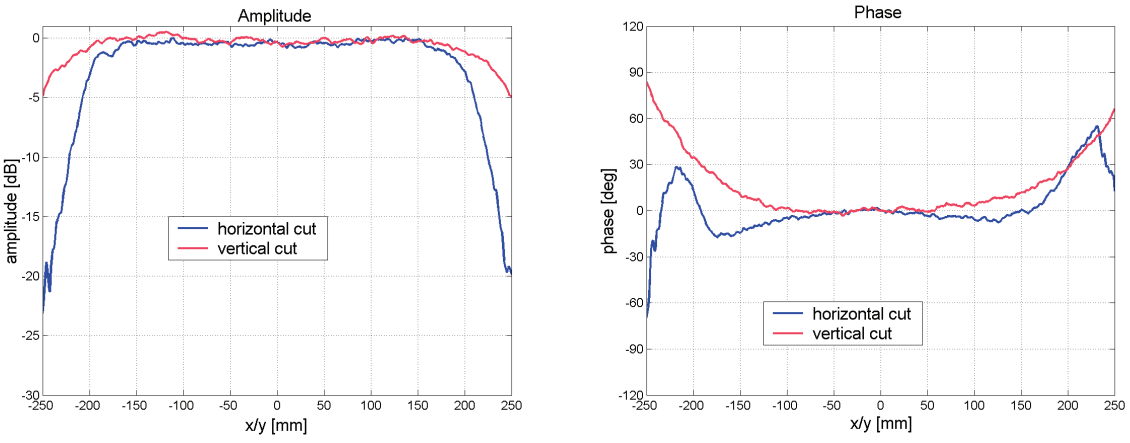

a) *b)*

Figure 6.3 *Measured cuts of the quiet-zone of the hologram illuminated with the corrugated horn a) amplitude and b) phase at 310 GHz at the co-polarisation.*

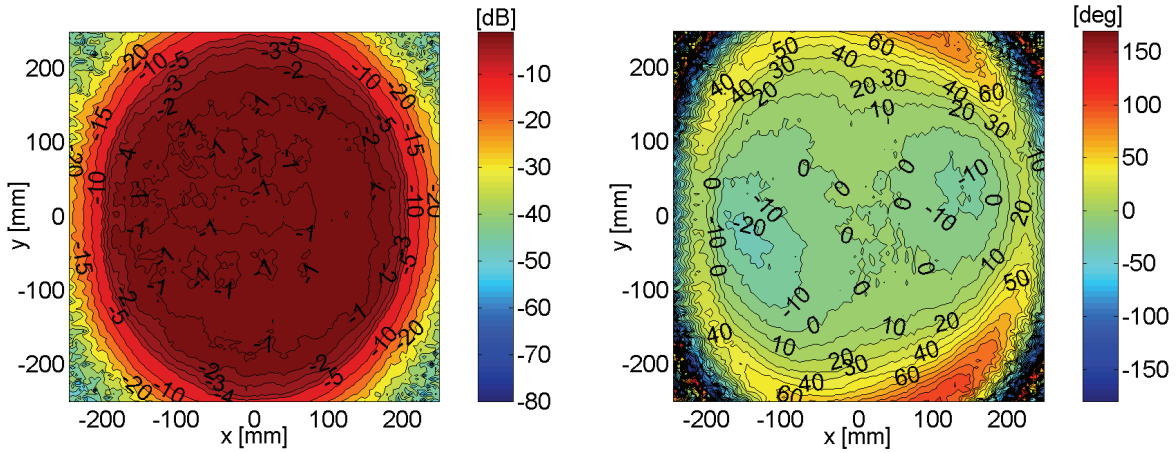

a) *b)*

Figure 6.4 *Measured contour maps of the quiet-zone of the hologram illuminated with the corrugated horn a) amplitude and b) phase at 310 GHz at the co-polarisation.*

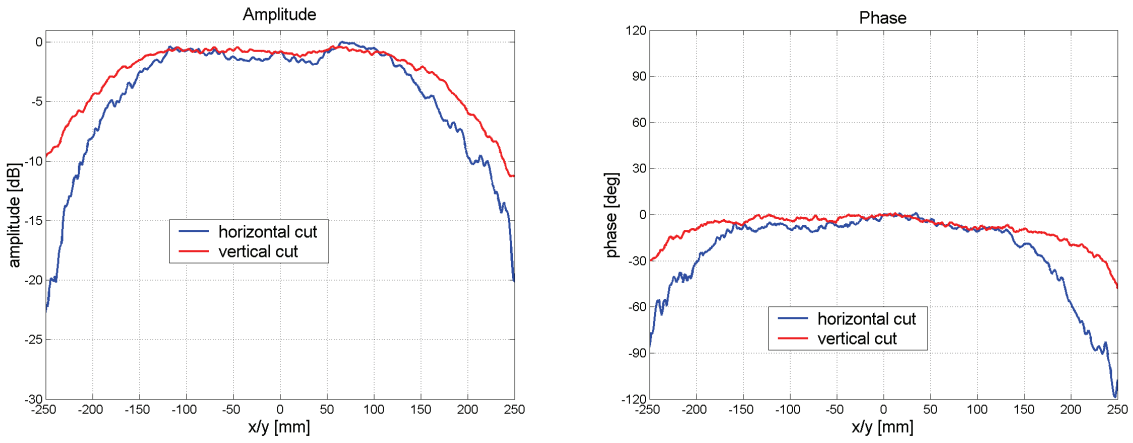

a) *b)*

Figure 6.5 *Measured cuts of the quiet-zone of the hologram illuminated with the DRFS a) amplitude and b) phase at 310 GHz at the co-polarisation.*

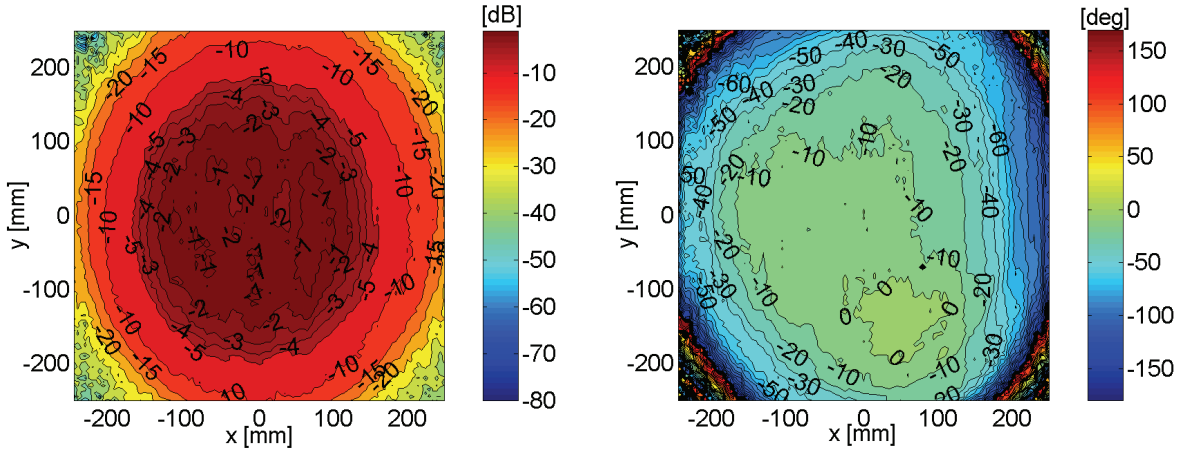

a) *b)*

Figure 6.6 *Measured contour maps of the quiet-zone of the hologram illuminated with the DRFS a) amplitude and b) phase at 310 GHz at the co-polarisation.*

The root mean squared (RMS) amplitude ripple inside a 250 mm diameter circle in the quiet-zone of the hologram illuminated with the DRFS is ±0.37 dB and the RMS phase ripple is ±4.6º. The RMS amplitude and phase ripples in the quiet-zone of the hologram fed by the horn directly are ±0.23 dB and ±4.8º. The quality of the both quiet-zones is in practice approximately identical considering the hologram pattern etching accuracy of the order of ±20 µm with a printed circuit board (PCB) photolithography process. The diameters of the quiet-zones are approximately 250–300 mm for both holograms. The phase deviations limit the quiet-zone size for the hologram illuminated with the horn directly and the conservatively selected DRFS beam width limits the quiet-zone size for the hologram illuminated with the DRFS. In principle, the quiet-zone size of the hologram illuminated with the DRFS can be enlarged by designing a DRFS with a wider beam to illuminate the hologram.

The phase front of the plane wave in the quiet-zone of the hologram illuminated by the horn directly form a saddle surface as the phase front in the horizontal cut is convex and the phase front in the vertical cut is concave. This phase behaviour was observed for the first time in these measurements because of the reduced measurement uncertainty and better understanding of the phase measurement errors and their causes. The saddle-shaped phase front was believed to be caused by uneven tensioning of the hologram film that causes stretching of the hologram pattern. Similar behaviour was later observed for the large 3-m hologram in the CATR constructed for the frequency of 322 GHz [O4] and the reason for the shape of the phase front was identified to be the different diameter of the hologram pattern in the vertical direction than in the horizontal direction, which corresponds to uneven stretching of the hologram film in the case of the 600-mm test hologram.

The quiet-zone amplitude of the hologram illuminated with the DRFS shows the shoulders present in the shaped hologram illumination and phase behaviour similar to the DRFS phase deviation from the spherical wave after compensation of the phase front curvature by moving the DRFS closer to the hologram (see Figure 5.35). As the quiet-zone field is directly affected by the deviations in the hologram illumination, higher DRFS beam quality should be pursued for high-precision measurements of the antenna patterns by improving the DRFS.

6.1.2.2 Cross-polarised quiet-zone field

The cross-polarised quiet-zone field was measured by rotating the probe by 90° around its *z*-axis to measure the horizontally polarised field component, which is the cross-polarisation for the vertical polarisation according to the Ludwig's first definition of the polarisation [43]. The measured cross-polarisation level in the quiet-zone of the hologram illuminated by the horn directly at 310 GHz is shown in Figure 6.7 and the cross-polarisation level in the quiet-zone of the hologram illuminated by the DRFS is shown in Figure 6.8.

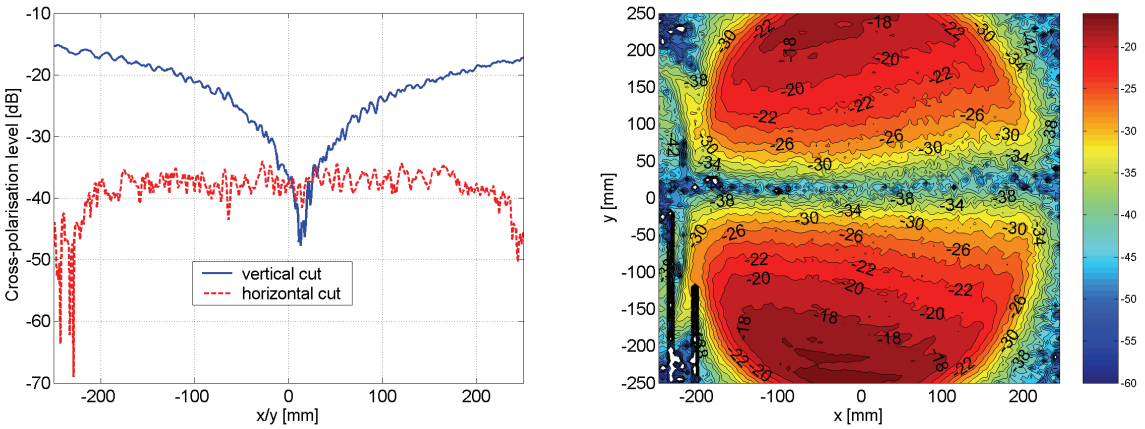

a) *b)*

Figure 6.7 *Measured cross-polarisation level at 310 GHz in the quiet-zone of the hologram illuminated with the corrugated horn:*
a) horizontal and vertical cuts,
b) contour map.

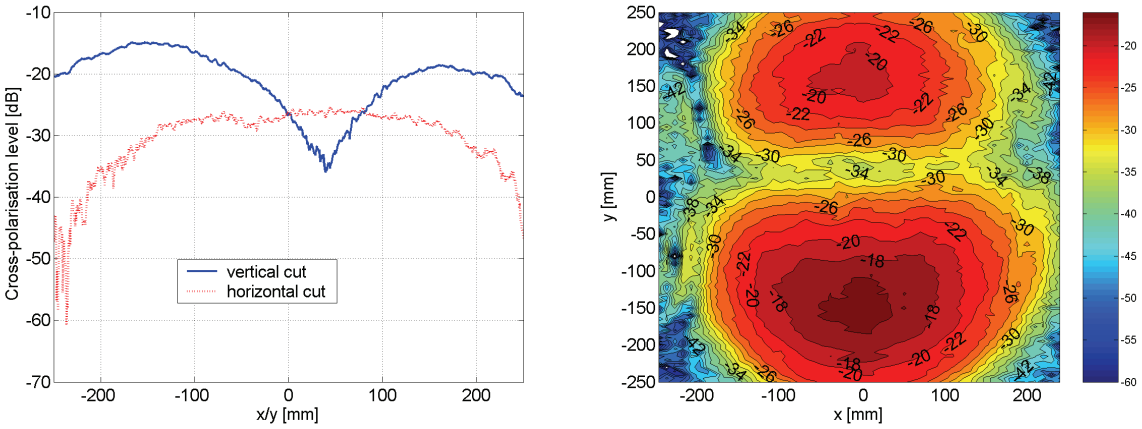

a) *b)*

Figure 6.8 *Measured cross-polarisation level [dB] at 310 GHz in the quiet-zone of the hologram illuminated with the DRFS:*
a) horizontal and vertical cuts,
b) contour map.

The maximum measured cross-polarisation level in relation to the maximum amplitude of the co-polarised field is approximately -15 dB in the quiet-zone of the hologram illuminated with the DRFS and it is approximately the same in the quiet-zone of the hologram illuminated with the corrugated horn. This level of cross-polarisation in the quiet-zone is somewhat high for measuring the cross-polarisation level of antennas with low cross-polarisation and for this purpose it should be lower.

The cross-polarised field component in the quiet-zone is caused by the cross-polarisation of the feed, which is transmitted into the quiet-zone, or by depolarisation of the field by the hologram itself. The cross-polarisation of the corrugated horn is much lower, about -40 dB according to the simulations in the diagonal pattern cut, than the measured cross-polarisation in the DRFS beam (at maximum about -23 dB). Therefore, the similar level of cross-polarisation in the quiet-zones of the both holograms can be either explained by the high level of the depolarisation by the holograms or the hologram illuminated with the DRFS produces less cross-polarisation but the higher cross-polarisation in the DRFS beam causes approximately the relatively high cross-polarisation level in the quiet-zone. This will be investigated further in Section 6.3 together with the possibilities to decrease the cross-polarisation in the quiet-zone of a CATR based on a hologram.

6.2 Improvements to the hologram CATR performance

The shaped hologram illumination allows improvements to the hologram performance in compact antenna test range applications. The potential improvements include facilitation of the hologram manufacturing, hologram operation at the horizontal polarisation, and reduced cross-polarisation level in the quiet-zone of the CATR. These potential performance improvements are discussed next in the following sections.

6.2.1 Facilitation of the hologram manufacturing

The main challenge in the realisation of large hologram based CATR for sub-mm wavelengths has been the manufacturing of the holograms with high pattern accuracy. Especially, the combination of the required high precision with extremely large pattern sizes up to several metres in diameter has been difficult to achieve and considerable effort has been made in the development of the hologram manufacturing over the years [O4, O32]. Currently the holograms are manufactured using direct laser exposure of the pattern on a photo-resist coated copper-plated polyester film (Mylar) and chemical wet etching. The maximum size of the pattern, which is limited by the equipment in the process used, is 1.5 m × 6.0 m. Available materials limit also the maximum width of the pattern: the currently used Mylar-film is only 1.35 m wide**.** Because of this limited maximum pattern size, large holograms have to be manufactured in pieces, which are joined to form the complete hologram pattern. The hologram patterns are joined by soldering the metal stripes in the pattern together [O4].

6.2.1.1 Etching of the hologram patterns

The hologram patterns are chemically wet etched after writing the pattern on the photosensitive resist with a laser. The hologram material used is a 50 μm thick polyester film with a laminated 17 μm thick copper layer. In a photolithography process, the typical uncertainty in the line widths is of the order of the metal thickness as the edges of the etched metal are typically not straight. Also, possible under- and over-etching require careful optimisation of the process parameters.

The amplitude taper in the hologram aperture is realised by tapering the slot widths in the case of hologram illumination with the Gaussian beam radiated by a corrugated horn. This tapering makes the slots in the pattern very narrow and difficult to etch near the hologram edges. As the shaped hologram illumination with DRFS eliminates the need for tapering the slot widths, the narrow slots are eliminated from the hologram pattern, which is especially significant at shorter sub-millimetre wavelengths as the slot width is proportional to the wavelength. The slots widths in the hologram illuminated by the DRFS and in the hologram illuminated with the feed horn directly are shown in Figure 6.9. The slot widths were measured with a microscope along the horizontal centrelines of the holograms by Tomi Koskinen.

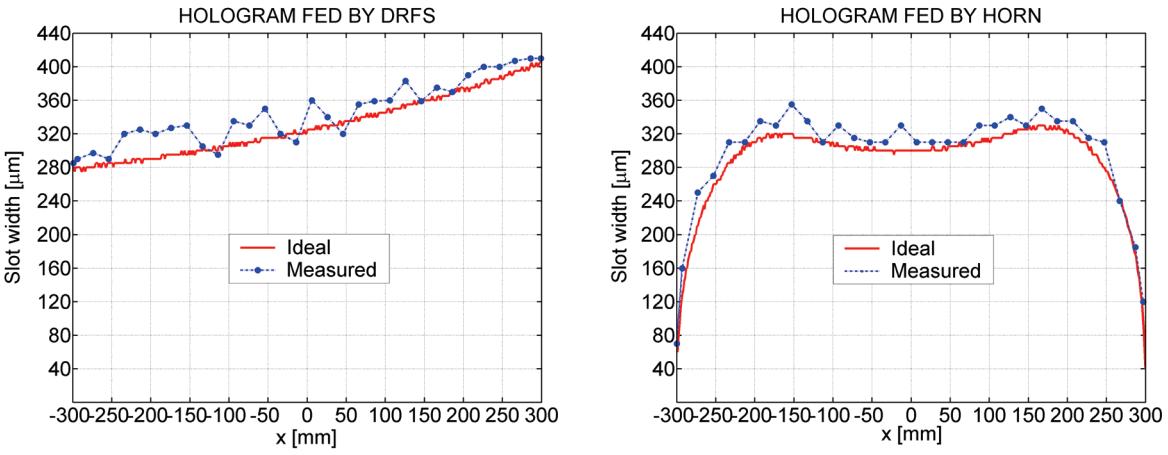

a) *b)*

Figure 6.9 *Measured slot widths a) in the hologram with shaped illumination, and b) in the hologram with Gaussian illumination with the feed horn [O2].*

As can be seen in Figure 6.9, the slots in the hologram designed to be illuminated with the DRFS are about 280–400 µm wide, which makes the slots significantly wider and more constant in width than in the hologram designed for the illumination with a corrugated horn, which has designed slot widths of approximately 30–330 µm. The root mean squared (RMS) slot width error due to manufacturing errors is about 20 µm for both holograms. This is of the order of the thickness of the metallisation (17 µm) on the hologram material (50 µm polyester film, Mylar).

In the hologram pattern manufacturing, the most common manufacturing error in the pattern is over-etching, i.e. the slots are often systematically too wide. This can be seen also in Figure 6.9, which is a typical example of the hologram pattern manufacturing using photolithography with photo-masks. The relative error in the slot width is larger for the narrow slots as the uncertainty in the slot width due to the photolithography process is approximately independent of the slot width. This results into an additional advantage of the shaped hologram illumination with the DRFS over the conventional Gaussian illumination with a corrugated horn as the wider slots are not only easier to etch, but they are also less sensitive to over-etching. This can be seen in Figure 6.10, where the simulated effect of a systematic error in the slot widths of the hologram pattern on the quiet-zone field is shown. The hologram simulations were carried out by Tomi Koskinen.

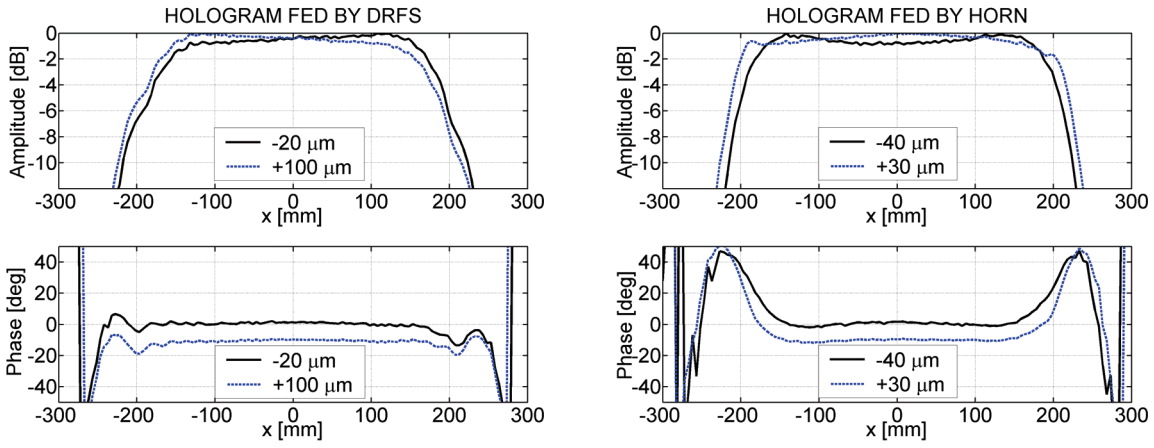

a) *b)*

Figure 6.10 *Simulated horizontal cut of the quiet-zone field a) for a hologram illuminated with the DRFS, and b) for a hologram illuminated with a corrugated horn when a systematic manufacturing error is added to the slot widths of the hologram pattern [O2].*

The hologram illuminated with the DRFS can tolerate over-etching of the slots up to 100 μm without significant degradation of the quiet-zone amplitude, as the hologram illuminated directly with the feed horn can tolerate only 30 μm of over-etching.

6.2.1.2 Enlargement of the quiet-zone size

Large holograms are manufactured by joining several separately etched pieces together to form the complete hologram. The pieces have to be aligned and positioned very precisely to form a continuous pattern as gaps or other discontinuities in the hologram pattern act as diffraction sources causing ripple to the quiet-zone field. The number of the pieces and the seams should be minimised in order to minimise the potential disturbances in the quiet-zone field.

As the maximum size of the hologram pieces is limited by the existing manufacturing equipment and available material width, the number of the pieces and seams in the hologram pattern can be minimised only by minimising the required hologram size, i.e., by maximising the size of the quiet-zone produced by the hologram. The quiet-zone size of a hologram is limited by the amplitude taper in the aperture field. In the case of the hologram illuminated with the horn, the tapered slots take up a part of the aperture reducing the quiet-zone size, and in the case of the hologram illuminated with the DRFS, the amplitude taper in the illumination extents over a significant portion of the hologram aperture.

In principle, the quiet-zone of the DRFS hologram can be increased by widening the shaped beam illuminating the hologram as the quiet-zone size is mostly determined by the -1 dB beam width in the illumination. In order to widen the DRFS beam, the reflector size in the DRFS has to be increased and the edge taper in the hologram illumination has to be decreased as the DRFS beam may not be too strongly shaped in order to keep the ripples in the beam small, i.e. the amplitude taper may not be too steep at the edges. The possibilities to increase

the beam width while keeping the ripples at minimum and the reflector sizes reasonable are being investigated in a Master's thesis under the author's instruction.

6.2.2 Polarisation performance

As the hologram operation is limited to the vertical polarisation, antenna testing cannot be done at other polarisations – for example, circularly polarised antennas cannot be tested fully. This is a serious limitation and therefore the hologram operation at the horizontal polarisation and also at both linear polarisations, i.e. at circular polarisation, has been pursued.

The holograms illuminated with a Gaussian beam operate properly only at the vertical polarisation as at the polarisation parallel to the slot, the slot width has a strong effect on the transmission coefficient, but at the polarisation perpendicular to the slot the transmission is only weakly affected by the slot width. The slots in the hologram pattern are vertical. The transmission coefficient of a narrow slot at the polarisation perpendicular and parallel to the slot are presented in Figure 6.11. Because the transmission of the slot does not depend on the slot width, the tapering of the slots towards the hologram edges does not produce amplitude taper to the aperture field at the horizontal polarisation and the quiet-zone field has large ripples due to strong edge diffraction [65]. The amplitude taper in the shaped hologram illumination allows the holograms to operate at the horizontal polarisation also.

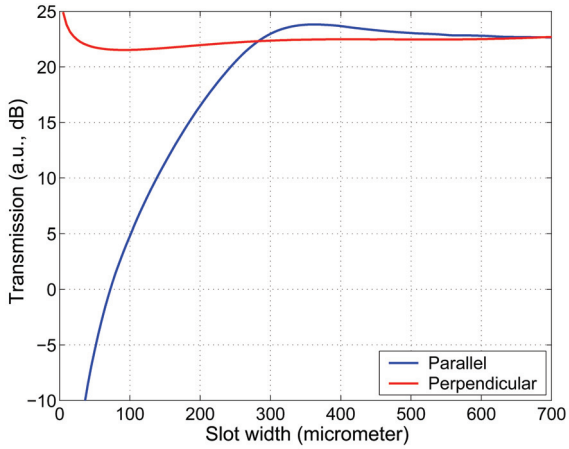

Figure 6.11 *Simulated transmission coefficient as the function of the slot width at the polarisation parallel and perpendicular to the slot at 310 GHz [O52].*

The hologram operation at the horizontal polarisation was first studied by measuring the quiet-zone field of the same test hologram illuminated with the DRFS that was measured at the vertical polarisation at the frequency of 310 GHz. The measured contour maps of amplitude and phase are presented in Figure 6.12.

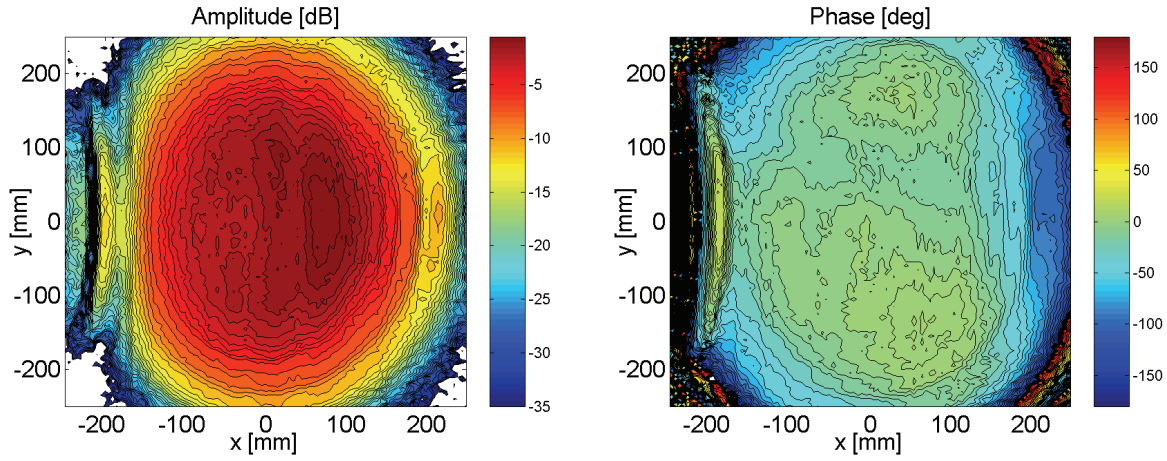

a) *b)*

Figure 6.12 *Measured quiet-zone field of the test hologram illuminated with the DRFS at 310 GHz at the linear horizontal polarisation:*
a) amplitude,
b) phase.

The test hologram was designed to operate at the vertical polarisation and it was optimised only for this polarisation. As can be seen in Figure 6.12, the amplitude in the quiet-zone is about 4 dB higher at the positive side of the *x*-axis than in the negative half. The hologram is optimised for the vertical polarisation and at the horizontal polarisation the amplitude becomes then higher on one edge of the quiet-zone than on the other as the slot transmission is nearly independent of the slot width. This non-symmetry in the quiet-zone field amplitude can be corrected by optimising the hologram pattern for the horizontal polarisation.

Two 600-mm diameter test holograms for 310 GHz were designed in the Radio Laboratory and one of them was optimised for the horizontal polarisation and the other one was optimised for both linear polarisations. Both holograms are illuminated with the dual reflector feed system. The designed slot widths for the hologram for the horizontal polarisation varied between 355–665 μm and the slot widths in the dual polarisation hologram were between 475–565 μm. The slots widths together with the widths of the metal strips between them are shown in Figure 6.13.

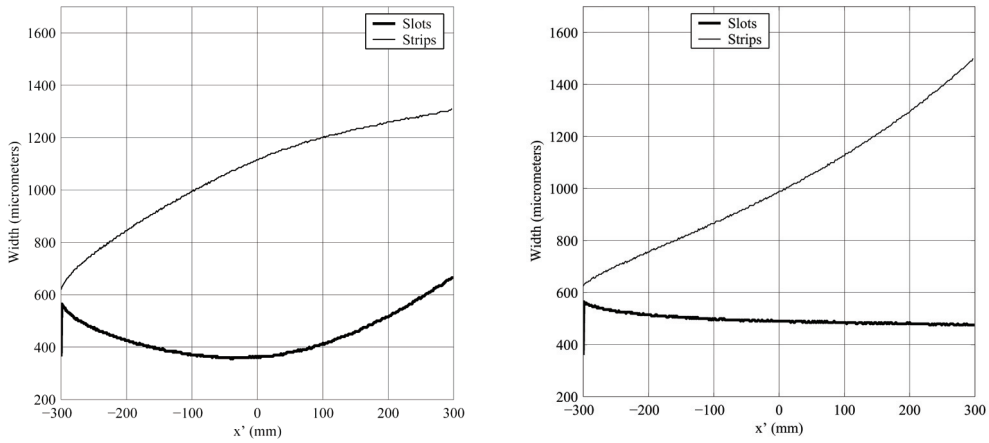

a) *b)*

Figure 6.13 *Designed slot and strip widths in the horizontal centre cut of the test holograms for 310 GHz:*
a) hologram optimised for the horizontal polarisation,
b) hologram optimised for both linear polarisations [111].

The quiet-zone fields of these holograms were probed similarly with the planar near-field scanner as was done in the case of the test hologram optimised for the vertical polarisations. Unfortunately, the near-field scanner broke down before these measurements and as automated measurements were not possible, no contour maps were measured. In addition, the probe position was known with less precision and, therefore, no error compensation methods were utilised for reducing the measurement uncertainty. In this case, the phase measurement uncertainty can be roughly estimated to be of the order of ±15°.

The measured quiet-zone field cuts at the frequency of 310 GHz are shown in Figures 6.14 and 6.15 for the horizontal polarisation (HH), and for the vertical polarisation (VV) in the case of the hologram optimised for the horizontal polarisation and in the case of the hologram optimised for both polarisation in Figures 6.17 and 6.18. The cross-polarisation measurement results for the horizontal polarisation (HV) and for the vertical polarisation (VH) are presented in Figures 6.16 and 6.19 for the hologram optimised for the horizontal polarisation and for the hologram optimised for both linear polarisations, respectively. The polarisations of the horns were changed using a waveguide twist to rotate the polarisation of the horns by 90° so that the probe and primary feed horn (or DRFS) positions and alignment were not changed.

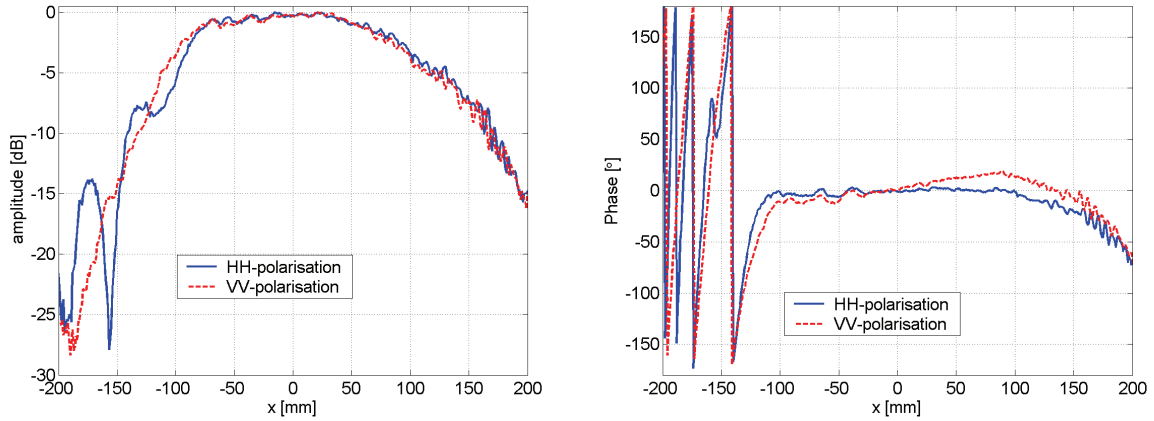

a) *b)*

Figure 6.14 *Measured horizontal cut of the quiet-zone field at 310 GHz at both linear polarisations for the hologram optimised for the horizontal (HH) polarisation:*
a) amplitude,
b) phase.

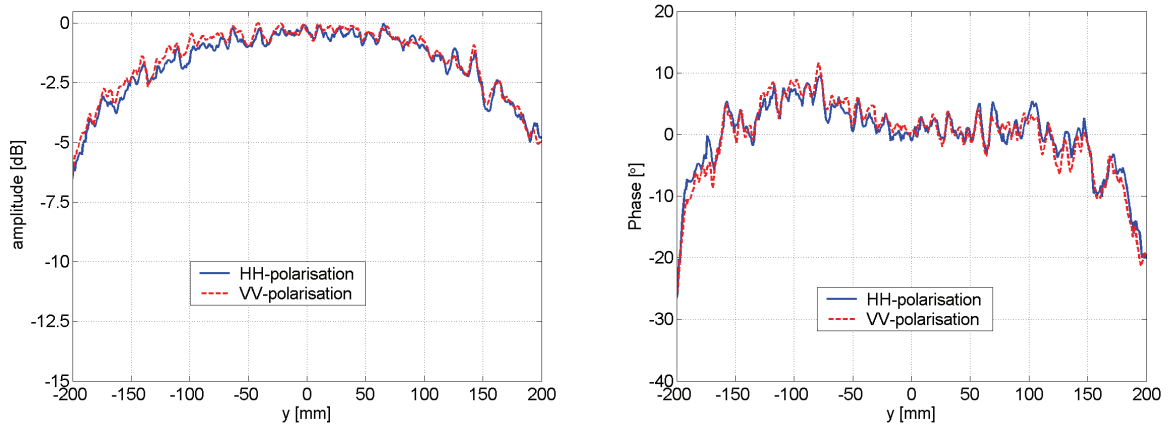

a) *b)*

Figure 6.15 *Measured vertical cut of the quiet-zone field at 310 GHz at both linear polarisations for the hologram optimised for the horizontal (HH) polarisation:*
a) amplitude,
b) phase.

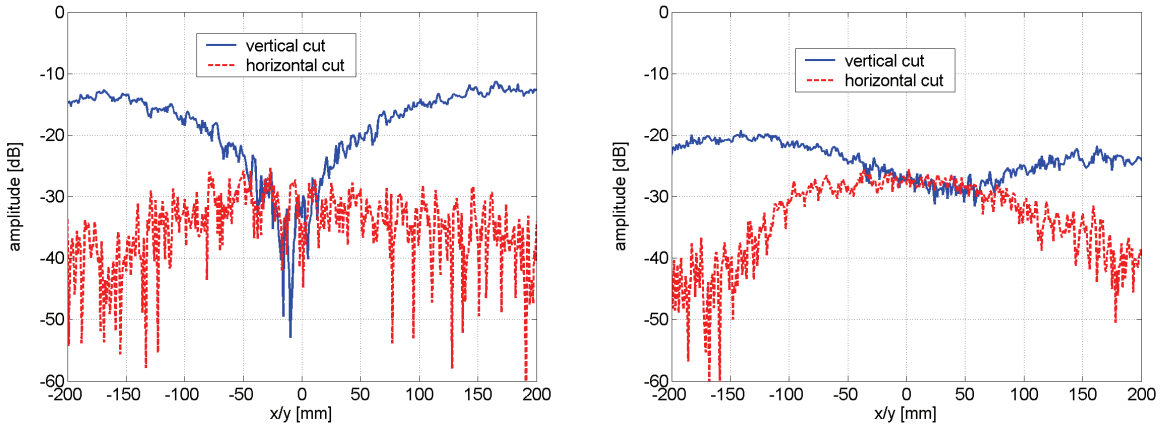

a) *b)*

Figure 6.16 *Measured cross-polarisation level in the cuts of the quiet-zone field at 310 GHz at both linear polarisations for the hologram optimised for the horizontal (HH) polarisation:*
a) for the horizontal polarization (HV),
b) for the vertical polarization (VH).

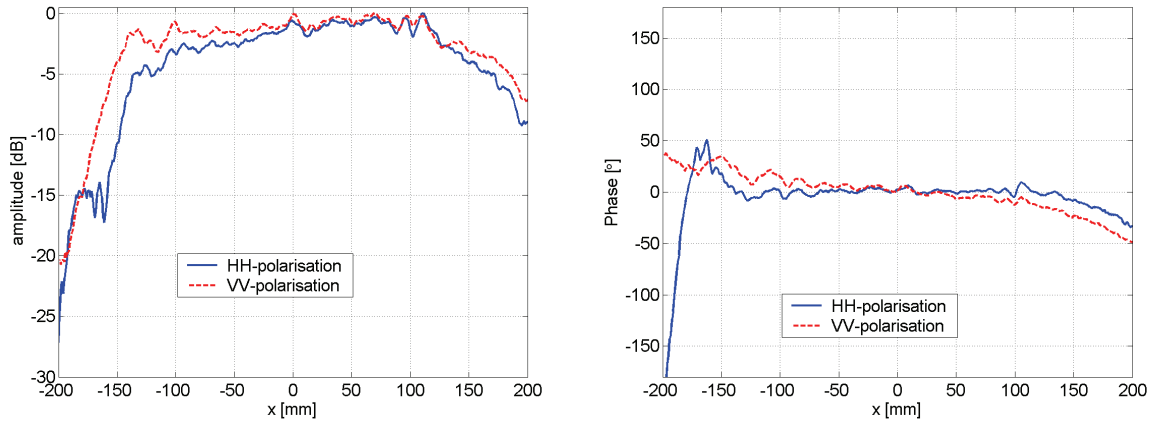

a) *b)*

Figure 6.17 *Measured horizontal cut of the quiet-zone field at 310 GHz at both polarisations for the hologram optimised for both linear polarisations:*
a) amplitude,
b) phase.

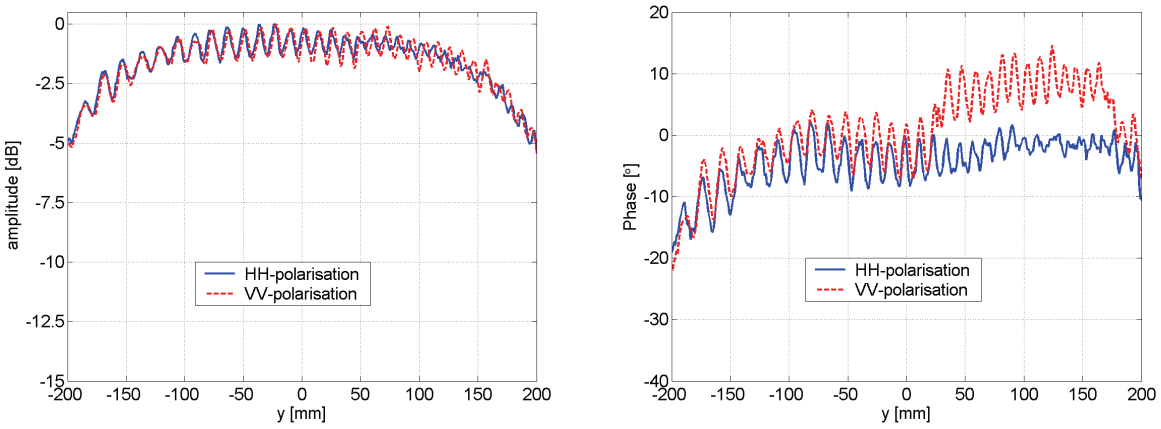

a) *b)*

Figure 6.18 *Measured vertical cut of the quiet-zone field at 310 GHz at both polarisations for the hologram optimised for both linear polarisations:*
a) amplitude,
b) phase.

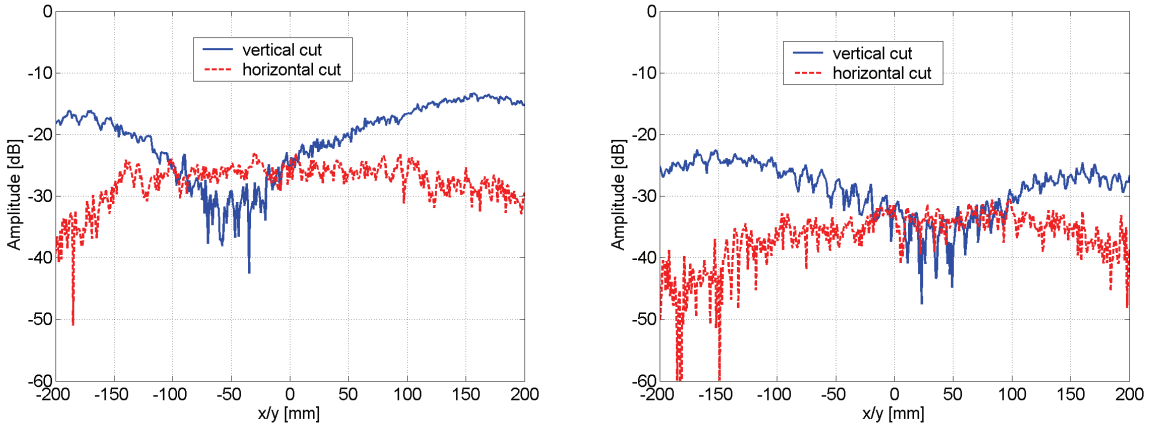

a) *b)*

Figure 6.19 *Measured cross-polarisation level in the cuts of the quiet-zone field at 310 GHz at both polarisations for the hologram optimised for both polarisations:*
a) for the horizontal polarization (HV),
b) for the vertical polarization (VH).

The dual reflector feed system positioning and alignment could have been optimized further to improve the quiet-zone field quality, but the problems with the near-field scanner increased the measurement time and finally the worsening mechanical vibrations in the scanner mechanics prevented the continuation of the measurements. The effect of the mechanical vibrations on the results can be seen in Figure 6.18 as sharp periodic ripple in the quiet-zone field amplitude and phase. Nevertheless, these first measurements results for the hologram operation at both linear polarizations show great promise and the research is being continued.

For both of the test holograms, the measured amplitude in the quiet-zone was about 5 dB higher for the vertical (VV) polarisation than for the horizontal (HH) polarisation. As can be

seen in Figure 6.13, the slot widths in the holograms are mostly of the order of 400–600 μm and the simulated transmission of the field polarised parallel to the vertical slots is also higher than the transmission for the perpendicular polarisation as shown in Figure 6.11. Another important observation is that the phase is tilted at one polarisation compared to the other polarisation, i.e., the direction of the plane wave radiated by the hologram is slightly different at the vertical polarisation than at the horizontal polarisation so that the hologram focus is at different locations at the different polarisations. In order to compensate this, the hologram feed has to be repositioned when the polarisation is changed and the hologram operation is limited to one linear polarisation at the time, i.e., circular polarisation cannot be used as the circular polarisation distorts to elliptical due to different transmission coefficient at the vertical and horizontal polarisations and quiet-zone field would also be distorted due to the different direction of propagation for the linear components of the polarisation.

It can be concluded that the hologram can be designed to operate at both linear polarisation by making the slots in the pattern constant in width so that the amplitude taper in the hologram aperture is solely produced by the shaped hologram illumination with the DRFS and the hologram is only used to change the phase of the transmitted field from the incident spherical wave into the transmitted plane wave propagating to the quiet-zone. It may be also possible that holograms can be designed to operate at the circular polarisation if the transmission can be equalised for both linear polarisations. In principle, the slot width can be selected to be such that the both linear polarisations have the same transmission coefficient as can seen in Figure 6.11. The dual polarisation operation is being investigated further in the hologram research group of the Radio Laboratory.

6.3 Cross-polarisation performance of the hologram CATR

The main disadvantages of the hologram based CATR compared to the reflector based CATR is the limitation of the operation to the linear vertical polarization and the relatively high cross-polarisation level of the order of -15…-20 dB in the quiet-zone compared to the dual reflector based CATRs, which have a cross-polarisation level of approximately -30…-40 dB [47]. On the other hand, the cross-polarisation level in the quiet-zone of the hologram CATR is comparable to the cross-polarisation of a single offset reflector. This level of cross-polarisation does not allow very high polarisation purity in the antenna testing, which can be a problem if an antenna with a low cross-polarisation is tested and the level of this cross-polarisation is to be investigated. The depolarisation of the linearly polarised field by the hologram causes the direction of the polarisation vector to change in the quiet-zone from the desired polarisation. In this section, the possibilities to reduce the cross-polarisation in the quiet-zone of a CATR based on a hologram, i.e., the change in the polarisation state of the field, are investigated.

The slots in the hologram pattern are curved forming arcs of ellipses and the direction of parallel and perpendicular polarisation changes as the slot direction changes causing depolarisation of the field. The cross-polarised field in the hologram illumination is also transmitted into the quiet-zone. In this section, the contributions of the feed cross-polarisation and the cross-polarisation generated by the hologram itself to the total cross-polarisation level in the quiet-zone are also investigated and the possibilities to decrease the cross-polarisation in the quiet-zone field are studied.

6.3.1 Polarisation grid

Polarisation grids can be used to change the polarisation of the incident field as the transmission and the reflection coefficients of a grid consisting of narrow metal strips or wires depends on the direction of the polarisation in relation to the strip or wire direction [112]. The maximum of the transmission occurs when the polarisation is perpendicular to the strips and the minimum of the transmission occur when the polarisation is parallel to the strips, and vice versa for the reflection. This property of the grid allows the polarisation grids to be used for modifying the direction of the polarisation vector, i.e., to polarise the field, by setting the orientation of strips to be perpendicular to the direction of the desired polarisation in the transmitted field. Polarisation sensitive grids can also be utilised for polarisation sensitive reflectors [113].

Polarisation grids can be used to suppress the cross-polarisation as the attenuation for the cross-polarised field component is much higher than the attenuation for the co-polarised field when the grid is oriented perpendicular to the co-polarisation in the case of the transmission and parallel to the co-polarisation in the case of the reflection –type operation. The ability of a polarisation grid to suppress the cross-polarisation is described by the ratio of the cross-polarised amplitude before and after the grid, which is called the cross-polarisation suppression ratio or the extinction factor in optics.

The structure of the polarisation grid is described by the period of the grating *P* and by the spacing of the strips *d* as illustrated in Figure 6.20. The grid may consist of straight strips or the strips can be curved with optimised shaped for improved characteristics [112]. Alternatively, the grid can be made from parallel thin wires tensioned into a frame so that no substrate is needed to support the strips and the wires can be reasonably thin. The polarisation selectivity of a grid is the higher the shorter the period *P* is compared to the wavelength [112]. The strips or the wires should be as narrow or thin as possible.

Figure 6.20 *Polarisation grid consisting of straight metal strips.*

For investigation of the hologram cross-polarisation characteristics, two polarisation grids were designed in the Radio Laboratory: one with *P*=200 μm and d=100 μm, and another with *P*=300 μm and d=150 μm. Both 400-mm diameter grids were manufactured by etching the 100 μm and 150 μm wide straight strips on copper-plated 50 μm thick mylar-film, where the metallisation was 17 μm thick. The material and manufacturer were the same as for the 600-mm test holograms. The second grid was designed and procured as a back-up to the denser one with narrower strips as the narrowest linewidth in the PCB-process used was 100 μm and there might have been more manufacturing errors in the narrower strips.

The operation of these polarisation grids was studied by probing the radiated field of a corrugated horn transmitted through the grids at 310 GHz when incident field polarisation was perpendicular (vertical) and parallel to the grid (horizontal) and by comparing the transmitted fields to the field radiated by the horn without a polarisation grid. The field was probed with the planar near-field scanner over an area of 600 mm × 600 mm at the distance of 1800 mm from the corrugated horn, which covers to the aperture of the 310 GHz test holograms. The measured co-polarised radiation pattern of the corrugated horn is shown in Figures 6.21 and 6.22. The error compensation methods described in Chapter 7 were not used in this measurement to reduce the phase measurement uncertainty as the main interest was in the amplitude measurements. The corrugated horn could not be aligned precisely and hence, also the exact position of the scanning area on the scanner plane was not recorded for the compensation of the planarity errors. The phase measurement uncertainty without the error compensations was estimated to be ±15° in the probing of a spherical wave. The probe was placed on an optical table into an alignment collar (see Chapter 7 for more details) and the table was aligned perpendicular to the scanner plane. Unfortunately, there were no precise mechanical references and the alignment uncertainty corresponds probably up to about ±50 µm uncertainty in the measurement distance in the scan area (up to about ±20° tilt in the phase at 310 GHz). As the probe used was a similar horn to the one under test, the measured phase deviation was divided by two assuming equal contribution by both horns. This also divides the measurement errors by two so the measurement uncertainty is increased as the errors are probably larger than the actual deviation of the phase from a spherical wave in the radiation pattern of the horn. As the contribution of the errors and the actual phase pattern of the horn to the measured phase deviation from the spherical wave is not known, a rough estimate of the measurement uncertainty is ±20°…±40°.

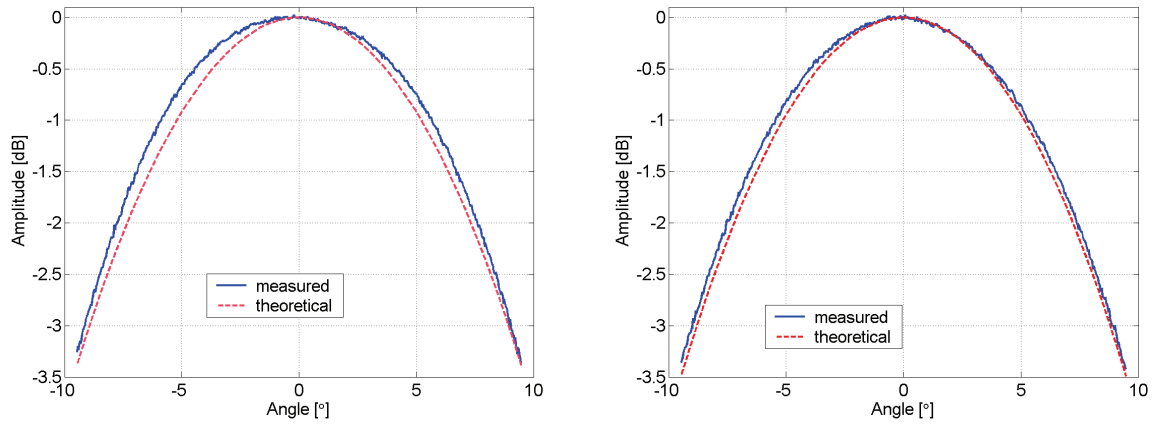

a) *b)*

Figure 6.21 *Measured cuts of the amplitude pattern of the corrugated horn at 310 GHz at the co-polarisation compared to the theoretical pattern of the horn:*
a) horizontal cut,
b) vertical cut.

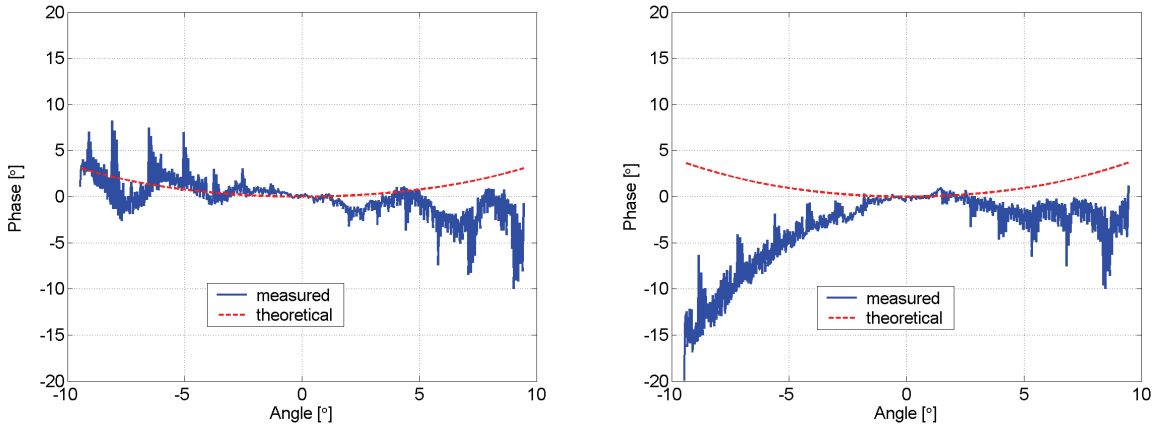

Figure 6.22 *Measured phase deviation from the spherical wave in the antenna pattern of the corrugated horn at 310 GHz at the co-polarisation compared to the theoretical phase pattern of the horn:*
a) horizontal cut,
b) vertical cut.

The measured amplitude of the corrugated horn at 310 GHz corresponds very well to the theoretical pattern as the maximum deviation in the horizontal cut is less than 0.2 dB within ±10°. The measured phase corresponds also very well to the theoretical phase considering the rather large measurement uncertainty. The purpose of these measurements was to provide the reference for the measurements of the transmitted field through the polarisation grids and a higher precision could have been obtained with specialised precision mechanics for the alignment of the horn. Another probe, such as an open-ended waveguide, could have been used in the measurements to investigate the potential difference in the radiation characteristics of the individual horns. In any case, these measurements provide an additional confirmation for using the theoretical horn pattern in the design of the dual reflector feed system.

In order to measure the transmission and the cross-polarisation suppression of the polarisation grids, the grids were placed between the transmitting horn and the near-field scanner on the optical table, where the horn was located, without turning off the transmitter or the receiver. This allowed direct comparison of the measured fields with and without the polarisation grid. Polarisation grids were turned by about 20° to direct the reflected waves away from the transmitter. The measured transmission through the polarisation grids at 310 GHz are presented in Figures 6.23 and 6.24 and the resulting cross-polarisation suppression ratio is shown in Figure 6.25.

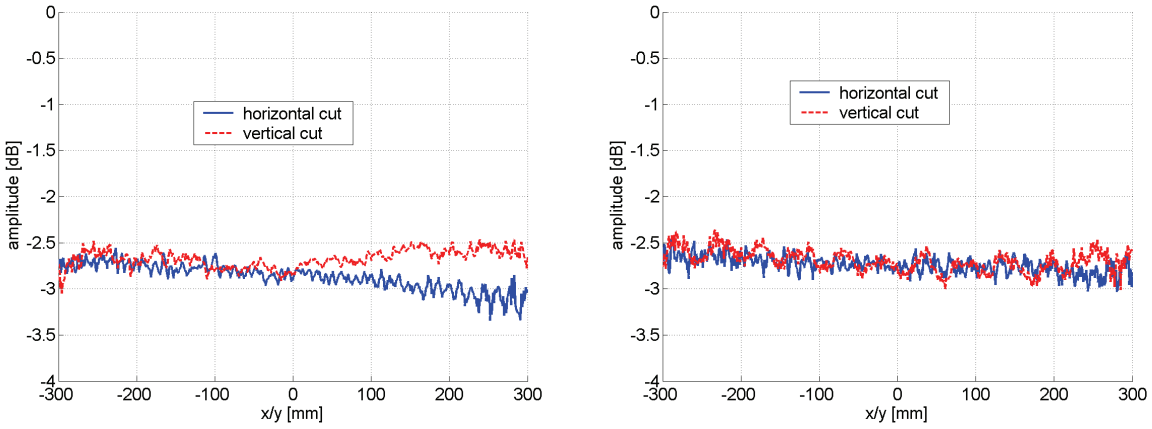

a) *b)*

Figure 6.23 *Measured transmission of the polarisation grids at the polarisation perpendicular to the grating (VV):*
a) 100 μm grid,
b) 150 μm grid.

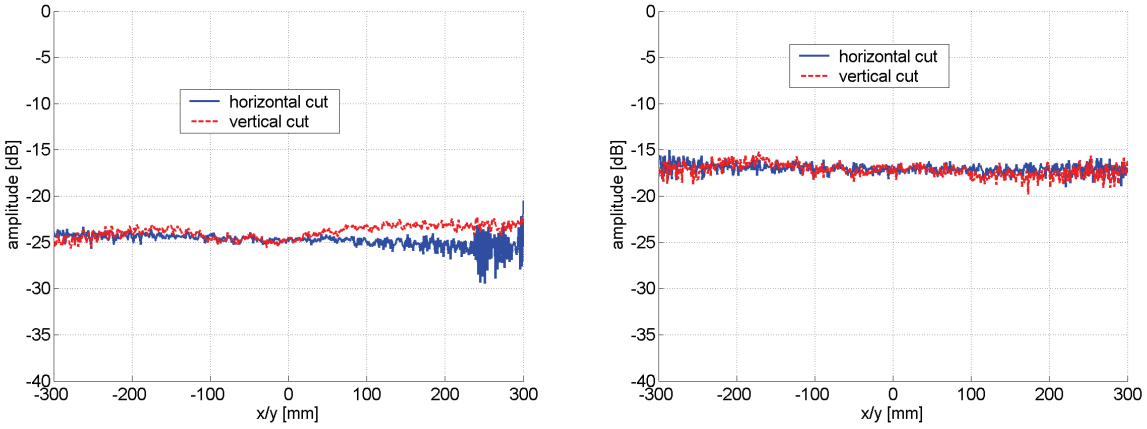

a) *b)*

Figure 6.24 *Measured transmission of the polarisation grids at the polarisation parallel to the grating (HH):*
a) 100 μm grid,
b) 150 μm grid.

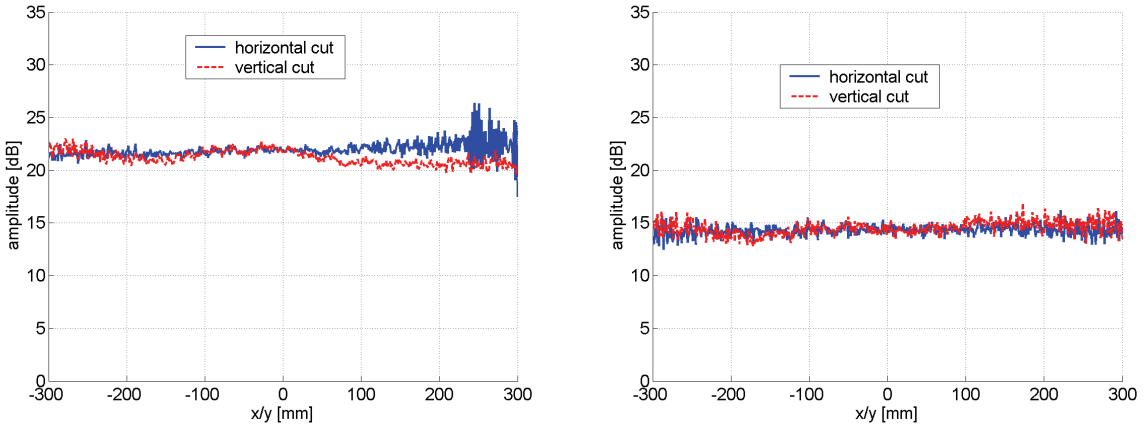

Figure 6.25 *The cross-polarisation suppression ratio of the polarisation grids at 310 GHz:*
a) 100 µm grid,
b) 150 µm grid.

The cross-polarisation suppression computed as the ratio of the measured attenuation of the perpendicular (VV) and the parallel polarisations (HH) is about 21 dB for the grid with 100 µm wide strips and about 14 dB for the grid with the 150 µm wide strips. The theoretical cross-polarisation suppression ratios excluding the effect of the dielectric film [112] are approximately 17 dB and 13 dB, respectively. The losses at the co-polarisation due to the polarisation grid are of the order of 3 dB. As the measured suppression ratio and the attenuation at the co-polarisation are higher than the theoretical values, the dielectric film has a significant effect on the operation of the polarisation grid – the transmission coefficient of the film is also polarisation dependent. The orientation of the grid is also important as the attenuation of the grid depends strongly on the polarisation relative to the grid direction and the results may have been affected by a possible slight tilt in the grid orientation from the horizontal. As the suppression ratio of the grid with 100 µm period is higher, it is used in the investigation of the cause of the hologram cross-polarisation together with test holograms.

6.3.2 Sources of the cross-polarisation

The total cross-polarisation in the quiet-zone of the compact antenna test range based on a hologram is caused by the cross-polarisation of the feed transmitted in the quiet-zone and by the cross-polarisation produced by the hologram itself. The contribution of these components to the total cross-polarised field was investigated by measuring the cross-polarisation level in the quiet-zone of the 600-mm hologram optimised for the horizontal polarisation with and without a polarisation grid in front of the dual reflector feed system illuminating the 600-mm hologram. The polarisation grid used was the one with 100 µm metal strips tested in Section 6.3.1 and the quiet-zone field was probed at the frequency of 310 GHz using the corrugated horn again as the probe. Measurement results for the cross-polarisation level are shown in Figure 6.26. The co-polarised quiet-zone field quality was in practice identical with and without the grid in front of the DRFS.

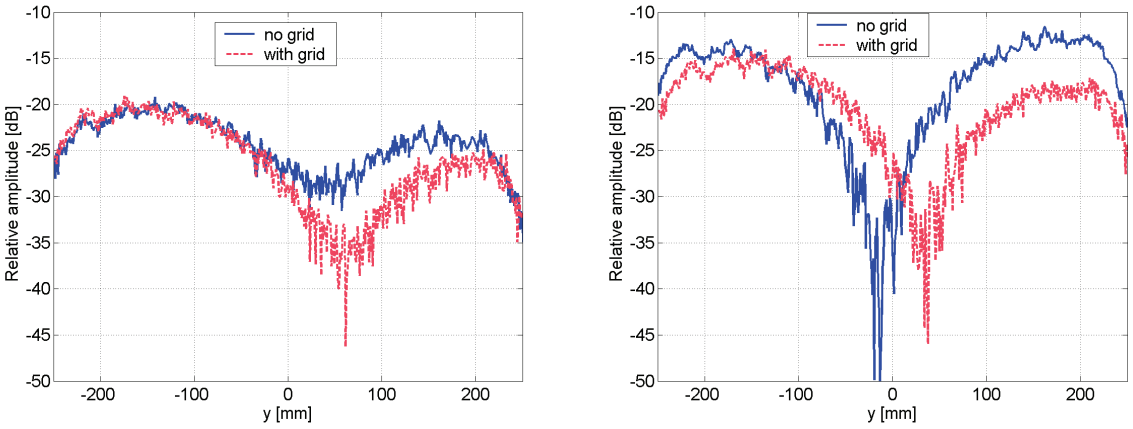

a) *b)*

Figure 6.26 *Measured cross-polarisation level in the vertical cut of the quiet-zone of a 600-mm hologram optimised for the horizontal polarisation at 310 GHz:*
a) vertical polarisation (VH),
b) horizontal polarisation (HV).

As can be seen in Figure 6.26, the reduced cross-polarisation in the hologram illumination by the DRFS with the polarisation grid does not significantly lower the maximum cross-polarisation level in the quiet-zone of the hologram. This indicates that the contribution of the cross-polarisation generated by the hologram itself dominates in the total cross-polarisation level. Therefore, the overall cross-polarisation level can only be reduced if the cross-polarisation by the hologram can be reduced.

Hologram simulations in the Radio Laboratory have shown that the cross-polarisation is caused by the curved slots in the hologram pattern as the local polarisation in relation to the slot direction changes and the transmission of the slots is different for perpendicular and parallel polarisations [111]. Also, the slot width affects the cross-polarisation level: narrow slots cause more cross-polarisation than wide slots. This allows lower cross-polarisation for the hologram illuminated with the dual reflector feed system as for the hologram illuminated directly with the corrugated horn as the slots can be designed to be wider in the DRFS hologram. The slot curvature and the cross-polarisation level can be reduced by increasing the hologram focal length. With the increased hologram focal length and with the shaped illumination with the DRFS, a cross-polarisation level of the order of -25 dB is possible according to the simulations [O52, 111].

6.3.3 Reduction of the cross-polarisation level in the quiet-zone with a polarisation grid

The cross-polarisation level in the quiet-zone of a hologram based compact antenna test range can be reduced by placing a polarisation grid between the hologram and the quiet-zone to suppress the cross-polarised field component. The test set-up is shown in Figure 6.27, and the hologram used was a 300-mm diameter hologram illuminated with the corrugated horn, as the other holograms are too large for the 400-mm diameter polarisation grid.

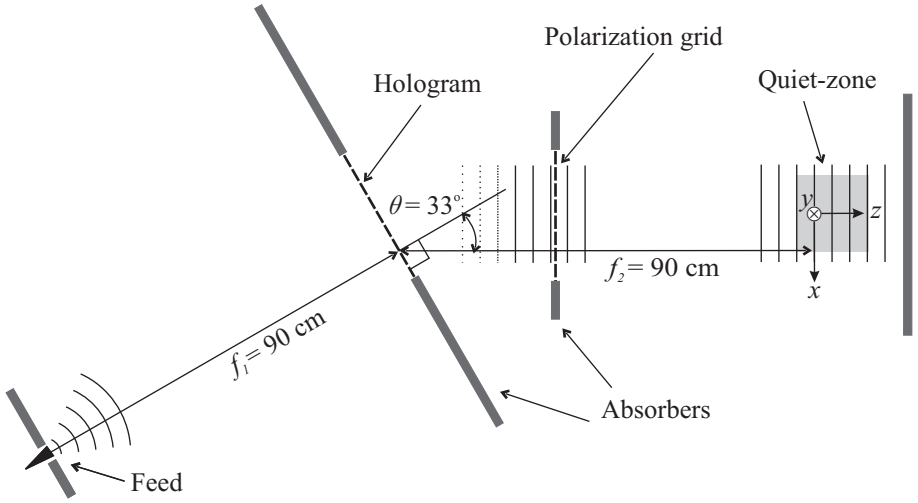

Figure 6.27 *Measurement set-up for investigating the effect of the polarisation grid after the hologram on the cross-polarisation level in the quiet-zone [O50].*

The quiet-zone field was measured using the corrugated horn as the probe at the vertical polarisation again at the frequency of 310 GHz and the results are shown in Figures 6.28 and 6.29. The cross-polarisation measurement results are the average of six consecutive scans as the dynamic range in the measurements was only about 50 dB and the signal-to-noise ratio at the power level of the cross-polarised field was already quite low when the polarisation grid was used.

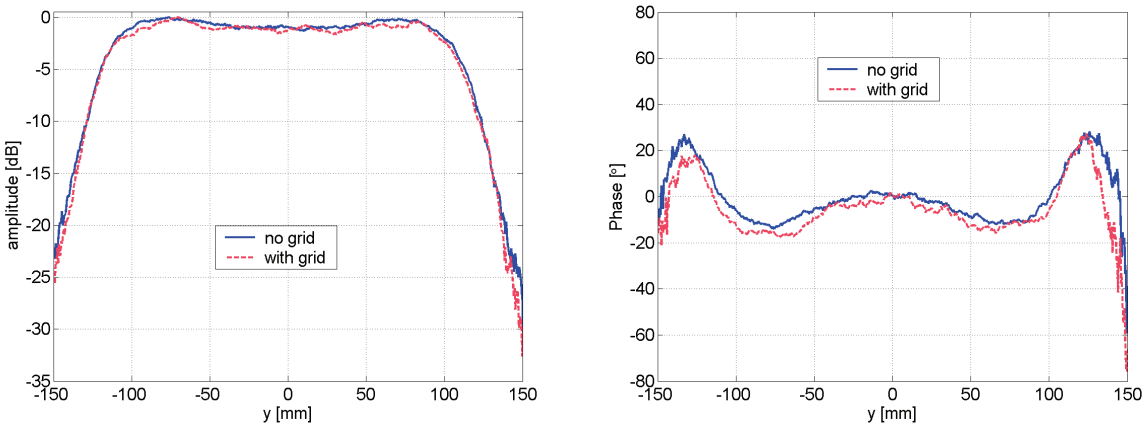

a) *b)*

Figure 6.28 *Measured vertical cuts of the quiet-zone of the 300-mm hologram at the co-polarisation (vertical, VV) at 310 GHz:*
a) amplitude,
b) phase.

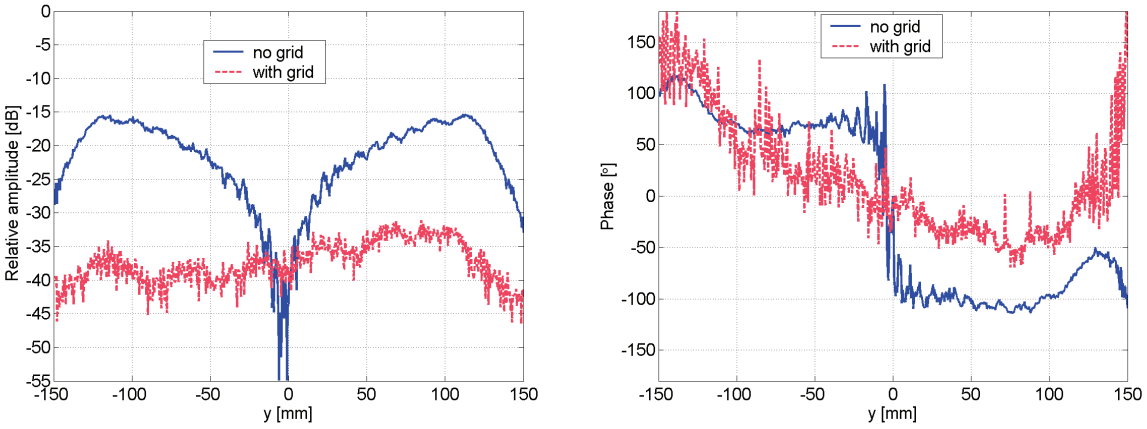

a) *b)*

Figure 6.29 *Measured a) cross-polarisation level (VH) and b) phase of the cross-polarised field (normalised) in the vertical cut of the quiet-zone of the 300-mm hologram at 310 GHz.*

Figure 6.28 shows that the polarisation grid does not distort the quiet-zone field when the grid is placed between the hologram and the quiet-zone and that the maximum cross-polarisation level is suppressed by almost 20 dB to about -40 dB…-33 dB. The slight tilt in the cross-polarisation level observed in Figure 6.29 may be caused by a small tilt in the orientation of the polarisation grid; the strips of the grid may not have been exactly horizontal.

The polarisation grid could be turned to a larger angle to avoid it being parallel to the quiet-zone and the antenna-under-test (AUT) in it in order to avoid potential standing waves between the AUT and the grid. Polarisation grids can be used to compensate the cross-polarisation caused by an offset reflector [112] as the grid can be used to adjust the direction of the polarisation vector. If the field incident on the reflector has the same level of cross-polarisation as the reflector produces but in opposite phase, the cross-polarised fields cancel

each other. Similar approach could be in principle used with holograms with a suitably designed polarisation grid placed between the feed and the hologram. The matter requires further consideration.

The results discussed in this section are promising for reducing the cross-polarisation level in the quiet-zone of a CATR based on a hologram. Using the DRFS to provide shaped illumination, holograms can be designed to produce less cross-polarisation and polarisation grids can be used to suppress the cross-polarisation either for the feed or the hologram if the grid is placed between the feed and hologram or between the hologram and the quiet-zone field, respectively. The use of the polarisation grid in the hologram CATR after the hologram is quite feasible as the hologram itself is a metallisation pattern on a dielectric film and large polarisation grids could be manufactured similarly as the large holograms. The improvement of the cross-polarisation performance of the hologram is being researched further in the Radio Laboratory in the hologram research group.

7 Measurement accuracy in sub-mm wave planar near-field probing

The radiated field of the dual reflector feed system and the quiet-zone fields for the test holograms were probed with a corrugated horn using a planar near-field scanner. This use of the scanner differs from the actual near-field measurements in that sense that the near-field to far-field transformation is not done as only the near-field data is needed for the analysis of the antenna under test operation. The scanner used is intended for microwave frequencies and extending the use of it to sub-millimetre wavelengths is not entirely straightforward. The understanding of the measurement error sources is important for reliable measurement results and even for making the dual reflector feed system testing at 310 GHz possible as the measurement system and procedures required improvements for more accurate results.

In this Chapter, the potential measurement error sources and the improvements done to the near-field measurement system before and after the DRFS testing are discussed. The measurement uncertainty is estimated and the techniques to reduce the uncertainty using error compensation techniques are described. This error analysis helps not only to improve the precision of the measurements but also to priorise the improvements of the measurement equipment and procedures as the most significant improvements are achieved by correcting the errors causing the largest uncertainties in the measurements.

7.1 Measurement error sources in planar near-field measurements

There can be two types of measurement errors in any kind of a measurement: systematic and random. The systematic errors are deterministic by nature and therefore repeatable but the random errors are by nature randomly varying in the measurements. The measurement errors in near-field measurements have been studied extensive in the literature over the past decades and examples of these studies include [114, 115]. In [114], the major components affecting the measurement accuracy are divided into the following categories based on their cause: 1) mechanical positioning and the positioning measurement system, b) facility, c) radio frequency system, d) antenna under test and e) computer and software. The paper describes a near-field measurement facility qualification methodology for proving the quality of the measurements.

In [115], an 18-term list of the error sources for planar near-field measurement is presented together with detailed analysis of the effect of the errors on the measured antenna pattern. These 18 error sources are sometimes called the NIST (National Institute of Standards and Technology, USA) 18-term error model for planar near-field measurements. The error sources are listed in Table 7.1.

Table 7.1 *Error sources in planar near-field measurements according to [115].*

Source of error
1) Probe relative pattern
2) Probe polarisation ratio
3) Probe gain measurement
4) Probe alignment error
5) Normalisation constant
6) Impedance mismatch factor
7) AUT alignment error
8) Data point spacing (aliasing)
9) Measurement area truncation
10) Probe *x,y*-position errors
11) Probe *z*-position errors
12) Multiple reflections (probe / AUT)
13) Receiver amplitude nonlinearity
14) System phase error due to: Receiver phase errors Flexing cables / rotary joints Temperature effects
15) Receiver dynamic range
16) Room scattering
17) Leakage and crosstalk
18) Random errors in amplitude / phase

These measurement error sources shown in Table 7.1 can be grouped into two categories; probe related uncertainties (error sources 1–5) and near-field measurement errors (error sources 5-18). All random errors are collected into the term number 18, i.e., into random errors in amplitude / phase. The other errors are considered systematic.

For improving the measurement system and procedures to allow reliable sub-mm wavelength near-field measurements for testing and analysing the designed dual reflector feed system and the test holograms at 310 GHz, the error sources in the NIST model were considered and the ones relevant for the near-field probing without the near-field to far-field transformation were identified. These error sources are the following:

1. Probe relative pattern
2. Probe polarisation ratio
3. Probe alignment error
4. Impedance mismatch factor (i.e., the losses in waveguides and transitions)
5. AUT alignment error
6. Probe *x,y*-position errors
7. Probe *z*-position errors
8. Multiple reflections between the probe and the AUT
9. System phase error due to receiver phase errors, flexing cables and temperature effects
10. Room scattering
11. RF-instrumentation induced errors
12. Random errors in amplitude/phase, i.e. noise.

The probe gain is not significant as only the relative amplitude patterns are measured so only the relative probe pattern is needed. As no far-field transformation is performed, the measurement errors no. 5, 8 and 9 in the NIST model shown in Table 7.1 are not significant. The sub-mm wave receiver is assumed linear and the dynamic range is considered sufficient for probing the fields. However, the dynamic range has an effect on the random errors as the signal-to-noise ratio decreases. This will be considered later in the following sections. The error analysis in the following sections is based on identification of the error sources as in the NIST error model [115], but the procedure for qualification of a near-field range described in [114] is also utilised. The phase measurement error sources and the relating uncertainty are also discussed in [O17].

7.2 Improvements to the measurement system

Prior to undertaking the testing of the dual reflector feed system the measurement hardware and the facility were improved. First, the probe mountings were replaced and more precise mechanical parts were procured for improved repeatability and accuracy of the probe position and alignment on the scanner. Second, the microwave absorbers used to cover the scanner frame, walls in the room and other parts of the measurement set-up were replaced with unpainted carbon loaded millimetre-wave absorber material to reduce the reflections in the room. Third, the planarity of the scanner motion was measured by a team from South Carelia Polytechnic using a tracking laser interferometer to produce a planarity error map of the scanner surface. Finally, the cable flexing induced phase error measurement and correction system [110] developed earlier in the Radio Laboratory was utilised as a part of the measurement system. The planar near-field scanner was also cleaned and lubricated.

After the dual reflector feed system testing, the gained experience allowed further improvements to the measurement facilities. Additional optical tables were procured and an air-conditioning system for maintaining a constant temperature in the room was installed. Also, the planarity of the scanner was re-measured and compared to the previously measured planarity. These improvements were utilised in the measurements of the test holograms and polarisation grids described in Section 6.3.

7.2.1 Probe mounting

The existing probe mountings were removed and replaced with more precise mechanical parts manufactured under the author's specifications in the workshop of the Metsähovi Radio Observatory before the DRFS testing. The receiver was mounted on a shelf attached to the scanner and this shelf and the other parts were machined with 30 μm tolerances. The shelf was aligned horizontally by attaching it perpendicularly to the vertical rail of the scanner. An alignment collar was placed on top of the shelf for repeatable and accurate probe positioning. In the measurements, the probe horn is inserted into the opening in the collar so that the flange of the horn is pressed against the collar. The opening is then tightened around the horn by pressing the top of the collar down with a screw to immobilise the probe.

A receiver positioner was constructed to allow the probe to be inserted to the opening with the receiver (ESA-2 extension of the AB Millimètre MVNA) attached to the probe via the waveguides and flanges. The positioner and the alignment collar were placed on a z-direction

translation stage allowing fine-tuning of the measurement distance for investigation of potential standing waves between the probe and the antenna under test. The probe and receiver mountings are shown in Figure 7.1.

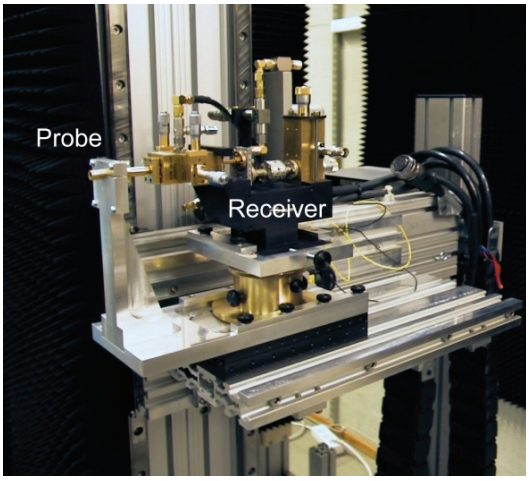

Figure 7.1 *Photograph of the probe and receiver mountings.*

The receiver, the shelf and the alignment collar are covered with absorbers during the measurements. The improved probe mountings allow a higher precision and repeatability in the alignment of the probe in relation the scanner plane and a more repeatable orientation of the probe polarisation, and probably also more accurate orientation of the probe for the vertical polarisation normally used in the measurements. Currently, the vertical rail in the scanner is assumed vertical and the orientation of the probe polarisation is based on the mechanical precision of the supporting components in reference to this rail. For exact orientation of the probe for very accurate polarisation measurements, the *xy*-motion of the scanner should be verified against a precise horizontal reference obtained with a granite reference plate levelled with high precision water scales and by then aligning the polarisation of the probe perpendicular to the horizontal reference plane. Water scales up to the reading precision of the tilt of 10 μm per 1 metre corresponding to the tilt angle of 0.00001° are commonly available and one was procured for the Radio Laboratory. Unfortunately, the precision of it is too high for determining the level of the probe mountings as the readings are off the scale, i.e., the horizontal plane is off by at least 100 μm per metre (0.0001°) and the whole 2 m × 2 m scanner frame cannot be re-levelled more precisely due to the size of the structure and more importantly, due to the lack of high precision mechanical references in the scanner structure.

7.2.2 Replacement of the absorbers

The absorbers covering the scanner and the measurement room were replaced with mm-wave absorber material (Eccosorb VFX-NRL2). In addition, the number of the absorbers used in the room was increased for better mimicking of an anechoic chamber with lower ambient reflection level. On the back wall behind the scanner, absorbers were placed semi-permanently in order to reduce the variation in the absorber placement affecting the scattered field in the room. The old microwave absorbers and the new unpainted mm-wave absorbers attached semipermanently to the scanner frame and the back wall are shown in the photographs in Figure 7.2.

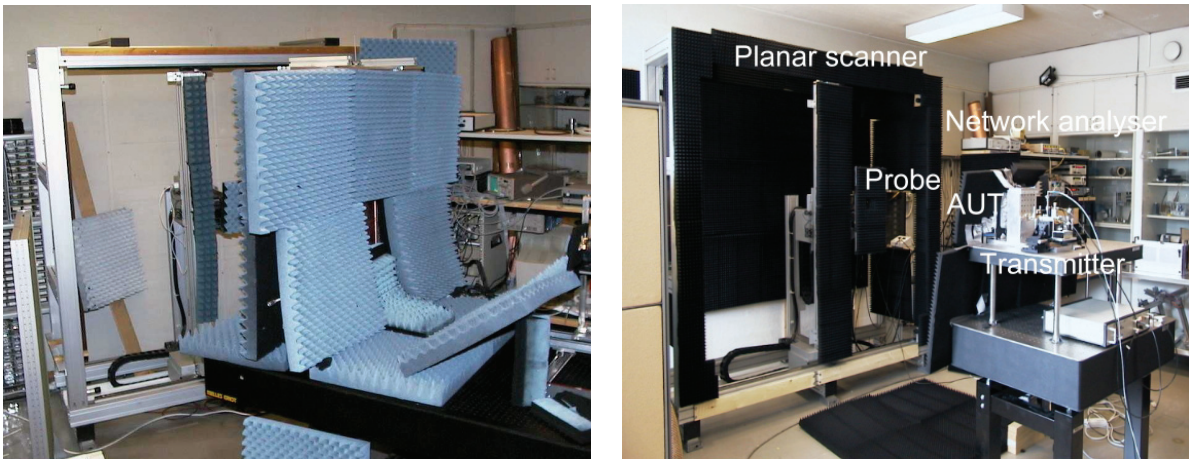

a) *b)*

Figure 7.2 *Photographs showing the microwave absorbers in a) old hologram test-set-up during the first sub-mm measurements and b) the new mm-absorbers during the DRFS testing. Some of the absorbers have been removed from both set-ups for the photos.*

The reflectivity of different types of the absorbers at sub-mm wavelengths have been studied in the Radio Laboratory for selecting suitable materials for the construction of different test measurement set-ups [116, 117]. For of absorbers used in the measurement set-ups (Eccosorb VFX-NRL2), the measured reflectivity for a perpendicular plane wave incidence is below -50 dB at 310 GHz [117]. Therefore, this material is highly suitable for sub-mm wavelengths – although the unpainted surface emits large amounts of carbon particles during handling, which can contaminate electronics and optics.

7.2.3 Measured probe movement in the scanner

The planarity of the probe movement was measured by a team from South Carelia Polytechnic with a tracking laser interferometer, i.e., a laser tracker by Leica. A target was attached to the probe mountings and the whole scanner surface was then scanned with the laser tracker following the target and recording the movement of the probe, which started from the bottom right corner of the 1.5 m × 1.5 m scan area. The scanner was measured in Cartesian coordinates with the positive z-axis pointing towards the scanner when viewed from the front and the positive y-axis pointed upwards. In this coordinate system, the variation of the measured z-coordinate corresponds to the planarity error in the scanner. The scanning was done as follows: first, the probe was moved up in a vertical scan and then the probe was moved sideways and another vertical scan was done this time with movement downwards, i.e., the two dimensional surface was scanned with a zigzag motion with 1 mm sampling spacing for the probe coordinate in the vertical scans. The spacing of the vertical scans was 40 mm. The planarity measurements were carried out twice: once before the DRFS testing and again two years later. The results are shown in Figure 7.3.

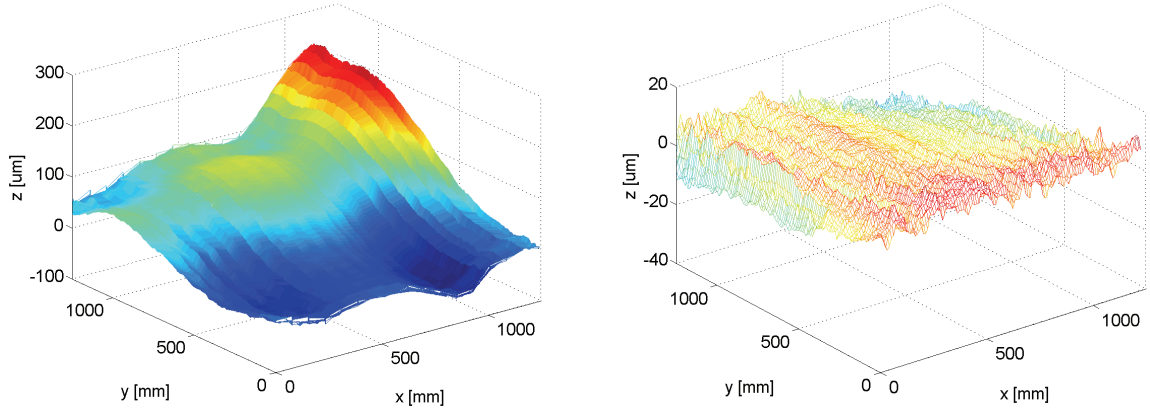

a) *b)*

Figure 7.3 *Measured planarity error of the scanner movement:*
a) before DRFS testing,
b) difference in the second measurement compared to the first measurement.

The measurement uncertainty of a coordinate with the laser tracker is 10µm + 5µm per metre of the measurement distance [118]. As the measurement distance was of the order of 2 metres, the uncertainty in the z-coordinate is ±20 µm. This uncertainty is the 3σ value corresponding to a larger than 99% confidence interval. In practise, the rapid noise like variation in the measured *z*-coordinate was typically approximately ±10 µm. As can be seen in Figure 7.3, the scanner surface is most planar around the central region of the scanning area and therefore this region has been mostly used for the near-field scanning. The two different measurements of the scanner surface gave almost identical planarity data for the scanner as the difference in the measured *z*-coordinates is within 40 µm peak-to-peak.

Later the *xy*-motion of the scanner was also investigated based on the laser tracker data on the *xyz*-probe coordinates during the 2D scan. The nominal precision of the probe position is 100 µm. The deviation of the sampling interval in the measured coordinates from the nominal interval is shown in Figure 7.4 for the *x*- and the *y*-coordinate of the probe position. Unfortunately, the absolute orientation of the scanner could not be verified as the laser tracker was not levelled and there was approximately 0.2° tilt between the horizontal *x*-axis in the tracker coordinates in relation to the horizontal axis of the scanner. The tilt has been computationally removed from the data shown in Figure 7.4.

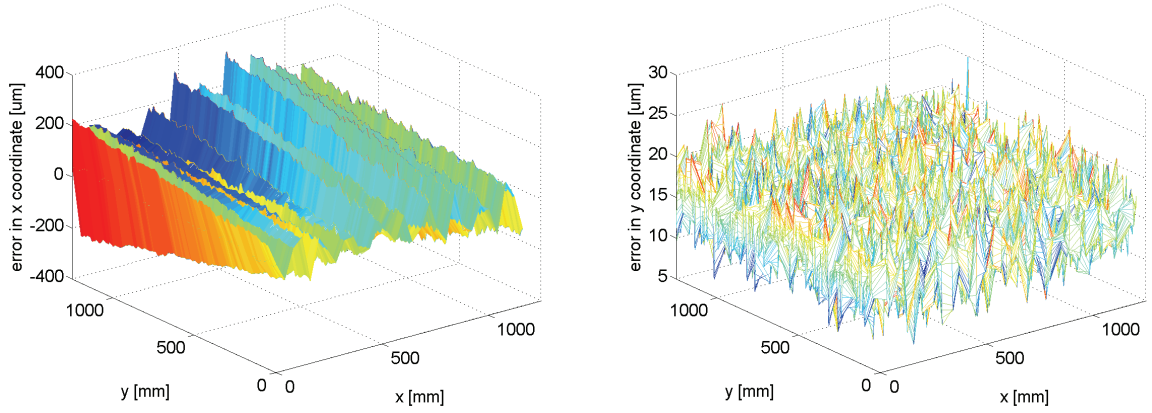

a) *b)*

Figure 7.4 *Measured probe position error in the scanner movement in two-dimensional scan consisting of consecutive vertical scans:*
a) x-coordinate error,
b) y-coordinate error.

Apparently, the position sensor for the vertical rail, on which the probe is mounted, is placed at the bottom of the rail as the *x*-position of the probe is correct within ±100 µm (the nominal position accuracy of the scanner) at the bottom near *y*=0 mm. The variation in the x-coordinate of the probe is cyclic; it is possible that the positioning control ignores errors smaller than 100 µm allowing the errors to built-up and the direction of the error built-up is periodically reversed when the maximum error of ±100 µm is reached. As scanning is done up and down in a zigzag fashion, the probe and the mass associated with it and its mountings moves up and down contributing to the periodical error, which is about three times larger in the upper end of the vertical rail. The non-linearity of the horizontal rails as the vertical rail moves along rails in the bottom and top of scanner may also contribute this larger error in the upper end of the vertical rail. The vertical rail wobbles in the *x*-direction in the two-dimensional scan. In one dimensional scan, as can be seen in Figure 7.4 b), the error in the probe position is very small based on the measured spacing of the points and it cannot be separated from the laser tracker coordinate measurement uncertainty of ±20 µm.

The wobble in the vertical rail during the scan can be a serious problem as the probe positioning error may be up to ±300 µm near the upper end of the vertical rail and also the orientation of the probe is rotated as there is a difference of up to 600 µm between the *x*-coordinates at the lower and upper ends of a vertical scan. This corresponds to a tilt of 0.03° in the probe orientation affecting the polarisation of the probe. In addition, the scan direction varies from the vertical as the rail wobbles during the two-dimensional scan.

In a one-dimensional scan, i.e., when horizontal or vertical field cuts are measured, the probe movement is not exactly linear and the *y*-position of the probe in the horizontal scans varies and correspondingly, the *x*-position varies in the vertical scans. This was investigated by measuring the probe movement during horizontal and vertical scans in the centre region of the scanner. The results for the horizontal and vertical scans are shown in Figure 7.5, where two consecutive scans measurement in 2002 are plotted together with scans done in 2004.

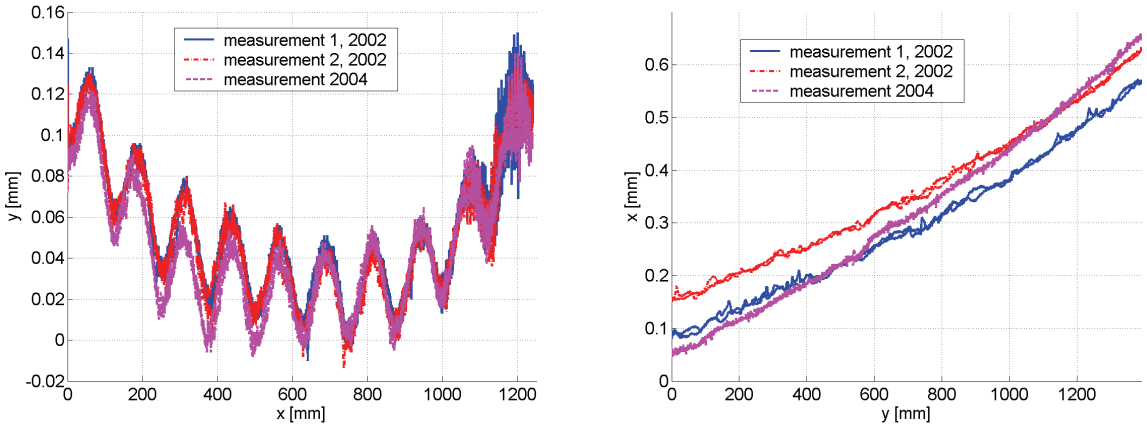

a) *b)*

Figure 7.5 *Measured probe position error in the scanner movement in one dimensional scans:*
a) error in the y-coordinate in horizontal scans,
b) error in the x-coordinate in vertical scans.

In the horizontal scan, there is a highly repeatable curvature in the vertical position of probe and a periodic error of about 60 µm peak-to-peak. The laser tracker measurement of the probe motion in vertical scans show that the *x*-coordinate of the starting points varies within the 100 µm lock window of the scanner and there is approximately 500-600 µm tilt in the direction of the probe motion. This indicates that also the wobble in the scanner movement is quite repeatable and the tilt in the direction of the vertical depends on the position on the scanner as shown in Figure 7.4 a).

7.2.4 Improved ambient temperature stability

The ambient temperature affects the operation of the measurement system and temperature changes cause changes to the operation of the system, which induce measurement errors. The properties of the cables change as the function of the temperature, i.e., their electrical length is affected by the operating temperature, and the electronic devices are also influenced by the temperature. The mechanical structures suffer from thermal expansion – for example, aluminium has a thermal expansion coefficient of about $2.3 \cdot 10^{-5}$ m/°C. As the scanner frame is built from aluminium with largest dimensions of the order of 2 metres, the thermal expansion can cause dimensional changes up to 50 µm per one degree in the temperature. This may affect the planarity of the scanner and the probe movement. The most significant effect of the varying ambient temperature on the measurement electronics is the thermal drift in the system, i.e., the time variance of the results.

In order to minimise the measurement errors caused by the temperature fluctuations, the ambient temperature should be kept as constant as possible. During the dual reflector system testing, the measurements were carried out at the time when the sun was not shining as the measurement room is located in the corner of the building on the top floor. The temperature was also regulated by controlling the ventilation in the room manually to keep the temperature at 22 ± 1°C. The uncontrolled daily temperature variation was up to 3-4°C in late spring when there is a large temperature difference between a sunny afternoon and the night.

After the experiences on the effects of the temperature fluctuations, an air-conditioning system was procured and installed into the room. The system is based on continuous air-flow and control of the output air temperature. In Figure 7.6, the ambient air temperature in the room measured with a high precision thermometer (Vaisala HMI38) is shown. The air-conditioning system was set to maintain different temperatures (by 0.5°C) in these measurements.

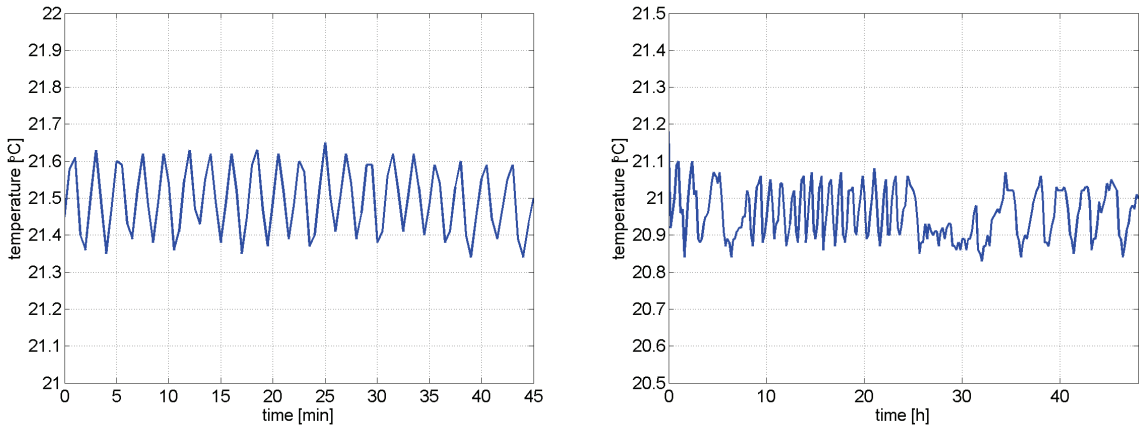

a) *b)*

Figure 7.6 *Measured air temperature in the measurement room:*
a) temperature stability during 45 minutes,
b) temperature stability during 48 hours.

The variation in the ambient temperature was about ±0.15 °C during a period of 45 minutes and about the same during 48 hours. The sampling interval was 30 seconds in the 45 minute measurement and 12 minutes in the 48-hour measurement, which results to under sampling of the temperature variations as seen Figure 7.6 b). No significant long term variations in the temperature can be observed. As the structures in the room have thermal capacity, the temperature of the mechanical structures remains in practise constant. The installation of the air conditioning has mostly eliminated the drift in the system.

7.3 Effect of the measurement errors on the measurement uncertainty

The error sources listed in Section 7.1 have a contribution to the total combined measurement uncertainty. In order to study the effect of the potential measurement errors on the measurement accuracy, two test cases are considered: a spherical wave and a plane wave. The spherical wave is a simplification of the dual reflector feed system beam and the plane wave represents the quiet-zone field of a hologram. The effects on both the amplitude and phase measurement uncertainty are considered in the co- and cross-polarisation measurements and the measurement uncertainty in relative amplitude and phase pattern measurements is estimated both in one-dimensional and two-dimensional scans. For simplicity, the uncertainty analysis is limited to the most significant central region (200 mm × 200 mm) in the scan area, where the co-polarised field amplitude is nearly constant. Outside this region, the exact measured values and the measurement uncertainty are less significant.

7.3.1 Probe pattern

The probe pattern is used for the probe correction in the measurements of a spherical wave, such as the DRFS radiation. The direction of arrival depends on the probe position in the scan area as the spherical wave originates from a single point, the phase centre. The scan area used was at maximum 600 mm × 600 mm and the focal length of the DRFS was 1800 mm, which corresponds to directions of arrival of approximately between ±9.5° in the horizontal and vertical cuts, and ±13.2° in the corners of the full two-dimensional scan. In the 200 mm × 200 mm area the directions of the arrival are ±6.3° and ±8.9°, respectively.

As the corrugated horn used is not an omnidirectional probe, the effect of the varying direction of the arrival for the spherical wave under measurement has to be compensated by removing the effect of the probe directional pattern from the measured data computationally. For this purpose, the theoretical radiation pattern of the probe is used as the uncertainty in the measured pattern shown in Figures 6.21 and 6.22 is too large for realistic determination of the possible error in the probe pattern. In this case, the probe pattern has no contribution to the overall measurement uncertainty. Alternative, a conservative estimate could be done for the uncertainty of the amplitude in the probe pattern by using the deviation between the measured pattern and theoretical pattern as the measure of the uncertainty in the probe pattern. The measured maximum amplitude deviation was about 0.2 dB and this provides the upper bound for the amplitude uncertainty due to the probe pattern as this result includes also the measurement uncertainty.

7.3.2 Probe alignment

During the near-field scanning the probe may point to the wrong direction, which corresponds to the rotation of the horn around the *x*- and *y*-axes. As the precision of the probe mounting mechanics is quite high and the wobbling of the vertical rail during two-dimensional corresponds less than 0.03° in the probe orientation, the corresponding total misalignment of the probe can be assumed only a fraction of a degree. These small potential rotations around the *x*- and *y*-axes do not have a significant effect on the direction of the arrival in the measurements. In addition, the probe pattern is rather wide so the effect of the probe alignment is negligible in the co-polarised amplitude and phase measurements.

7.3.3 Probe polarisation

The probe orientation affects the probe polarisation. This and other probe related issues affecting the cross-polarisation level measurements are considered next.

7.3.3.1 Polarisation properties of the probe

The polarisation of the probe is determined by the co-polarised and cross-polarised component of the probe field. The ratio of the cross-polarised power $P_{probe,x\text{-}pol}$ to the co-polarised power $P_{probe,co\text{-}pol}$ is the polarisation ratio χ of the probe

$$\chi = \frac{P_{probe,x\text{-}pol}}{P_{probe,co\text{-}pol}}. \tag{7.1}$$

The received power in the cross-polarised incident field component is suppressed by this ratio χ in comparison to the power of the co-polarised field component. These polarisations of the incident field are in relation to the probe polarisation. The total measured power P_r is the sum of the powers received at both probe polarisations:

$$P_r = P_{probe,co\text{-}pol} + \chi P_{probe,x\text{-}pol}, \tag{7.2}$$

where $P_{probe,x\text{-}pol}$ and $P_{probe,co\text{-}pol}$, are the incident power at the co-polarisation and cross-polarisation of the probe and χ is the polarisation ratio of the probe. The received power when the probe is oriented along the co-polarisation of the incident field, i.e., when the co-polarisation of the probe and the incident field are parallel, can be written in the case of the linear vertical polarisation as

$$P_{r,co\text{-}pol} = \frac{1}{2\eta}\left(\left(E_{ver}\right)^2 + \chi\left(E_{hor}\right)^2\right), \tag{7.3}$$

where E_{ver} and E_{hor} are the amplitudes of the vertical and horizontal components in the incident field. When the cross-polarised field is measured, the probe is turned by 90° so that the probe co-polarisation is aligned parallel to the cross-polarisation of the incident field and the received power becomes

$$P_{r,x\text{-pol}} = \frac{1}{2\eta}\left(\left(E_{hor}\right)^2 + \chi\left(E_{ver}\right)^2\right). \tag{7.4}$$

In (7.3) and (7.4), the probe is assumed to receive all the incident power. For simplicity, let us consider the case of an incident field with linear vertical co-polarisation and linear horizontal polarisation as the cross-polarisation. The amplitude (and power) of the incident field is constant and normalised to 0 dB. The cross-polarised power is determined in relation to co-polarised power with the cross-polarisation level X

$$\mathrm{X} = \frac{P_{i,x\text{-}pol}}{P_{i,co\text{-}pol}}, \tag{7.5}$$

where $P_{i,x\text{-}pol}$ is the cross-polarised and $P_{i,co\text{-}pol}$ is the co-polarised power in the incident field. This situation corresponds to the quiet-zone of the hologram and the central region of the DRFS beam, where the amplitude is nearly constant. The measured power at the co-polarisation of the incident field can be computed with (7.3) and the measurement error due to the coupling of the cross-polarised power to the co-polarisation can be computed with

$$P_{error,co\text{-}pol} = \chi P_{i,x\text{-}pol}, \tag{7.5}$$

where $P_{i,x\text{-}pol}$ is the cross-polarised incident power. Similarly, the error in the measured power at the cross-polarisation due to the coupling of the co-polarised power to the cross-polarisation is

$$P_{error,x\text{-}pol} = \chi P_{i,co\text{-}pol} \,. \tag{7.6}$$

The error in the measured cross-polarisation level is caused by the error in the co-polarised power and the error in the measurement of the cross-polarised power. The measured cross-polarisation level is the ratio of the measured cross-polarised power $P_{r,x\text{-pol}}$ to the measured co-polarised power $P_{r,co\text{-pol}}$

$$\mathrm{X}_{measured} = \frac{P_{r,x\text{-pol}}}{P_{r,co\text{-pol}}} = \frac{E_{hor}{}^2 + \chi E_{ver}{}^2}{E_{ver}{}^2 + \chi E_{hor}{}^2} = \frac{\mathrm{X}E_{ver}{}^2 + \chi E_{ver}{}^2}{E_{ver}{}^2 + \chi \mathrm{X} E_{ver}{}^2} = \frac{\mathrm{X} + \chi}{1 + \chi \mathrm{X}} \tag{7.7}$$

In Figure 7.7, the computed cross-polarisation in the diagonal pattern cut of the corrugated horn used as the probe is shown together with the cross-polarisation level measurement error computed with (7.7) for different probe cross-polarisation ratios.

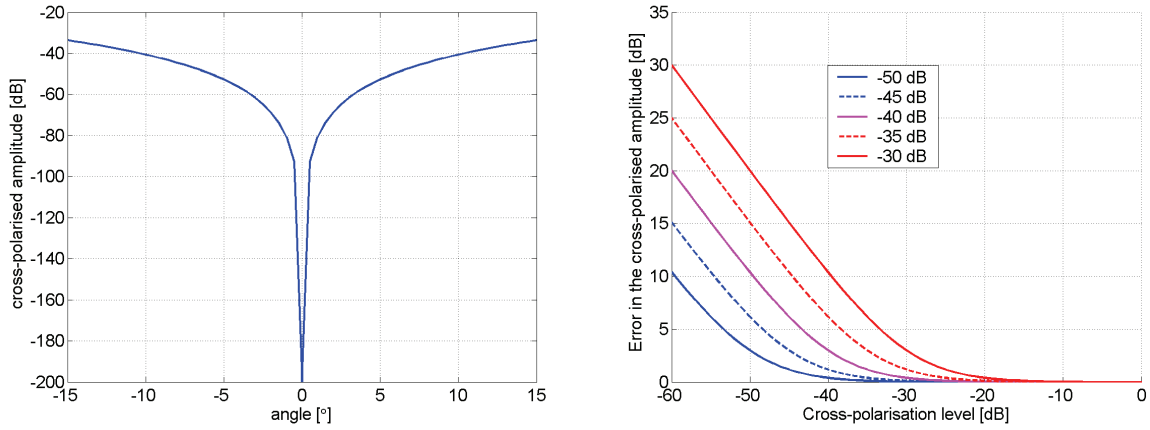

a) *b)*

Figure 7.7 *Computed cross-polarisation:*
a) polarisation ratio of the probe,
b) measurement error due to different probe polarisation ratios.

The theoretical cross-polarisation ratio of the probe is -42.6 dB in the corners of the 200 mm × 200 mm scan area in the two-dimensional scans. In theory, the corrugated horn has no cross-polarisation in the horizontal and vertical pattern cuts and therefore, the probe receives only the co-polarised field in these directions. In practise, the physical structure of the probe introduces some level of cross-polarisation to the actual probe pattern. As an conservative estimated, the polarisation ratio in the diagonal direction is used in all directions of arrival for the corrugated horn probe. This approach results to cross-polarisation ratio of -48.6 dB in horizontal and vertical cuts at the edges of the 200 mm × 200 mm scan area. In determination of the polarisation measurement uncertainties, this maximum cross-polarisation level is assumed for the probe used.

As can be seen in Figure 7.7 b), the measured cross-polarisation level saturates to a value approximately equal to the cross-polarisation suppression ratio (cross-polarisation) of the probe and cross-polarised fields with amplitude below this cannot be measured accurately as the cross-coupling from the co-polarised field dominates in the measured amplitude.

At the co-polarisation, the error in the measurements due to the cross-polarisation of the probe in the quiet-zone of a hologram CATR or inside the most significant central region of the DRFS beam is negligible. In the edges of the scan area, the cross-polarised field amplitude can be higher than the co-polarised field amplitude and this error becomes more significant, but in the central 200 mm × 200 mm region the co-polarised field amplitude is always at least 10 dB larger than the cross-polarisation. In this region, the error in the measured co-polarisation amplitude is less than 0.01 dB.

7.3.3.2 Effect of the probe orientation

The rotation around the *z*-axis, i.e., the probe orientation, affects the cross-polarisation level measurements – the orientation error can be caused by two factors: the probe may be rotated in the probe mountings in relation probe *z*-axis and/or the probe movement track may be tilted in relation to the polarisation of the antenna under test. The orientation of the probe motion can also vary; for example, the wobble or a tilt in the scanner orientation in relation to the antenna under test may affect the direction of the probe movement. In addition, the probe rotation may deviate from 90° when the polarisation of the probe is change using a waveguide twist.

Let us again consider for simplicity the typical case in the measurements described in this thesis, where the co-polarisation is the linear vertical polarisation and the cross-polarisation is the linear horizontal polarisation. When the probe is tilted by angle α in the co-polarised measurements and by γ in the cross-polarised field measurements, these polarisations are no longer vertical and horizontal for the probe polarisation. The situation is illustrated in Figure 7.8. For simplicity, only positive angles are considered as only absolute values are needed for the worst-case analysis.

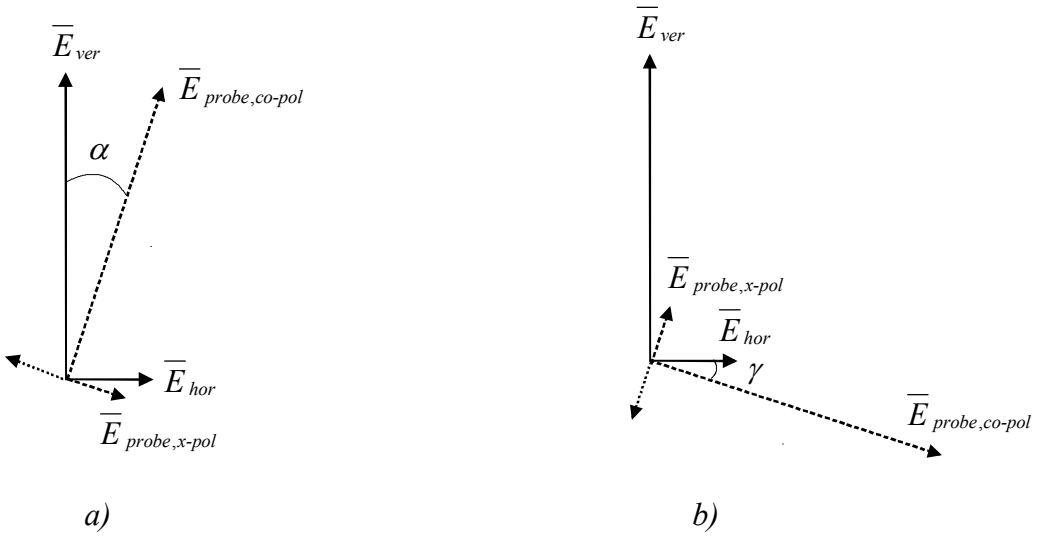

Figure 7.8 *Rotation of the probe polarisation in relation to the polarisation of the incident field:*
a) co-polarisation measurement,
b) cross-polarisation measurement.

The effective cross-polarisation ratio of the probe depends on the orientation of the probe as the coupling from the co-polarisation to the cross-polarisation increases when the tilt angle increases. The total power received is the sum of the powers received at both polarisations as given in (7.2) and the incident amplitude at the co- and cross-polarisation of the probe in the co-polarisation measurement can be written as

$$E_{probe,co\text{-pol}} = \cos\alpha \bullet E_{ver} + \sin\alpha \bullet E_{hor}, \tag{7.8}$$

$$E_{probe,x\text{-pol}} = \sin\alpha \bullet E_{ver} + \cos\alpha \bullet E_{hor}, \tag{7.9}$$

where E_{ver} and E_{hor} are the vertical (co-polarised) and horizontal (cross-polarised) incident field amplitudes. Similarly, when the probe is rotated to measure the cross-polarised field amplitude

$$E'_{probe,co\text{-pol}} = \sin\gamma \bullet E_{ver} + \cos\gamma \bullet E_{hor}, \tag{7.10}$$

$$E'_{probe,x\text{-pol}} = \cos\gamma \bullet E_{ver} + \sin\gamma \bullet E_{hor}. \tag{7.11}$$

The angle γ is defined as

$$\gamma = \alpha + \beta, \tag{7.12}$$

where α is the tilt of the probe and β is the deviation of the probe rotation from 90° when the polarisation is changed. The received power in the co-polarisation measurement for a lossless probe is given by

$$P_{r,co\text{-pol}} = \frac{1}{2\eta}\left(\left(\cos\alpha \bullet E_{ver}\right)^2 + \left(\sin\alpha \bullet E_{hor}\right)^2 + \chi\left(\left(\sin\alpha \bullet E_{ver}\right)^2 + \left(\cos\alpha \bullet E_{hor}\right)^2\right)\right), \tag{7.13}$$

and the received power in the cross-polarisation measurement is

$$P_{r,x\text{-pol}} = \frac{1}{2\eta}\left(\left(\sin\gamma \bullet E_{ver}\right)^2 + \left(\cos\gamma \bullet E_{hor}\right)^2 + \chi\left(\left(\cos\gamma \bullet E_{ver}\right)^2 + \left(\sin\gamma \bullet E_{hor}\right)^2\right)\right). \tag{7.14}$$

The cross-polarisation level is computed with (7.5) from the measured powers at the both polarisations, so the measured cross-polarisation level can be written as

$$\begin{aligned}
\mathrm{X}_{measured} &= \frac{P_{r,x\text{-pol}}}{P_{r,co\text{-pol}}} = \frac{\left(\sin\gamma \bullet E_{ver}\right)^2 + \left(\cos\gamma \bullet E_{hor}\right)^2 + \chi\left(\left(\cos\gamma \bullet E_{ver}\right)^2 + \left(\sin\gamma \bullet E_{hor}\right)^2\right)}{\left(\cos\alpha \bullet E_{ver}\right)^2 + \left(\sin\alpha \bullet E_{hor}\right)^2 + \chi\left(\left(\sin\alpha \bullet E_{ver}\right)^2 + \left(\cos\alpha \bullet E_{hor}\right)^2\right)} \\
&= \frac{\sin^2\gamma {E_{ver}}^2 + \mathrm{X}\cos^2\gamma {E_{ver}}^2 + \chi\cos^2\gamma {E_{ver}}^2 + \chi\mathrm{X}\sin^2\gamma {E_{ver}}^2}{\cos^2\alpha {E_{ver}}^2 + \mathrm{X}\sin^2\alpha {E_{ver}}^2 + \chi\sin^2\alpha {E_{ver}}^2 + \chi\mathrm{X}\cos^2\alpha {E_{ver}}^2} \\
&= \frac{\sin^2\gamma\left(1+\chi\mathrm{X}\right) + \cos^2\gamma\left(\chi+\mathrm{X}\right)}{\sin^2\alpha\left(\chi+\mathrm{X}\right) + \cos^2\alpha\left(1+\chi\mathrm{X}\right)} \\
&= \frac{\chi + \mathrm{X} + \tan^2\gamma\left(1+\chi\mathrm{X}\right)}{1+\chi\mathrm{X} + \tan^2\alpha\left(\chi+\mathrm{X}\right)},
\end{aligned} \tag{7.15}$$

where X is the cross-polarisation level in the incident field and χ is the polarisation ratio of the probe. In the case of β=0°, i.e., γ=α and the probe is rotated exactly 90° when the polarisation is changed, (7.15) becomes

$$\mathrm{X}_{measured} = \frac{\chi + \mathrm{X} + \tan^2\alpha\left(1+\chi\mathrm{X}\right)}{1+\chi\mathrm{X} + \tan^2\alpha\left(\chi+\mathrm{X}\right)}, \tag{7.16}$$

and in the case when α=0° (no probe tilt at the co-polarisation) (7.15) becomes

$$\mathrm{X}_{measured} = \frac{\chi + \mathrm{X} + \tan^2\beta\left(1+\chi\mathrm{X}\right)}{1+\chi\mathrm{X}}. \tag{7.17}$$

In Figure 7.9 a), the effect of an error in the probe orientation, i.e., probe tilt, on the measured cross-polarisation level is shown with different errors in the probe orientation and in Figure 7.9 b) the effect of an error in the 90° rotation of probe when the polarisation is changed is presented. The probe cross-polarisation ratio is -40 dB in the plots.

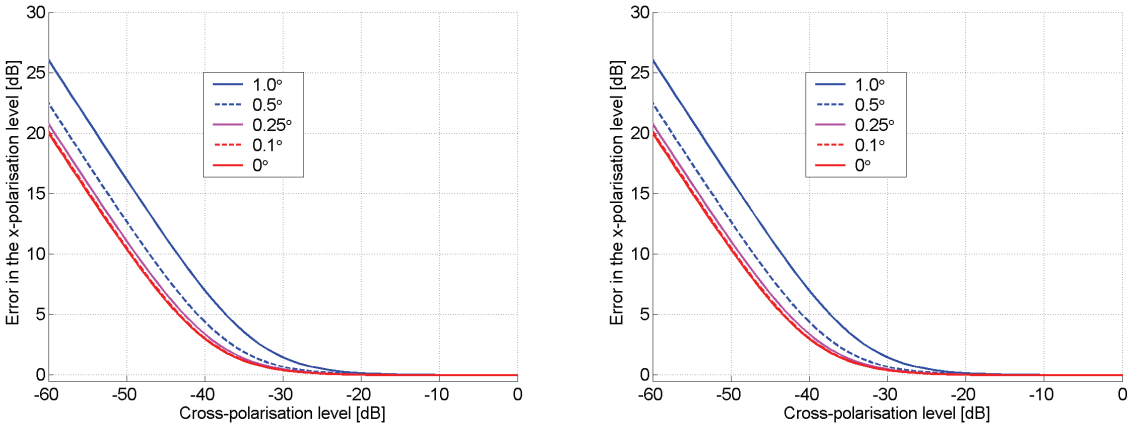

a) *b)*

Figure 7.9 *Effect of the rotation of the probe polarisation in relation to the polarisation of the incident field:*
a) tilted probe orientation,
b) error in the probe rotation in the cross-polarisation measurements.

By comparing Figures 7.9 a) and b), it can be seen that there is no significant difference whether the probe is tilted or the polarisation twist is not exactly 90° – there is a similar error in both cases as (7.16) and (7.17) also indicate for small values of α, β and γ. If the vertical axis of the probe differs from the direction of the vertical polarisation of the incident field by 0.5°, the corresponding tilt is about 8.7 mm per metre, which is unlikely to exists in the system or in the measurement set-up as such a tilt should be clearly visible. In the case of the 0.5° error in the probe rotation when the polarisation is changed, the corresponding distance on the approximately 25 mm circumference of the probe surface is about 35 µm, which is on the other hand quite feasible as the probe and receiver mountings affect the probe orientation also. Therefore, the polarisation twist is a more significant error source in the cross-polarisation level measurements. It should be also noted that (7.15) can be approximated as

$$\mathrm{X}_{measured} = \frac{P_{r,x\text{-pol}}}{P_{r,co\text{-pol}}} \approx \frac{\mathrm{X} + \tan^2\gamma}{1 + \mathrm{X}\tan^2\alpha} \approx \mathrm{X} + \tan^2\gamma\,, \tag{7.18}$$

when $\chi << X$, $X << 0$ dB and the angles α and γ are small, i.e. when the cross-polarisation level of the probe is much lower than the cross-polarisation level under measurement, the cross-polarisation level under measurement is low and the probe orientation error is small.

The error in the co-polarised field measurements due to the orientation error of the probe in the quiet-zone of a hologram CATR or inside the significant central region of the DRFS beam is negligible as the co-polarised field amplitude is always at least 10 dB larger than the cross-polarisation in the most interesting region. The error in the measured co-polarisation amplitude is then much less than 0.01 dB.

7.3.4 Antenna under test alignment and positioning

The planar near-field scanner is used in this thesis to probe the field radiated by the DRFS or the hologram. In the case of the hologram, the hologram is aligned into the angle of 33° in relation to the scanner so that the radiated plane wave is perpendicular to the scanner surface. The alignment is done using a laser distance meter or measuring tape. Both methods have a measurement uncertainty of the order of ±1 mm, which means alignment uncertainty of about ±0.2°. This uncertainty is insignificant, as the feed position and alignment are optimised to produce a plane perpendicular to the scanner surface, i.e., the hologram misalignment is compensated with the feed positioning and alignment. In the case of the DRFS, a digimatic indicator (Mitutoyo IDC-112B) attached to an extension arm was used to measure difference in distance from the probe mount to horizontal and vertical surfaces on the outer surface of the DRFS. The digimatic indicator has a nominal precision of ±2 μm, but the steel feeler pin scrapes the aluminium on the DRFS surface to the dept of about 5–10 μm making the actual uncertainty in the relative distance measurement ±10 μm. The baselines were 320 mm and 160 mm in the horizontal and vertical surfaces. This makes the corresponding alignment uncertainties ±0.008° and ±0.004° as the DRFS was aligned perpendicular to the scanner within the ±10 μm precision in the relative distance measurement. This alignment uncertainty gives the uncertainty for the potential DRFS beam direction measurement. However, as only the relative beam amplitude and phase were measured in relation to the beam centre defined as the closest point on the scanner to the DRFS focus, the DRFS alignment is not very significant in these measurements and the achieved alignment accuracy was excellent.

The measured relative amplitude and phase in the quiet-zone of a hologram are not very sensitive to measurement distance as the propagating field is essentially a plane wave and the ±1 mm uncertainty in the measurement distance is extremely low for these measurements. In the case of the spherical wave originating from the DRFS focus or phase centre, the measurement distance is more significant as the measured phase depends on the relative electrical path length at the measured point in relation to the beam centre. The measurement geometry is illustrated in Figure 7.10.

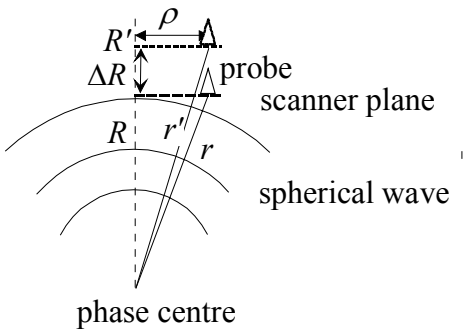

Figure 7.10 *Effect of the incorrect probing distance on a measurement of a spherical wave.*

The distance r from the phase centre is given by

$$r = \sqrt{R^2 + \rho^2} = \sqrt{R^2 + x^2 + y^2}\,, \tag{7.19}$$

where R is the measurement distance defined as the shortest distance from the phase centre to the scanner plane and the radial distance ρ is defined by the xy-position of the probe in relation to the beam centre. The error in the relative electrical path length Δr can be determined with

$$\begin{aligned}\Delta r &= (r'\text{-R}') - (r - \text{R}) = \sqrt{(R+\Delta R)^2 + \rho^2} - (R+\Delta R) - \sqrt{R^2+\rho^2} + \text{R} \\ &= \sqrt{(R+\Delta R)^2 + \rho^2} - \sqrt{R^2+\rho^2} - \Delta R\end{aligned}, \tag{7.20}$$

where $R'=R+\Delta R$, ΔR is the error in the measurement distance and x,y are the probe coordinates. For $x=y$=200 mm, R=1800 mm and ΔR =±1 mm, the resulting relative electrical path length error is about ±12 μm, which corresponds approximately to a phase error of ±4.3° at the frequency of 310 GHz. This error is rather large and the measurement distance is significant when the relative phase of a spherical wave is measured using a planar near-field scanner. The measurement distance and the AUT alignment are much less significant in the amplitude measurements.

7.3.5 Probe positioning

The probe xy-position is especially important when the phase of a spherical wave is being measured as the phase changes quickly over the scanning plane and an incorrect probe position may result into quite large measurement error. In the case of the plane wave, this probe position error is less significant – provided that the sampling spacing is small enough for accurate sampling of the ripple in the quiet-zone. Similarly, the amplitude is nearly constant in the most interesting central region of the DRFS beam and in the quiet-zone of a hologram. The probing geometry is illustrated in Figure 7.11.

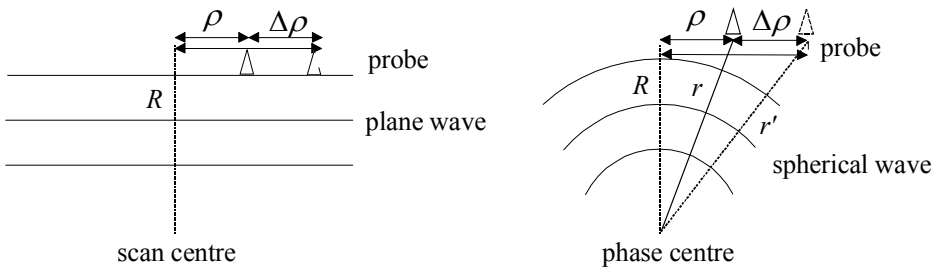

Figure 7.11 *Probing geometry with a planar near-field scanner:*
a) incident plane wave,
b) spherical wave.

The distance r from the phase centre is given by (7.19) and the error in the electrical path length Δr can be then determined with

$$\Delta r = r'\text{-}r = \sqrt{R^2+\rho'^2}\text{-}\sqrt{R^2+\rho^2} = \sqrt{R^2+(x+\Delta x)^2+(y+\Delta y)^2}\text{-}\sqrt{R^2+x^2+y^2}\,, \tag{7.21}$$

where R is the measurement distance, x,y are the probe coordinates, and Δx , Δy are the error in the probe coordinate. When R=1800 mm, $x=y$=200 mm and the worst-case error is

$\Delta x = \Delta y = \pm 100$ μm, the electrical path length error Δr is ±22 μm, which corresponds to approximately ±8° at 310 GHz. The probe *xy*-position error is caused by the 100-μm lock-window in the scanner probe positioning system and by the non-ideal probe motion discussed in Section 7.2.3.

In addition to the probe positioning errors, the probe movement during the sampling causes a slight positioning error. Typical integration time for one sample is 0.01 s and the minimum probe speed in horizontal and vertical scans was 2 mm /s, which means that the probe moves during the integration time 20 μm. The effective probe position is then offsetted by 10 μm. Two-dimensional scans for measuring contour maps of the incident field are measured with higher speeds to reduce the otherwise very long measurement time. The speed used was 10 mm /s, which results into 100 μm during the sample integration and into 50 μm offset in the effective probe position in the direction of the probe movement. The offset in the probe position can be compensated by adding these offsets to the probe position.

7.3.6 Scanner planarity

The scanner non-planarity causes variation of the probe *z*-coordinate, which affects the measurement distance. The error does not affect the measured amplitude significantly. However, it has a significant effect on the measured phase as the resulting phase error $\Delta\Psi$ is

$$\Delta\Psi = -\frac{\Delta z}{\lambda} \bullet 360°, \tag{7.22}$$

where Δz is the deviation of the probe position from the scanning plane and λ is the wavelength. This equation is valid only for incident plane wave, but as the resulting difference in the path length error due to an incidence angle of below ±10° is less than 2 %, (7.22) can be used for correcting the scanner planarity errors in the phase measurements also for the spherical wave. In Figure 7.12, the planarity of the probe motion in the 300 mm × 300 mm scan area is shown when the linear slope has been removed together with the resulting phase measurement error. The AUT is aligned perpendicular to scanner surface and the linear slope is then compensated in the actual measurements also.

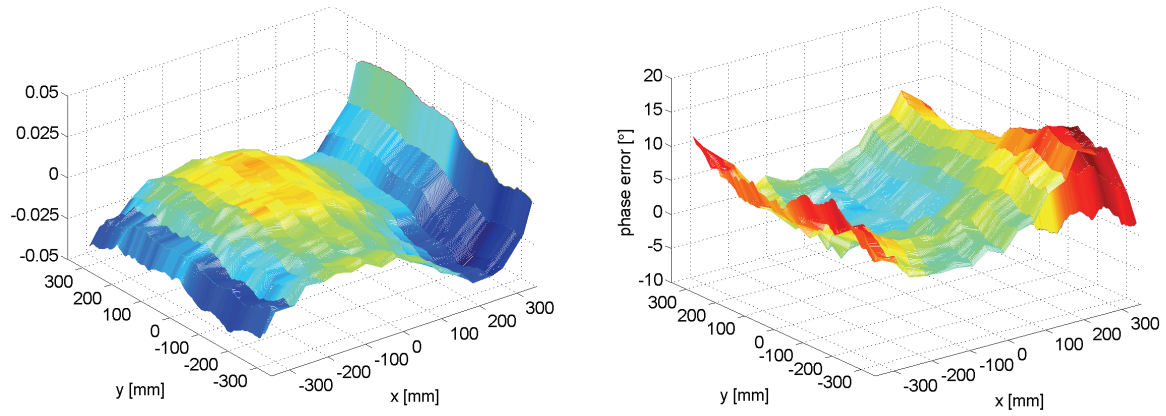

a) *b)*

Figure 7.12 *Measured planarity of the near-field scanner:*
a) scanning surface in the area used for the measurements,
b) corresponding phase measurement error.

The maximum planarity error in the area used for the measurements is 70 µm peak-to-peak, which corresponds to a maximum phase error of 26° peak-to-peak at the frequency of 310 GHz.

7.3.7 Sub-mm wavelength instrumentation

The sub-mm wavelength instrumentation consists of the electrical equipment needed for the amplitude and phase measurements: the transmitter, the receiver, the connecting cables, waveguides, the network analyser and the control computer. The network analyser is MVNA-8-350 by AB Millimètre and it is equipped with sub-mm wave extensions ESA-1 and ESA-2, which are used as the transmitter and the receiver in the near-field measurements. The ESA-1 is a Gunn-diode based frequency multiplier followed by the necessary filters and other components and ESA-2, the receiver, is a Gunn-diode pumped harmonic Schottky-diode mixer with the associated components. The output or input waveguide, where the corrugated horn is attached, is WR-3 waveguide with a standard UG-387/U-M flange. The transmitter and receiver are phase-locked to a common reference in the MVNA, which enables the measurements of both amplitude and phase. A waveguide twist is used to change the orientation of the horn for the horizontal polarization.

In this section, the measurement error sources related to the sub-mm wave instrumentation and their contribution to the measurement uncertainty are considered. The system has an overall measurement uncertainty dependent on the signal-to-noise ratio (S/N) in the measurements. Other error sources include the cables as ESA-2 receiver uses remote mixing and the flexing of the local oscillator cable of the phase-locking circuit of the Gunn-diode source affects the measurement results. In addition, the waveguide connections affect the repeatability of the measurements.

7.3.7.1 Effect of the noise on the precision of the vector network analyser

As the measurement system is based on the vector network analyser with the sub-mm wavelength extensions, the precision of this system is the basis of the precision of the whole system. According the MVNA 8-350 specifications [119], the precision of the network analyser is better than 0.1 dB in amplitude and 1° in phase when the signal-to-noise ratio is larger than 40 dB, and when S/N > 15 dB, better than 2 dB and 10°. When S/N=20–30 dB, the uncertainties are 1.5–4° in phase and 0.35–1 dB. The typical dynamic range in the measurements is about 50–60 dB, which means S/N > 30 dB in the co-polarisation measurements and in the cross-polarisation measurement for cross-polarisation levels higher than -20 dB. The S/N for the -30 dB cross-polarisation level is close to 30 dB in most cases and always larger than 20 dB. Therefore, the uncertainty in the cross-polarisation level measurements is approximately ±0.4 dB. The uncertainty is also affected by the integration time, which affects the S/N, but these values based on MVNA specifications are assumed sufficiently accurate.

7.3.7.2 Cable flexing induced phase measurement errors

The movement of the receiver on the scanner together with the probe bends the local oscillator signal (17.2 GHz) cable of the phase locking system for the Gunn diode providing the LO for the Schottky-diode mixer in the ESA-2. This changes the electrical length of the cable. In the Radio Laboratory, a 14.5 GHz pilot signal based measurement system for measuring the effective electrical length of the cable and for correcting the resulting phase measurement system have been developed [110]. In Figure 7.13 a), the measured phase error due to the cable bending during horizontal and vertical scans is presented and in Figure 7.15 b) the error in the correction is shown. This error was measured by Dr. Jussi Säily by flexing the cable using the near-field scanner while the transmitter and the receiver wave kept stationary so that the measured phase variation is caused by the cable bending [120].

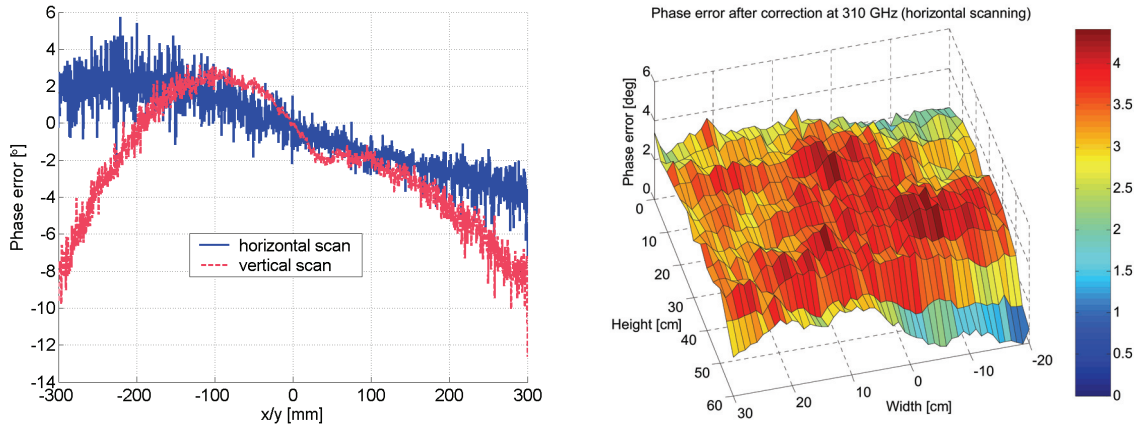

a) *b)*

Figure 7.13 *Cable flexing induced phase measurement errors:*
a) measured phase error due to the cable bending at 310 GHz [O17],
b) accuracy of the cable flexing correction system [120].

The cable bending causes phase measurement errors approximately up to ±4° in the 200 mm × 200 mm scan area and the uncertainty in the measured phase at the frequency of 310 GHz after the cable flexing correction is about ±2°. The phase error becomes more significant when larger areas are scanned as the cable bending becomes more severe.

7.3.7.3 Repeatability of the waveguide connections

The repeatability of the measurements is especially significant in the cross-polarisation level measurements as the measured amplitude at the cross-polarisation is compared to the amplitude at the co-polarisation. In co-polarisation measurements, the potential variation in the measured amplitude is not significant as usually only relative values are needed and the amplitude is normalised in the scans. The receiver (or the transmitter also) is switched off when the polarisation is changed using a waveguide twist. In order to investigate the repeatability of the measurements, the polarisation was switched back to the co-polarisation by removing the waveguide twist after cross-polarisation measurements and the results were compared to the co-polarisation measurements done before changing the polarisation. The phase was not compared, as the phase lock is lost when the receiver is switched off. The attenuation of the waveguide twists and flanges was not investigated as the losses are quite low and difficult to measure precisely. The maximum difference in the measured amplitude was about 0.4 dB in four separate tests. Therefore, the uncertainty in the measured power level is about ±0.4 dB due to the variation in the receiver operation point and the waveguide connections.

7.3.8 Measurement environment

The measurement environment affects the measurement results in many ways: scattering from the room causes measurement errors, vibrations in the building affect especially the measured phase and the changes in the ambient temperature affect the operation of the measurement electronics and causes distortions to the shape of the mechanical structures caused by the thermal expansion. The effect of the ambient temperature changes on the measurement accuracy is considered next as this the most significant of these error and it is most easily investigated.

7.3.8.1 Ambient temperature

Before installation of the air-conditioning, the daily variation in the room temperature was up to 3–4°C in late March in Finland, when there can be close to +10°C and sunshine in the afternoon and -10°C before the sunrise at night. The measured relative phase in the horizontal cut of the quiet-zone of a hologram at 310 GHz at different temperatures during the same day is shown in Figure 7.14. In this measurement, the feed position was not optimised for best quiet-zone field quality nor was the measured planarity of the scanner surface taken into account. The phase was normalised to 0° at the centre of the scan in order to study only the changes in the shape of the phase front as the function of the ambient temperature.

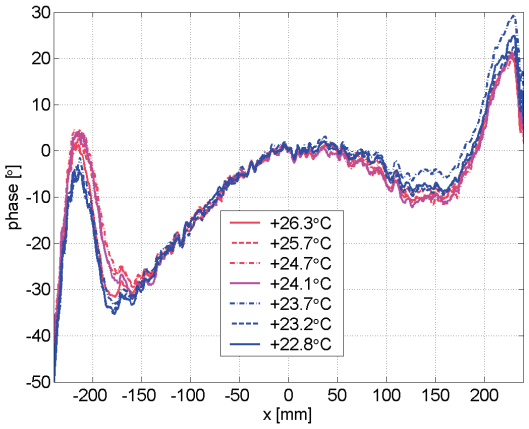

Figure 7.14 *Measured quiet-zone phase at 310 GHz at different ambient temperatures.*

The maximum variation inside the ±200 mm central region of the scan corresponding to the quiet-zone of the hologram is close to 10° peak-to-peak, which is about 30 µm in the electrical path length at 310 GHz. This measured difference in the phase front shape includes naturally the phase measurement uncertainty but nevertheless, as the set-up was not changed in any way between the measurements, it can be concluded that the ambient temperature has an effect on the measured phase pattern probably due to the thermal distortions in the scanner structure as discussed in Section 7.2.4.

The ambient temperature variation has also a significant effect on the drift in the measurement system. Figure 7.15 a) shows the change in the measured phase at 310 GHz in two measurements of the quiet-zone phase done with a two-hour interval between them and Figure 7.15 b) shows the effect of the phase drift on the measured phase in an approximately two-

hour long two-dimensional scan. The horizontal cut in the two-dimensional scan is compared to a separately measured horizontal scan as the two-dimensional scan consists of consecutive vertical scans.

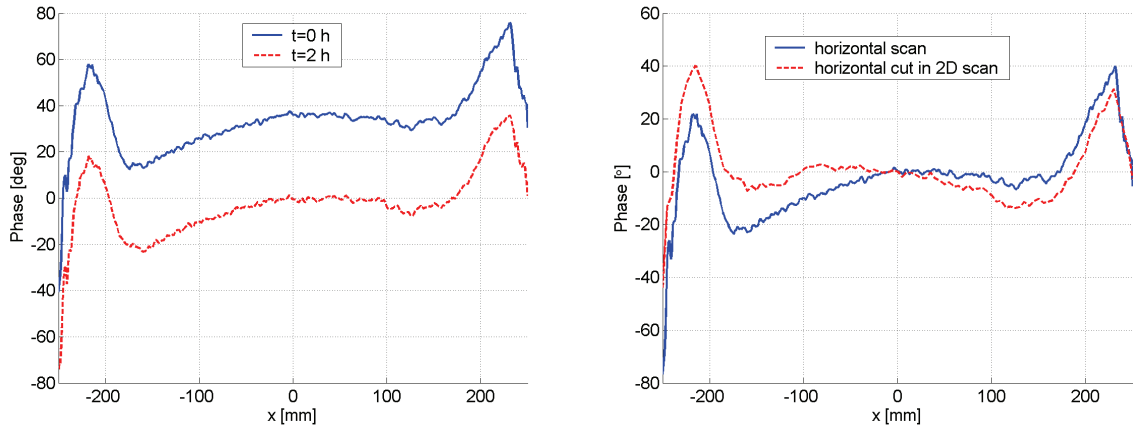

a) *b)*

Figure 7.15 *Measured phase drift in the measurement system:*
a) measured phase drift in two hours at 310 GHz,
b) effect of the phase drift in a two-dimensional scan taking about two hours.

The phase drift during two hours was about -35° and this drift tilts the measured phase front in the two-dimensional scan. The corresponding amplitude drift was about -0.5 dB. This drift during a typical two-dimensional near-field scan results into phase uncertainty of about ±12° within a 200 mm × 200 mm scan area (approximately ±0.35 dB in amplitude) due to the potential phase tilt caused by the drift during the scan of the 200 mm × 200 mm area. Note that the measurement result in Figure 7.16 b) is a separate measurement from 7.16 a) and as the drift is not linear, the actual phase error may vary. In one-dimensional cuts, the drift is negligible as the scan takes at maximum a couple of minutes.

It was later discovered that main contribution to the drift in the measurement electronics comes from the cable flexing phase correction system and a temperature-stabilised version of the system is being developed in the Radio Laboratory. The installation of the precision air-conditioning system in the measurement room has in practise eliminated the drift in the measurement instrumentation.

7.4 Methods for reducing the measurement uncertainty further in planar near-field probing

According to [114] error compensation techniques can be classified into hardware, software and procedural methods. In the near-field probing used in this thesis, the cable flexing induced phase error correction system developed in the Radio Laboratory is essentially a hardware-based method although the measured phase error is computationally corrected in the data. The error measurement is carried out at the same time as the actual measurements. Software compensation is based on previously measured repeatable errors that are computationally corrected in the measurement data and procedural compensation is based on averaging or on measuring additional data for error compensation. The scanner planarity correction based on the laser tracker measurements is an example of a software compensation method, and procedural compensation methods include averaging of the data to reduce random errors and tie-scans for drift compensation.

In this Section, the procedural error compensation methods for reducing random probe positioning errors and for drift compensation in two-dimensional scans are discussed. The cable flexing induced phase error correction system was discussed in Section 7.3.7.2 and the scanner planarity in Section 7.3.6.

7.4.1 Averaging of measurements for reducing random probe position errors

The probe *xy*-position is affected by two factors: the *xy*-position lock window of 100 μm and by the errors in the probe movement over the scanner surface, which causes an approximately random and a systematic error into the probe position, respectively. Random errors can be reduced by averaging several measurements, or scans, so that the final measurement result is the average of all scans. The probe *x*- and *y*-position can be written as the sum of the nominal probe position (x_0, y_0), the systematic $(\Delta x_{systematic}, \Delta y_{systematic})$ and random position errors $(\Delta x_{random}, \Delta y_{random})$

$$x(i) = x_0 + \Delta x_{systematic} + \Delta x_{random}(i), \tag{7.22}$$

$$y(i) = y_0 + \Delta y_{systematic} + \Delta y_{random}(i), \tag{7.23}$$

where index *i* refers to the measurement in the question. The effective probe position is obtained by averaging the *x*- and *y*-position in the individual scans

$$x_{effective} = \frac{1}{n}\sum_{i=1}^{n} x_i = \frac{1}{n}\sum_{i=1}^{n}\left(x_0 + \Delta x_{systematic} + \Delta x_{random}(i)\right) = x_0 + \Delta x_{systematic} + \frac{1}{n}\sum_{i=1}^{n}\Delta x_{random}(i), \tag{7.24}$$

$$y_{effective} = y_0 + \Delta y_{systematic} + \frac{1}{n}\sum_{i=1}^{n}\Delta y_{random}(i), \tag{7.25}$$

where *n* is the number of scans. It can be assumed that the nominal probe position and the systematic error are the same in all of the scans and that when $n \to \infty$, the mean of the random error approaches zero. The random error in the scans forms a sample of the random

error caused by the scanner lock-window. The standard deviation of the sample mean is referred as the standard error of the mean [121], i.e., the standard deviation of the mean of the random error component in the probe positions in the scans to be averaged corresponds to the standard error in the estimation of the mean of the random component of the probe position error. The mean of the random component is assumed zero. The standard error of the sample mean σ is given by [121]

$$\sigma = \frac{\sigma'}{\sqrt{n}}, \tag{7.26}$$

where σ' is standard deviation of the random probe position due to the scanner lock-window and n is the number of scans. Assuming the scanner lock-window w to correspond to 3 σ', the uncertainty in the probe position corresponding to 3 σ caused by the random probe position errors can be written as

$$u_{x,random} = u_{y,random} = \frac{3\sigma'}{\sqrt{n}} = \frac{w}{\sqrt{n}}. \tag{7.27}$$

Standard distribution of the probe position error is assumed. Using (7.27) with w=100 μm and n=10, the uncertainty in the probe position due to the random probe position errors is 32 μm, i.e. this uncertainty component is reduced by a factor of 3.16 by averaging of 10 consecutive scans. The averaging of the scans reduces also other random errors, such as the noise in the system, but this is a less significant benefit as typically the signal-to-noise –ratio is rather higher even without the averaging.

The systematic error in the probe position is caused by non-ideal movement of the probe in the scanner, which was discussed in Section 7.2.3. The periodic probe y-coordinate error in a typical x-direction scan is shown in Figure 7.5 a) and the resulting uncertainty due to the systematic y-position error in an x-direction scan is about ±30 μm in the ±200 mm central scan area. In the x-position error, there is only a random error as only the starting point of the scan varies within the lock-window and the error in the sample spacing is negligible as shown in Figure 7.4 b) for the y-direction scans but the result is also valid for the x-direction scans. Similarly, a y-direction scan has the same random error causing the y-coordinate uncertainty and a systematic x-position error due to the wobbling of the scanner vertical rail as shown in Figures 7.4 and 7.5. There is a slope of about 200 μm in the x-coordinate in the ±200 mm central scan area and as the direction of the slope is not known in an individual vertical scan; the direction can be assumed random with the resulting x-coordinate uncertainty of approximately ±100 μm. A two-dimensional scan consists of consecutive y-direction scans with step-by-step increasing x-coordinate. The y-coordinate of each sampling point has a random y-coordinate error with the uncertainty of ±100 μm due to the scanner lock-window and a systematic x-coordinate error as in a y-direction scan with the resulting x-position uncertainty of ±100 μm in the central scan area.

7.4.2 Drift compensation

As can be seen in Figure 7.16, the phase drift in the measurement system may have a very significant effect on the measurement results in time-consuming two-dimensional scans. The drift can be compensated by measuring the drift using for example so-called tie-scans or by measuring a reference point two or several times at different times during the measurement and comparing the results for determining the amount of drift in the system. An example of this approach is described in [122].

In the two-dimensional scans of the DRFS beam and quiet-zones of the test holograms at 310 GHz, the tie-scan approach is used to compensate the effect of the drift in the system. The two-dimensional scans consist of consecutive vertical scans and the horizontal cut of the scanned field is compared to a separately measured horizontal scan with same sampling points. In principle, the difference between the measured values in these two measurements is caused by the drift as the measurement set-up and the AUT operates otherwise exactly the same way in both measurements. For each vertical scan in the two-dimensional scan, a correction term is determined from the measured error compared to the separately measured horizontal scan and this term is added to measured values at each vertical scan. The accuracy of this drift correction depends on the measurement uncertainty in the two-dimensional scan and in the reference horizontal scan as the measured values are compared to each other in order to determine the correction terms – therefore, any other error in either of these measurements affects the error correction accuracy. Typically, about 5-10 horizontal scans are averaged for the reference scan.

7.5 Combined measurement uncertainty

In this Section, the contributions of the different measurement error sources to the measurement uncertainty are first summarised and then the error budgets are computed for the measured co-polarised relative amplitude and phase, and for the cross-polarisation level of -20 dB and -30 dB at 310 GHz for the planar near-field measurements of a spherical and a plane wave. The relative amplitude and phase means that each individual measurement result is normalised to 0 dB or 0° at the centre or other reference point, and all of the measured values are compared this reference. The measurement uncertainty is estimated for the corners or edges of the 200 mm × 200 mm scan area in horizontal, vertical and two-dimensional scans. These scans cover the area, inside which the field under measurement has nearly constant amplitude. This is also the most significant area in the DRFS beam and it contains the quiet-zones of the test holograms. The individual uncertainties are combined as square root of the sum of the squares (RSS) of the 3σ values for the random errors and the worst case estimates of the systematic errors.

7.5.1 Probe related measurement errors

The probe most significant probe related error sources are the relative probe pattern, the probe polarisation ratio, the probe orientation and an error in the polarisation twist affecting the probe polarisation. The uncertainty in the probe pattern is assumed negligible, as it could not be verified reliably. The polarisation ratio of the probe causes an uncertainty of 0.01 dB in the co-polarised amplitude measurements and 0.96 dB in the measured cross-polarisation level in

the horizontal and vertical scans at the -30 dB level, and 0.31 dB at the -20 dB level. These values are propably quite conservative as the probe cross-polarisation in the horizontal and vertical directions is actually lower than the assumed diagonal direction cross-polarisation level in these directions. The cross-polarisation level uncertainties in the two-dimensional scan are 1.83 dB and 0.61 dB, respectively.

The orientation of the probe affects the orientation of the probe polarisation in relation to the polarisation of the field under measurement. The orientation error is caused by a tilt of the probe orientation or a tilt in the AUT polarisation in respect to the scanner. An error in the 90° -polarisation twist causes also coupling of the co-polarised power to the measured cross-polarised power. The AUT tilt can be assumed to be ±1 mm per metre and the wobbling of the vertical rail of the scanner in the horizontal direction can be up to ±0.25 mm per metre, i.e., a worst case effective probe polarisation tilt of about 0.14° may exist in the set-up. This results into uncertainty of less than 0.01 dB in all cross-polarisation level measurements. The error in the 90° polarisation twist may be up to 0.5° based on a rough estimate on the effect of manufacturing tolerances for the waveguides, flanges and other parts in the receiver, which results into lower than 0.02 dB uncertainty in the measured cross-polarisation level at levels higher than -30 dB. At lower cross-polarisation levels this error becomes more significant.

The uncertainty in the co-polarisation amplitude is less than 0.01 dB due to the probe orientation errors and the uncertainty in the phase measurements due to coupling of the power from the other polarisation is assumed negligible.

7.5.2 Antenna-under-test related measurement errors

The antenna under test alignment errors are not significant as in the case of the hologram, the quiet-zone field is optimised onto the scanner plane and the DRFS radiates a nearly spherical wavefront and it is aligned very precisely. In the measurements of a spherical phase, the error in the measurement distance is a significant error source. The phase uncertainty due to ±1 mm error in the 1800 mm distance is ±4.3° in the corners of the two-dimensional scan and ±2.2° at the ends of the horizontal and vertical scans.

The AUT positioning error does not have a significant contribution to the amplitude uncertainty and the potentional tilt of the AUT polarisation due to a tilt in the AUT orientation is considered to contribute to the effective probe orientation. The primary feed is considered as a part of the DRFS and all feed related errors are part of the DRFS under test. In the case of hologram quiet-zone measurements, the potential feed horn polarisation tilt combines with the potential tilt in the hologram orientation increasing the effective probe polarisation tilt.

7.5.3 Near-field scanner related measurement errors

The planar near-field scanner induced measurement errors are caused by errors in the probe *xyz*-positioning due to non-ideal scanner operation. The probe position errors are caused by errors in the probe positioning in the scanner, movement of the probe during the sample integration, by the planarity errors of the scanner, and by other errors in the scanner operations such as vibrations. The most significant errors are caused by the probe position errors, but the errors are reasonably small so that they do not cause significant amplitude measurements errors.

7.5.3.1 Scanner planarity

The phase measurement errors due to the probe position errors can be significant especially in the spherical wave measurements. Both in plane wave and in spherical wave measurements the planarity error of the scanner causes a probe *z*-coordinate error, which corresponds to an error in the electrical path length. The maximum planarity error inside the 200 mm × 200 mm scan area used is ±35 μm, which corresponds to phase uncertainty of ±13° at 310 GHz. The measured planarity error can be compensated computationally in the phase measurements using the laser tracker measurement data on the planarity. The uncertainty in the measurement of the planarity of the probe motion is ±20 μm and the corresponding uncertainty in the correction is ±7°.

7.5.3.2 Probe xy-position

The probe *xy*-position errors are not significant in the plane wave measurements provided that the sampling spacing is short enough to resolve the ripples. In the case of the spherical wave, the *xy*-position is however significant as the phase changes rapidly as the function of the probe position. In a horizontal scan, the *x*-coordinate uncertainty is ±100 μm, causing a phase uncertainty of ±4°, and the *y*-coordinate uncertainty is ±30 μm corresponding to ±1° in phase. The *y*-coordinate uncertainty in a vertical scan is also ±100 μm with the corresponding uncertainty of ±4° and the *x*-coordinate uncertainty is ±100 μm, which results into ±4° in phase. Averaging can be used to reduce the random positioning error, i.e. the *x*-coordinate error in horizontal scans and *y*-coordinate error in vertical scans. The averaging of 10 consecutive scan reduces the phase uncertainty to ±1.3° for these probe position errors along the scanning direction. The total phase measurement uncertainty due to the probe *xy*-position errors is about ±6° in a vertical scan and about ±4° in a horizontal scan. The averaging of 10 scans reduces these uncertainties to about ±4° and ±2°, respectively. In a two-dimensional scan, the uncertainty in both in the *x*- and *y*-coordinate of the probe position is ±100 μm and the RSS phase uncertainty is then ±6°.

7.5.4 Measurement instrumentation related measurement errors

The main error sources in the measurement instrumentation consisting of the vector network analyser, the sub-mm wavelength extensions used as the transmitter and receiver, and the associated cables and waveguides, are the noise in the system, cable flexing induced phase errors, repeatability of the waveguide twist connections and receiver operation, and the drift.

7.5.4.1 Vector network analyser noise

The noise in the vector network analyser affects the co-polarised amplitude, phase and the measured cross-polarisation level. In co-polarisation measurements, the uncertainty in the amplitude is ±0.1 dB and ±1° in the phase. The uncertainty in the cross-polarisation level is the RSS sum of the co-polarisation amplitude uncertainty and the uncertainty in the cross-polarised amplitude (±0.4 dB), i.e., approximately ±0.4 dB. The noise can be reduced by

increasing the integration time or by averaging n measurements, when the noise is reduced by the factor of $\sqrt{n}$.

7.5.4.2 Cable flexing

The bending of the LO-cable for the phase-locking circuit in the receiver (ESA-2 extension of the MVNA) causes changes in the electrical length of the cable and errors in the measured phase. The measured phase errors cause an uncertainty of ±4° in the phase, which can be reduced to ±2° with the cable flexing phase error correction system.

7.5.4.3 Repeatability of the amplitude measurements

When the cross-polarisation level is measured, the measured cross-polarised power is compared to the measured maximum of the co-polarised power. The polarisation is changed using a 90° waveguide twist and the receiver is switched off for attaching the twist. The repeatability in the probe polarisation change was ±0.4 dB in co-polarised amplitude and a similar uncertainty can be assumed to exist in the measured cross-polarised amplitude. The combined RSS uncertainty in the cross-polarisation level is therefore ±0.6 dB.

7.5.4.3 Drift

The drift in horizontal and vertical scans is assumed negligible as these scans are done quite quickly within 1-2 minutes. Two-dimensional scans take typically over two hours to complete and the drift becomes significant causing an amplitude uncertainty of ±0.35 dB and a phase uncertainty of ±12°. The drift is corrected by comparing a horizontal cut in the two-dimensional data to a separate measured horizontal cut. As the reference scan is done immediately after the two-dimensional scan without changing the measurement set-up or the conditions, the only error sources contribution to the uncertainty of the drift correction are the probe *xy*-position errors and the vector network analyser noise in the measurements. In the two-dimensional scan, these cause an uncertainty of ±8° in phase and ±0.1 dB in amplitude. The corresponding uncertainties in the horizontal reference scan are ±4° and ±0.1 dB (±2° if 10 scans are averaged) and the combined uncertainty for the drift correction is ±9° (±8° if the reference scans is the average of 10 scans) in phase and ±0.14 dB in amplitude. The installation of the air-conditioning system has mostly eliminated the drift and the need for drift correction in two-dimensional scans.

In the two-dimensional cross-polarisation level measurements, the uncertainty caused by the drift is the same as in the co-polarisation measurements (±0.35 dB) as the cross-polarised amplitude is compared to the maximum co-polarised amplitude measured immediately before or after the cross-polarisation measurement.

7.5.5 Measurement environment related measurement errors

The ambient temperature changes distort the scanner frame causing the planarity of the scanner to change. These changes were eliminated by the installed air-conditiong before the measurements of the holograms designed to operate at the horizontal polarisation and the polarisation grid tests. In the earlier measurements, i.e., in the DRFS testing, the temperature was manually regulated by adjusting the ventilation to within approximately ±0.5°C and the corresponding phase uncertainty is ±2° in all measurement as a ±2°C temperature variation causes about ±5° phase uncertainty.

7.5.6 Error budgets

The total measurement uncertainty can be combined using error budgets. The error budget for co-polarised amplitude measurements is shown in Table 7.2, for the phase without any error corrections in Table 7.3 and after error corrections in Table 7.4. The error budget for the measured cross-polarisation level is presented in Table 7.5.

Table 7.2 *Amplitude measurement error budget for relative co-polarisation measurements.*

Error source	Horizontal scan	Vertical scan	Two-dimensional scan
Probe pattern	-	-	-
Probe polarisation ratio	0.01 dB	0.01 dB	0.01 dB
Probe orientation	0.01 dB	0.01 dB	0.01 dB
Polarisation twist	0.01 dB	0.01 dB	0.01 dB
AUT positioning	-	-	-
Scanner planarity	-	-	-
Probe *x*-position	-	-	-
Probe *y*-position	-	-	-
MVNA noise	0.1 dB	0.1 dB	0.1 dB
Cable flexing	-	-	-
Repeatability	-	-	-
Drift	-	-	0.35 dB / 0.14 dB*
Ambient temperature	-	-	-
RSS	0.1 dB	0.1 dB	0.4 dB / 0.2 dB*

** with drift correction*

The combined amplitude measurement uncertainty obtained as the root sum of the squares (RSS) of the individual uncertainties is ±0.1 dB in the horizontal and vertical scans. In two-dimensional scans, the RSS uncertainty is ±0.4 dB without drift compensation and ±0.2 dB with the drift compensation in the 200 mm × 200 mm area corresponding to the quiet-zones of the test holograms and to the region with nearly constant amplitude in the hologram illumination with the DRFS. The uncertainties apply to the relative amplitude measurements, i.e., in each measurement the amplitude at the centre of the scan is normalised to 0 dB and the uncertainty is then the uncertainty of the measured amplitude at the edges of the scan area in relation to the amplitude in the centre. In the relative amplitude measurements, the dominating

error is the noise in the vector network analyser in the horizontal and vertical scans. Prior to the installation of the air conditioning, the largest error source in two-dimensional scans was the drift. In the measurements done with the air-conditioning, the uncertainty should be only about 0.1 dB as in one-dimensional scans.

Table 7.3 *Relative phase measurement error budget for measurements without error corrections.*

	Horizontal scan		Vertical scan		Two-dimensional scan	
Plane wave	x		x		x	
Spherical wave		x		x		x
Error source						
Probe pattern	-	-	-	-	-	-
Probe polarisation ratio	-	-	-	-	-	-
Probe orientation	-	-	-	-	-	-
Polarisation twist	-	-	-	-	-	-
AUT positioning	-	2.2°	-	2.2°	-	4.3°
Scanner planarity	13°	13°	13°	13°	13°	13°
Probe *x*-position	-	4°	-	4°	-	4°
Probe *y*-position	-	1°	-	4°	-	4°
MVNA noise	1°	1°	1°	1°	1°	1°
Cable flexing	4°	4°	4°	4°	4°	4°
Repeatability	-	-	-	-	-	-
Drift	-	-	-	-	12°	12°
Ambient temperature	5°	5°	5°	5°	5°	5°
RSS	14°	15°	14°	15°	18°	20°

The RSS relative phase measurement uncertainty is ±14°–15° in the one-dimensional scans and ±18°–20° in the two-dimensional scans. The most significant error sources are the scanner planarity, the ambient temperature changes and the drift (in the two-dimensional scans). As the drift also depends on the temperature stability, the air-conditioning system was procured to eliminate the temperature fluctuations. Tracking laser interferometer measurements were organised to investigate and correct the probe *xyz*-position errors. Previously developed cable flexing error correction system was utilised in antenna testing for the first time in the measurements described in this thesis. Unfortunately, the first version of the system developed in the Radio Laboratory prior the use in these measurement was responsible for most of the drift in the system before installation of the air-condition. The cable flexing correction system is currently being upgraded to be temperature stabilised for use in non-air-conditioned rooms also.

Table 7.4 *Relative phase measurement error budget for measurements using error corrections techniques.*

	Horizontal scan		Vertical scan		Two-dimensional scan	
Plane wave	x		x		x	
Spherical wave		x		x		x
Error source						
Probe pattern	-	-	-	-	-	-
Probe polarisation ratio	-	-	-	-	-	-
Probe orientation	-	-	-	-	-	-
Polarisation twist	-	-	-	-	-	-
AUT positioning	-	2.2°	-	2.2°	-	4.3°
Scanner planarity	7°	7°	7°	7°	7°	7°
Probe *x*-position	-	1.3°	-	4°	-	4°
Probe *y*-position	-	1°	-	1.3°	-	4°
MVNA noise[(1)]	0.3°	0.3°	0.3°	0.3°	1°	1°
Cable flexing	2°	2°	2°	2°	2°	2°
Repeatability	-	-	-	-	-	-
Drift	-	-	-	-	9°	9°
Ambient temperature[(2)]	2°	2°	2°	2°	2°	2°
RSS	8°	8°	8°	9°	12°	14°

[(1)]Average of 10 consecutive one-dimensional scans
[(2)]Stabilised by controlling the ventilation of the room

The combined total phase measurement uncertainty is ±8° in one-dimensional scans of a plane wave and ±8–9° in the one-dimensional scans of a spherical wave. In the two-dimensional scans, the uncertainties are ±12° in the plane wave measurement and ±14° in the spherical wave measurements. The largest contributions to the combined measurement uncertainty are caused by the planarity of the scanner, the probe *xy*-position and by the AUT position in the spherical wave measurements and by the drift in the two-dimensional scans. The scanner is currently being replaced with a more precise near-field scanner.

Table 7.5 *Relative cross-polarisation level measurement error budget for the measurements of a spherical wave.*

	Horizontal scan		Vertical scan		Two-dimensional scan	
Cross-polarisation level	-30 dB	-20 dB	-30 dB	-20 dB	-30 dB	-20 dB
Error source						
Probe pattern	-	-	-	-	-	-
Probe polarisation ratio[1]	1 dB[2]	0.3 dB[2]	1 dB[2]	0.3 dB[2]	1.8 dB	0.6 dB
Probe orientation	0.01 dB	0.01 dB	0.01 dB	0.01 dB	0.01 dB	0.01 dB
Polarisation twist	0.02 dB	0.02 dB	0.02 dB	0.02 dB	0.02 dB	0.02 dB
AUT positioning	-	-	-	-	-	-
Scanner planarity	-	-	-	-	-	-
Probe *x*-position	-	-	-	-	-	-
Probe *y*-position	-	-	-	-	-	-
MVNA noise	0.4 dB	0.4 dB	0.4 dB	0.4 dB	0.4 dB	0.4 dB
Cable flexing	-	-	-	-	-	-
Repeatability	0.6 dB	0.6 dB	0.6 dB	0.6 dB	0.6 dB	0.6 dB
Drift	-	-	-	-	0.35 dB	0.35dB
Ambient temperature	-	-	-	-	-	-
RSS	1.2 dB	0.8 dB	1.2 dB	0.8 dB	2.0 dB	1.0 dB

[1]At the edges of the 200 mm × 200 mm scan area, much lower at small incidence angles.
[2]Assuming the maximum probe cross-polarisation in all directions of arrival.

The combined uncertainty in the cross-polarisation level measurements is ±0.8 dB–2.0 dB and it can be concluded that the uncertainty of the maximum cross-polarisation level in the quiet-zones of the test holograms have the uncertainty of ±1 dB (±0.8 dB in the one-dimensional scans). The combined uncertainty is mostly affected by the polarisation ratio of the probe and by the repeatability of the power level in the receiver when the polarisation is changed. The MVNA noise is also an important error source.

8 Sub-mm antenna testing in a CATR based on a hologram

The hologram based compact antenna test range has been used to test a 1.5 m reflector antenna at 322 GHz. For this purpose, manufacturing techniques were developed for large sub-mm wavelength holograms [O32]. The design of the CATR and the associated instruments together with the planning of the measurements were done in the hologram research group in the Radio Laboratory as a team effort. Similarly, the construction of the CATR, the measurements and the disassembly of the CATR after the antenna tests were done as a collective effort in the group, which the author participated.

In this Chapter, the structure and the construction of the hologram based CATR are briefly discussed. More details can be found in [O4,O20]. The CATR operation was verified and optimised using a simple plane polar near-field scanner to measure the quiet-zone field at 322 GHz. The quiet-zone test results are described in this Chapter together with the antenna test results. The effect of the quiet-zone non-idealities on the measured antenna pattern is discussed. The antenna test results and their analysis has been published in [O3].

8.1 The hologram based CATR for 322 GHz

The 3-m hologram based compact antenna test range was specially constructed for the antenna tests in question. The assembly of the CATR , the verification of the quiet-zone field , the antenna tests and the disassembly of the range after the tests were all carried out in about two months during summer 2003.

8.1.1 Assembly of the CATR

The instrumentation for the CATR, the quiet-zone field measurement system, the plane polar near-field scanner for the quiet-zone tests, and the antenna positioner and the associated software were developed in the Radio Laboratory. The hologram design was carried out by Tomi Koskinen as described in Chapter 3 for operation at the vertical linear polarisation.

8.1.1.1 Antenna positioner

The mechanical engineering for the CATR instrumentation was done at the Laboratory of Machine Design of the Helsinki University of the Technology (TKK). A Bofors 40-mm anti-aircraft gun originally from the Second World War was modified into a high precision antenna positioner. Only the base and the azimuth gear were conserved and a cradle-type elevation stage was constructed from steel profile. The antenna positioner has the angular range of 360° in the azimuth direction and -12°…+90° in the elevation, but in practice about ±12° was feasible in elevation scans during the antenna tests. Twenty six-bit absolute angle encoders, which have the precision of 0.0001°, were installed directly on the axes. Using these encoders the measured repeatability of the azimuth rotation was 0.004°.

8.1.1.2 Quiet-zone field scanner

For quiet-zone field measurements, a plane polar near-field scanner was constructed from a 2-m long linear translation stage that can be rotated to four positions for measuring the horizontal, vertical and both horizontal cuts of the quiet-zone field. The plane polar scanner is mounted on the antenna positioner so that the quiet-zone is measured at the location of the AUT aperture. A photograph of the plane polar scanner mounted on the antenna positioner is shown in Figure 8.1. The photograph was taken during the construction before all the absorber were attached on the antenna positioner.

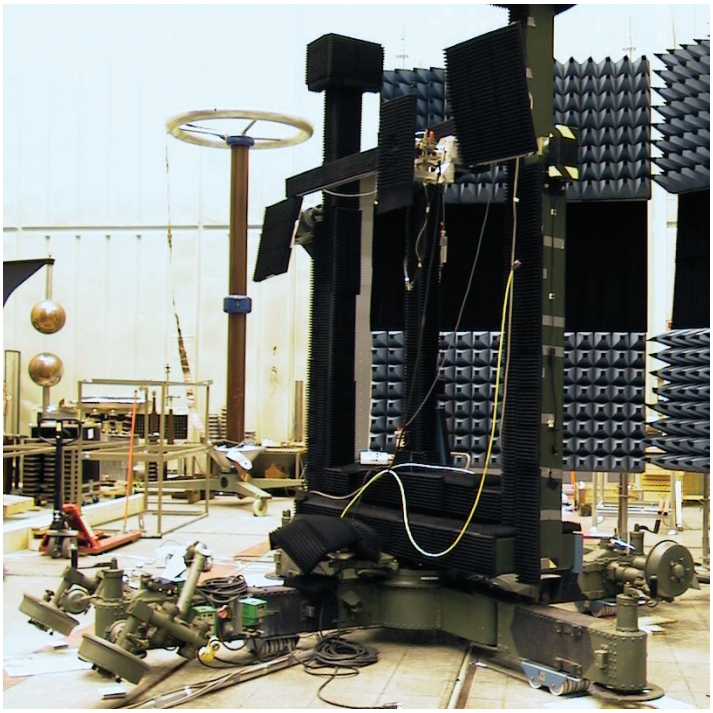

Figure 8.1 *Photograph of the plane polar scanner mounted on the antenna positioner.*

The scanner and the antenna positioner were covered with millimetre wavelength absorber material during the measurements. Prior to the quiet-zone field testing, the planarity of the scanner at the different positions was measured using the same laser tracker that was used to measure the planarity of the near-field scanner as described in Chapter 7. The measured planarity at the horizontal and vertical positions of the plane polar scanner are presented in Figure 8.2.

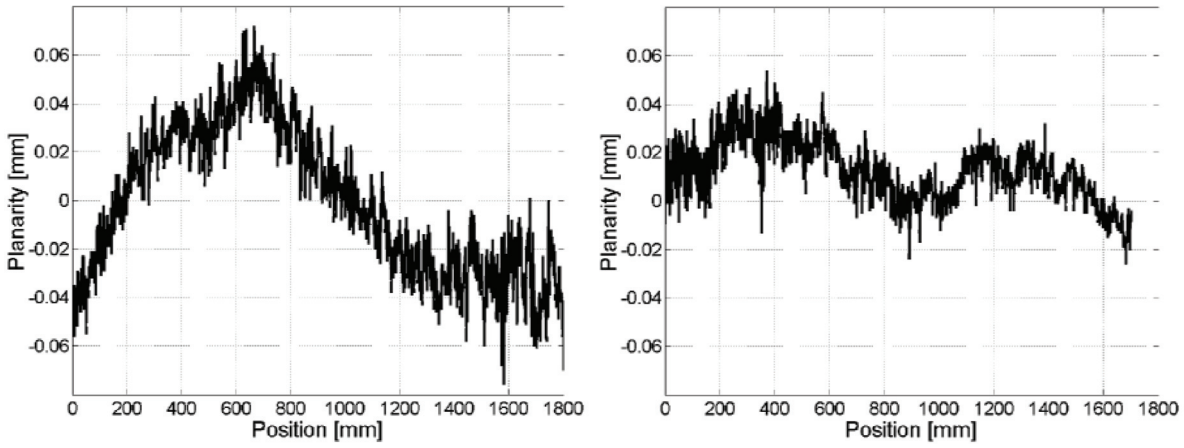

a) *b)*

Figure 8.2 *Measured planarity of the plane polar scanner [123]:*
a) in a horizontal scanner position,
b) in a vertical scanner position.

The planarity of the scanner was measured four times for each scanner orientation and the results were averaged to form a correction table for the measured phase. The maximum phase errors at the frequency of 322 GHz resulting from the non-planarity of the probe movement in the four scanning directions were: 40° peak-to-peak in the horizontal orientation, 15° in the vertical orientation, and 20° and 90° peak-to-peak in the diagonal quiet-zone cuts [123]. These errors were computationally removed from the phase measurement results.

8.1.1.3 Sub-mm wavelength instrumentation

The measurement instrumentation was based on the MVNA-8-350 millimetre wave vector analyser with a high power transmitter (2.6–5.4 dBm) supplied with the antenna under test for use in these tests by EADS Astrium[124]. The receiver in the quiet-zone test was the ESA-2 extension of the MVNA and in the antenna tests the receiver supplied with the antenna was used. In the quiet-zone field measurements, both the transmitter and the receiver were phase-locked onto a common reference, which allowed coherent measurements. A spectrum analyser was used as power meter for the received power in the antenna measurements. The cable flexing error correction systems described in Chapter 7 was also used in the quiet-zone field measurements. The measurement system was controlled by a computer using an in-house developed LabVIEW-based software.

8.1.1.4 The 322 GHz hologram

The compact antenna test range was based on a 3-m diameter hologram operating at the linear vertical polarisation. This hologram was constructed from three 1 m × 3 m pieces, which were aligned using overlapping alignment markers and a microscope. The overlap was cut away using a surgical blade attached to a linear rail and the pieces were then joined together by soldering the copper stripes in the hologram pattern together. The joining was done on a specially constructed vacuum table that uses sucktion to hold the mylar-films in place during the soldering. In total about 3840 metal strips were soldered manually together in the two

horizontal seams in the 3-m hologram. The hologram was attached to a frame and the frame was lifted up. The hologram was tensioned in the frame to ensure the planarity of the hologram surface. [O4]

8.1.1.4 Layout of the compact antenna test range

The CATR based on the 3-m hologram was constructed in the 31 m × 19 m × 16 m High Voltage research hall at TKK in Espoo, Finland. In Figure 8.3, the layout of the CATR is presented and in Figure 8.4 a photograph of the range is shown. Absorber walls were constructed using scaffolding and plywood boards. These walls were used to block the direct feed radiation into the quiet-zone and to reduce reflections inside the metal-walled hall. The high-quality millimetre wavelength absorbers were used only around the most critical areas, i.e., around the hologram, the feed and the antenna under test. At the less critical areas, less expensive microwave absorbers and other materials were used.

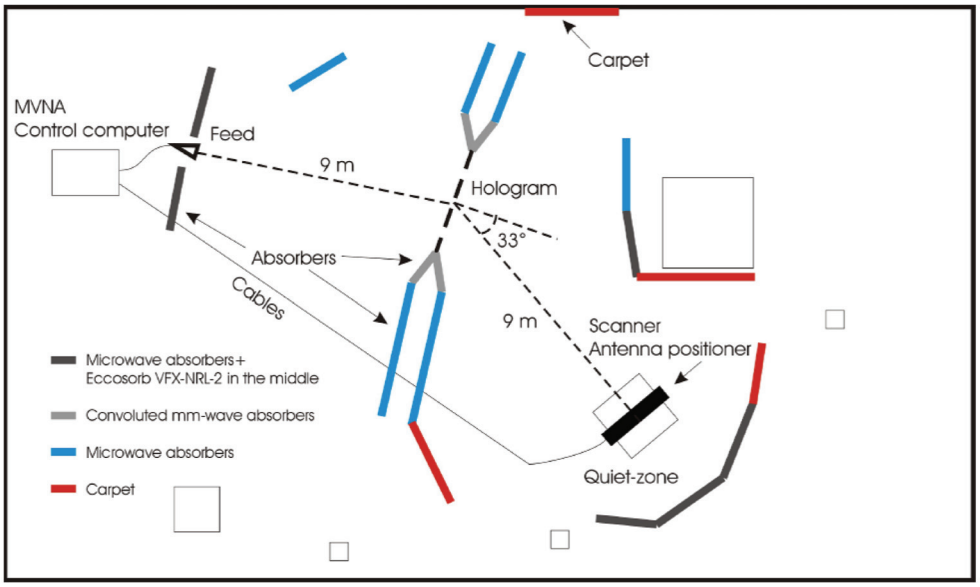

Figure 8.3 *Layout of the CATR based on a hologram.*

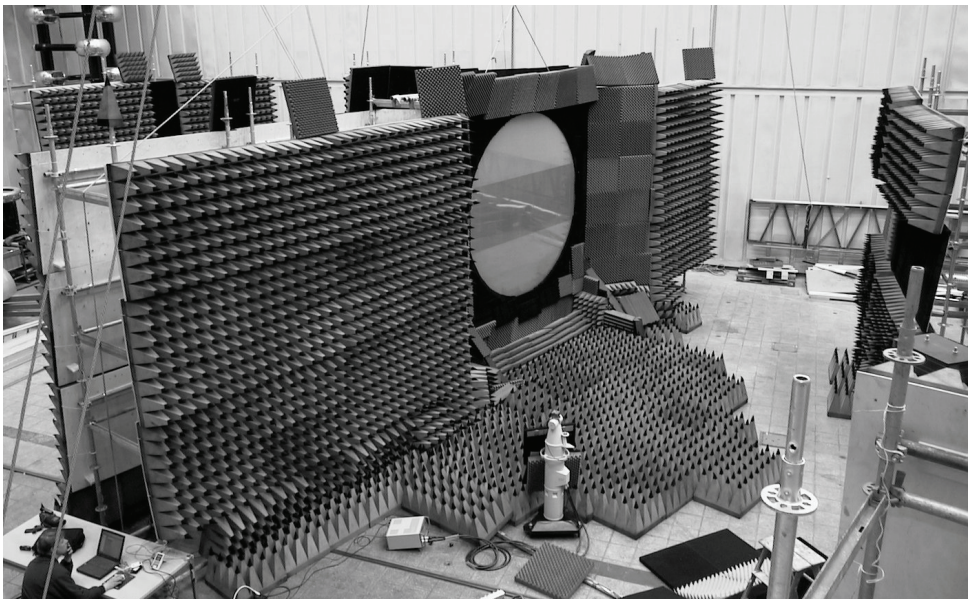

Figure 8.4 *Photograph of the CATR based on a hologram for 322 GHz [O3].*

8.1.2 Verification of the CATR quiet-zone field

The quiet-zone field amplitude and phase were probed with a corrugated horn using the plane polar scanner. The feed horn position and alignment were optimised to produce the best possible quiet-zone field quality in the horizontal and vertical cuts. The dynamic range in the quiet-zone measurements was about 52 dB. The quiet-zone field measurement results inside the 1.5 m aperture of the antenna under test are shown in Figure 8.5.

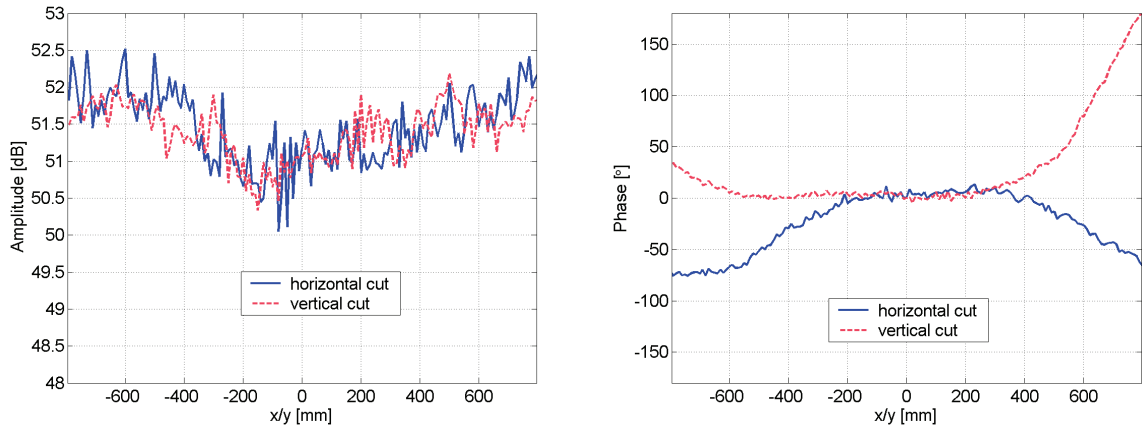

a) *b)*

Figure 8.5 *Measured quiet-zone field at the vertical polarisation at 322 GHz [O3]:*
a) amplitude,
b) normalised phase.

The measured quiet-zone amplitude shows an approximately 1 dB dip in the middle and the phasefront was saddle-shape as the phasefront is concave in the vertical cut and convex in the horizontal cut. The maximum measured deviations are 2.6 dB in amplitude and 250° in phase

peak-to-peak with typical peak-to-peak ripple of 1 dB and 10°, respectively. In the diagonal quiet-zone cuts the phase deviations were about 45° peak-to-peak.

The causes of the distortions to the plane in the quiet-zone were investigated in the Radio Laboratory after the antenna test campaign [O4]. The dip in the amplitude is probably caused by inaccurate modelling of the hologram structure in the FDTD simulations; the cell size was too large in the simulations and using smaller cell size the simulations show the 1 dB dip in the amplitude. Therefore, in the future a smaller cell size will be used in the hologram simulations despite the increased computation time on a super-computer.

The dimensions of the hologram were checked before the disassembly of the CATR and it was discovered that while the width of the hologram was 3000 ± 1 mm, the height of the hologram was only about 2990 mm. This elliptical shape of the hologram pattern is mostly responsible for the saddle-shape phasefront in the quiet-zone as the hologram has a different focal length in the horizontal and vertical directions. The pattern deformations are most likely caused by an error in the etching of the hologram pieces which was discovered after the antenna tests: the three pieces have different widths but the correct length of 3000 mm. This made the alignment of the final hologram piece difficult after the first two had been soldered together; there was a misalignment of approximately 0.6–1.0 mm along the seams near the edges of the upper seam. This misalignment contributes to the overall quiet-zone field phase distortions.

8.2 Antenna measurements

After the verification and optimisation of the quiet-zone field, the plane polar scanner was removed and the antenna under test was mounted on the positioner. The radiation pattern of the AUT was measured relative to the main beam peak at the linear vertical polarisation at the frequency of 322 GHz.

8.2.1 Antenna under test

The antenna under test was the ADMIRALS RTO (Representative Test Object) constructed by EADS Astrium for comparison of the measurement facilities [50]. The RTO has a 1.5 m diameter single offset paraboloid reflector with focal length of 3 metres. The feed offset angle is 19.6° and the feed is located at the end of a 3-m beam. The surface roughness of the reflector surface was measured at EADS Astrium to be 0.35 μm peak-to-peak and the RMS surface contour accuracy was 30 μm. A photograph of the RTO mounted on the antenna positioner is shown in Figure 8.6.

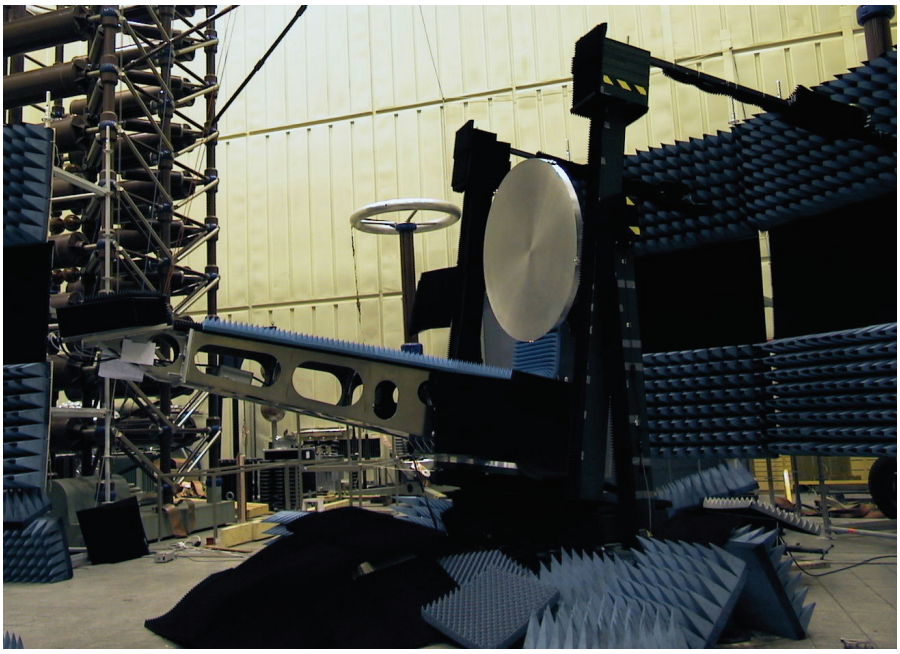

Figure 8.6 *The antenna under test (ADMIRALS RTO).*

8.2.2 Measured radiation pattern

The radiation pattern of the ADMIRALS RTO was measured in *E*-plane (vertical) and in the *H*-plane (horizontal) cuts, and also a two-dimensional contour map was measured. The angular range was ±12° in the *E*-plane and ±85° in the *H*-plane. In Figure 8.7, the *H*-plane antenna pattern cut is shown and in Figure 8.8, the *E*-plane pattern cut is presented together with the contour map of the antenna pattern around the main beam region. The measured power is normalised to 0 dB at the main beam peak and the dynamic range in the measurements was approximately 85 dB.

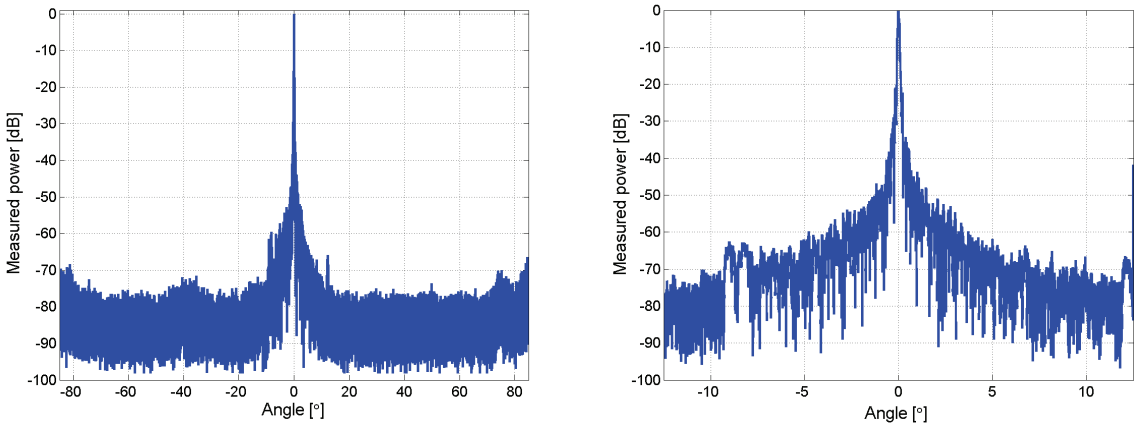

Figure 8.7 *Measured H-plane radiation pattern cut at 322 GHz.*

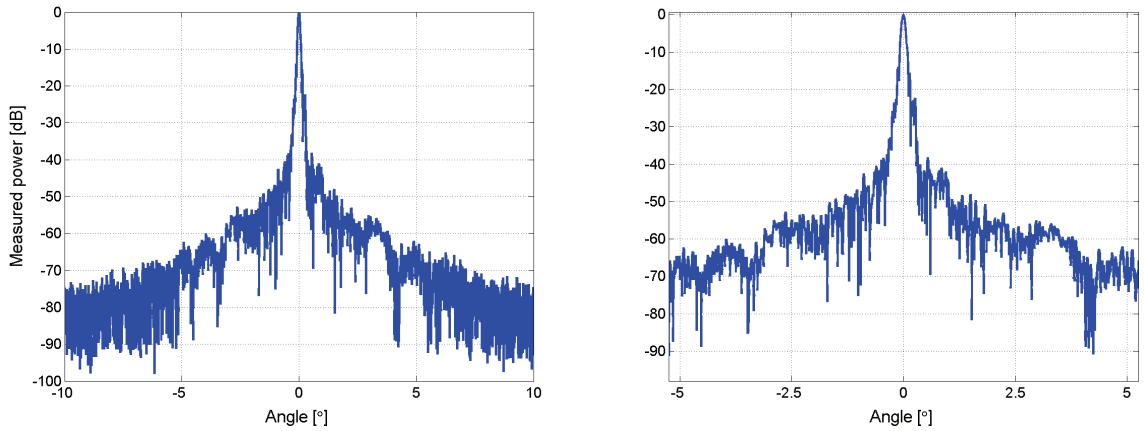

Figure 8.8 *Measured E-plane radiation pattern cut at 322 GHz.*

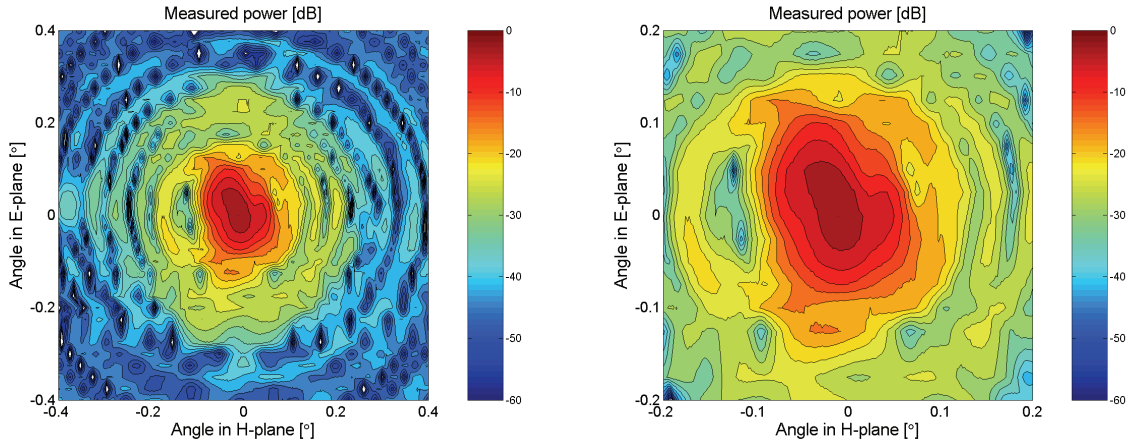

Figure 8.9 *Measured contour map of the radiation pattern at 322 GHz with 3 dB contour intervals.*

The measured *H*-plane antenna pattern cut shows unusual sidelobes around the direction of -8.5° and +12°. The causes for these lobes are discussed later. Inside the rapid variation of the peaks and nulls in the *E*-plane pattern cut in Figure 8.8 there can be seen lobes around direction of ±3° in the vertical plane. It should be noted that the horizontal seams in the hologram are seen approximately at the angles of ±3.2° in the *E*-plane by the AUT, so these lobes might be caused by the quiet-zone field distortions by the seams in the hologram.

The cross-polarisation pattern of the RTO was measured by switching the polarisation in the receiver to horizontal and the measured power at this cross-polarisation compared to the co-polarised main beam peak is shown in Figure 8.10.

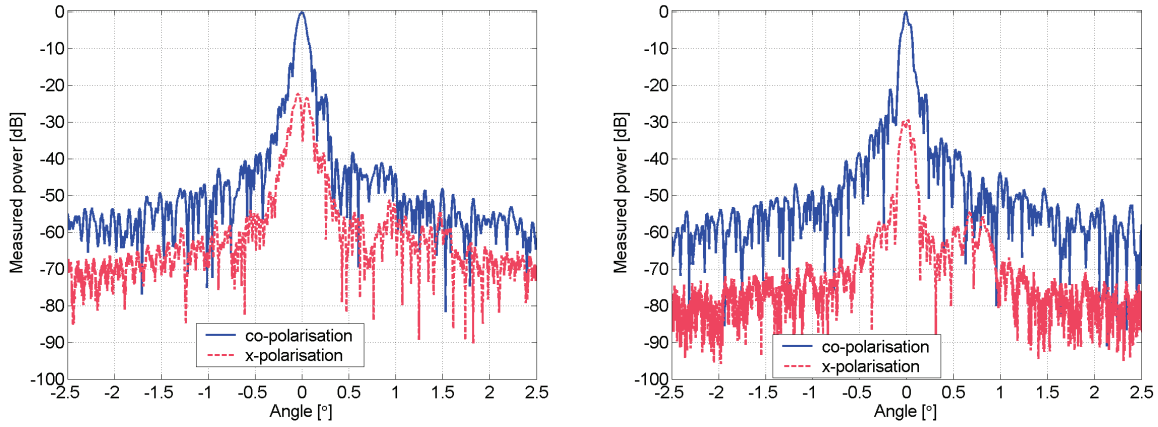

a) *b)*

Figure 8.10 *Measured cross-polarisation pattern at 322 GHz:*
a) E-plane cut,
b) H-plane cut.

The typical cross-polarisation level of the holograms is of the order of -20 dB, so the measured cross-polarisation level is greatly affected by the cross-polarisation in the quiet-zone field and the measured cross-polarisation level in Figure 8.10 cannot be considered exact.

8.2.2 Comparison of the measured pattern to the simulations

The radiation of the RTO was simulated with GRASP8W using physical optics (PO) and physical theory of diffraction (PTD). The reflector surface distortions from the ideal paraboloid were included into the in the simulations based on measurements of the reflector surface before the antenna was assembled and based on the estimated bending of the reflector when it is mounted on the antenna. These measurements and the estimation on the reflector bending were carried out at EADS Astrium. The reflector was illuminated with a Gaussian beam with -10.5 dB taper at the angle of 13.5°, which corresponds approximately to the reflector rim. The simulated and measured antenna pattern cuts are shown in Figure 8.11.

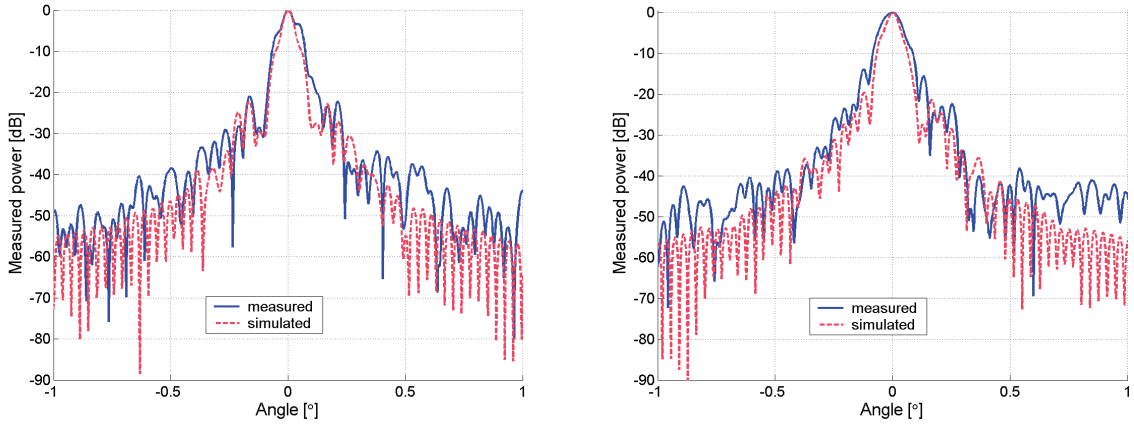

Figure 8.11 *Measured and simulated radiation patterns at 322 GHz:*
a) H-plane cut,
b) E-plane cut.

The measured -3 dB beam widths are 0.086° in the *E*-plane and 0.050° in the *H*-plane. The corresponding simulated beam width are somewhat smaller; 0.053° and 0.045°, respectively. In addition, the measured sidelobe level is higher than the simulated sidelobe level. The reasons for these discrepancies are discussed next.

8.2.3 Analysis of the antenna test results

The measured antenna pattern is affected by measurement errors, most importantly by the quiet-zone field. As a reflector antenna, the RTO can be considered as a radiating aperture with the effective aperture field $\overline{E}_{effective}(x,y)$ [125]

$$\overline{E}_{effective}(x,y) = \overline{E}_{aperture}(x,y) \bullet \overline{E}_{quiet\text{-}zone}(x,y), \tag{8.1}$$

where $\overline{E}_{aperture}(x,y)$ is the aperture field of the AUT, $\overline{E}_{quiet\text{-}zone}(x,y)$ is the field incident on the aperture, and x,y are the coordinates in the aperture. The radiation of the aperture can be computed from the aperture field as described in Section 2.2.

8.2.3.1 Effect of the non-ideal quiet-zone field

The field distortions from the plane wave in the quiet-zone can be divided into two categories: into systematic deviations, and into ripple. The systematic deviations include amplitude taper or the dip in this case, and the phasefront curvature. The ripple is caused by stray signals, i.e., by unwanted waves that sum to the plane wave. The stray signals are usually mostly caused by scattering in the measurement environment or by edge diffraction, but also errors in the operation of the collimating element may cause them. When the main beam of the antenna points in the direction of the stray signal, for example towards a scatterer in the measurement environment, the stray signal is received by the main beam. This causes a significant error to

the sidelobe under measurement, i.e., so-called grating lobe, as the side-lobe level is much lower than that of the main beam. Several methods have been developed to reduce the error in the sidelobe measurements due to the stray signals, for example [O12, 126].

The reflectivity level in an anechoic chamber can be evaluated using the antenna pattern comparison (APC) technique [127]. In APC, the radiation pattern of the AUT is measured at several locations inside the quiet-zone of the CATR and the variation in the measured pattern corresponds to the reflectivity level. This variation in the measured antenna pattern is caused by the variation in the field incident on the antenna because the antenna is moved to different location inside the quiet-zone and the stray signals sum at different phase to the plane wave at the different location. The measured variation in the radiation pattern gives also an estimated on the measurement uncertainty. Using superposition of the measurements, the error caused by the stray signals can be eliminated [126].

In a CATR based on a hologram, the direction of the plane wave progating into the quiet-zone can be changed by changing the feed position. This feed scanning technique can also be used for APC-measurements as the phase difference between the plane wave and stray signals incident on the AUT is changed [O12]. Unfortunately, the use of this technique for antenna pattern correction was discovered only after the RTO test campaign and the method could not be used for antenna pattern correction in the RTO measurements. Conventional APC-measurements were not possible as the AUT could not be moved inside the quiet-zone. The feed scanning APC was used to investigate potential grating lobes around -8.5° in the measured RTO antenna pattern. The direction of the plane wave was steered by 0.22° and the resulting change in the measured radiation pattern around the potential grating lobe around -8.5° direction in the *H*-plane cut is shown in Figure 8.12.

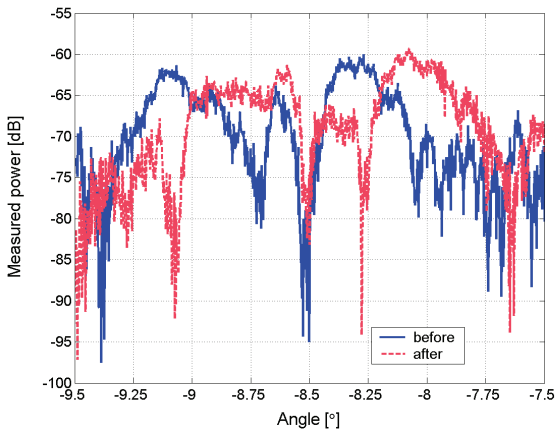

Figure 8.12 *Closeup of a measured sidelobe before and after steering the plane wave direction by 0.22° [O3].*

As can be seen in Figure 8.12, the position of the sibelobes changes in the relation to the main beam peak direction by the amount of the plane wave steering, which indicate that the sidelobes originate from a fixed point in the CATR, not from the antenna itself. Therefore, it can be concluded that these lobes are grating lobes. The direction of -8.5° is inside the hologram in the CATR, so the stray signals causing these grating lobes may originate from the feed side of the hologram and the main beam sees them through the hologram, or the main beam sees a reflection of a stray signal from the hologram. Another sibelobe that is much higher than the general level of the sidelobes can be seen around +12° in the *H*-plane. As this

lobe is not affected by the plane wave steering, it can be concluded to be a real sidelobe of the antenna or an erroneous lobe caused by scattering from the antenna positioner structures.

Several scatterer identification methods have been developed for compact antenna test ranges. The quiet-zone field can be described as a sum of plane waves, i.e., with a plane wave spectrum (PWS). This angular spectrum of the field can used to determine the directions of arrival for the stray signals and to estimate the locations of the scatterers in the CATR using for example Fourier-transformation to obtain the angular spectrum, multiple signal classification (MUSIC) –methods [128] or superresolution techniques. The scatterer identication methods were studied together with the effect of the possible quiet-zone distortions on the radiation pattern of an antenna in a Master's thesis instructed by the author [129].

For investigation of the scatterer identification methods at sub-mm wavelengths and for trying to locate potential scatterers in the CATR during the construction of the range, the horizontal cut of the quiet-zone was probed with 0.45 mm (0.48 λ at 322 GHz) sample spacing using an open-ended waveguide probe. The plane wave spectrum computed using Fourier-transformation [O3, 129] is presented in Figure 8.13.

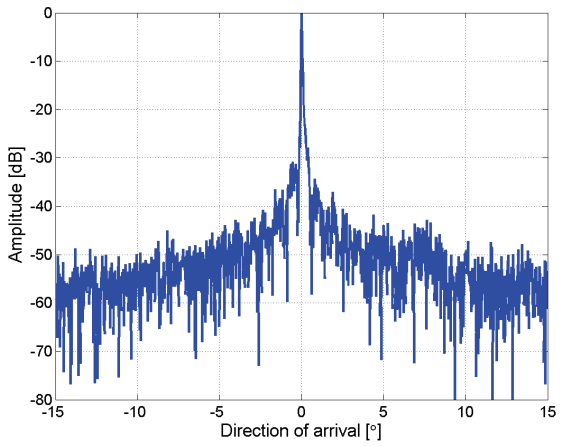

Figure 8.13 *Angular spectrum of the horizontal quiet-zone field cut.*

Unfortunately, the resolution and sensitivity of the angular spectrum did not allow identification of the scatters in the CATR but a weak stray signal can be seen around angle of arvival of +8–9°. This corresponds to the grating lobes around the -8.5° direction in the measured *H*-plane antenna pattern cut. During the antenna testing, additional absorbers were added on the walls of the measurement hall to reduce the reflections and erroneous sidelobes at large angles in the *H*-plane pattern cut.

Systematic distortions in the quiet-zone field affect also the main beam shape in the measured radiation pattern. Equation (8.1) can be used the evaluate the effect of the quiet-zone field on the effective aperture field and on the antenna pattern of the RTO. Unfortunately, the full two-dimensional quiet-zone field is not known as it could not measured – and the capability to measure it accurately using a near-field scanner would make the developed of a sub-mm wavelength CATR somewhat redundant. The two-dimensional quiet-zone field incident on the AUT aperture was estimated by interpolation from the measured four field cuts. The

interpolated quiet-zone field is presented in Figure 8.14 with circles marking the measured data.

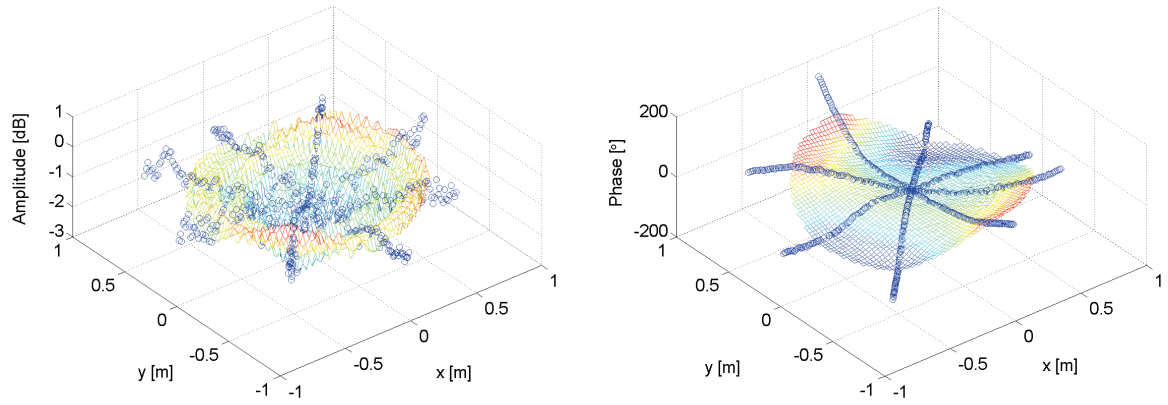

a) *b)*

Figure 8.14 *Estimated two-dimensional quiet-zone field [129]:*
a) amplitude,
b) phase.

The relatively few measured samples of the quiet-zone field do not allow very accurate predictions of the effect on the quiet-zone field on the antenna pattern over a wide angular range, but an estimate can be done around the main beam direction. In general, a phasefront curvature in the effective aperture field causes shoulders to the main beam, widens it and also increases the sidelobe level [44]. A dip in the amplitude acts opposite to amplitude taper increasing the sidelobe level. As can be seen in Figure 8.11, the measured main has a shoulder and the sidelobe level is higher than in the simulations. The potential errors in the antenna structure affect also the effective aperture field and the distortions in the antenna pattern are not caused only by the quiet-zone distortions.

The *H*- and *E*-plane cuts of the RTO simulated using GRASP8W with PO+PTD-analysis compared to the measured antenna pattern cuts and to the radiation of the distorted effective aperture field computed with (8.1) are shown in Figure 8.15. In Figure 8.16, the contour maps of the simulated RTO radiation pattern and the radiation pattern of the estimated effective aperture field are shown. The radiation pattern of the effective aperture field was computed using a program written by Ville Viikari for his Master's thesis [129].

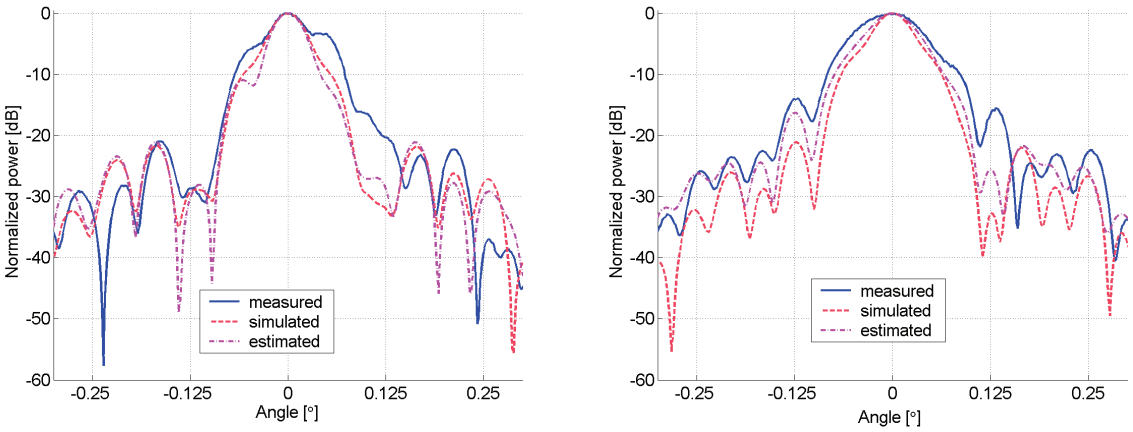

Figure 8.15 *Comparison of the measured, simulated and estimated radiation pattern of the RTO including the effect of the quiet-zone field on the simulated aperture field of the antenna:*
a) H-plane cut,
b) E-plane cut.

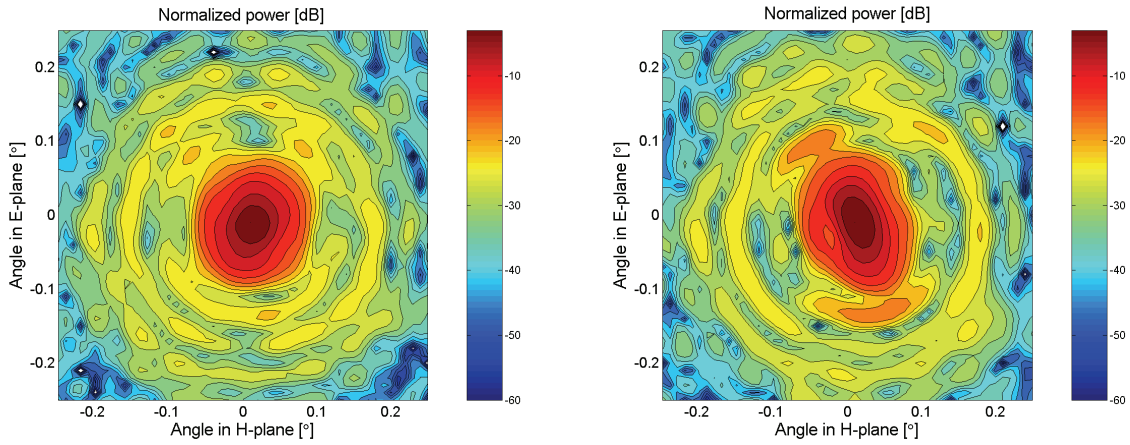

Figure 8.16 *Contour maps of the antenna pattern:*
a) simulated radiation pattern,
b) simulated radiation pattern including the estimated effect of the quiet-zone field.

The non-ideal quiet-zone field distorts the radiation pattern as can be seen in Figures 8.15 and 8.16. The effect is less significant in the pattern cuts shown in Figure 8.15, but especially in the *E*-plane cut the sidelobes match the measurement results better when the effect of the quiet-zone field is taken into account in the simulations. The effect of the quiet-zone field is quite dramatic in the contour maps shown in Figure 8.16: the shape elliptical contours is distorted and more importantly, the orientation of the elliptical contours is tilted to match approximately the orientation of the measured contours in Figure 8.9. The phase error in the quiet-zone field has a more significant effect on the measured radiation pattern than the amplitude error [129]. This means that the RTO radiation resembles the radiation of a contoured beam antenna, and the contour maps have to be measured to determine shapes of

the contours for complete understanding of the radiation pattern of the antenna. If only pattern cuts are measured, the overall shape of the antenna beam is not completely known as can be seen from the apparently moderate effect of the quiet-zone field on the antenna pattern cuts – the cuts may not so significant distortions but the overall pattern may still suffer from them. As the quiet-zone field distortions do not cause all the discrepancies between the simulations and measurements, it can be concluded that the ADMIRALS RTO structure deviates from the simulation model. The potential differencies in the structure are considered next.

8.2.3.2 Effect of the errors in the antenna structure

In addition to the quiet-zone field, the antenna itself affects the measured radiation pattern as the actual antenna is never entirely ideal and the antenna structure may deviate from the simulated structure due to manufacturing tolerances and errors. The objective of the antenna testing is to determine quantitatively the difference between the actual antenna radiation pattern and the designed antenna pattern – and the reasons for the discrepancies so that the antenna may be corrected if needed.

The radiation pattern of the RTO may deviated from the designed because of four reasons: there can be an error in the reflector surface, the reflector and/or feed position and alignment may be incorrect, the feed radiation illuminating the reflector may deviate from Gaussian, and because of scattering from the support structures. The support structures were covered with absorbers during the measurements and no difference could be observed in the results when the absorbers were removed. Therefore, it can be concluded that scattering from the support structures in the RTO does not contribute to the radiation pattern of the antenna. The receiver of the antenna has a quasi-optical network [124] and the possible phase errors in the beam are not known as no phase measurement data is available.

The reflector surface was measured at EADS Astrium with 396 points before the RTO was assembled. The measured distortions from the paraboloid are shown in Figure 8.17 a) and the simulated *H*-plane cut of the radiation pattern of the RTO reflector is compared to the simulated radiation pattern of the ideal paraboloid at 322 GHz in Figure 8.17 b).

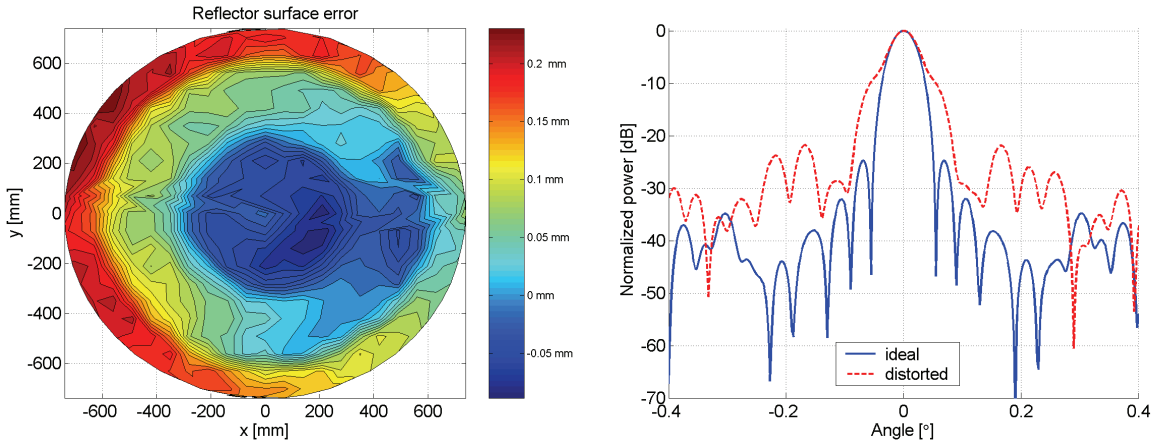

a) *b)*

Figure 8.17 *Distortions from the paraboloid:*
a) measured distortions in the reflector surface,
b) effect of the surface distortion on the simulated antenna pattern in a H-plane cut.

The maximum deviation from the ideal paraboloid surface are approximately 0.3 mm peak-to-peak, which is quite large compared to the wavelength of 0.93 mm. This surface error causes quite large phase error to the aperture field as can been seen in the simulated pattern cut compared to the radiation of the ideal paraboloid shown in Figure 8.17 b). As the radiation pattern of the distorted reflector surface differs greatly from the radiation of an ideal paraboloid even a reasonably slight deviation of the actual reflector surface from the measured shape may cause large discrepancies between the measurements and simulations.

The effect of feed dislocation and misalignment was also considered. As the f/D of the RTO is rather large with focal length f=3 m and antenna diameter D=1.5 m, the feed misalignment should also be rather large and visible when it causes significant beam distortions. The feed dislocation causes phase errors to the aperture field causing distortions to the antenna pattern. In order to study the potential feed offset, the feed (x,y,z)-coordinate was varied and the aperture field of the RTO was simulated. The z-axis was towards the reflector and x-axis was the horizontal axis. The effect of the quiet-zone field was taken into the account in the computation of the radiation pattern cuts that were compared to the measured cuts. The best fit to the measured H-plane cut in the main region was found at (+4, 0, -6) in millimetres and to the measured E-plane cut at (+1.5, +0.5, -4). The simulated pattern cuts including the effect of the quiet-zone field compared to the measured antenna pattern cuts are presented in Figure 8.18.

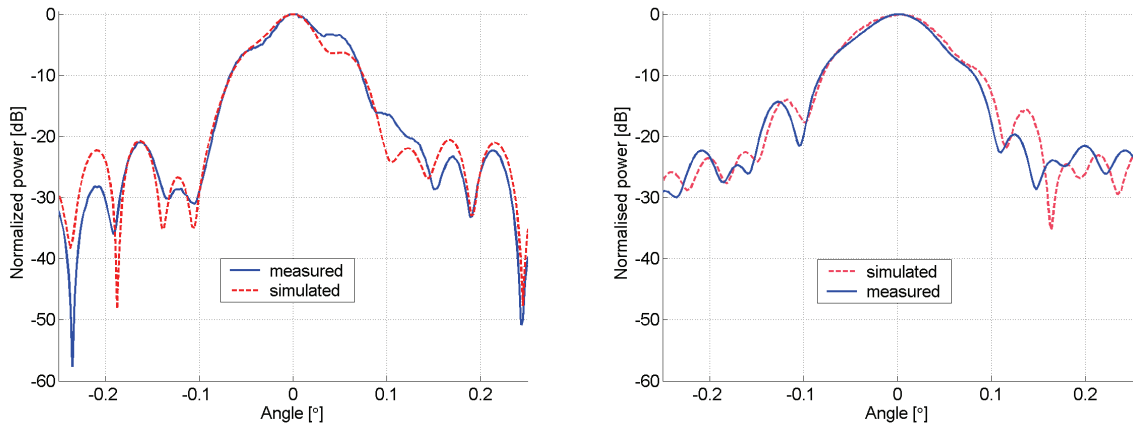

a) *b)*

Figure 8.18 *Simulated radiation pattern including the effect of the quiet-zone compared to the measured antenna pattern:*
a) H-plane cut
b) E-plane cut.

These feed offsets giving the best match to the main beam shape are too large to be real as this large offset should be clearly visible in the antenna structure. In addition, the best fit to the antenna pattern cuts is achieved at different locations, which indicates that the error is not the feed offset, but an aperture phase error caused either by the RTO feed phase error and/or by the reflector surface errors. The potential feed offset also contributes to this phase error. It has come to the author's attention that the RTO reflector surface has been measured again at EADS Astrium and there is a significant difference between the new more precise surface measurement and the original one done before the assembly of the antenna.

8.2.4 Results of the ADMIRALS RTO testing at 322 GHz

The radiation pattern of the ADMIRALS RTO was measured at the vertical polarisation at the frequency of 322 GHz in a compact antenna test range based on a hologram. The measured -3 dB beam width is 0.086° in the *E*-plane and 0.050° in the *H*-plane, which are somewhat larger than the simulated beam widths of 0.053° and 0.045°, respectively. The corresponce of the measurements and simulations is quite good and very good considering the challenges in sub-millimetre wave antenna testing as even the accurate manufacturing of the antennas is a challenge. The quiet-zone field distortions account some of the discrepancies between the measurements and simulations, but not all. Therefore, it can be concluded that the RTO operation differs from the simulations.

The difference in the RTO radiation from the simulations is mainly caused by reflector surface errors, i.e., the actual reflector surface differs from the measured surface, and/or by errors in the reflector illumination by the feed. In addition, the feed dislocation and misalignment may contribute to the distortions in the radiation pattern and also, the quiet-zone field may have a greater than the estimated effect on the measurement results as the two-dimensional quiet-zone was not complete known. For more precise test results more data are need - more data on the reflector surface and on the RTO feed radiation, especially on the phase in the antenna illumination.

The quiet-zone field quality was, althought the phase error was quite large, the best obtained in any CATR at sub-mm wavelengths to the author's knowledge as no phase measurement data for a sub-mm wavelength CATR quiet-zone have been published. Nevertheless, the quiet-zone field phase should still be better for precise antenna testing. In a on-going project funded by the European Space Agency (ESA), a hologram CATR for 650 GHz is being developed with intention to test a 1.5 m class antenna in the CATR to be constructed. The objective is to improve also the quiet-zone field quality.

9 Conclusions

In this thesis, a ray-tracing based shaped dual reflector synthesis procedure was developed for designing a sub-millimetre wavelength dual reflector feed system for a hologram-based compact antenna test range. The wavefronts and the reflector surfaces are approximated with local tangential planes, which allows a simple numerical implementation of the procedure. Approximately 200 × 200 rays are needed for the synthesis of the reflectors with smaller than λ/100 numerical surface errors at 310 GHz, but 423 × 401 were used to ensure sufficient numerical precision.

The developed synthesis procedure was used to design a dual reflector feed system (DRFS) consisting of two shaped hyperboloid-type reflectors. The DRFS is designed to illuminate the hologram in a CATR with a shaped beam with an amplitude described with a Butterworth-function and a spherical phasefront originating from the system focus. The transition from the shaped surface to the metal plate surface, on which the reflector are milled, was rounded to reduce edge diffraction disturbances to the DRFS beam. The resulting reflector sizes were 122 mm × 83 mm × 4.6 mm for the concave sub-reflector and 165 mm × 119 mm × 2.8 mm for the convex main-reflector. The DRFS design was verified with GRASP-simulations at the frequency of 310 GHz, where physical optics (PO) and physical theory of diffraction (PTD) were used to compute the radiated beam illuminating the hologram. The simulated DRFS beam corresponds well to the desired hologram illumination; the maximum deviation is less than 1 dB in amplitude and less than 20° in phase in the most significant region of the hologram illumination. The phase deviation can be mostly compensated by decreasing the distance of the DRFS from the hologram.

As the DRFS beam shape does not vary significantly over the distance, the designed DRFS can be used to illuminate holograms of different size. The performance of the designed DRFS is mostly affected by edge diffraction effects, which are not included in the synthesis procedure. At the highly shaped regions, the approximation of the reflector surfaces with local tangential planes may cause numerical inaccuracy in the synthesis as the tangential plane for each point is determined at a previously computed point on the reflector surfaces and there is a delay in the change of the surface tangent due to this. In addition to these simplifications in the synthesis, the amplitude and phase are assumed decoupled, i.e., the amplitude is shaped using the sub-reflector under the assumption that the phase is not affected, and the phase is corrected using the main reflector assuming that the amplitude is not changed. This assumption is not entirely correct and for more precise synthesis both the amplitude and phase should be modified simultaneously.

The manufacturing tolerances for the DRFS were estimated using GRASP-simulations with varying reflector positions and alignment for obtaining the maximum allowed errors in these. It can be concluded that the manufacturing tolerance for the reflector surface shape is ±5 μm and ±10 μm for the dimensions of the DRFS, i.e., for the reflector positions and alignment. In order to meet these tight tolerances, the DRFS was manufactured as an integrated quasi-optical system at Thomas Keating Ltd in England.

The DRFS beam was measured using a planar near-field scanner to probe the field incident on a hologram at 310 GHz using a corrugated horn as a probe. The measured beam corresponds very well to the simulated beam, and to the desired hologram illumination, as the measured amplitude is within ±0.3 dB of the simulated one and the measured phase is within 20° from the simulated phase in the central region of the beam. The DRFS was also used to illuminate a 600-mm diameter test hologram at 310 GHz to verify the applicability of the feed system for illuminating holograms in CATRs.

The quiet-zone of the hologram illuminated with the DRFS was compared to the quiet-zone of a hologram illuminated with a Gaussian beam from a corrugated horn: the RMS ripple was ±0.37 dB in amplitude and ±4.6° in phase for the hologram illuminated with the DRFS and ±0.23 dB in amplitude and ±4.8° in phase for the other hologram inside the 250 mm region corresponding to the quiet-zone. Considering the potential manufacturing errors in the holograms, the operation of these holograms is in practise identical. The hologram illuminated with the DRFS has much wider slots in the hologram pattern that are easier to etch.

The improvements to the hologram CATR performance using the shaped illumination with the DRFS were investigated experimentally with test holograms at 310 GHz. The main advantages of the DRFS are the improved manufacturability of the holograms and the operation of the holograms also at the horizontal polarisation. The shaped hologram illumination contains the amplitude taper needed to reduce edge diffraction eliminating the need for tapering the slots in the hologram pattern near the edges. As narrow slots are difficult to etch accurately and they are more sensitive to etching errors, hologram patterns with wider slots are easier to manufacture. This is a significant advantage especially for higher frequencies as the slot width is proportional to the wavelength. The tapering of the slots is not applicable for introducing amplitude taper to the hologram aperture at the horizontal polarisation as the transmission of the slots is only weakly dependent on the slot width at this polarisation. The shaped hologram illumination with the DRFS allows the holograms to operate also at the horizontal polarisation.

The relatively high cross-polarisation level in the quiet-zone of a hologram may be caused by the cross-polarisation of the hologram feed or by the cross-polarisation generated by the hologram itself. To determine which one of these factors causes the cross-polarisation level in the quiet-zone, a polarisation grid was placed between the DRFS and the hologram. The polarisation grid suppresses the cross-polarisation by approximately 21 dB. Based on this experiment, it is concluded that the hologram causes most of the cross-polarisation and therefore, the reduction of the cross-polarisation of the hologram is needed for improved cross-polarisation performance in hologram-based CATRs. The polarisation grid can be also placed between the hologram and the quiet-zone and then the cross-polarisation level is reduced to below -33 dB in the quiet-zone.

In order to improve the measurement accuracy in the near-field measurements using the existing planar near-field scanner, the measurement error sources and their contribution to the combined uncertainty at 310 GHz in the co-polarised amplitude and phase, and cross-polarisation level measurements were investigated. Based on this analysis, improvements to the measurement system and facilities were carried out. In the near-field measurements done for this thesis, the combined uncertainties for the relative co-polarised amplitude was ±0.1 dB in one-dimensional scans and ±0.2 dB in two-dimensional scans (contour maps), for the relative co-polarised phase ±14°–15° depending whether a plane wave or a spherical wave is under measurement in one-dimensional scans, and ±18°–20° in two-dimensional scans. The phase measurement uncertainty can be reduced further using error compensation techniques based on separate error measurements and computationally removing the measured error from the results. The phase measurement uncertainty is reduced to ±8°–9° in one-dimensional scans and to ±12°–14° in the two-dimensional scans. The uncertainty in the cross-polarisation level measurements was ±0.6 dB and ±1.0 dB in the one- and two-dimensional scans, respectively.

A CATR based on a 3-m diameter hologram at the frequency of 322 GHz was constructed for testing a 1.5 m reflector antenna, the ADMIRALS RTO. The CATR was assembled, the quiet-zone field was verified and optimised, the antenna tests were carried out and the range was disassembled in about two months. The measured quiet-zone field amplitude deviation was at maximum 2.6 dB peak-to-peak and the phase deviation was 250° peak-to-peak. Horizontal and vertical cuts were measured together with two-dimensional contour maps of the radiation pattern at the vertical polarisation. The measurement results were compared to the simulated antenna pattern; the correspondence was reasonable, but the quiet-zone field distortions have a significant effect on the measured pattern. However, they do not explain all the differences between the measured and simulated antenna pattern. Therefore, it is concluded that the shape of the reflector in the RTO is different from the measured surface used for modelling the antenna in the simulations.

The results and findings described in this research have produced additional or planned research activities in the Radio Laboratory, for example Master's thesis. The development of the DRFS for hologram-based CATRs continues and the benefits of using the shaped hologram illumination are being investigated further.

In summary, the main new scientific results of this thesis are:
1) the design of a shaped dual reflector feed system for sub-millimetre wavelength hologram based CATRs using the developed ray-tracing based reflector synthesis procedure,
2) the improvement of the hologram operation, especially, the hologram operation at the horizontal polarisation using the dual reflector feed system,
3) the facilitation of the hologram manufacturing using the dual reflector feed system
4) increased knowledge on the hologram CATR operation, especially the mechanisms contributing to the cross-polarisation level in the quiet-zone,
5) development of methods to improve measurement accuracy in planar-near field measurements allowing the extension of the usability of an existing near-field scanner for higher frequencies, and
6) demonstration of the applicability of the hologram-based CATR for sub-mm wave antenna testing and the analysis of the operation of a 1.5 m reflector antenna under test at 322 GHz.

References

[O1] J. Häkli, J. Ala-Laurinaho, A. V. Räisänen, "Numerical synthesis method for designing a shaped dual reflector feed system," *IEE Proceedings Microwaves, Antennas and Propagation*, vol.152, no. 5, pp. 311-318, 2005.

[O2] J. Häkli, T. Koskinen, J. Ala-Laurinaho, A. V. Räisänen, "Dual reflector feed system for hologram based compact antenna test range," *IEEE Transactions on Antennas and Propagation*, vol. 53, no. 12, pp. 3940–3948, 2005.

[O3] J. Häkli, T. Koskinen, A. Lönnqvist, J. Säily, J. Mallat, J. Ala-Laurinaho, V. Viikari, A. V. Räisänen, J. Tuovinen, "Testing of a 1.5 m reflector antenna at 322 GHz in a CATR based on a hologram," *IEEE Transactions on Antennas and Propagation*, vol. 53, no. 10, pp. 3142–3150, 2005.

[O4] A. Lönnqvist, T. Koskinen, J. Häkli, J. Säily, J. Ala-Laurinaho, J. Mallat, V. Viikari, J. Tuovinen, A. V. Räisänen, "Hologram-based compact range for submillimeter wave antenna testing," *IEEE Transactions on Antennas and Propagation* vol. 53, no. 10, pp. 3151–3159, 2005.

[O5] J. Häkli, J. Ala-Laurinaho, T. Koskinen, J. Lemanczyk, A. Lönnqvist, J. Mallat, A. V. Räisänen, J. Säily, J. Tuovinen, V. Viikari, "Sub-mm antenna tests in a hologram based CATR," *IEEE Antenna and Propagation Magazine*, vol. 47, issue 5, pp. 237–240, 2005.

[O6] J. Säily, J. Ala-Laurinaho, J. Häkli, J. Tuovinen, A. Lehto, A.V. Räisänen, "Test results of 310 GHz hologram compact antenna test range," *Electronics Letters*, vol. 36, no. 2,pp. 111–112, 2000.

[O7] J. Salo, J. Meltaus, E. Noponen, J. Westerholm, M. M. Salomaa, A. Lönnqvist, J. Säily, J. Häkli, J. Ala-Laurinaho, A.V. Räisänen, "Millimetre-wave Bessel beam using computer holograms," *Electronics Letters*, vol. 37, no. 13, pp. 834–835, 2001.

[O8] J. Salo, J. Meltaus, E. Noponen, M. M. Salomaa, A. Lönnqvist, T. Koskinen, V. Viikari, J. Säily, J. Häkli, J. Ala-Laurinaho, J. Mallat, and A. V. Räisänen, "Holograms for shaping radio-wave fields," *Journal of Optics A: Pure and Applied Optics*, pp. S161–S167, 2002.

[O9] J. Säily, J. Ala-Laurinaho, J. Häkli, T. Koskinen, A. Lönnqvist, J. Tuovinen, A.V. Räisänen, "Testing of satellite antennas with compact antenna test range based on a hologram," *IEEE Aerospace and Electronic Systems Magazine*, vol. 17, no. 5, pp.13-19, 2002.

[O10] J. Meltaus, J. Salo, E. Noponen, M. M. Salomaa, V. Viikari, A. Lönnqvist, T. Koskinen, J. Säily , J. Häkli , J. Ala-Laurinaho , J. Mallat , and A. V. Räisänen, "Millimeter-wave beam shaping using holograms," *IEEE Transactions on Microwave Theory and Techniques*, vol. 51, no. 4, pp. 1274-1280, 2003.

[O11] T. Koskinen, A. Lönnqvist, J. Ala-Laurinaho, J. Säily, J. Häkli, J. Mallat, J. Tuovinen, A.V. Räisänen, "Experimental Study on a Hologram Based Compact Antenna Test Range at 650 GHz," *IEEE Transactions on Microwave Theory and Techniques*, vol. 53, no. 9, pp. 2999–3006, 2005.

[O12] V. Viikari, J. Häkli, J. Ala-Laurinaho, J. Mallat, A. V. Räisänen, "A Feed Scanning Based APC Technique for Compact Antenna Test Ranges," *IEEE Transactions on Antennas and Propagation*, vol. 53, no. 10, 2005, pp. 3160–3165.

[O13] V. Viikari, J. Ala-Laurinaho, J. Mallat, J. Häkli, A. V. Räisänen, "A frequency shift technique for pattern correction in hologram-based CATRs," *IEEE Transactions on Antennas and Propagation*, submitted for publication.

[O14] J. Häkli, J. Säily J. Ala-Laurinaho, T. Koskinen, A. Lönnqvist, A. Lehto, J. Tuovinen, A. V. Räisänen, "Development of a hologram CATR for submm-wavelengths,"in *Proceedings of the 12th International Symposium on Space Terahertz Technology,* San Diego, California, USA, February 14–16, 2001, pp. 390–399.

[O15] J. Häkli, J. Ala-Laurinaho, J. Säily, T. Koskinen, A. Lönnqvist, J. Mallat, J. Tuovinen, A. V. Räisänen, "A dual reflector feed system for a sub-mm hologram CATR", in *Proceedings of the 13th International Symposium on Space Terahertz Technology,* Boston, USA, March 26 – 28, 2002, pp. 327-336.

[O16] J. Häkli, J. Ala-Laurinaho, T. Koskinen, J. Säily, A. Lönnqvist, J. Mallat, J. Tuovinen, A. V. Räisänen, "Synthesis of a dual reflector feed system for a hologram CATR," in *Digest of 2002 IEEE Antennas and Propagation Society International Symposium*, vol. 4, 2002, pp. 580-583.

[O17] J. Häkli, J. Säily, J. Ala-Laurinaho, A. Lönnqvist, T. Koskinen, J. Mallat, A. V. Räisänen, "Improving the measurement accuracy of a planar near-field scanner for submillimetre wave antenna testing," in *Proceedings of 3rd ESA Workshop on Millimetre Wave Technology and Applications*, Espoo, Finland, 21-23 May 2003, pp. 399-405.

[O18] J. Häkli, T. Koskinen, A. Lönnqvist , J. Ala-Laurinaho, J. Säily, J. Mallat, J. Tuovinen, A. V. Räisänen, J. Lemanczyk, "Dual reflector feed system for sub-mm wave region hologram CATR," in *Proceedings of 3rd ESA Workshop on Millimetre Wave Technology and Applications*, Espoo, Finland, 21-23 May 2003, pp. 353-358.

[O19] J. Häkli, J. Ala-Laurinaho, A.V. Räisänen, "Dual reflector feed system for a CATR based on a hologram," in *Proceedings of the 25th Annual Meeting & Symposium of the Antenna Measurement Techniques Association (AMTA)*, Irvine, CA., USA, Oct. 19-24, 2003, pp. 269–274.

[O20] J. Häkli, J. Ala-Laurinaho, T. Koskinen, J. Lemanczyk, A. Lönnqvist, J. Mallat, A. V. Räisänen, J. Säily, J. Tuovinen, V. Viikari, "Sub-mm antenna tests in a hologram based CATR," in *Proceedings of the AMTA2004 26th Annual Antenna Measurement Techniques Association Meeting and Symposium*, October 17-22 2004, Atlanta, USA, pp. 238–242.

[O21] J. Häkli, J. Ala-Laurinaho, T. Koskinen, A. Lönnqvist, J. Mallat, V. Viikari, J. Säily, A. V. Räisänen, J. Tuovinen, J. Lemanczyk, ”Mm- and sub-mm wave hologram based compact antenna test ranges used for electrical antenna testing,” in *Proceedings of the 28th Antenna Workshop on Space Antenna Systems and Technologies*, 31 May–3 June 2005, ESTEC, Noordwijk, the Netherlands, pp. 401–406.

[O22] J. Ala-Laurinaho, J. Säily, J. Häkli, J. Tuovinen, A. Lehto, A.V. Räisänen, ”Design of a 310 GHz Hologram Compact Antenna Test Range,” in *Proceedings of the 22nd ESTEC Antenna Workshop on Antenna Measurements*, ESTEC, Noordwijk, The Netherlands, 1999, pp. 159–162.

[O23] J .Säily, J. Ala-Laurinaho, J. Häkli, J. Tuovinen, A. Lehto, A.V. Räisänen, “Development of a 310 GHz hologram compact antenna test range,” in *Proceedings of the AMTA’99 Meeting and Symposium*, Monterey, CA, 1999, pp. 464–469.

[O24] J .Tuovinen, J. Ala-Laurinaho, J. Säily, J. Häkli, A .Lehto, A.V. Räisänen, ”Hologram - modern optics for millimetre and sub-millimetre wave antenna testing,” in *Proceedings of AP2000 Millenium Conference on Antennas and Propagation*, Davos, Switzerland, April 9–14, 2000.

[O25] J. Säily, J. Ala-Laurinaho, J. Häkli, J. Tuovinen, A. Lehto, A.V. Räisänen, “Instrumentation and testing of submillimeter wave compact antenna test range,” in *Proceedings of 11th International Symposium on Space Terahertz Technology*, May 1-3, Ann Arbor, USA, 2000, pp. 590–597.

[O26] A. V. Räisänen, J. Ala-Laurinaho, J. Säily, J. Häkli, T. Koskinen, A. Lönnqvist, J. Tuovinen, “Radio hologram CATR - a feasible method for FIRST/Herschel Space Observatory antenna testing?,” presented at *FIRST Science Workshop*, San Diego,USA, February 12–13, 2001.

[O27] A. V. Räisänen, J. Ala-Laurinaho, J. Säily, J. Häkli, T. Koskinen, A. Lönnqvist, E. Noponen, J. Salo, J. Meltaus, J. Westerholm, M. M. Salomaa, “Experimental studies on radio holograms at mm- and submm-wavelengths (invited paper),” in *Proceedings of the Fourth International Kharkov Symposium on Physics and Engineering of Millimeter and Submillimeter Waves (MSMW‘2001)*, June 4-9, Kharkov, Ukraine, 2001, pp. 57–62.

[O28] J. Salo, J. Meltaus, E. Noponen, J. Westerholm, M. M. Salomaa, A. Lönnqvist, J. Säily, J. Häkli, J. Ala-Laurinaho, J. Mallat, A.V. Räisänen, “Generation of millimeter-wave Bessel beams using amplitude and phase holograms, presented at European Optical Society, topical meeting, *Electromagnetic Optics 2,* Paris, France, August 26–30, 2001, p. 57.

[O29] A. V. Räisänen, J. Ala-Laurinaho, J. Säily, J. Häkli, T. Koskinen, A. Lönnqvist, V. Viikari, J. Mallat, E. Noponen, J. Salo, J. Meltaus, M. Weber, M. Salomaa, ”Computer generated holograms for mm- and submm-wave applications: CATR, Bessel beams and radiowave vortices (invited paper),” presented at 9th International Conference on Terahertz Electronics, October 15–16, Charlottesville, United States, 2001.

[O30] T. Koskinen, A. Ala-Laurinaho, J. Säily J. Häkli, A. Lönnqvist, J., Mallat, J. Tuovinen, A. V. Räisänen,"On the Design of Sub-MM Wave Amplitude Holograms for CATR," in *Proceedings of the 13th International Symposium on Space Terahertz Technology,* Boston, USA, March 26 – 28, 2002, pp. 537-543.

[O31] J. Meltaus, J. Salo, E. Noponen, M. M. Salomaa, A. Lönnqvist, T. Koskinen, J. Säily, J. Häkli, J. Ala-Laurinaho, J. Mallat, A. V. Räisänen, "Radio-wave beam shaping using holograms", in *Proceedings of the IEEE MTT-S International Microwave Symposium*, Seattle, Washington, June 2-7, 2002, pp. 1305-1308.

[O32] A. Lönnqvist, J. Ala-Laurinaho, J. Häkli, T. Koskinen, V. Viikari, J. Säily, J. Mallat, J. Tuovinen, A.V. Räisänen, "Manufacturing of large-sized amplitude holograms for a submm-wave CATR," in *Digest of 2002 IEEE Antennas and Propagation Society International Symposium*, Vol. 4, 2002, pp. 394-397.

[O33] T. Koskinen, J. Häkli, J. Säily, A. Lönnqvist, J. Ala-Laurinaho, J. Mallat, J. Tuovinen, A. V. Räisänen, J. Lemanczyk, "Hologram CATRs for 322 GHz and 650 GHz: A progress Report," *Proceedings of 25th ESA Antenna Workshop on Satellite Antenna Technology*, 18-20 September 2002, ESTEC, Noordwijk, The Netherlands, pp. 165–171.

[O34] A. V. Räisänen, J. Meltaus, J. Salo, T. Koskinen, A. Lönnqvist, J. Häkli, J. Säily, J. Ala-Laurinaho, J. Mallat, E. Noponen, M. M. Salomaa, "Computer-generated holograms for mm- and submm-wave beam shaping", (invited paper)," in *Conf. Digest of the 27th IEEE Int. Conf. On Infrared and Millimeter Waves, IRMMW2002*, San Diego, California, USA, 2002, pp. 113-114.

[O35] A. Lönnqvist, J. Mallat, E. Noponen, J. Ala-Laurinaho, J. Säily, T. Koskinen, J. Häkli, A.V. Räisänen, "A phase hologram compact RCS range for scale model measurements", in *Proceedings of 3rd ESA Workshop on Millimetre Wave Technology and Applications*, Espoo, Finland, 21-23 May 2003, pp. 511-516.

[O36] J. Ala-Laurinaho, J. Säily, T. Koskinen, J. Häkli, A. Lönnqvist, J. Mallat, J. Tuovinen, A.V. Räisänen, J. Lemanczyk, "Preparations for testing the ADMIRALS RTO in an ad hoc CATR based on a hologram", in *Proceedings of 3rd ESA Workshop on Millimetre Wave Technology and Applications*, Espoo, Finland, 21-23 May 2003, pp. 389-394.

[O37] T. Koskinen, J. Mallat, A. Lönnqvist, J. Säily, J. Häkli, J. Ala-Laurinaho, J. Tuovinen, A.V. Räisänen, "Performance of a small 650 GHz hologram," in *Digest of 2003 IEEE International Antennas and Propagation Symposium*, Columbus, OH, USA, vol. 3, 2003, pp. 532-535.

[O38] E. Noponen, A. Lönnqvist, J. Säily, J. Häkli, T. Koskinen, V. Viikari, J. Ala-Laurinaho, J. Mallat, A.V. Räisänen, J. Salo, J. Meltaus, M.M. Salomaa, "Phase-type diffractive element for planar millimeter-wave generation at 310 GHz," in *Proceedings of Northern Optics 2003, The joint conference of the Optical Societies of Denmark, Finland, Norway and Sweden*, June 16-18, 2003, Espoo, Finland, paper P097, p. 135.

[O39] A.V. Räisänen, A. Lönnqvist, J. Mallat, E. Noponen, J. Ala-Laurinaho, J. Säily, T. Koskinen, J. Häkli, "A compact RCS-range based on a phase hologram for scale model measurements at submm-wavelengths (invited plenary talk)," in *Proceedings of the 11th Microcoll*, Budapest, Hungary, September 10-11, 2003, pp. 105-108.

[O40] A.V. Räisänen, A. Lönnqvist, J. Mallat, E. Noponen, J. Ala-Laurinaho, J. Säily, T. Koskinen, J. Häkli, "A compact RCS-range based on a phase hologram for scale model measurements at submm-wavelengths (invited plenary talk)," in *Proceedings of the International Topical Meeting on Microwave Photonics, MWP2003*, Budapest, Hungary, September 10-12, 2003, pp. 55-58.

[O41] A.V. Räisänen, J. Ala-Laurinaho, T. Koskinen, A. Lönnqvist, J. Säily, J. Häkli, J. Mallat, V. Viikari, S. Ranvier, J. Tuovinen, "Computer-generated hologram and its use for submm-wave antenna measurement," in *2004 IEEE Aerospace Conference Proceedings*, Big Sky, MO, March 6-13, 2004, CD-ROM, ISBN: 0-7803-8156-4.

[O42] A.V. Räisänen, T. Koskinen, A. Lönnqvist, J. Häkli, J. Ala-Laurinaho, J. Mallat, J. Säily, "Recent results on using computer-generated submm-wave holograms for antenna and RCS measurements," in *MSMW'04 Symposium Proceedings, The Fifth International Kharkov Symposium on Physics an Engineering of Microwaves, Millimeter, and SubMillimeter Waves*, Kharkov, Ukraine, June 21–26, 2004, pp. 22–25.

[O43] A. Lönnqvist, J. Ala-Laurinaho, J. Häkli, T. Koskinen, J. Mallat, A.V. Räisänen, J. Säily, J. Tuovinen, "Antenna testing at 322 GHz in a hologram CATR," in *Proceedings of the 34th European Microwave Conference (EuMC),* 12-14 October 2004, Amsterdam, The Netherlands, pp. 553-556.

[O44] V. Viikari , J. Häkli, J. Ala-Laurinaho, J. Mallat, A. Lönnqvist, A. V. Räisänen, "Sub-mm antenna tests in a hologram based CATR," in *Proceedings of the AMTA2004 26th Annual Antenna Measurement Techniques Association Meeting and Symposium*, October 17-22 2004, Atlanta, USA, pp. 227–231.

[O45] T. Koskinen, J. Häkli, J. Ala-Laurinaho, A. Lönnqvist, V. Viikari, J. Mallat, A. V. Räisänen, "Study on the dual polarized operation of the hologram based compact antenna test range," in *Proceedings of the 28th Antenna Workshop on Space Antenna Systems and Technologies*, 31 May–3 June 2005, ESTEC, Noordwijk, the Netherlands, pp. 395–400.

[O46] J. Ala-Laurinaho, J. Mallat, J. Häkli, T. Koskinen, A. Lönnqvist, V. Viikari, V. Möttönen, S. Dudorov, D. Lioubtchenko, A. Lehto, A. V. Räisänen, " Millimetre wave antenna research at Helsinki University of Technology," in *Proceedings of ANTEM 2005* (invited paper), Saint Malo, France, June 1517, 2005, pp. 430-431.

[O47] A. Lönnqvist, J. Ala-Laurinaho, J. Häkli, T. Koskinen, J. Mallat, V. Viikari, A. V. Räisänen, "Hologram based compact ranges for antenna and RCS testing at submm waves," in *Proceedings of the 11th International Symposium on Antenna Technology and Applied Electromagnetics*, 2005, pp. 222-223.

[O48] T. Koskinen, V. Viikari, J. Häkli, A. Lönnqvist, J. Ala-Laurinaho, J. Mallat, A. V. Räisänen, ”A reflection-type amplitude hologram as a collimating element in the compact antenna test range,” in *Proceedings of the AMTA2005* October 17-22 2004, Atlanta, USA, pp. 417–421.

[O49] V. Viikari, J. Mallat, J. Ala-Laurinaho, J. Häkli, A. V. Räisänen, ”A reflection-type amplitude hologram as a collimating element in the compact antenna test range,” in *Proceedings of the AMTA2005* October 17-22 2004, Atlanta, USA, pp. 341–345.

[O50] T. Koskinen, J. Häkli, J. Ala-Laurinaho, A. Lönnqvist, J. Mallat, V. Viikari, A.V. Räisänen, ”Reduction of cross-polarisation in sub-millimetre-wave hologram-based CATR by using a polarisation grid,” in *Proceedings of 4th ESA Workshop on Millimetre Wave Technology and Applications*, Espoo, Finland, 15-17 February 2006, pp. 143-146.

[O51] E. Noponen, J. Häkli, T. Koskinen, A. Lönnqvist, V. Viikari, J. Ala-Laurinaho, J. Mallat, A. V. Räisänen, ”Synthesis of reflection-type phase hologram for compact antenna test range at 310 GHz,” in *Proceedings of 4th ESA Workshop on Millimetre Wave Technology and Applications*, Espoo, Finland, 15-17 February 2006, pp. 391-396.

[O52] J. Ala-Laurinaho, J. Häkli, A. Karttunen, T. Koskinen, A. Lönnqvist, E. Noponen, J. Mallat, M. Vaaja, V. Viikari, A. V. Räisänen, J. Lemanczyk, ”Hologram based CATR measurement of a 1.5 m antenna at 650 GHz: progress report,” in *Proceedings of 4th ESA Workshop on Millimetre Wave Technology and Applications*, Espoo, Finland, 15-17 February 2006, pp. 437-442.

[1] *Oxford English Dictionary*, 2nd Edition, Oxford University Press, 1989, [Online] available: http://dictionary.oed.com.

[2] A. D. Olver, P. J. B. Clarricoats, A. A. Kishk, L. Shafai, *Microwave Horns and Feeds*, The Institution of Electrical Engineers, London, England, 1994, 490 p.

[3] R. E. Collin, F. J. Zucker, *Antenna Theory, Part 2*, Inter-University Electronics Series,vol. 7, McGraw-Hill Book Company, New York, United States of America, 1969, 683 p.

[4] T. Li, “A study of spherical reflectors as wide-angle scanning antennas,” *IRE Transactions on Antennas and Propagation*, vol. 7, issue 3, pp. 223 – 226, 1959.

[5] B. Shen, W. L. Stutzman, “A scanning spherical tri-reflector antenna with a moving flat mirror,” *IEEE Transactions on Antennas and Propagation*, vol. 43, no. 3, pp. 270–276, 1995.

[6] Y. Mizugutch, M. Akagawa, H. Yokoi, “Offset dual reflector antenna,” in *Proceedings of Antennas and Propagation Society International Symposium*, vol. 14, 1976, pp. 2–5.

[7] F. S. Holt, E. L. Bouche, “A Gregorian corrector for spherical reflectors,” *IEEE Transactions on Antennas and Propagation*, vol. 12, Issue 1, pp. 44–47, 1964.

[8] D.-C. Chang, C.-C. Yang, S.-Y. Yang, "Dual-reflector system with a spherical main reflector and shaped subreflector for compact range," *IEE Proceedings Microwaves, Antennas and Propagation*, vol. 144, no. 2, pp. 97–102, 1997.

[9] R. E. Collin, *Antennas and Radiowave Propagation*, McGraw-Hill Book Company, United States of America, 1985, 508 p.

[10] P.-S. Kildal, L. A. Baker, T. Hagfors, "The Arecibo upgrading: electrical design and expected performance of the dual-reflector feed system," in *Proceedings of the IEEE*, vol. 82, no. 5, 1994, pp. 714–724.

[11] P.-S. Kildal, "Synthesis and analysis of a dual-reflector feed for the radiotelescope in Nancay," *IEE Proceedings Microwaves, Antennas and Propagation*, vol. 144, no. 5, pp. 289–296, 1997.

[12] C. Granet, G. L. James, J. Pezzani, "A new dual-reflector feed system for the Nancay radio telescope," *IEEE Transactions on Antennas and Propagation*, vol. 45, no. 9, pp. 1366–1373, 1997.

[13] J. R. Descardeci, C. G. Parini, "Trireflector compact antenna test range," *IEE Proceedings Microwaves, Antennas and Propagation*, vol. 144, no. 5, pp. 305–310, 1997.

[14] P. J. B. Clarricoats, A.D. Monk, H. Zhou, "Array-fed reconfigurable reflector for spacecraft applications," *IEE Proceedings Microwaves, Antennas and Propagation*, vol. 141, No. 6, pp. 531–535, 1994.

[15] G. Washington, H.-S. Yoon, M. Angelino, W. H. Theunissen, "Design, modelling and optimization of mechanically reconfigurable aperture antennas," *IEEE Transactions on Antennas and Propagation*, vol. 50, no. 5, pp. 628–637, 2002.

[16] R. E. Collin, F. J. Zucker, *Antenna Theory, Part 1*, Inter-University Electronics Series, vol. 7, McGraw-Hill Book Company, New York, United States of America, 1969, 666 p.

[17] K. Pontoppidan, *Technical Description of GRASP8*, TICRA Engineering Consultants, Denmark, 2002, 376 p.

[18] M. Kline, I. W. Kay, *Electromagnetic theory and geometrical optics*, John Wiley & Sons, Inc., New York, United States of America, 1965, 527 p.

[19] R. G. Kouyoumjian, P. H. Pathak, "A uniform geometrical theory of diffraction for an edge in a perfectly conducting surface," *Proceedings of the IEEE*, vol. 62, no. 11, pp. 1448–1461, 1974.

[20] J. D. Jackson, *Classical Electrodynamics*, John Wiley & Sons, Inc., New York, United States of America, 1999, 808 p.

[21] J. B. Keller, “Geometrical theory of diffraction,” *Journal of the Optical Society of America*, vol. 52, no. 2, 1962, pp. 116–130, 1962.

[22] C. A. Balanis, *Antenna Theory: Analysis and Design*, Harper & Row, Publishers, Inc., New York, United States of America, 1982, 790 p.

[23] D.-W. Duan, Y. Rahmat-Samii, ”A generalized diffraction synthesis technique for high performance reflector antennas,” *IEEE Transactions on Antennas and Propagation*, vol. 43, no. 1, pp. 27–40, 1995.

[24] A. Michaeli, “Equivalent edge currents for arbitrary aspects of observation,” *IEEE Transactions on Antennas and Propagation*, vol. AP-32, no. 3, pp. 252–258, 1984.

[25] A. Michaeli, “Correction to equivalent edge currents for arbitrary aspects of observation,” *IEEE Transactions on Antennas and Propagation*, vol. AP-33, no. 2, p. 227, 1985.

[26] J. Bergmann, R. C. Brown, P. J. B. Clarricoats, H. Zhou, “Synthesis of shaped-beam reflector antenna patterns,” *IEE Proceedings*, vol. 135, Pt. H, no. 1, pp. 48–53, 1988.

[27] B. S. Westcott, A. A. Zaporozhets, “Fast synthesis of aperture distributions for contoured beam reflector antennas,” *Electronics Letters*, vol. 29, no. 20, pp. 1735–1737, 1993.

[28] M. J. Mehler, “Spherical wave expansion for shaped beam synthesis,” *IEE Proceedings*, vol. 135, Pt. H, no. 5, pp. 327–332, 1988.

[29] B. S. Westcott, F. A. Stevens, F. Brickell, “GO synthesis of offset dual reflectors,” *IEE Proceedings*, vol. 128, Pt. H, no. 1, pp. 11–18, 1981.

[30] B. S. Westcott, F. Brickell, “Geometrical-optic synthesis of dual-reflector antennas with distributed sources,” *IEE Proceedings*, vol. 136, Pt. H, no. 5, pp. 361–366, 1989.

[31] V. Galindo-Israel, R. Mittra, A. G. Cha, “Aperture amplitude and phase control of offset dual reflectors,” *IEEE Transactions on Antennas and Propagation*, vol. AP-27, no. 2, pp. 154–164, 1979.

[32] V. Galindo-Israel, W. A. Imbriale, R. Mittra, “On the theory of the synthesis of single and dual offset shaped reflector antennas,” *IEEE Transactions on Antennas and Propagation*, vol. 35, no. 8, pp. 887–896, 1987.

[33] P.-S. Kildal, “Synthesis of multireflector antennas by kinematic and dynamic ray tracing,” *IEEE Transactions on Antennas and Propagation*, vol. 38, no. 10, pp. 1587–1599, 1990.

[34] P.-S. Kildal, “Analysis of numerically specified multireflector antennas by kinematic and dynamic ray tracing,” *IEEE Transactions on Antennas and Propagation*, vol. 38, no. 10, pp. 1600–1606, 1990.

[35] J. J. Lee, L. I. Parad, R. S. Chu, ”A shaped offset-fed dual-reflector antenna,” *IEEE Transactions on Antennas and Propagation*, vol. AP-27, no. 2, 1979, pp. 165–171, 1979.

[36] C. S. Lee, “A simple method of dual-reflector geometrical optics synthesis,” *Microwave and Optical Technology Letters*, vol. 1, no. 10, pp. 367–371, 1988.

[37] J. O. Rubiños-López, A. García-Pino, “A ray-by-ray algorithm for shaping dual-offset reflector antennas,” *Microwave and Optical Technology Letters*, vol. 15, no. 1, pp. 20–26, 1997.

[38] B. S. Westcott, A. A. Zaporozhets, “Dual-reflector synthesis based on analytical gradient-iteration procedures,” *IEE Proceedings Microwaves, Antennas and Propagation*, vol. 142, no. 2, pp. 129–135, 1995.

[39] S. G. Hay, “Dual-shaped-reflector directivity pattern synthesis using the successive projections method,” *IEE Proceedings on Microwaves, Antennas and Propagation*, vol. 146, no. 2, pp. 119–124, 1999.

[40] *IEEE Standard Definitions of Terms for Antennas*, IEEE Standard 145-1993, the Institute of Electrical and Electronics Engineers, United States of America, 1993, 36 p.

[41] *IEEE Standard Test Procedure for Antennas*, IEEE Standard 149-1979, the Institute of Electrical and Electronics Engineers, United States of America, 1979, 143 p.

[42] G. E. Evans, *Antenna Measurement Techniques*, Artech House, United States of America, 1990, 229 p.

[43] A. C. Ludwig, “The definition of cross polarization,” *IEEE Transactions on Antennas and Propagation*, vol. AP-21, no. 1, pp. 116–119, 1973.

[44] P. S. Hacker, H. E. Schrank, “Range distance requirements for measuring low and ultralow sidelobe antenna patterns,” *IEEE Transactions on Antennas and Propagation*, vol. AP-30, no. 5, pp. 956–966, 1982.

[45] R. C. Hansen, “Measurement distance effects on low sidelobe patterns,” *IEEE Transactions on Antennas and Propagation*, vol. AP-32, no. 6, pp. 591–594, 1984.

[46] M. A. Holdaway, J. R. Pardo, “*Modeling of the submillimeter opacity on Chajnantor*,” MMA Memo 187, available: http://www.alma.nrao.edu/memos/html-memos/alma187/memo187.html.

[47] A. D. Olver, “Compact antenna test ranges*,”* in *Proceedings of the Seventh International Conference on Antennas and Propagation (ICAP 91)*, 15-18 Apr 1991, vol.1, pp. 99–108.

[48] C. G. Parini, “Radiation pattern measurements of electrically large antennas using a compact antenna test range at 180 GHz,” *Electronics Letters*, vol. 24, no. 25, pp. 1552–1554, 1988.

[49] J. Habersack, H.-J. Steiner, E. Dudok, “Millimetre wave application up to 204 GHz of the compensated compact range,” in *IEE Colloquium on Antenna Measurements using the Compact Antenna Test Range*, 25 Jan 1991, pp. 3/1 - 3/7.

[50] J. Hartmann, J. Habersack, H.-J. Steiner, J. Lemanczyk, P. de Maagt, “Calibration and verification measurements in compensated compact ranges up to 500 GHz,” in *Proceedings of the 23rd AMTA Symposium*, Denver, 2001, pp. 377–382.

[51] R. C. Johnson, H. A. Ecker, R. A. Moore, “Compact range techniques and measurements,” *IEEE Transactions on Antennas and Propagation*, vol. 17, no. 5, pp. 568–576, 1969.

[52] V. J. Vokurka, “Compact-antenna range performance at 70 GHz,” in *Proceedings of the IEEE Antennas and Propagation Society Symposium*, Quebec, vol. 1, 1980, pp. 260–263.

[53] C. W. Pistorius, G. C. Clerici, W. D. Burnside, ”A dual chamber Gregorian subreflector system for compact range applications,” *IEEE Transactions on Antennas and Propagation*, vol. 37, no. 3, pp. 305–313, 1989.

[54] V. Galindo-Israel, S. R. Rengarajan, W. A. Imbriale, R. Mittra, “Offset dual-shaped reflectors for dual chamber compact ranges,” *IEEE Transactions on Antennas and Propagation*, vol. 39, no. 7, pp. 1007–1013, 1991.

[55] C. Parini, M. Rayner, C. Rieckmann, ”Design and construction of a 200 GHz demonstrator of a trireflector compact antenna test range with spherical main reflector,” in *Proceedings of the 22nd ESTEC Antenna Workshop on Antenna Measurements*, Noordwijk, Netherlands, 1999, pp. 147-152.

[56] A. D. Olver, A. A. Saleeb, “Lens type compact antenna range,” *Electronics Letters*, vol. 15, pp. 409–410, 1979.

[57] W. Menzel, B. Huder, “Compact range for millimeter-wave frequencies using a dielectric lens,” *Electronics Letters*, vol. 20, pp. 768–769, 1984.

[58] T. Hirvonen, J. Tuovinen, A. Räisänen, ”Lens-type compact antenna test range at mm-waves,” *Proceedings of the 21st European Microwave Conference*, Stuttgart, 1991, pp. 1079–1083.

[59] D. Gabor, “*Holography, 1948–1971*,” Nobel lecture, Available: URL: http://www.nobel.se/physics/laureates/1971/gabor-lecture.html.

[60] W.-H. Lee, ”Computer-generated holograms: techniques and applications,” in *Progress in Optics XVI*, E. Wolf, Ed. Amsterdam, the Netherlands, North-Holland, 1978, pp. 121–231.

[61] J. Tuovinen, A. Vasara, A. Räisänen, ”A new type of compact antenna test range,”in *Proceedings of the 22nd European Microwave Conference*, Espoo, 1992, pp. 503–508.

[62] T. Sehm, J. Ala-Laurinaho T. Hirvonen, A. V. Räisänen, ”Antenna measurements using a hologram CATR”, *Electronics Letters*, vol. 35, no. 10, pp. 757–758, 1999.

[63] J. Ala-Laurinaho, T. Hirvonen, P. Piironen, A. Lehto, J. Tuovinen, A. V. Räisänen, U. Frisk, ”Measurement of the Odin telescope at 119 GHz with a hologram type CATR,” *IEEE Transactions on Antennas and Propagation*, vol. 49, no. 9, pp. 1264–1270, 2001.

[64] T. Hirvonen, J. Ala-Laurinaho, J. Tuovinen, A. V. Räisänen, ”A compact antenna test range based on a hologram,” *IEEE Transactions on Antennas and Propagation*, vol. 45, no. 8, pp. 1270–1276, 1997.

[65] J. Ala-Laurinaho, T. Hirvonen, J. Tuovinen, A. V. Räisänen, ”Numerical modeling of a nonuniform grating with FDTD,” *Microwave and Optical Technology Letters*, vol. 15, no. 3, pp. 134–139, 1997.

[66] J. Ala-Laurinaho, *Numerical studies on a radio frequency hologram and its use in antenna measurements*, Doctoral Thesis, Helsinki University of Technology, 2001, 122 p.

[67] T. Koskinen, *Submillimetre wave compact antenna test range based on a hologram*, Licentiate Thesis, Helsinki University of Technology, 2004, 73 p.

[68] T. Hirvonen, J. Ala-Laurinaho, A. V. Räisänen, ”Performance analysis of a submillimeter wave hologram CATR,” in *Proceedings of the 27th European Microwave Conference*, Jerusalem, Israel, September 8–12, 1997, pp. 681–686.

[69] J. Ala-Laurinaho, T. Hirvonen, A. V. Räisänen, ”On the planarity errors of the hologram of the CATR,” in *Proceedings of the IEEE Antennas and Propagation International Symposium*, Orlando, Florida, USA, July 11–16, 1999, pp. 2166–2169.

[70] T. Koskinen, *Simulation of a hologram* (in Finnish), Master’s Thesis, Helsinki University of Technology, 2001, 77 p.

[71] A. Lönnqvist, J. Mallat, A. V. Räisänen, ”A phase hologram based compact RCS range for scale models,” in *Proceedings of the 25th AMTA Symposium,* Los Angeles, California, USA, 2003, pp. 118–123.

[72] J. Ala-Laurinaho, T. Sehm, J. Säily, A. V. Räisänen, ”Cross-polarization performance of the hologram compact antenna test range,” *Microwave and Optical Technology Letters*, vol. 27, no. 4, pp. 225–229, 2000.

[73] P. Petre, T. K. Sarkar, “Planar near-field to far-field transformation using an equivalent magnetic current approach,” *IEEE Transactions on Antennas and Propagation*, vol. 40, no. 11, pp. 1348–1356, 1992.

[74] A. D. Yaghjian, “An overview of near-field antenna measurements,” *IEEE Transactions on Antennas and Propagation*, vol. 34, no. 1, pp. 30–45, 1986.

[75] E. S. Gillespie, “A brief history of the compact range and the near-field range”,in *Proceedings of the IEEE Antennas and Propagation International Symposium*, vol. 4, July 8–13, 2001, pp. 436–439.

[76] D. Slater, “A 550 GHz near-field antenna measurement system for the NASA submillimeter wave astronomy satellite,” in *Proceedings of the 16th AMTA Symposium,* Long Beach, California, USA, 1994, pp. 267–272.

[77] Y. Rahmat-Samii, V. Galindo-Israel, R. Mittra, ”A plane-polar approach for far-field construction from near-field measurements,” *IEEE Transactions on Antennas and Propagation*, vol. 28, no. 2, pp. 216–230, 1980.

[78] L. I. Williams, Y. Rahmat-Samii, R. G. Yaccarino, “The bi-polar planar near-field measurement technique, part I: implementation and measurement comparisons,” *IEEE Transactions on Antennas and Propagation*, vol. 42, no. 2, pp. 184–195, 1994.

[79] E. B. Joy, D. T. Paris, “Spatial sampling and filtering in near-field measurements,” *IEEE Transactions on Antennas and Propagation*, vol. 20, no. 3, pp. 253–261, 1972.

[80] A. D. Yaghjian, “Antenna coupling and near-field sampling in a plane-polar coordinates,” *IEEE Transactions on Antennas and Propagation*, vol. 40, no. 3, pp. 304–312, 1992.

[81] M. S. Gatti, Y. Rahmat-Samii, ”FFT applications to plane-polar near-field antenna measurements,”, *IEEE Transactions on Antennas and Propagation*, vol. 36, no. 6, pp. 781–791, 1988.

[82] O. M. Bucci, C. Gennarelli, C. Savarese, “Fast and accurate near-field–far-field transformation by sampling interpolation of plane polar measurements,” *IEEE Transactions on Antennas and Propagation*, vol. 39, no. 1, pp. 48–55, 1991.

[83] R. G. Yaccarino, Y. Rahmat-Samii, L. I. Williams, ”The bi-polar planar near-field measurement technology, part II: near-field to far-field transformation and holographic imaging methods,” *IEEE Transactions on Antennas and Propagation*, vol. 42, no. 2, pp. 196–204, 1994.

[84] S. Blanch, R. G. Yaccarino, J. Romeu, Y. Rahmat-Samii, “Near-field to far-field transformation of bi-polar measurements by equivalent magnetic current approach,” in *Proceedings of the IEEE Antennas and Propagation International Symposium*, vol. 1, July 21–26, 1996, pp. 561–564.

[85] R. G. Yaccarino, L. I. Williams, Y. Rahmat-Samii, ”Linear spiral sampling for the bipolar planar near-field antenna measurement technique,” *IEEE Transactions on Antennas and Propagation*, vol. 44, no. 7, pp. 1049–1051, 1996.

[86] W. M. Leach, Jr., D. T. Paris, “Probe compensated near-field measurements on a cylinder,” *IEEE Transactions on Antennas and Propagation*, vol. 21, no. 4, pp. 435–445, 1973.

[87] F. Las-Heras, “Sequential reconstruction of equivalent currents from cylindrical near field,” *Electronics Letters*, vol. 35, no. 3, pp. 211–212, 1999.

[88] O. M. Bucci, C. Gennarelli, “Use of sampling expansions in near-field–far-field transformations: the cylindrical case,” *IEEE Transactions on Antennas and Propagation*, vol. 36, no. 6, pp. 830–835, 1988.

[89] S. Pierce, J. Langston,”Implementation of a geometric-error correction system for extremely high probe position accuracy in spherical near-field scanning,” in *Proceedings of the 26th AMTA Symposium,* Atlanta, Georgia, USA, 2004, pp. 93–97.

[90] J. E. Hansen, *Spherical Near-Field Antenna Measurements*, Peter Peregrinus Ltd., London, United Kingdom, 1988, 387 p.

[91] F. Jensen, A. Frandsen, “On the number of modes in spherical wave expansions,” in *Proceedings of the 26th AMTA Symposium,* Atlanta, Georgia, USA, 2004, pp. 489–494.

[92] F. Las-Heras, T. K. Sarkar, ”Radial field retrieval in spherical scanning for current reconstruction and NF–FF transformation,” *IEEE Transactions on Antennas and Propagation*, vol. 50, no. 6, pp. 866–874, 2002.

[93] J. C. Bennett, A. P. Anderson, P. A. McInnes, A. J. T. Whitaker, “Microwave holographic metrology of large reflector antennas,” *IEEE Transactions on Antennas and Propagation*, vol. 24, no. 3, pp. 295–303, 1976.

[94] Y. Rahmat-Samii, J. Lemanczyk, ”Application of spherical near-field measurements to microwave holographic diagnosis of antennas,” *IEEE Transactions on Antennas and Propagation*, vol. 36, no. 6, pp. 869–878, 1988.

[95] *Mmwave Antenna Testing Techniques – Phase 2*, MAAS Report 304, Issue no. 2, ESTEC Contract No 11641/95/NL/PB(SC), December 1996.

[96] R. C. Wittmann, B. K. Alpert, M. H. Francis, “Near-field antenna measurements using nonideal measurement locations,” *IEEE Transactions on Antennas and Propagation*, vol. 46, no. 5, pp. 716–722, 1998.

[97] R. C. Wittmann, B. K. Alpert, M. H. Francis, “Near-field, spherical scanning antenna measurements with nonideal measurement locations,” *IEEE Transactions on Antennas and Propagation*, vol. 52, no. 8, pp. 2184–2186, 2004.

[98] A. Repjar, D. P. Kremer, “Accurate evaluation of a millimetre wave compact antenna test range using planar near-field scanning,” *IEEE Transactions on Antennas and Propagation*, vol. 30, no. 3, pp. 419–425, 1982.

[99] P.-S. Kildal, J. J. Stamnes, “Asymptotic transition region theory for edge diffraction, part I: tracing transition regions via reflectors,” *IEEE Transactions on Antennas and Propagation*, vol. 38, no. 9, pp. 1350–1358, 1990.

[100] P.-S. Kildal, “Laws of geometrical optics mapping in multi-reflector antennas with application to elliptical apertures,” *IEE Proceedings*, vol. 136, Pt. H, no. 6, pp. 445–453, 1989.

[101] A. Murk, A. Magun, ”Characterization of Corrugated Horn Antennas for HIFI,” in *Proceedings of the 25th ESA Antenna Workshop on Satellite Antenna Technology*, ESTEC, Noordwijk, The Netherlands, 2002, pp. 159–164.

[102] *Performance of Corrugated horns at 600 GHz*, Thomas Keating Ltd., Available: URL: http://www.terahertz.co.uk/TKI/600GHzhorn/Bern.htm .

[103] T.-H. Lee, W. D. Burnside, “Performance trade-off between serrated edge and blended rolled edge compact range reflectors,” *IEEE Transactions on Antennas and Propagation*, vol. 44, no. 1, pp. 87–96, 1996.

[104] W. D. Burnside, M. C. Gilreath, B. M. Kent, G. L. Clerici, “Curved edge modification of compact range reflector,” *IEEE Transactions on Antennas and Propagation*, vol. 35, no. 2, pp. 176–182, 1987.

[105] I. J. Gupta, K. P. Ericksen, W.D. Burnside, “A method to design blended rolled edges for compact range reflectors,” *IEEE Transactions on Antennas and Propagation*, vol. 38, no. 6, pp. 853–861, 1990.

[106] M. S. A. Mahmoud, T.-H. Lee, W. D. Burnside, ”Enchanged compact range reflector concept using an R-card fence: two dimensional case,” *IEEE Transactions on Antennas and Propagation*, vol. 49, no. 3, pp. 57–65, 2001.

[107] H. H. S. Luh, ”Antenna geometries for shaped dual reflector antennas,” in *Digest of the IEEE Antennas and Propagation Society International Symposium*, vol. 2, 1997, pp. 1398–1401.

[108] C. Rieckmann, M. R. Rayner, C. G. Parini, “Optimisation of cross-polarisation performance for tri-reflector CATR with spherical main reflector,” *Electronics Letters*, vol. 35, no. 17, pp. 1403–1404, 1999.

[109] *Interferometric calibration gives sub 3u accuracy milling*, Thomas Keating Ltd., Available: URL: http://www.terahertz.co.uk/tki/DMG50V/accuracy.htm

[110] J. Säily, P. Eskelinen, A.V. Räisänen, “Pilot signal based real-time measurement and correction of phase errors caused by microwave cable flexing in planar near-field tests,” *IEEE Transactions on Antennas and Propagation*, vol. 51, no. 2, February, pp. 195–200, 2003.

[111] *A 650 GHz Hologram Compact Antenna Test Range*, Task 1 Report: Improvement of the hologram performance, ESTEC Contract No. 19131/05/NL/LvH, 2005, 38 p, unpublished.

[112] K. Nakamura, M. Ando, “A full-wave analysis of offset reflector antennas with polarization grids,” *IEEE Transactions on Antennas and Propagation*, vol. 36, no. 2, pp. 164–170, 1988.

[113] M. Ando, K. Takei, “Reflection and transmission coefficients of a thin strip grating for antenna application,” *IEEE Transactions on Antennas and Propagation*, vol. 35, no. 4, pp. 367–371, 1987.

[114] E. B. Joy, “Near-field range qualification methology,” *IEEE Transactions on Antennas and Propagation*, vol. 36, no. 6, pp. 836–844, 1988.

[115] A. C. Newell, “Error analysis techniques for planar near-field measurements,” *IEEE Transactions on Antennas and Propagation*, vol. 36, no. 6, pp. 754–768, 1988.

[116] J. Säily, A. V. Räisänen, “Characterization of submillimeter wave absorbers from 200–200 GHz,” International Journal of Infrared and Millimeter Waves, vol. 25, no. 1, pp. 71–99, 2004.

[117] A. Lönnqvist, A. Tamminen, J. Mallat, A. V. Räisänen, "Monostatic Reflectivity Measurement of Radar Absorbing Materials at 310 GHz*", IEEE Transactions on Microwave Theory and Techniques*, submitted for publication.

[118] *Leica Laser Tracker Features & Benefits*, Leica geosystems, Available: URL: http://www.leica-geosystems.com/metrology/en/products/laser_tracker/lgs_36108.htm.

[119] *MVNA-8-350 Millimeter Vector Network Analyzer 8-350 GHz (8–1000 GHz, option)*, AB Millimetre, supplement to the user manual, 1992.

[120] J. Säily, *Instrumentation of a Submillimetre Wave Hologram Compact Antenna Test Range*, Doctoral Thesis, Helsinki University of Technology, 2003, 89 p.

[121] G. E. Evans, *Introduction to Propability and Statistics*, McGaw-Hill, Inc., Singapore, 1995, 811 p.

[122] J. C. Bennett, K. S. Farhat, “Near-field measurements on plane-polar facility,” *IEE Proceedings*, vol. 136, Pt. H, no. 3, pp. 202–208, 1989.

[123] *Sub-millimetre wave antenna testing using a hologram CATR, Task 4 Report: Design and testing of a hologram CATR at 322 GHz*, Dno. Subholo-FR-Tko-01-03, 2003, 36 p, unpublished.

[124] J. Hartmann, J. Habersack, H.-J. Steiner, T. Rose, P. Zimmermann, “Transmit and receive modules for measurement of future space applications in the terahertz region,” in *Proceedings of the 23rd AMTA Symposium*, Denver, CO, 2001, pp. 171–176.

[125] T.-H. Lee, R. C. Rudduck, K. M. Lambert, “Pattern measurements of reflector antennas in the compact range and validation with computer code simulation,” *IEEE Transactions on Antennas and Propagation*, vol. 38, no. 6, pp. 889–894, 1990.

[126] W. D. Burnside, I. J. Gupta, “A method to reduce stray signal errors in antenna pattern measurements,” *IEEE Transactions on Antennas and Propagation*, vol. 42, no. 3, pp. 399–405, 1994.

[127] J. Appel-Hansen, “Reflectivity level of radio anechoic chambers,” *IEEE Transactions on Antennas and Propagation*, vol. 21, no. 4, 1973, pp. 490–498, 1973.

[128] R. O. Schmidt, “Multiple emitter location and signal parameter estimation,” *IEEE Transactions on Antennas and Propagation*, vol. 34, no. 3, pp. 276–280, 1986.

[129] V. Viikari, *Numerical studies on a radio frequency hologram and its use in antenna measurements (In Finnish)*, Master’s Thesis, Helsinki University of Technology, 2004, 66 p.